Stability Analysis of Supercritical Water Cooled Reactors

by

Jiyun Zhao

M.S., Nuclear Engineering, Tsinghua University, China (2000)
B.S., Thermal Engineering, Huazhong University of Sci. and Tech., China (1997)

SUBMITTED TO THE DEPARTMENT OF NUCLEAR SCIENCE AND ENGINEERING IN PARTIAL FULFILLMENT OF THE REQUIREMENTS FOR THE DEGREE OF

DOCTOR OF PHILOSOPHY IN NUCLEAR SCIENCE AND ENGINEERING

at the
MASSACHUSETTS INSTITUTE OF TECHNOLOGY
JULY 2005
[September 2005]

Signature of Author .....
Department of Nuclear Science and Engineering
July 28, 2005

Certified by .....
Mujid S. Kazimi, Ph.D.
TEPCO Professor of Nuclear Science and Engineering,
Professor of Mechanical Engineering
Thesis Supervisor

Certified by .....
Pradip Saha, Ph.D.
Research Scientist of Nuclear Science and Engineering
Thesis Reader

Accepted by .....
Jeffrey A. Coderre, Ph.D.
Chairman, Department Committee on Graduate Students

Stability Analysis of Supercritical Water Cooled Reactors

by
Jiyun Zhao

Submitted to the Department of Nuclear Science and Engineering on July 28, 2005, in partial fulfillment of the requirements for the degree of Doctor of Philosophy

Abstract

The Supercritical Water-Cooled Reactor (SCWR) is a concept for an advanced reactor that will operate at high pressure (25MPa) and high temperature (500°C average core exit). The high coolant temperature as it leaves the reactor core gives the SCWR the potential for high thermal efficiency (45%). However, near the supercritical thermodynamic point, coolant density is very sensitive to temperature which raises concerns about instabilities in the supercritical water-cooled nuclear reactors. To ensure a proper design of SCWR without instability problems, the U.S. reference SCWR design was investigated. The objectives of this work are: (1) to develop a methodology for stability assessment of both thermal-hydraulic and nuclear-coupled stabilities under supercritical pressure conditions, (2) to compare the stability of the proposed SCWR to that of the BWR, and (3) to develop guidance for SCWR designers to avoid instabilities with large margins.

Two kinds of instabilities, namely Ledinegg-type flow excursion and Density Wave Oscillations (DWO), have been studied. The DWO analysis was conducted for three oscillation modes: Single channel thermal-hydraulic stability, Coupled-nuclear Out-of-Phase stability and Coupled-nuclear In-Phase stability. Although the supercritical water does not experience phase change, the thermodynamic properties exhibit boiling-like drastic changes around some pseudo-saturation temperature. A three-region model consisting of a heavy fluid region, a heavy-light fluid mixture region and a light fluid region has been used to simulate the supercritical coolant flowing through the core. New non-dimensional governing parameters, namely, the Expansion Number (N_{exp}) and the Pseudo-Subcooling Number (N_{psub}) have been identified. A stability map that defines the onset of DWO instabilities has been constructed in the N_{exp}-N_{psub} plane based on a frequency domain method. It has been found that the U.S. reference SCWR will be stable at full power operating condition with large margin once the proper inlet orifices are chosen.

Although the SCWR operates in the supercritical pressure region at steady state, operation at subcritical pressure will occur during a sliding pressure startup process. At subcritical pressure, the stability maps have been developed based on the traditional Subcooling Number and Phase Change Number (also called as Zuber Number). The sensitivity of stability boundaries to different two phase flow models has been studied. It has been found that the Homogenous-Nonequilibrium model (HNEM) yields more conservative results at high subcooling numbers while the Homogenous Equilibrium (HEM) model is more conservative at low subcooling numbers. Based on the stability map, a stable sliding pressure startup procedure has been suggested for the U.S. reference SCWR design.

To evaluate the stability performance of the U.S. reference SCWR design, comparisons with a typical BWR (Peach Bottom 2) have been conducted. Models for BWR stability analysis (Single channel, Coupled-nuclear In-Phase and Out-of-Phase) have been constructed. It is found that, although the SCWR can be stable by proper inlet orificing, it is more sensitive to operating parameters, such as power and flow rate, than a typical BWR.

To validate the models developed for both the SCWR and BWR stability analysis, the analytical results were compared with experimental data. The Peach Bottom 2 stability tests were chosen to evaluate the coupled-nuclear stability analysis model. It was found that the analytical model matched the experiment reasonably well for both the oscillation decay ratios and frequencies. Also, the analytical model predicts the same stability trends as the experiment results. Although there are plenty of tests available for model evaluations at subcritical pressure, the tests at supercritical pressure are very limited. The only test publicly found was for the single channel stability mode. It was found that the three-region model predicts reasonable results compared with the limited test data.

Thesis supervisor: Dr. Mujid S. Kazimi
Title: TEPCO Professor of Nuclear Engineering; Professor of Mechanical Engineering;

Thesis reader: Dr. Pradip Saha
Title: Research Scientist of Nuclear Science and Engineering

Acknowledgements

The author would like to express his deepest sense of gratitude to his thesis advisor, Professor Mujid S. Kazimi, for continuous guidance and numerous discussions, for introducing the author to the interest area of flow stability, for many enlightening ideas and suggestions throughout the thesis work, without which this work could not be completed.

Special thanks are extended to Dr. Pradip Saha, for patient guidance, numerous suggestions and general assistances, such as for the non-dimensional analysis and helping in obtaining Dr. Zuber's very useful early work. The author also deeply appreciates the unforgettable weekly meetings with Dr. Saha, from which the author obtained numerous inspirations and comments.

It is author's great pleasure to thank Dr. Pavel Hejzlar for valuable suggestions, guidance and comments. His suggestions were very helpful in the SCWR in-phase stability analysis. The author also wants to take this opportunity to express his thanks to Dr. Hejzlar for his assistance in the early part of the thesis work, such as debugging of the ASME software for water properties.

The author is grateful to Professor Jacopo Buongiorno for providing the U.S. reference SCWR design information, without which the work could not be done successfully. Thanks are also due to Professor Kent F. Hansen for his kind guidance to the neutronic modal expansions. Special thanks are extended to Dr. Lin-wen Hu for her valuable suggestions and assistances.

The author also would like to express deep appreciation to his wife, Jie He, for her continuous love, encouragement and support. Half of the author's achievement belongs to her dedication.

Finally, the author is indebted to financial support partly from U.S. Department of Energy and partly from the Nuclear Regulatory Commission during his studies at MIT.

Table of contents

List of Figures

List of Tables

Chapter 1

Introduction

The supercritical water-cooled reactor (SCWR) is one of the six reactor types that are being investigated in the GEN-IV international advanced reactor development program. The SCWR is a combination of the traditional LWR and the supercritical FPP (Fossil Power Plant). It has a higher thermal efficiency for electricity generation than the present LWR. Since water will undergo no phase change above the thermodynamic critical point of 22.1MPa, the SCWR can operate at a high temperature level without the DNB (Departure from Nucleate Boiling) problem that limits the traditional LWR operating temperature. In the U.S. reference SCWR design [Buongiorno, 2003], supercritical water at 25MPa and 500°C exits the reactor core, which yields a plant thermal to electrical energy conversion efficiency of about 45%. However, the large temperature change in the reactor core (280°C at the inlet to 500°C at the exit) leads to a large water density reduction (780kg/m^3 to 90kg/m^3) through the SCWR core compared to that in the traditional GE BWR/6, where the coolant density changes roughly from 750kg/m^3 to 198kg/m^3. This gives rise to a concern about flow instabilities in the SCWR.

According to Lahey and Moody [1993], the instability types that are of interest in the BWR technology can be categorized into static and dynamic instabilities. The three static instability types are: flow excursion (Ledinegg) instability, flow regime "relaxation" instability and geysering type instability. The four dynamic instability types are: density-

wave oscillations, pressure drop oscillations, flow regime-induced instability and acoustic instability. From the reactor designer's viewpoint, the most important instability types are the Ledinegg instability and the density wave oscillations (DWO).

Recently, Podowski (2003) summarized the DWO instability types for BWR. According to Podowski, there are three types of DWOs for BWR. The first one is a single channel type, which means that only one channel or a small fraction of the parallel channels oscillates, while the other channels remain at steady state. This imposes a constant pressure drop boundary condition across the oscillating channel or channels. This type of DWO was also called as parallel channel type DWO by Podowski (2003). During the single channel oscillation, only a small fraction of the core flow oscillates while the bulk flow remains at steady state. Therefore, the neutronic feedback due to this small fraction oscillation can be neglected. In other words, the thermal-hydraulic dynamics is decoupled from the neutronic dynamics in the single channel oscillation. The second type is the region wide (or out-of-phase) instability. In this type of instability, about half of the core behaves out-of-phase from the other half [March-Leuba, 1993]. During the oscillation, half of the core rise in power while the other half decrease to maintain an approximately constant total core power. Also, the system adjusts flow from one half of the core to the other half while keeping the total flow rate almost constant. All of the channels will have the same but oscillating pressure drop [Munoz-Cobo, et al, 2002]. The third type was called the core wide in-phase instability, where the flow and the power in all of the channels oscillate in phase throughout the whole core.

Besides stability concerns at full power operation for the SCWR, stability at partial load operation during startup should also be considered. As discussed by Nakatsuka *et al.* (2001), two types of reactor startup procedures, namely the constant pressure and the sliding pressure, are possible. It is expected that the sliding pressure startup procedure will be less challenging to the pressure vessel material and will reduce cost by simplifying the plant and reducing the component size. Since the reactor may experience two-phase flow during the sliding pressure startup, it is also necessary to investigate the two-phase flow instability for the SCWR design.

In this thesis, the Ledinegg static instability, and three DWO modes instabilities mentioned above will be analyzed for the U.S. reference SCWR design both at steady state and sliding pressure startup. For comparison of the SCWR design with the traditional BWR design from stability view point, stability features for a typical BWR are also analyzed.

1.1 Literature review

Since the density wave oscillation is a well known phenomenon, substantial work has been done in this area. In the following, a brief literature review of the stability analysis for both subcritical and supercritical pressures is conducted.

1.1.1 Literature review for stability analysis at subcritical pressure

For a single heated two phase flow channel, Ishii (1971) constructed a stability boundary map to provide the stability margin for a specific operating condition. Once the stability boundary is provided, it is very easy for the designers to check the stability feature of their designs based on guidance of the stability maps. A thermal equilibrium two phase model was applied by Ishii (1971). A drift flux model was applied to take into account the non-homogenous feature of the two phase flow. It was found that the system pressure effects can be absorbed by the stability boundary, which means that the stability boundary is the same for different system pressures. Therefore, once a stability boundary map was constructed for a specific system pressure, it could be applied to other pressures also.

Saha (1974) improved Ishii's model by using a simplified non-equilibrium two phase flow model. By comparing the model with an experiment conducted by using a Freon-113 boiling loop, Saha (1974) found that the model matched the experimental data well.

Wang (1994) constructed a stability boundary map for a two phase natural circulation loop. A homogenous equilibrium two-phase flow model was used. He found that in addition to the density wave instability at high power level, an instability can occur at low power level.

Recently, Podowski (2003) studied the effects of different two phase flow models on stability boundary maps. The two-fluid model, drift flux model and HEM model were compared. It was found that the HEM model predicts a most conservative stability boundary.

As will be described later, a non-equilibrium non-homogenous two-phase flow model was developed by Zhao et al (2005) to construct a stability boundary map. The map has been applied to the stability analysis of the U.S. reference SCWR design sliding pressure startup process.

For the BWR coupled neutronic in-phase and out-of-phase stability, substantial works have been done and plenty of literature can be found. Detailed literature reviews can be found in Kao (1996), Karve (1998) and Hanggi (2001). The following papers have been useful during the present work.

March-Leuba (1993) provided a review of the state of the art for the coupled neutronic instabilities in boiling water cooled reactors. The topics discussed by this paper are: the observed instability modes in BWRs, physical mechanisms leading to instabilities in BWRs, sensitivity to physical parameters and codes used for BWR stability calculations.

Podowski (2003) provided a review of the BWRs stability analysis methods. The analysis methodologies were discussed for three density wave oscillation modes occurred in the BWRs, i.e. single channel, in-phase and out-of-phase. And the stability analysis effects of different two phase flow models were also discussed, as mentioned earlier.

Lahey (1993) provided a methodology for coupled neutronics core wide in-phase stability analysis of the BWR. The linear model in the frequency domain was discussed by Lahey. Although a very simple model was used, this book provides the general theory and method of the BWR stability analysis.

Kao (1996) developed a simulator for the BWRs in-phase stability analysis. Both the time domain and frequency domain methods were discussed and the models were benchmarked with the Peach Bottom-2 stability test data. The reactor core was simulated by two channels and a point kinetics neutronic dynamics model was applied.

Hanggi (2001) developed a linear code MATSTAB to analyze both the in-phase and out-of-phase stabilities in the BWRs. Using a response matrix method, this code solves the differential equations set directly without Laplace transform. This code implements detailed 3D neutronics model and Drift-Flux Non-Equilibrium thermal-hydraulics model. It simulates all the assembly channels in the core.

March-Leuba and Blakeman (1991) discussed the mechanism of the out-of-phase oscillations in Boiling Water Reactors. To demonstrate the out-of-phase oscillation, they coupled the first subcritical neutronic dynamics model with a thermal-hydraulics model, and found that the out-of-phase instability can occur even if the core-wide in-phase oscillation is stable. They indicated that for any operating condition, there is a threshold reactivity value above which the out-of-phase mode is more unstable that the in-phase mode. Then, they modified the frequency domain stability analysis code LAPUR to include the out-of-phase analysis capability.

Hashimoto (1993) conducted an out-of-phase stability analysis of BWRs and concluded that the absolute value of the reactivity coefficient should not be made too large in reactor design and the subcriticality should be kept as large as possible in fuel management and reactor operations to avoid the instability.

While March-Leuba and Blakeman (1991) and Hashimoto (1993) applied a linear model, a non-linear model was developed by Munoz-Cobo, et. al (1996, 2000). They integrated the momentum equation in the time domain and demonstrated the out-of-phase instability by increasing the feedback gain of the first subcritical mode.

Van der Hagen et al (2000) questioned the use of decay ratio (DR) in BWR stability monitoring. They argue that the DR can not give the stability margin which will mislead the operator, since a small DR does not mean a high stability margin. They appeal that instead of merely focusing on DRs, it would be beneficial to compare the sensitivity of the predicted DR-values to independent reactor variables as well.

1.1.2 Literature review for supercritical pressure stability analysis

Although flow instability studies of BWRs have a long history and there is extensive literature on instabilities in subcritical pressure two-phase flow, the literature on stability analysis in the supercritical pressure is very limited.

One of the early works in this area was that due to Zuber (1966). Recently, several papers were published on the Supercritical Water Cooled Reactor (SCWR) stability analysis.

The single channel stability for the U.S. reference design was analyzed by Yang (2003), but assuming no water rods heating. Following this paper, Yang (2005) expanded the model to consider the water rods heating effects.

Koshizuka et al (2003) and Yi et al (2004) analyzed the single channel stability for the Japanese SCWR design. Using a single channel core model, Yi et al (2004) studied the coupled neutronic in-phase stability feature of the Japan SCWR design.

Using a matrix multiplication method, Zhao et al (2004) studied the single channel stability features for both U.S. reference SCWR design and Supercritical CO_2 Cooled

Reactors. Stability boundary maps like in the subcritical pressure region have been developed by Zhao et al (2005) for the supercritical pressure region. The detailed methodology will be discussed in this thesis.

1.2 Research Objective

To ensure the proper design of SCWR without instability problems, a methodology of SCWR stability analysis has been developed in this work. The objectives of this thesis are:

(1) To develop a methodology for SCWR stability assessment both for thermal-hydraulic and nuclear-coupled stabilities,

(2) To compare the stability of the designs proposed to that of the BWR,

(3) To develop guidance for SCWR designers to avoid instabilities with large margins.

1.3 Review of the stability analysis methodologies

The methodologies that commonly applied for both Ledinegg instability analysis and density wave oscillations analysis were discussed in this section.

1.3.1 Ledinegg instability analysis

The Ledinegg type instability, also called as flow excursion, is a static instability since this kind of instability phenomenon can be explained by static laws.

The typical relationship of fluid pressure drop across a boiling channel versus inlet flow velocity is shown in Fig. 1-1 and marked as Δp_{system}. For parallel channels as in the SCWR core, the constant pressure drop boundary condition can be taken as $\Delta p_{external}$.

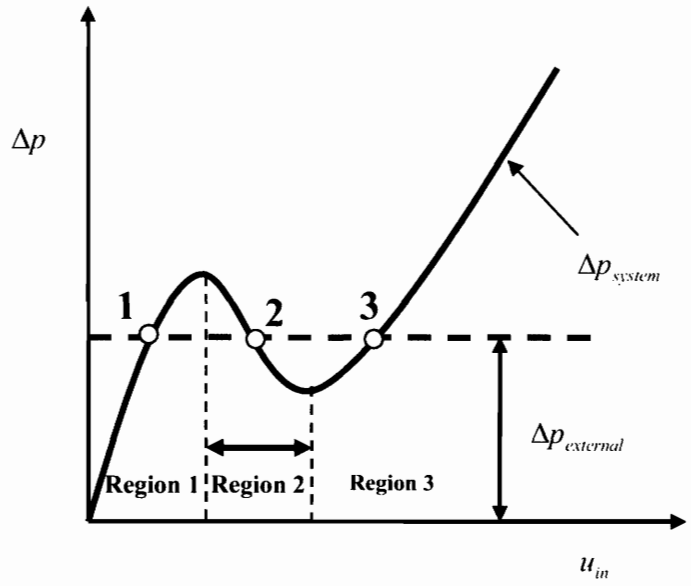

Fig. 1-1: Ledinegg instability (flow excursion)

From Fig. 1, it is seen that the system may operate in three regions. If the operating condition is in region 1, such as point 1, the system will be stable. Because if the inlet flow has a small perturbation, such as a small increase, the fluid pressure drop across the channel will be above the constant external pressure drop condition which will decrease the inlet flow rate such that the operating point will go back to point 1. Thus, the system can operate at point 1 stably. The same phenomenon will happen in region 3 which is also a stable region. However, if the operating point is in region 2, such as at operating point 2, a small increase of inlet flow will decrease the channel pressure drop below the constant external pressure drop. Thus, the inlet flow will increase again, until the operation shifts to point 3. On the other hand, a decrease in the flow of point 2 will shift the system to point 1. Thus, the operation in region 2 is unstable.

As seen from Fig.1-1, a stable boiling channel with constant external pressure drop should satisfy the follow relationship:

$$\frac{\partial(\Delta p_{system})}{\partial u_{in}} > 0 \qquad (1\text{-}1)$$

The relationship will be applied to SCWR channels to check for Ledinegg instability

1.3.2 DWO analysis methodology

For obtaining the reactor system DWO dynamic features analytically, there exist two ways to simulate the system: a non-linear model and a linear model.

In the non-linear stability analysis, two kinds of methods are widely used. One method is a numerical integration of the non-linear differential equations in the time domain. Many sophisticated transient codes, such as RAMONA-5B, RELAP5, RETRAN-3D and TRAC-G, can undertake this kind of analysis. The other kind of methods is so called theoretical methods, such as Hopf's bifurcations [Lahey and Podowski, 1989], the method of Lyapunov and harmonic quasi-linearization. Although the theoretical approach is capable of providing interesting insights into the nature of instabilities and identifying the stability boundaries for a simple model, the transient time domain codes are used more often for non-linear stability analysis.

For the linear stability analysis, the system models are simplified through linearization of the complex non-linear differential equations. The linear differential equations can be solved through Laplace transform in the frequency domain or directly solved in system response matrix form in the time domain. By using a system response matrix method, the complicated transfer function derivation which must be done in the frequency domain method, can be avoided. However, the system response matrix method collects all of the system information into one matrix, which makes the matrix very complicated. To

increase the computational speed, the matrix computation techniques such as sparse matrix and matrix partition must be applied [Hanggi, 2001].

Although some transient information is lost through model linearization, the high computational efficiency and relatively accurate results make the linear analysis methodology attractive, especially for prediction of the onset of instability. In fact, BWRs have been experimentally found to behave as linear systems under normal operating conditions [Carmichael, 1978]. Obviously, the transient codes are expected to represent the system more accurately without major simplifications, but the computational time consumption and numerical stability difficulties often plague the application of this method to determine the onset of instability. The linear model will be used in this thesis.

1.3.3 Thesis organization

Chapter 2 describes the U.S. reference SCWR design. The single channel stability analysis is presented in Chapters 3, 4, 5, 6 and 7. The coupled neutronics out-of-phase stability is analyzed in chapter 8 and the in-phase stability is in Chapter 9. Chapter 10 presents the conclusions and recommendations for future work.

Chapter 3 describes the response matrix method and its application to SCWR single channel stability analysis. A sensitivity analysis was conducted to investigate various parametric effects on decay ratio. Also, the Ledinegg type stability feature was checked.

In Chapter 4, a three region model for supercritical water is developed and the governing stability parameters are determined by non-dimensional analysis of the conservation equations. Finally, a stability map that defines the onset of instability is plotted in that governing parameters plane. The single channel stability model at supercritical pressure is validated by published experimental data. Also, the results calculated by using Laplace transformation method are compared with the response matrix method in this chapter.

In Chapter 5, the stability maps for the subcritical pressure region are developed. The effects of non-homogenous and non-equilibrium nature of two phase flow on the stability boundary are evaluated. This subcritical pressure stability model is also validated by experimental data. A suitable sliding pressure startup procedure free from flow instability and burnout problem is suggested.

A constant fuel surface heat flux model is applied for analysis in early chapters. To investigate the fuel dynamics effects on stability, a lumped fuel dynamics model is coupled with the coolant model in Chapter 6. Since the U.S. reference SCWR design introduce water rods to provide additional neutronic moderation, the water rods heating effects are also studied in this chapter.

The single channel stability comparison between the U.S. reference SCWR design and a typical BWR is conducted in Chapter 7. The stability sensitivities to power and flow are studied and compared for SCWR and BWR.

The region-wide out-of-phase and the core-wide in-phase instability modes are investigated in Chapter 8 and 9, respectively. The stability features of U.S. reference SCWR design are compared with typical BWR. The water rods heating effects on coupled neutronic stability modes are also studied. The coupled neutronic BWR stability model is benchmarked against the Peach Bottom-2 stability tests.

Chapter 2

Description of U. S. Reference Design

The U.S. reference SCWR design is a thermal neutron spectrum using supercritical water as the coolant. The system pressure is 25MPa with an inlet water temperature of 280°C and core average outlet temperature of 500°C. Due to the small coolant density, especially in the upper part of the core, water rods are required to provide additional moderation. The supercritical water flows into the reactor vessel through the inlet nozzle; then it splits and flows partly through the downcomer and partly through the water rods. After mixing in the lower plenum, water flows upward through the core channels to remove the fission energy. For the upward core flow, inlet orificing is expected to be used for improving the power to flow ratio and for stabilizing the SCWR system. The inlet orifice coefficient for the SCWR assemblies must be carefully selected to direct more flow to the higher power assemblies so as to minimize the differences in coolant enthalpy increase among different assemblies

2.1 Coolant flow path and conditions in SCWR

The coolant flow path in the Reactor Pressure Vessel (RPV) is illustrated in Fig. 2-1 [Buongiorno, 2003]:

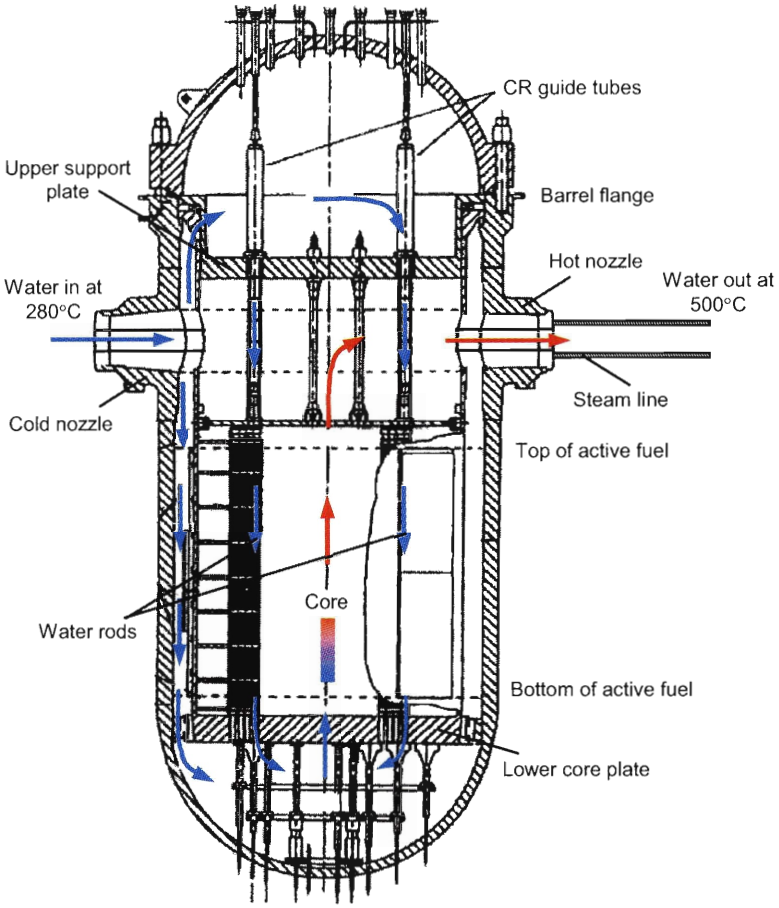

Fig. 2-1: SCWR Reactor Pressure Vessel

The supercritical water at 25MPa and 280°C flows into the RPV through the cold nozzle and splits into two parts. One part, about 10% of total inlet flow, goes down through the downcomer into the lower plenum. The other part, about 90% of total inlet flow, goes up into the upper plenum then flows down through the water rods and finally is mixed with that from the downcomer in the lower plenum. Then, the total flow goes up through the core to take out the fission energy. The coolant conditions and core power are summarized in Table 2-1.

Table 2-1: The SCWR coolant conditions and reactor power

Fluid	Water
Operating pressure	25MPa
Inlet/outlet temperature	280/500°C
Reactor flow rate	1843 kg/s
Total water rods flow (percentage)	90%
Thermal power	3575 MWt
Thermal efficiency for electricity generation	44.8%

2.2 SCWR core and fuel assembly description

Just like a BWR assembly, the SCWR assembly is also contained in a channel box to avoid coolant mixing among different assemblies. The reference design of the SCWR includes 145 such fuel assemblies. The core average power density is 70kW/L with a target power peaking factor of 2.0. The core pressure drop target is 0.15MPa which is comparable to the traditional PWR core pressure drop. The cross section of the SCWR core is illustrated in Fig. 2-2 [Buongiorno, 2003].

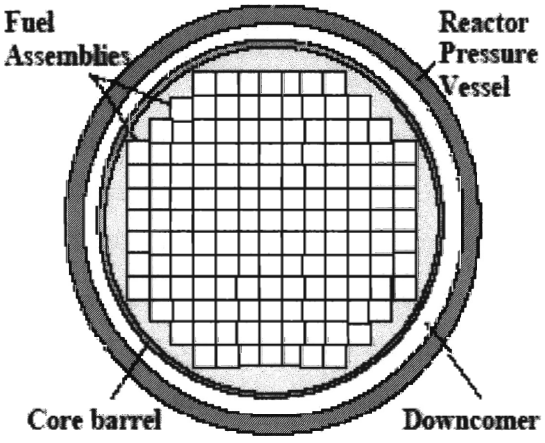

Fig. 2-2: U. S. reference SCWR core cross section

The cross section of the U.S. reference SCWR fuel assembly can be seen in Fig. 2-3 [Buongiorno, 2003]. The square water rods were introduced to provide additional neutronic moderation in the top part of the core, since the water density is quite low at that part of the core. Also, 16 control rods are placed in the water rods as shown in Fig. 2-3. The basic design parameters of the SCWR core and assembly are listed in Table 2-2. Due to introduction of water rods, the SCWR assembly hydraulic diameter is small, only about 3.4 mm.

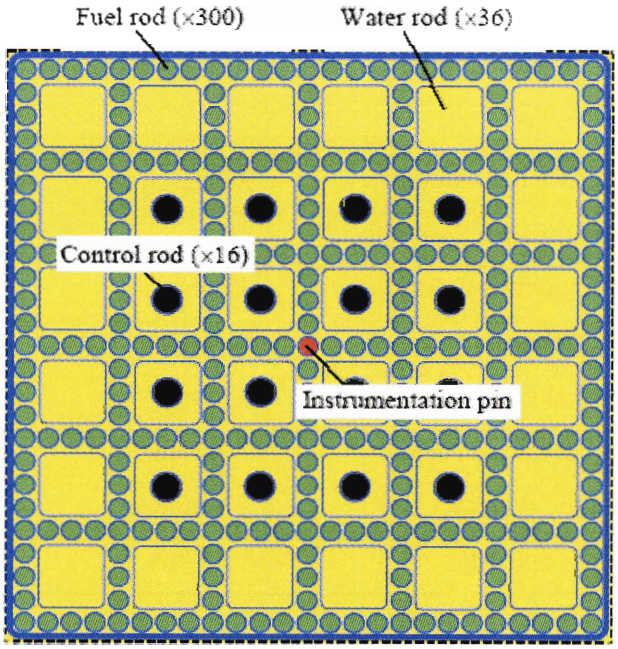

Fig. 2-3: SCWR fuel assembly

Table 2-2: SCWR U.S. reference design core and assembly parameters

Core	
Number of fuel assembly	145
Axial/Radial/Local/Total Peaking Factor	1.4/1.3/1.1/2.0 (best estimate)
Average power density	69.4 kW/L
Average linear power	19.2 kW/m
Peak linear power at steady state	39 kW/m
Target core pressure drop	0.15MPa
Water rod flow	1659 kg/s (90% of nominal flow rate)
Fuel assembly	
Number of Fuel pins per assembly	300
Number of water rods per assembly	36
Water rod side (outside dimension)	33.6 mm
Water rod wall thickness	0.4 mm
Assembly duct thickness	3 mm
Assembly side (outside dimension)	286 mm
Assembly hydraulic diameter	3.4 mm
Average inlet flow velocity	1.55 m/s

2.3 SCWR fuel pin description

Although the fuel pin diameter is comparable to that of the traditional LWRs, the fuel length of U.S. reference SCWR design is somewhat longer than that of the traditional LWRs. The basic design parameters of the fuel pin can be found in Table 2-3.

Table 2-3: U.S. reference design SCWR fuel pin parameters

Fuel pin OD	10.2 mm
Fuel pin pitch	11.2 mm
Heated length	4.27 m
Fission gas plenum length	0.6 m
Total fuel pin height	4.87m

2.4 Hot channel description

From Table 2-2, a radial power peaking factor of 1.3 has been chosen for the hot channel with an assumption of uniform axial heat flux. Since inlet orifices can be applied for the SCWR and the orifice coefficient can be adjusted to deliver more flow to the hot channel, the hot channel and average channel can have the same enthalpy rise.

It should be noted that, in reality, the same enthalpy rise in the hot and average channels may not be achieved exactly because of two reasons. First, the radial power profile changes with time and, secondly, due to design constraints, only zone-by-zone orificing can be provided (i.e., grouping together assemblies with similar power). However, orifice optimization can be sought to achieve a condition of similar enthalpy rise in all channels.

Chapter 3

Response matrix method and its application to SCWR single channel stability analysis

As shown in Fig. 2-3, the SCWR fuel assembly is contained in a channel box similar to a BWR assembly to avoid coolant mixing between different assemblies. During a single channel flow instability, the flow rate fluctuation of the unstable channel will not affect the flow of the remaining channels because the single channel flow is only a small fraction of the whole core flow. Therefore, a constant pressure drop boundary condition can be imposed on that single channel as shown in Fig. 3-1.

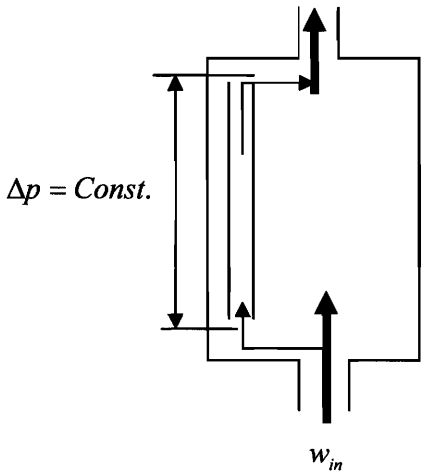

Fig. 3-1: Single channel illustration

Due to the small fraction of the single channel flow compared to that of the whole reactor core, the neutronic feedback due to the flow fluctuation of a single channel will not affect the whole core neutronic properties much. Therefore, a single channel can oscillate on its own without the neutronic feedback [March-Leuba and Rey, 1993]. Due to this reason, the single channel stability analysis of SCWR has not been coupled with neutronics. In other words, only the thermal-hydraulics model was implemented for the single channel stability analysis.

3.1 Analysis methodology

For investigating the dynamic features of a thermal-hydraulic system, the three governing equations are: the mass conservation equation, the momentum conservation equation and the energy conservation equation. These conservation equations along with the constitutive equations will close the system. Accordingly, the variables can be categorized to be state variables which are described by differential equations and constitutive variables which are described by algebraic equations. A detailed description of the response matrix method can be found in [Hanggi, 2001]. The set of system equations can be represented as follows:

$$\begin{aligned} \frac{d}{dt}x(t) &= f(x(t), y(t)) \\ 0 &= g(x(t), y(t)) \end{aligned} \text{, and} \qquad (3\text{-}1)$$

Where, $x(t)$ is the vector of state variables, and $y(t)$ is the constitutive variables.

Perturbation and linearization of Equation (3-1) yields the following first order ordinary differential and algebraic equations.

$$\frac{d}{dt}\delta x = \frac{\partial f}{\partial x}\delta x + \frac{\partial f}{\partial y}\delta y = A\delta x + B\delta y \qquad (3\text{-}2)$$

$$0 = \frac{\partial g}{\partial x}\delta x + \frac{\partial g}{\partial y}\delta y = C\delta x + D\delta y \tag{3-3}$$

If we solve the constitutive variables from Equation (3-3) and substitute them into Equation (3-2), we obtain a new differential equation set, which includes only the state variables, as:

$$\frac{d}{dt}\delta x = (A - BD^{-1}C)\delta x = A_s \delta x \tag{3-4}$$

The matrix A_s in the above Equation (3-4) is called the system matrix. However, the system equations considered here are very complicated. To avoid this kind of algebraic derivation work, a generalized system matrix will be constructed and the generalized eigenvalue problem will be solved as shown below.

$$\frac{d}{dt}\begin{bmatrix}\delta x \\ 0\end{bmatrix} = A_{general}\begin{bmatrix}\delta x \\ \delta y\end{bmatrix} \tag{3-5}$$

The generalized eigenvalue problem can be described as follows:

$$A_{general}e_i = \lambda_i B e_i \tag{3-6}$$

Where, the matrix B has the following form:

$$B = \begin{bmatrix} 1 & 0 & \cdots & 0 \\ 0 & \ddots & & \\ & & 1 & \\ \vdots & & 0 & \vdots \\ & & & \ddots \\ 0 & & & 0 \end{bmatrix}$$

Referring to the state variables

The detailed description of the generalized eigenvalue problem can be found in [Golub, 1996].

From the dynamic theory, if all of the eigenvalues of a system matrix $A_{general}$ have negative real parts, the disturbance will asymptotically decay away and the system is stable in that case. After sufficient time, the system oscillation can be determined by the eigenvalue which has the largest real part. This eigenvalue is called the dominant eigenvalue. For calculating the dominant eigenvalue, an inverse iteration combined with Newton's method was applied in this work. Details about this method can be found in [Peters and Wilkinson, 1979] and [Ilse, 1997]. This iteration method consists of the following algorithm:

1. Start with guess of e_o and λ_0
2. $$\begin{bmatrix} e_{k+1} - e_k \\ \lambda_{k+1} - \lambda_k \end{bmatrix} = -\begin{bmatrix} u_1^T & 0 \\ A_{general} - \lambda_k B & -Be_k \end{bmatrix} \backslash \begin{bmatrix} u_1^T e_k - 1 \\ (A_{general} - \lambda_k B)e_k \end{bmatrix}$$

Where, $u_1^T = [1,0,\cdots 0]$ is of the same size as e_k. The back slash "\" is a mathematic function in MATLAB; "A\b" means inverse "A" times "b" or "$A^{-1}b$".

3. $e_{k+1} = e_k + \Delta e$
4. $\lambda_{k+1} = \lambda_k + \Delta\lambda$
5. If $\left\| A_{general} e_{k+1} - \lambda_{k+1} e_{k+1} \right\| > tolerance$ goto step 2.

Using the above algorithm, the dominant eigenvalue $\lambda_1 = \sigma + i\varpi$ can be calculated very quickly. The system response to the dominant eigenvalue is illustrated in Fig. 3-2.

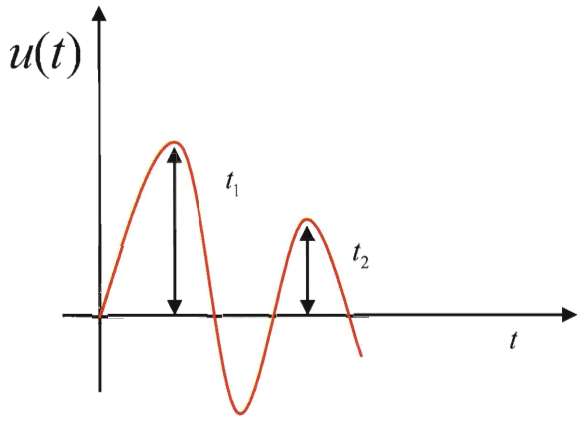

Fig. 3-2: Inlet velocity response corresponding to the dominant eigenvalue

Therefore, the decay ratio, DR, can be defined as the ratio of the amplitudes at time t_1 and t_2, i.e. at sequential oscillating periods.

$$DR = \frac{u(t_2)}{u(t_1)} = \exp(-2\pi \frac{\|\sigma\|}{\|\varpi\|}) \tag{3-7}$$

In the following section, this methodology is applied to calculate the Decay Ratio for a single channel of SCWR at supercritical pressure.

3.2 Decay ratio calculation for U.S. reference SCWR

The governing equations for SCWR at steady state for a single channel can be written as:

a) Mass conservation equation

$$\frac{\partial \rho}{\partial t} + \frac{\partial (\rho u)}{\partial z} = 0 \tag{3-8}$$

b) Energy conservation equation

$$\frac{\partial \rho h}{\partial t} + \frac{\partial (\rho u h)}{\partial z} = \frac{\partial p}{\partial t} + u\frac{\partial p}{\partial z} + \frac{P_h}{A_c} q''(z,t) \tag{3-9}$$

c) Momentum conservation equation

$$\frac{\partial (\rho u)}{\partial t} + \frac{\partial (\rho u^2)}{\partial z} = -\frac{\partial p}{\partial z} - \rho g - \frac{f}{D_e}\frac{\rho u^2}{2} \tag{3-10}$$

d) Coolant state equation

$$\rho = \rho(p,h) \tag{3-11}$$

Out of the above four equations, the coolant state equation is the constitutive equation while the mass, momentum and energy conservation equations are the system state equations. After linearization and perturbation of the above four equations, one can obtain three first order differential equations corresponding to three state variables. The state variables were chosen as: pressure p, enthalpy h and coolant velocity u. If the system is divided into n axial nodes, the fluctuation of coolant density at node i can be obtained from the state equation:

$$\delta\rho_i = \xi_i \delta h_i + \eta_i \delta p_i \tag{3-12}$$

Where, ξ_i and η_i are the derivatives of the coolant density with respect to enthalpy and pressure at node i.

$$\xi_i = \left(\frac{\partial \rho}{\partial h}\bigg|_p\right)_i$$

$$\eta_i = \left(\frac{\partial \rho}{\partial p}\bigg|_h\right)_i \tag{3-13}$$

Applying the above constitutive equation to node i and ignoring the fluctuation of surface heat flux, we obtain the following three differential equations:

$$\frac{d\delta h_i}{dt} = \frac{u_{i-1}(h_{i-1}-h_i)\xi_{i-1}+\rho_{i-1}u_{i-1}}{\Delta z\rho_i}\delta h_{i-1} + \frac{u_{i-1}(h_{i-1}-h_i)\eta_{i-1}}{\Delta z\rho_i}\delta p_{i-1} + \frac{\rho_{i-1}(h_{i-1}-h_i)}{\Delta z\rho_i}\delta u_{i-1}$$

$$-\frac{\rho_{i-1}u_{i-1}}{\Delta z\rho_i}\delta h_i \qquad (3\text{-}14)$$

$$\frac{d\delta u_i}{dt} = \frac{1-u_{i-1}(u_i-u_{i-1})\eta_{i-1}}{\Delta z\rho_i}\delta p_{i-1} - [\frac{1}{\Delta z\rho_i}+(\frac{g}{\rho_i}+\frac{f_i u_i^2}{2D_e\rho_i})\eta_i]\delta p_i - \frac{u_{i-1}(u_i-u_{i-1})\xi_{i-1}}{\Delta z\rho_i}\delta h_{i-1}$$

$$-(\frac{g}{\rho_i}+\frac{f_i u_i^2}{2D_e\rho_i})\xi_i\delta h_i - \frac{\rho_{i-1}(u_i-2u_{i-1})}{\Delta z\rho_i}\delta u_{i-1} - (\frac{\rho_{i-1}u_{i-1}}{\Delta z\rho_i}+\frac{f_i u_i}{D_e})\delta u_i \qquad (3\text{-}15)$$

$$\frac{d\delta p_i}{dt} = [\frac{\rho_{i-1}}{\Delta z\eta_i} - \frac{\rho_{i-1}(h_{i-1}-h_i)}{\Delta z\rho_i\eta_i}\xi_i]\delta u_{i-1} - \frac{\rho_i}{\Delta z\eta_i}\delta u_i + \frac{\rho_{i-1}u_{i-1}-\rho_i u_i}{\Delta z\rho_i\eta_i}\xi_i\delta h_i - \frac{u_i}{\Delta z}\delta p_i$$

$$+[\frac{u_{i-1}\xi_{i-1}}{\Delta z\eta_i} - \frac{u_{i-1}(h_{i-1}-h_i)\xi_{i-1}+\rho_{i-1}u_{i-1}}{\Delta z\rho_i\eta_i}\xi_i]\delta h_{i-1} + [\frac{u_{i-1}\eta_{i-1}}{\Delta z\eta_i} - \frac{u_{i-1}(h_{i-1}-h_i)}{\Delta z\rho_i\eta_i}\xi_i\eta_{i-1}]\delta p_{i-1}$$

(3-16)

The single channel nodalization and perturbations of the state variables are illustrated in Fig. 3-3.

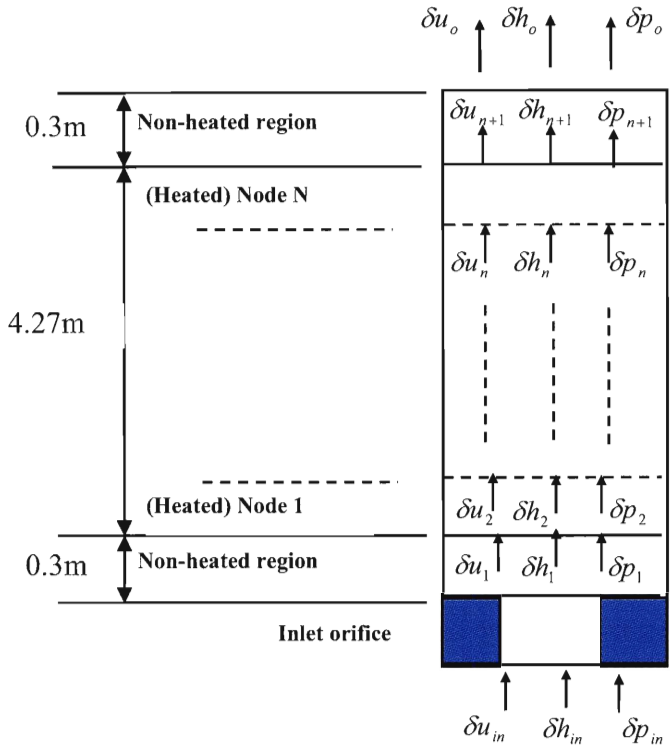

Fig. 3-3: SCWR single channel nodalization and perturbation

It can be seen from Fig. 3-3 that there are $(N+3)$ nodes in the single channel consisting of N heated nodes, one inlet orifice node, one lower gas plenum (non-heated) node and one upper gas plenum (non-heated) node. Therefore, there are in total $3(N+4)$ state variables, since the variables are defined at node boundaries. Applying Equations (3-14) to (3-16) at every node, $3(N+3)$ equations can be obtained. Thus, 3 additional equations or boundary conditions are required to close the system. The boundary conditions used in the present analysis are as follows:

a). Ignore the fluctuation of inlet enthalpy, i.e. $\delta h_{in} = 0$

b). If the inlet and outlet pressures are assumed constant, $\delta p_{in} = 0$ and $\delta p_{exit} = 0$, this automatically satisfies the constant pressure drop boundary condition $\delta \Delta p = 0$ across the single channel.

Writing the above mentioned $3(N+4)$ equations in matrix form described as Equation (3-5), one can obtain the generalized system matrix $A_{general}$. Then, using the decay ratio calculation methodology described in section 3.1, we calculate the decay ratios for single hot and average channels.

3.3 Results for U.S. reference SCWR design

As mentioned earlier, for SCWR, an inlet orifice scheme is expected to be used to adjust the flow distribution among fuel assemblies to ensure that the hot and the average channels have almost the same coolant properties at any height within the core. From Table 2, it can be seen that the radial power peaking factor of the hot channel is 1.3; thus, to obtain the same enthalpy rise in the hot and the average channels, the flow rate of the hot channel should also be 1.3 times that of the average channel.

A uniform axial heat flux profile was assumed. The usual BWR thermal-hydraulic stability criterion of decay ratio less than 0.5 was assumed for both the hot and the average channel analyses.

3.3.1 The axial mesh size effects on decay ratio

Using a traditional Laplace transformation method, Yang and Zavaljevski (2003) found that the decay ratio is significantly dependent on the axial mesh size. To obtain the decay ratios at zero mesh size, the decay ratios at several axial mesh sizes were calculated and extrapolated to zero mesh size. To determine the axial mesh size effects on decay ratio for the response matrix method, the decay ratios at different mesh sizes were calculated for the hot channel at inlet orifice coefficient 20. The results are presented in Table 3-1.

Table 3-1: Mesh size effects on decay ratio for the hot channel (inlet orifice coefficient 20)

Axial nodes number	40	60	80	100
Axial mesh size (m)	0.1068	0.0712	0.0534	0.0427
Decay ratio	0.1066	0.1107	0.1132	0.1143

The data in Table 3-1 is shown graphically in Fig. 3-4.

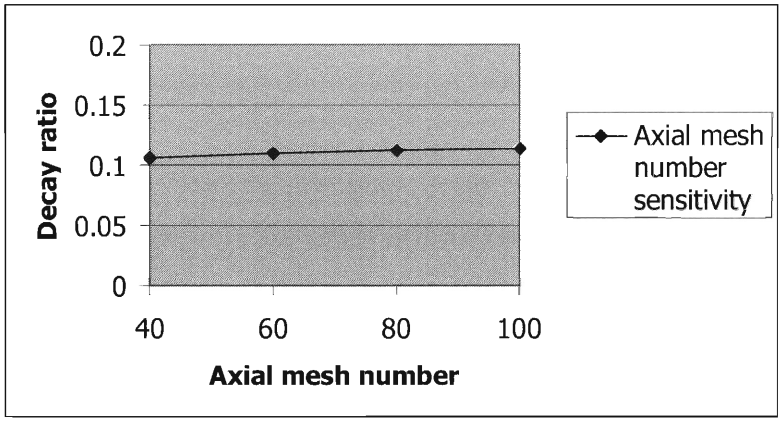

Fig. 3-4: Decay ratio dependence on axial mesh number

From Table 3-1 and Fig. 3-4, it is seen that the decay ratio is not significantly dependent on mesh size, especially at high node number, say above 40. Therefore, eighty (80) nodes were applied axially for the following analysis.

3.3.2 Minimum inlet orifice coefficient for the hot channel

The inlet orifice coefficient has a very important role in the system stability characteristics. The decay ratios at different inlet orifice coefficient values for the hot channel are plotted in Fig. 3-5.

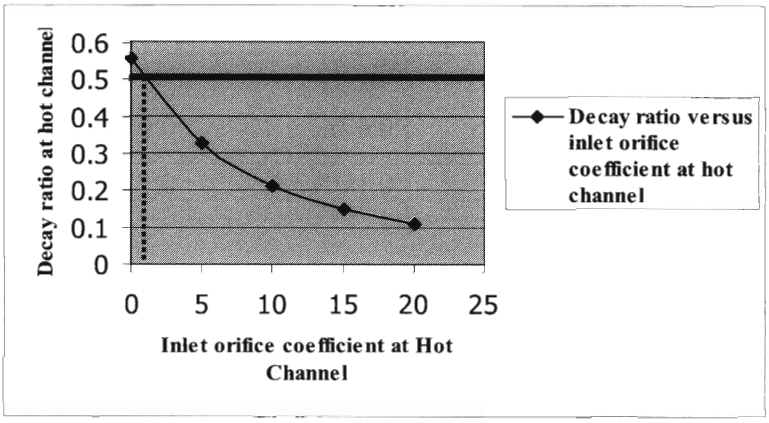

Fig. 3-5: SCWR hot channel decay ratios at different inlet orifice coefficient

From Fig. 3-5, it is seen that the decay ratio will be below 0.5 if the inlet orifice coefficient for the hot channel is greater than about 1.0. However, to have a more stable system and to account for uncertainties and off-normal conditions, the designer should select a larger value; say 10 to 20, for the hot channel inlet orifice coefficient.

The choice of the inlet orifice coefficient has dual influences. A higher orifice coefficient will stabilize the system. On the other hand, a higher orifice coefficient will produce a higher core pressure drop, and that means higher coolant pumping power, which, in turn, is harmful from the economics viewpoint. However, an inlet orifice coefficient of 20.0 for the hot channel would produce a core pressure drop of 0.163MPa which is quite close to the target core pressure drop of 0.15MPa, and thus should be acceptable.

With the inlet orifice coefficient of 20.0, the decay ratio for the hot channel is only 0.11 as seen from Fig. 3-5. Thus, the hot channel will be very stable, and in all the following calculations, the inlet orifice coefficient of the hot channel has been assumed to be 20.0. For comparison, a typical BWR/4 has an inlet orifice coefficient of 27.8 at the hot channel [Lahey & Moody, 1993].

3.3.3 Sensitivity analysis of hot channel stability with inlet orifice coefficient of 20.0

The decay ratio sensitivity analysis for three key system parameters is addressed in this part: mass flow rate, power and system pressure. Full 100% nominal flow rate and full 100% nominal power at a system pressure of 25MPa are taken as the reference conditions.

1. Mass flow rate sensitivity analysis

The decay ratios have been calculated for reduced mass flow rate, while keeping the power and the pressure at reference conditions. The results are illustrated in Fig. 3-6.

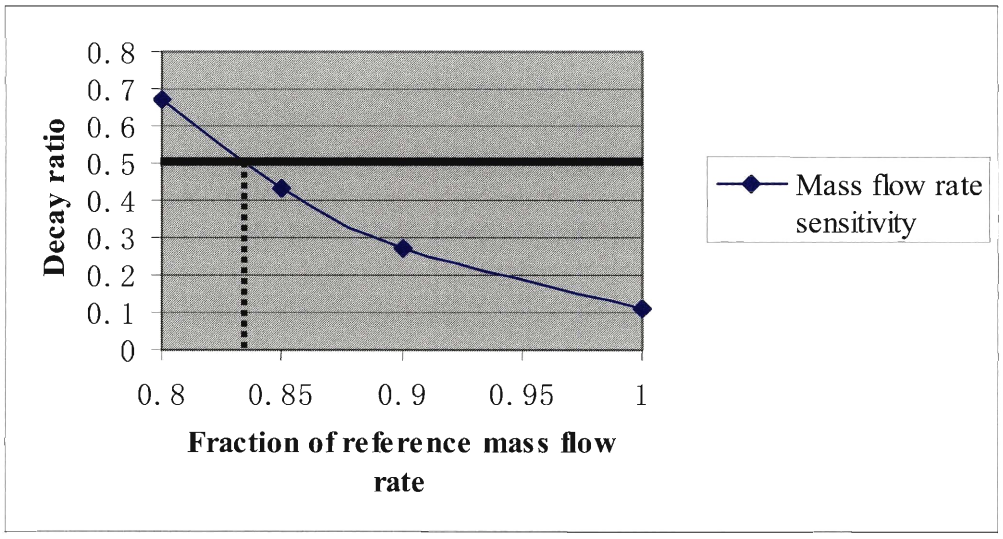

Fig. 3-6: SCWR mass flow rate sensitivity analysis

From Fig. 3-6, it is seen that the decay ratio will be above 0.5 at flow rates below about 83% of the reference case. This means that a reduction in mass flow rate, while keeping the power constant, has a destabilizing effect.

2. Power sensitivity analysis

The decay ratios are calculated by changing the power level, with constant mass flow rate and pressure equal to the reference condition. The results are illustrated in Fig. 3-7.

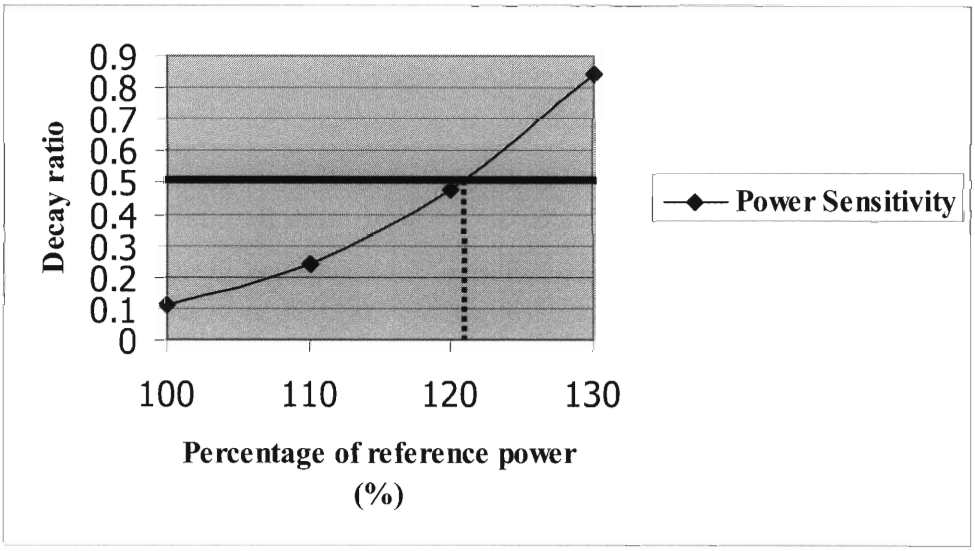

Fig. 3-7: SCWR power sensitivity analysis

From Fig. 3-7, it is seen that the decay ratio will be above 0.5 as the power rises above 121% of the reference case. This means that an increase in power, while keeping the mass flow rate constant, has a destabilizing effect.

3. Pressure sensitivity analysis

The decay ratios have been calculated for a range of the system pressure, while keeping the mass flow rate and power at the reference condition. The results are illustrated in Fig. 3-8.

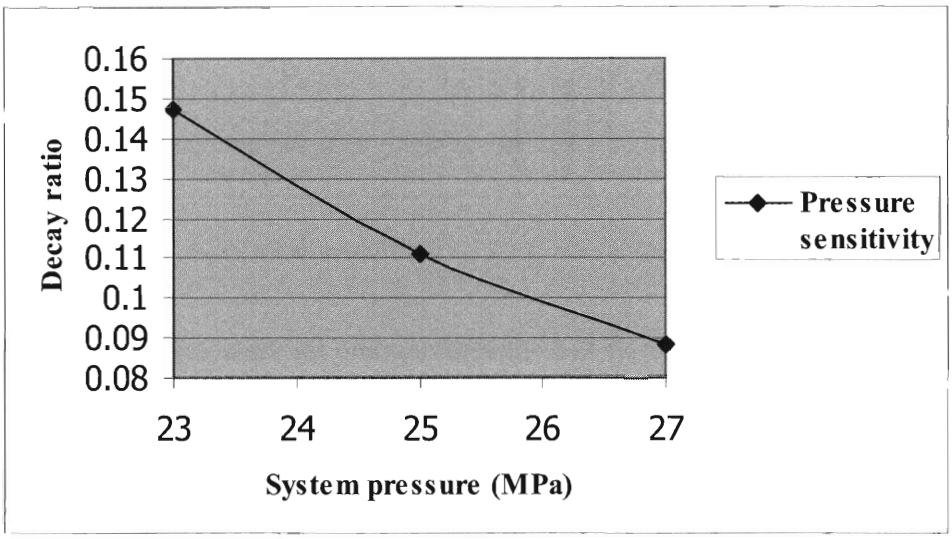

Fig. 3-8: SCWR system pressure sensitivity analysis

From Fig. 3-8, it is seen that the decay ratio will decrease as the pressure increases, which means that a higher system pressure will stabilize the system. Conversely, a lower system pressure will de-stabilize the system, although the decay ratio increases only slightly when the system pressure is lowered from 25MPa to 23MPa, thus indicating that the effect of system pressure is less important compared to that of flow rate and/or power.

These results are similar to what were obtained using the Laplace transformation method and reported in [Zhao, et al, 2004]. The slight difference in the two sets of results originates from the different reference SCWR designs since the SCWR design is still undergoing revision. The results presented here correspond to the latest design parameters of U.S. SCWR [Buongiorno, 2003].

3.3.4 Average channel analysis

The inlet orifice coefficient for the average channel is calculated to be 115.0 to satisfy both the requirements of:

(a) The same power-to-flow rate ratio as the hot channel

(b) The core pressure drop of 0.163MPa which yields the hot channel inlet orifice coefficient of 20.0.

With an inlet orifice coefficient of 115.0, the decay ratio for the average channel is found to be only 0.01. With such a small decay ratio, the average channel will be very stable. To check if the large inlet orifice coefficient such as 115.0 is feasible from manufacturing point of view, the following analysis was conducted.

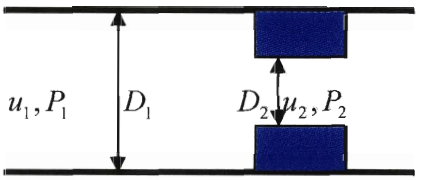

Fig. 3-9: Orifice illustration

For incompressible flow, from the Bernoulli equation,

$$p_1 + \frac{\rho u_1^2}{2} + \rho g z_1 = p_2 + \frac{\rho u_2^2}{2} + \rho g z_2 \tag{3-17}$$

Then,

$$p_1 - p_2 = \frac{1}{2}\rho u_1^2[(D_1 / D_2)^4 - 1] \tag{3-18}$$

Where, subscript 1 designates the "upstream" or "pipe" condition and subscript 2 designates the "downstream" or "orifice" condition. From Table 7.1 of [Holman, 2001], it was found that the permanent pressure loss factor of a square-edged orifice is 0.8. Then,

$$\Delta p_{loss} = 0.8(p_1 - p_2) = K_{orifice}\frac{\rho u_1^2}{2} \tag{3-19}$$

Therefore,

$$K_{orifice} = 0.8[(D_1 / D_2)^4 - 1] \tag{3-20}$$

For $K_{orifice}$ = 20 (as suggested for the hot channel), D_1/D_2 = 2.26. For $K_{orifice}$ = 115 (as suggested for the average channel), D_1/D_2 = 3.47. Thus, both of the above diameter ratios ($D_{pipe}/D_{orifice}$) are quite reasonable. For the U. S. SCWR assembly, the equivalent inlet pipe diameter would be about 11.8 cm. Therefore, for the hot channel, the orifice diameter would be ~5.2 cm corresponding to an inlet orifice coefficient of 20. For the average channel, the orifice diameter would be ~3.4 cm corresponding to the inlet orifice coefficient of 115. Therefore, there should be no difficulty in manufacturing this orifice.

From the above calculations, it is seen that the U.S. reference SCWR design should have no density-wave instability problem at a core pressure drop of 0.163MPa with proper inlet orifices for both the hot and average channels for full-power normal operating condition.

3.4 Ledinegg stability for hot and average channels

The pressure drop versus inlet flow velocity of the hot channel (with inlet orifice coefficient of 20.0) and the average channel (with inlet orifice coefficient of 115.0) were calculated and plotted in Fig. 3-10 and Fig. 3-11, respectively.

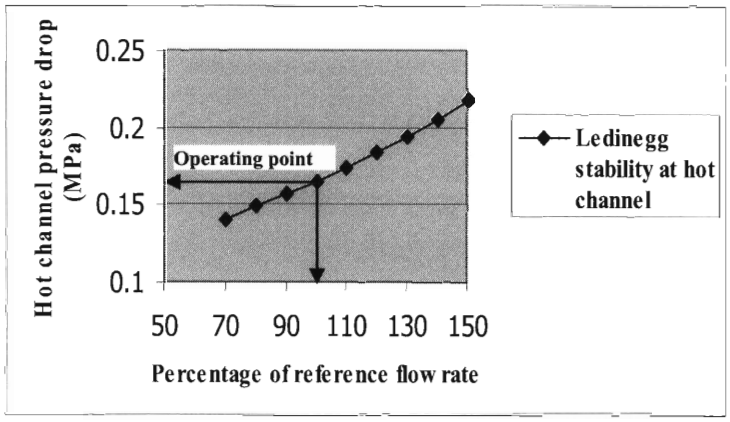

Fig. 3-10: Ledinegg stability for hot channel

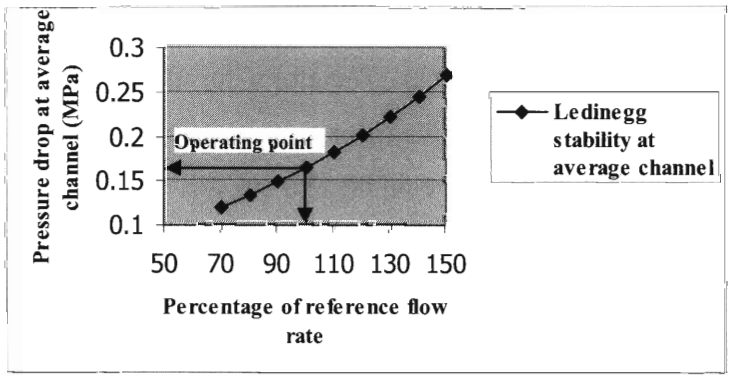

Fig. 3-11: Ledinegg stability for average channel

From Fig. 3-10 and Fig. 3-11, it is easy to see that the slope of pressure drop versus flow rate at the operating point is positive for both the hot and the average channels. Thus, the criterion of the Ledinegg stability described by Equation (1-1) is satisfied and there will be no Ledinegg instability in the SCWR at full power operating conditions.

In the following chapters, stability maps, or boundaries, that define the onset of density wave instability will be constructed. While the SCWR operates at supercritical pressure during steady state full power operation, it will experience subcritical two phase conditions during a sliding pressure startup operation. Stability maps have been developed for both the full power operating condition and the sliding pressure partial power conditions.

Chapter 4

Stability map construction for supercritical pressure

Recent SCWR stability analyses reported by Koshizuka *et al.* (2003), Yang and Zavaljevski (2003) and Zhao *et al.* (2004) followed the traditional momentum pulse decay ratio approach by linearizing and Laplace transforming the mass, momentum and energy equations in dimensional form. Although the analyses provided useful information on the SCWR stability, a non-dimensional approach is more appealing for determining the important non-dimensional parameters that control the stability at supercritical pressure and for construction of "stability maps" using those important parameters. We introduce a three-region model for this purpose.

The three-region model follows the density regions as defined by the International Association for Properties of Water and Steam – Industrial Formulation 1997, i.e., IAPWS-IF97 [Wagner *et al.*, 2000]. Based on this model, two new governing parameters named Pseudo-subcooling number and Expansion number have been derived by non-dimensional analysis of the conservation equations. The stability map is then plotted on the plane defined by the Pseudo-subcooling number versus Expansion number.

4.1 Three-region model

Although there is no phase change in supercritical pressure, the coolant does experience a dramatic density dilution at some specific temperature range just like boiling. The water density change with temperature at 25MPa is calculated using the ASME properties [1998] based on IAPWS-IF97 and is plotted in Fig. 4-1.

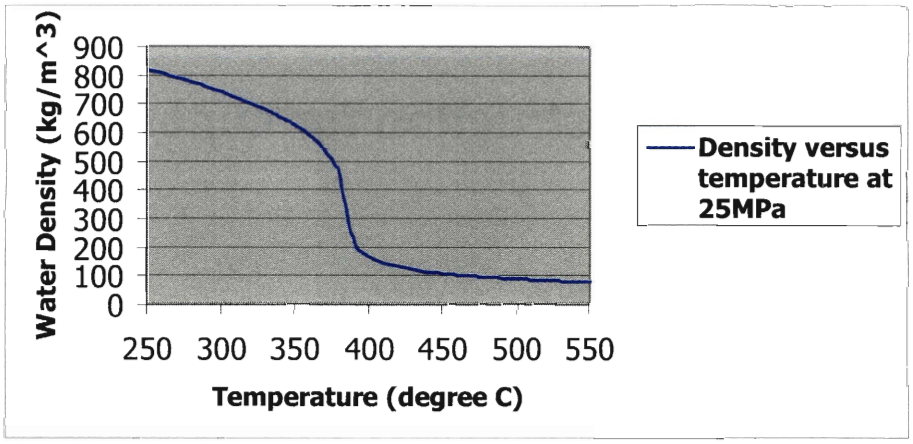

Fig. 4-1: Water density versus temperature at 25MPa

Besides the density, other thermal and transport properties such as specific heat, dynamic viscosity, thermal conductivity, etc. also experience this kind of drastic change with temperature. This can be seen in Fig 4-2, 4-3 and 4-4.

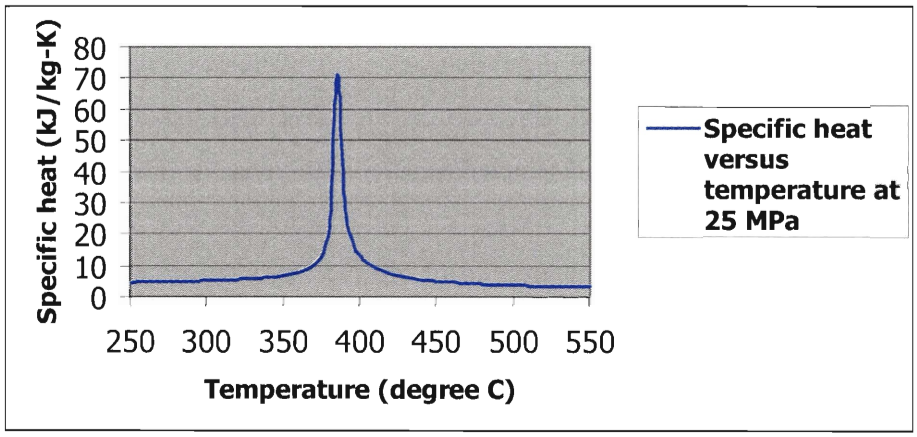

Fig. 4-2: Specific heat versus temperature at 25MPa

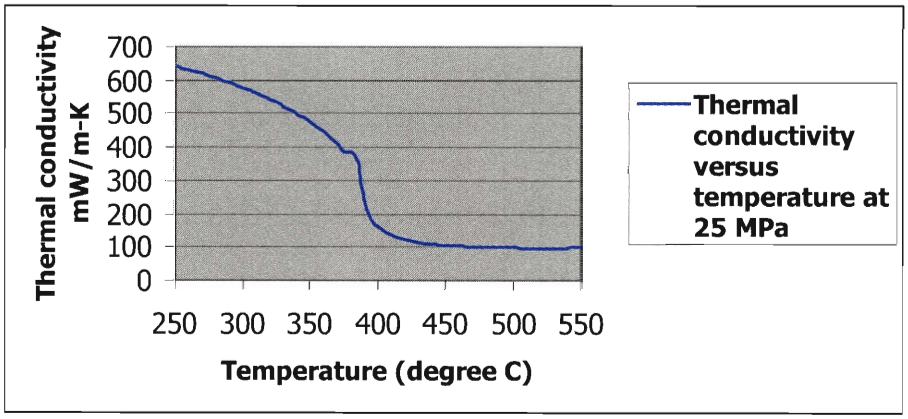

Fig. 4-3: Thermal conductivity versus temperature at 25MPa

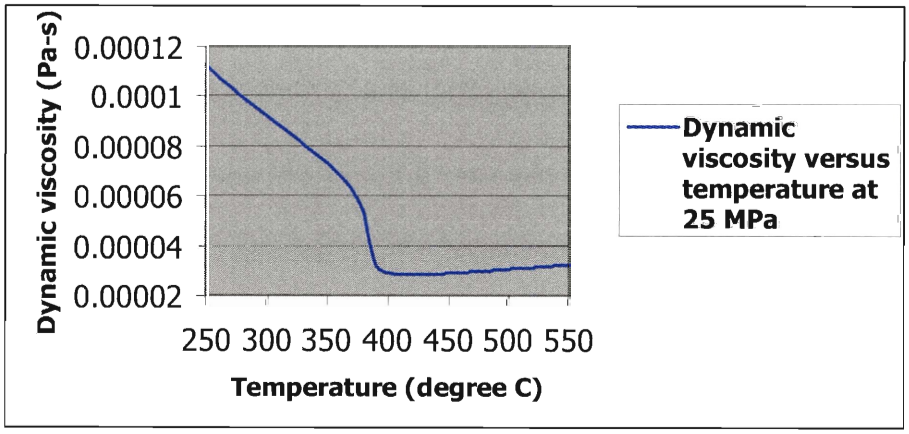

Fig. 4-4: Dynamic viscosity versus temperature at 25MPa

The region where the properties undergo rapid change or exhibit "spikes" can be assumed as a "pseudo-boiling" region where the fluid can be considered as a mixture of "heavy" and "light" fluids. A Homogenous Equilibrium Model (HEM) can be applied to this region since the two fluids are well coupled at such high pressure. Therefore, the three-region model for stability analysis consists of: (1) a region for the "heavy fluid" with constant density, (2) a region of a mixture of "heavy" and "light" fluids similar to a homogeneous-equilibrium two-phase mixture, and finally (3) a region for the "light fluid" which behaves like an ideal gas or superheated steam. This three region model is illustrated in Fig. 4-5.

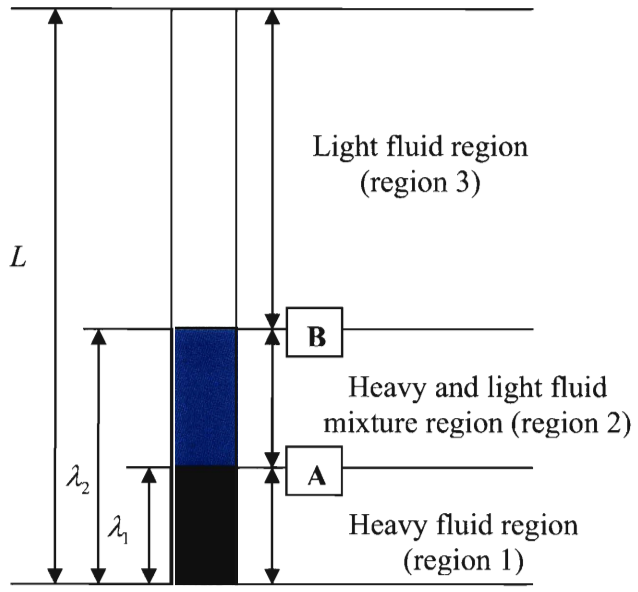

Fig. 4-5: Supercritical water simulation by three-region model

The boundaries of the different regions have different definitions in the literature. For example, Antoni and Dumaz [2003] obtained the pseudo-saturation point at $(\frac{\partial c_p}{\partial T})_P = 0$, and a "latent heat" of 400J/kg was defined for the "two phase mixture". In the present work, the boundary definitions of IAPWS-IF 97, as illustrated in Fig. 4-6, are used.

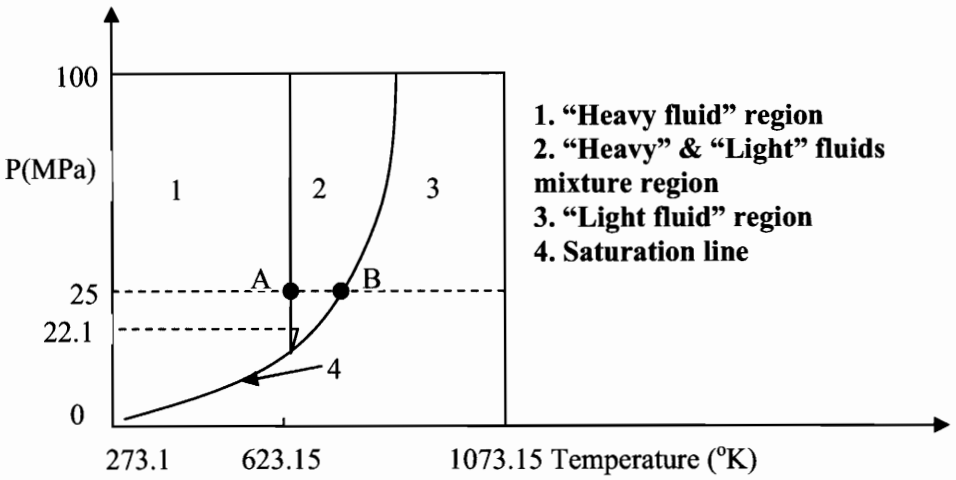

Fig. 4-6: IAPWS-IF 97 regions in P,T plane

The boundary between region 1 and region 2 is defined at the temperature $T_A = 350^o C$ for all of the supercritical states. The coolant at this boundary is in pseudo saturation liquid state. The boundary between region 2 and 3 is defined at temperature T_B which was calculated using Equation (4-1). The coolant at this boundary is in pseudo saturation vapor state.

$$T_B = n_2 + (\frac{p - n_3}{n_1})^{0.5} \qquad (4\text{-}1)$$

Where,

n_1 = 0.101 929 700 393 26 E-02

n_2 = 0.572 544 598 627 46 E+03

n_3 = 0.139 188 397 788 70 E+02

and p is the system pressure.

The unit for T_B is Kelvin and that for pressure is MPa in the above formula.

Using these definitions, the boundaries among the three regions at 25MPa are the points A and B. By definition, the temperature at point A is 350°C and the temperature at B can

be obtained from Equation (4-1), which is 404°C by calculation. Once the pseudo saturation temperatures are obtained, all the coolant properties at pseudo saturation states at 25MPa can be easily calculated.

In an early work by Zuber [1966], a two-region model was applied for the stability analysis. In that two region model, the state of supercritical water was simulated by two regions: (1) "liquid like region" and (2) "gas like region". The transition point between these two regions was determined by the point of maximum specific heat c_p . A comparison between the two-region model and the three-region model can be seen in Fig.4-7 together with the results calculated by the ASME software [1998]. The figure has been plotted on the specific volume versus enthalpy plane.

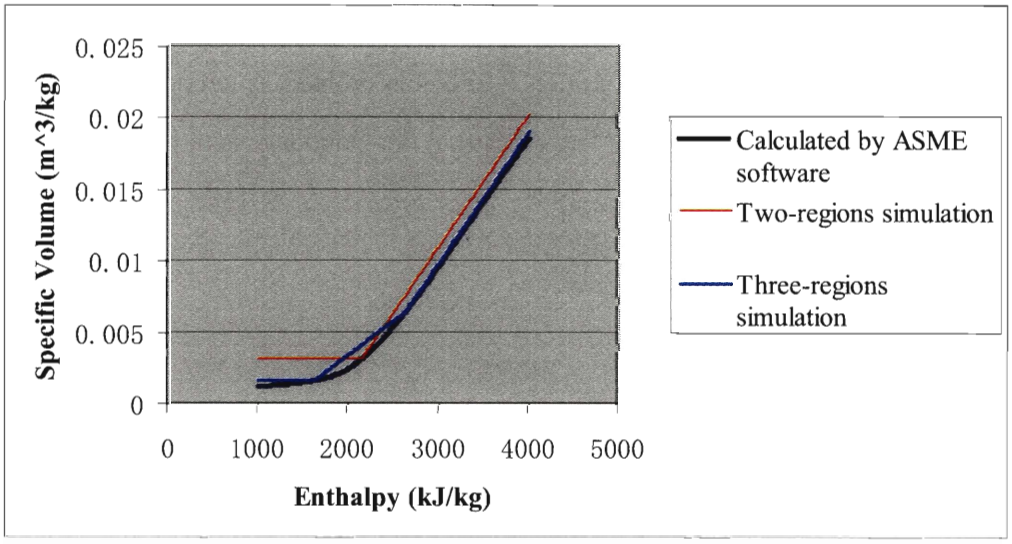

Fig. 4-7: Comparison of the Zuber two-region model and the ASME three-region model

It is seen that the three-region model provides a good simulation of the supercritical water.

4.2 Friction factors for the three region model

After a detailed literature survey, Pioro, et al [2004] found that experimental studies dealing with hydraulic resistance of supercritical fluids are mainly in circular tubes. The

publications dealing with other geometries are very limited. Only one experiment conducted by Dyadyakin and Popov [1977] dealt with pressure drop in tight helically finned bundles, which is not typical in nuclear reactors since the reactor bundles are smooth.

According to Filonenko [1954], the friction factor for a supercritical fluid in a smooth tube can be calculated as:

$$f = (1.82\log_{10}(\mathrm{Re}_b) - 1.64)^{-2.0} \tag{4-2}$$

For a Reynolds number range of $4\times10^3 - 10^{12}$ and the Reynolds number is based on arithmetic average of inlet and outlet values.

Kirillov, et al (1990) proposed to calculate the frictional resistance coefficient for isothermal stabilized turbulent flow of fluid by using Filonenko's correlation with reduced pressure range $\frac{p}{p_{cr}} = 1.016 - 1.22$ and $\mathrm{Re} = 8\times10^4 - 1.5\times10^6$. For a heated tube, within the same parameters range, they proposed the following correction:

$$\frac{f}{f_{iso}} = (\frac{\rho_w}{\rho_b})^{0.4} \tag{4-3}$$

Where, f_{iso} is the isothermal friction factor, ρ_w is the coolant density evaluated at the wall temperature while ρ_b is the density calculated at the bulk temperature.

The effect of the heated wall is simulated in RELAP5 using the above suggested density ratio term. The user can select whether or not the heated wall effect is to be calculated and the value of the exponent on the density ratio term [Buongiorno, 2003]. Therefore, for simplicity, the heated wall effect on the friction factor was not considered further in this thesis.

For the three regions in the single coolant channel, the friction factor is calculated by the following strategy.

(1) "Heavy fluid" region

The Reynolds number is calculated at the pseudo saturation liquid state (Point A). Then, the friction factor f_1 is calculated by applying that Reynolds number to Equation (4-2). The friction factor in this region is termed as f_1.

(2) "Heavy and light fluids mixture" region

In this region, the Reynolds number is calculated based on the arithmetic average of values at the pseudo saturation liquid point (Point A) and pseudo saturation vapor (Point B). Then, the friction factor f_2 is calculated by applying that Reynolds number to Equation (4-2). The friction factor in this region is termed as f_2.

(3) "Light fluid" region

The Reynolds number is calculated at the pseudo saturation vapor point (Point B). Then, the friction factor f_3 is calculated by applying that Reynolds number to Equation (4-2). The friction factor in this region is termed as f_3.

4.3 Derivation of nondimensional parameters

Ishii and Zuber [1970] and Ishii [1971] determined that the primary governing parameters for two phase flow instability at subcritical pressure were the Subcooling Number and the Phase Change number. The subcooling number was defined as:

$$N_{sub} = \frac{(h_f - h_{in})}{h_{fg}} \frac{\Delta\rho}{\rho_g} \tag{4-4}$$

The subcooling number scales the inlet subcooling and is the dimensionless residence time of a fluid particle in the single phase liquid region. The phase change number was defined as:

$$N_{pch} = \frac{v_{fg}}{h_{fg}} \frac{q'' P_h}{A_c} \frac{L}{u_{in}} \tag{4-5}$$

The phase change number scales the rate of phase change due to heat addition.

The derivation of N_{sub} and N_{pch} was conducted by non-dimensional analysis of the conservation equations which can be found in [Ishii, 1971]. The N_{sub} and N_{pch} were based on the system with only two regions, a single phase liquid region and a two phase mixture region, since the exit equilibrium quality was below 1.0. However, for the supercritical system analyzed here, it has to be represented by three regions. The coolant at the channel exit will definitely be superheated since the SCWR exit temperature is 500°C while the pseudo saturation vapor temperature is 404°C at 25MPa. Thus, the stability at supercritical pressure should be governed by other governing parameters. It is proposed that the governing parameters for the supercritical system are a Pseudo-subcooling number and an Expansion number which can be derived from the following non-dimensional analysis.

(1) "Heavy fluid" region

The density at point A in Figure 3-5 was assumed the same as that in this region. The conservation equations are described by equations (4-5) to (4-7).

$$\frac{\partial u}{\partial z} = 0 \quad (\rho(z) = \rho_A = Const.) \tag{4-5}$$

$$\rho_A \frac{\partial h}{\partial t} + \rho_A u_{in} \frac{\partial h}{\partial z} = \frac{q'' P_h}{A_c} \tag{4-6}$$

$$-\frac{\partial p}{\partial z} = \rho_A \frac{du_{in}}{dt} + \frac{f_1 \rho_A u_{in}^2}{2D_e} + \rho_A g \tag{4-7}$$

In this region, the characteristic length can be chosen to be λ_1 which is defined in Figure 3-5 and the non-dimensional variables are chosen as follows.

$$u^* = \frac{u}{\Omega_1 \lambda_1},\ z^* = \frac{z}{\lambda_1},\ \rho_A^* = \frac{\rho}{\rho_A},\ u_{in}^* = \frac{u_{in}}{\Omega_1 \lambda_1},\ h^* = \frac{h}{h_{AB}},\ q''^* = \frac{q''}{G h_{AB}},\ P_h^* = \frac{P_h}{\lambda_1}$$

$$A_c^* = \frac{A_c}{\lambda_1^2},\ t^* = t\Omega_1,\ p^* = \frac{p}{(\Omega_1 \lambda_1)^2 \rho_A},\ D_e^* = \frac{D_e}{\lambda_1},\ g^* = \frac{g}{\Omega_1^2 \lambda_1}$$

Where,

$\Omega_1 = \frac{v_{AB}}{h_{AB}} \frac{q'' P_h}{A_c}$: The characteristic frequency of phase change which scales the rate of phase change, or the rate of transformation of "heavy" fluid to "light" fluid due to heat addition.

$v_{AB} = v_B - v_A$: The specific volume difference between pseudo saturated vapor and pseudo saturated liquid.

$h_{AB} = h_B - h_A$: The specific enthalpy difference between pseudo saturated vapor and pseudo saturated liquid.

Plugging the above non-dimensional variables into Equations (4-5), (4-6) and (4-7), one obtains:

$$\frac{\partial u^*}{\partial z^*} = 0 \tag{4-8}$$

$$\rho_A^* \frac{\partial h^*}{\partial t^*} + \rho_A^* u_{in}^* \frac{\partial h^*}{\partial z^*} = \frac{1}{N_1} \frac{q''^* P_h^*}{A_c^*} \tag{4-9}$$

$$-\frac{\partial p^*}{\partial z^*} = \rho_A^* \frac{du_{in}^*}{dt^*} + f_1 \frac{\rho_A^* u_{in}^{*2}}{2D_e^*} + \rho_A^* g^* \tag{27}$$

From the above equations, the non-dimensional variable groups are two:

Friction factor: f_1, and

Pseudo Subcooling number: $N_1 = \frac{\Omega_1 \lambda_1}{u_{in}} = \frac{(h_A - h_{in})}{h_{AB}} \frac{\rho_A - \rho_B}{\rho_B}$ (4-10)

It is seen that N_1 comes from the energy equation of the heavy fluid region and has a similar expression as the subcooling number for subcritical pressure. We propose to call N_1 a Pseudo Subcooling number which is the ratio of the residence time of a fluid particle in the heavy fluid region compared to the time it takes to convert a heavy fluid into a light fluid in the channel.

(2) "Heavy and light fluid mixture" region

Since the coolant flow in this region is simulated by the HEM model, the conservation equations for this region can be described as follows:

1. Mixture mass conservation equation

$$\frac{\partial \rho_m}{\partial t} + \frac{\partial}{\partial z}(\rho_m u_m) = 0 \tag{4-11}$$

2. Vapor phase mass conservation equation

$$\frac{\partial}{\partial t}(\alpha\rho_g)+\frac{\partial}{\partial z}(\alpha\rho_g u_g)=\Gamma_g \tag{4-12}$$

For homogenous flow, the following mixture velocity equation can be derived from the above two mass conservation equations. The detailed derivation can be found in [Lahey and Moody, 1993]

$$\frac{\partial u_m}{\partial z}=\Omega_1=\frac{\Gamma_g\Delta\rho}{\rho_f\rho_g} \tag{4-13}$$

3. Mixture momentum conservation equation

$$-\frac{\partial p}{\partial z}=\frac{\partial G}{\partial t}+\frac{\partial}{\partial z}(G^2/\rho_m)+\frac{f_2\rho_m u_m^2}{2D_e}+\rho_m g \tag{4-14}$$

4. Mixture energy conservation equation

$$\rho_m\frac{\partial h_m}{\partial t}+\rho_m u_m\frac{\partial h_m}{\partial z}=\frac{q^{"}P_h}{A_c} \tag{4-15}$$

In this region, the characteristic length is chosen to be λ_2 and the non-dimensional variables are chosen as follows.

$$u_m^*=\frac{u_m}{\Omega_1\lambda_2},\ z^*=\frac{z}{\lambda_2},\ \rho_m^*=\frac{\rho_m}{\rho_A},\ h_m^*=\frac{h_m}{h_{AB}},\ q^{"*}=\frac{q^{"}}{Gh_{AB}},\ P_h^*=\frac{P_h}{\lambda_2},\ \Omega_1^*=\frac{\Omega_1}{\Omega_1}$$

$$A_c^*=\frac{A_c}{\lambda_2^2},\ t^*=t\Omega_1,\ p^*=\frac{p}{(\Omega_1\lambda_2)^2\rho_A},\ D_e^*=\frac{D_e}{\lambda_2},\ g^*=\frac{g}{\Omega_1^2\lambda_2}$$

Plugging the above non-dimensional variables into equations (4-13), (4-14) and (4-15), one obtains:

$$\frac{\partial u_m^*}{\partial z^*} = \Omega_1^* \tag{4-16}$$

$$\rho_m^*(\frac{\partial u_m^*}{\partial t^*} + u_m^* \frac{\partial u_m^*}{\partial z^*}) = -\frac{\partial p_m^*}{\partial z^*} - f_2 \frac{\rho_A^* u_m^{*2}}{2D_e^*} - \rho_m^* g^* \tag{4-17}$$

$$\rho_m^*(\frac{\partial h_m^*}{\partial t^*} + u_m^* \frac{\partial h_m^*}{\partial z^*}) = \frac{1}{N_2} q^* \tag{4-18}$$

From the above equations, the non-dimensional variable groups are two:

Friction factor: f_2, and

Variable group N_2: $N_2 = \frac{\Omega_1 \lambda_2}{u_{in}} = \frac{(h_B - h_{in})}{h_{AB}} \frac{\rho_A - \rho_B}{\rho_B}$ (4-19)

(3) "Light fluid" region

In this region, ideal gas behavior is assumed (see Fig. 3-5). Comparison with the more rigorous ASME property table shows that it is a good approximation in this pseudo superheated vapor region. The single phase conservation equations can be expressed as:

1. Mass conservation equation

$$\frac{\partial \rho}{\partial t} + \frac{\partial}{\partial z}(\rho u) = 0 \tag{4-20}$$

2. Momentum conservation equation

$$-\frac{\partial p}{\partial z} = \frac{\partial G}{\partial t} + \frac{\partial}{\partial z}(G^2 / \rho) + \frac{f_3 \rho u^2}{2D_e} + \rho g \tag{4-21}$$

3. Energy conservation equation

$$\rho\frac{\partial h}{\partial t}+\rho u\frac{\partial h}{\partial z}=\frac{q^{"}P_h}{A_c} \tag{4-22}$$

Compared to the two phase mixture flow at subcritical pressure, heat addition in this region of supercritical pressure will dilute the pseudo superheated vapor instead of cause phase change. The velocity divergence of this region can be derived according to Zuber [1966] as follows:

Rearranging the mass Equation (4-20), one obtains:

$$\frac{\partial u}{\partial z}=-\frac{1}{\rho}(\frac{\partial \rho}{\partial t}+u\frac{\partial \rho}{\partial z}) \tag{4-23}$$

Since the pressure drop is small compared to the system pressure, a constant pressure was assumed in this region. Therefore, the density is a function of enthalpy only. Thus,

$$\frac{\partial \rho}{\partial t}+u\frac{\partial \rho}{\partial z}=\frac{d\rho}{dh}(\frac{\partial h}{\partial t}+u\frac{\partial h}{\partial z}) \tag{4-24}$$

Combining the above equation with the energy Equation (4-22), one can obtain:

$$\frac{\partial \rho}{\partial t}+u\frac{\partial \rho}{\partial z}=\frac{1}{\rho}\frac{q^{"}P_h}{A_c}\frac{d\rho}{dh} \tag{4-25}$$

Plugging it into equation (4-23), one obtains:

$$\frac{\partial u}{\partial z}=-\frac{1}{\rho^2}(\frac{d\rho}{dh})_p\frac{q^{"}P_h}{A_c} \tag{4-26}$$

From the ideal gas state equation with constant pressure:

$$pv = RT \tag{4-27}$$

$$pdv = RdT$$

$$pdv = R\frac{dh}{c_p}$$

Therefore,

$$(\frac{dv}{dh})_p = -\frac{1}{\rho^2}(\frac{d\rho}{dh})_p = \frac{R}{pc_p} \tag{4-28}$$

Plugging it into Equation (4-26), the divergence of the pseudo superheated vapor region (or the spatial acceleration) can be expressed as:

$$\frac{\partial u}{\partial z} = \Omega_2 \tag{4-29}$$

Where, $\Omega_2 = \frac{R}{pc_p}\frac{q^{"}P_h}{A_c}$

R: ideal gas constant

c_p: ideal gas specific heat at constant pressure

p: system pressure

In this region, the characteristic length was chosen to be L and the non-dimensional variables were chosen as follows:

$$u^* = \frac{u}{\Omega_2 L},\ z^* = \frac{z}{L},\ \rho^* = \frac{\rho}{\rho_A},\ h^* = \frac{h}{h_{AB}},\ q^{"*} = \frac{q^{"}}{Gh_{AB}},\ P_h^* = \frac{P_h}{L},\ \Omega_2^* = \frac{\Omega_2}{\Omega_2}$$

$$A_c^* = \frac{A_c}{L^2},\ t^* = t\Omega_2,\ p^* = \frac{p}{(\Omega_2 L)^2 \rho_A},\ D_e^* = \frac{D_e}{L},\ g^* = \frac{g}{\Omega_2^2 L}$$

Plugging the above non-dimensional variables into Equations (4-29), (4-21) and (4-22), one obtains:

$$\frac{\partial u^*}{\partial z^*} = \Omega_2^* \tag{4-30}$$

$$\rho^*(\frac{\partial u^*}{\partial t^*} + u^* \frac{\partial u^*}{\partial z^*}) = -\frac{\partial p^*}{\partial z^*} - f_3 \frac{\rho_f^* u^{*2}}{2D_e^*} - \rho^* g^* \tag{4-31}$$

$$\rho^*(\frac{\partial h^*}{\partial t^*} + u^* \frac{\partial h^*}{\partial z^*}) = \frac{1}{N_3} q_w^{"*} \tag{4-32}$$

From the above equations, the non-dimensional variable groups are two:

Friction factor: f_3, and

Expansion number: $N_3 = \frac{\Omega_2 L}{u_{in}} = \frac{R}{pC_p} \frac{q^{"} P_h}{A_c} \frac{L}{u_{in}}$ (4-33)

We propose to call N_3 the expansion number. The expansion number has a similar formula as the phase change number N_{pch} in the subcritical pressure region. The name expansion number is proposed since the heat addition at supercritical pressure will cause the coolant volume expansion instead of phase change.

(4) Summary of the governing non-dimensional groups

From the above analysis, the following six non-dimensional groups emerge:

Friction factors in three regions: f_1, f_2, f_3,

$N_{psub} = N_1 = \frac{\Omega_1 \lambda_1}{u_{in}} = \frac{(h_A - h_{in})}{h_{AB}} \frac{\rho_A - \rho_B}{\rho_B}$,

$N_2 = \frac{\Omega_1 \lambda_2}{u_{in}} = \frac{(h_B - h_{in})}{h_{AB}} \frac{\rho_A - \rho_B}{\rho_B}$, and

$$N_{\exp} = N_3 = \frac{\Omega_2 L}{u_{in}} = \frac{R}{pC_p}\frac{q'' P_h}{A_c}\frac{L}{u_{in}}$$

Rearranging group N_2, one obtains:

$$N_2 = \frac{\Omega_1 \lambda_2}{u_{in}} = \frac{(h_B - h_{in})}{h_{AB}}\frac{\rho_A - \rho_B}{\rho_B}$$

$$= \frac{(h_B - h_A) + (h_A - h_{in})}{h_{AB}}\frac{\rho_A - \rho_B}{\rho_B}$$

$$= N_{psub} + \frac{\Delta\rho}{\rho_B} \qquad (4\text{-}34)$$

For a specific supercritical system, its geometric variables are constant. If the pressure and inlet velocity are specified, the friction factors f_1, f_2, f_3 will be defined from section 4.2. At a particular pressure, $\frac{\Delta\rho}{\rho_B}$ is constant in Equation (4-34). Therefore, the group N_2 will be accommodated by the Pseudo subcooling number, N_{psub}. Thus, the only remaining non-dimensional groups are N_{psub} and $N_{\exp}$.

It is concluded that the dynamics of a heated channel at supercritical pressure will be governed by two non-dimensional parameters, N_{psub} and $N_{\exp}$, for particular pressure, inlet velocity and geometry including orifice coefficient.

4.4 Single channel density wave oscillation mechanism sand characteristic equation

The mechanism of single channel DWO in a parallel channel system can be illustrated by Fig. 4-8.

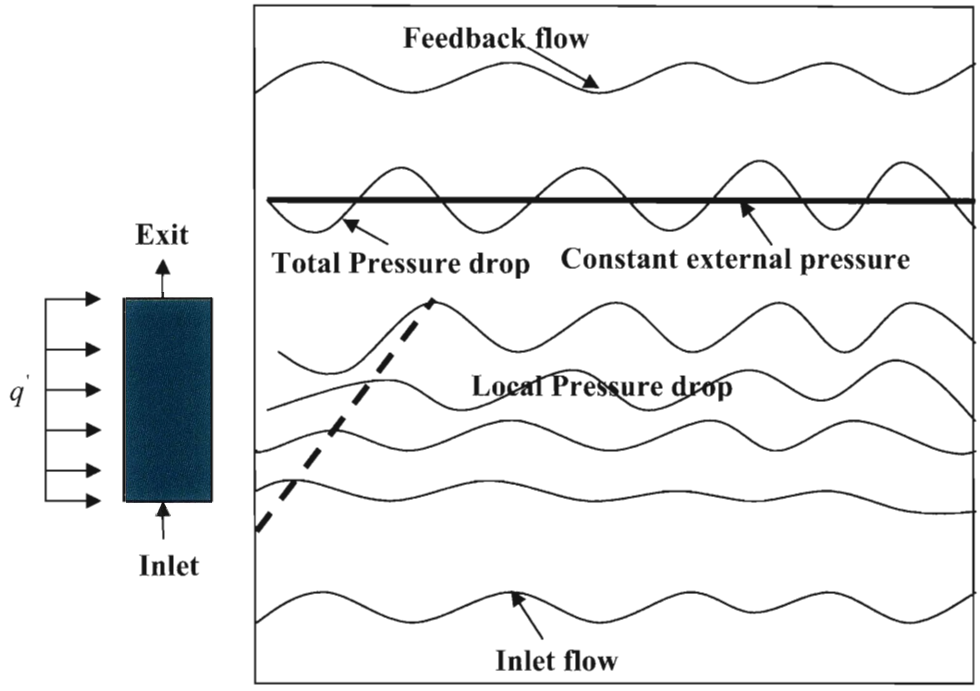

Fig. 4-8: Mechanism of DWO instability in a single heated channel

If some external forces or disturbances create an oscillation in the inlet flow, the local coolant density in a two-phase or compressible system will experience a fluctuation and a density wave will propagate towards the exit along with the flow. This density wave will cause the local pressure drop to fluctuate or oscillate with some time delay with respect to the inlet flow. In some situations, the channel total pressure drop may experience an 180° phase lag with respect to the inlet flow as shown in Fig. 4-8. The constant external pressure boundary condition of a parallel channel system such as a BWR or SCWR will then generate a positive inlet velocity feedback to the oscillating channel, which will increase the oscillation amplitude of the original flow and the system will become unstable.

For the three-region supercritical water flow channel shown in Figure 4-5, the feedback mechanism can be illustrated by Fig. 4-9. If $\Gamma_1(s)$, $\Gamma_2(s)$ and $\Gamma_3(s)$ are the transfer functions between the inlet flow oscillation and the pressure drop oscillations

corresponding to region 1, 2 and 3, respectively, the system characteristic equation can be determined as follows:

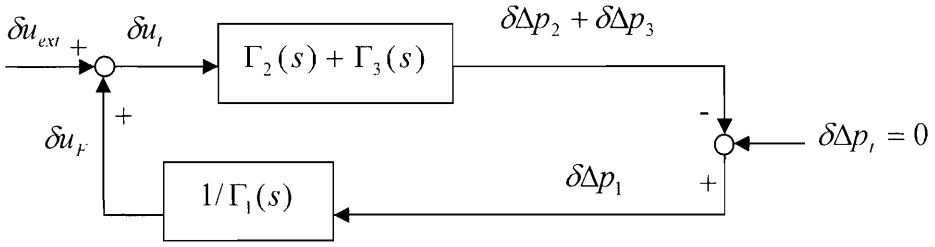

Fig. 4-9: Block diagram of the flow feedback mechanism

If δu_{ext} is the external disturbance of the inlet flow and δu_F is the flow feedback, the total disturbance of the inlet flow is:

$$\delta u_t = \delta u_{ext} + \delta u_F \tag{4-35}$$

Recognizing that the effect on pressure drop can be obtained from:

$$\delta\Delta p_1 = \Gamma_1(s)\delta u_F \tag{4-36}$$

$$\delta\Delta p_2 = \Gamma_2(s)\delta u_t \tag{4-37}$$

$$\delta\Delta p_3 = \Gamma_3(s)\delta u_t \tag{4-38}$$

$$\delta\Delta p_t = \delta\Delta p_1 + \delta\Delta p_2 + \delta\Delta p_3 \tag{4-39}$$

And

$$\delta\Delta p_t = 0 \tag{4-40}$$

One can obtain the following relationship between δu_t and δu_{ext}:

$$\delta u_t = \frac{\Gamma_1(s)}{\Gamma_1(s) + \Gamma_2(s) + \Gamma_3(s)} \delta u_{ext} \tag{4-41}$$

If $\Pi(s) = \Gamma_1(s) + \Gamma_2(s) + \Gamma_3(s)$, then $\Pi(s)$ is the transfer function of the inlet flow oscillation to the total pressure drop oscillation across the channel. If any zero of $\Pi(s)$ has a positive real part, a small external disturbance of the inlet flow will grow and the system will become unstable. To make the system stable, all the zeros of $\Pi(s)$ must have negative real parts. Therefore, the characteristic equation of the single channel stability is:

$$\Pi(s) = 0 \tag{4-42}$$

The single flow channel of the SCWR core is divided into three parts, namely the inlet orifice, the heated part (three-region model) and the lower and upper non-heated gas plenum parts. After perturbation, linearization and Laplace transformation of the conservation equations for the above three parts, the characteristic equation of this single channel was analytically derived by integration of the momentum equations.

4.5 Derivation of the characteristic equation

The characteristic equation for the SCWR single channel stability in form of Equation (4-42) was derived from the conservation equations for the previously mentioned three-region model. A uniformly distributed constant fuel surface heat flux is applied, and the water rods are assumed to be insulated perfectly. In other words, there is no heat transfer to water rods. The fuel temperature dynamics and water rods heating effects on stability will be addressed in Chapter 6.

The single flow channel of the SCWR core is divided into four parts, namely the inlet orifice, the lower non-heated part, the heated part and the upper non-heated part. These four parts are shown in Fig. 4-10.

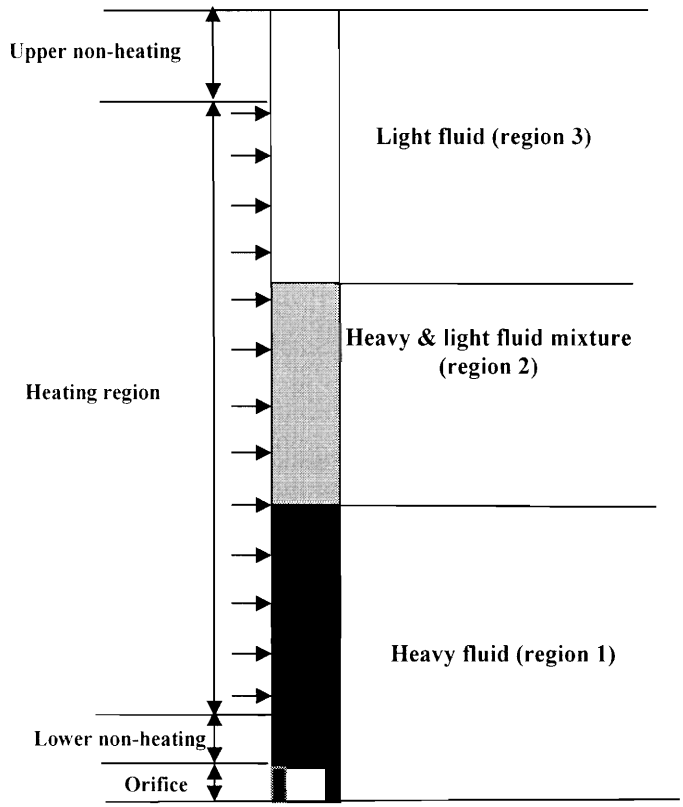

Fig. 4-10: Four parts of the flow channel

The governing equations for the four parts are as follows:

(1) Inlet orifice

The momentum equation for the inlet orifice can be expressed as:

$$\Delta p_{ori} = k_{in} \frac{\rho_A u_{in}^2}{2} \tag{4-43}$$

Where k_{in} is the inlet orifice coefficient.

Perturbation and Laplace transformation of the above equation yields:

$$\delta \Delta p_{ori} = k_{in} \rho_A u_{in} \delta u_{in} \tag{4-44}$$

(2) Heated part

The procedure of deriving the characteristic equation is similar to that in [Lahey and Moody, 1993].

(2-A) "Heavy fluid" region

In this region, the water density is assumed to be constant and equal to the pseudo-saturation water density ρ_A. Perturbation and Laplace transformation of the energy Equation (4-6), yields:

$$\frac{d\delta h}{dz} + \frac{s}{u_{in}}\delta h + \frac{q^{"}P_h}{A_c \rho_A u_{in}^2}\delta u_{in} = 0 \tag{4-45}$$

Equation (4-45) is a Bernoulli-type ordinary differential equation that can be readily integrated from the inlet to some axial point "z". Then, the enthalpy perturbation at the exit or boundary of the region is:

$$\delta h(s,\lambda_1) = \exp(-s\lambda_1 / u_{in})\delta h_{in} - \frac{q^{"}P_h}{\rho_A u_{in} A_c s}[1-\exp(-s\lambda_1 / u_{in})]\delta u_{in} \tag{4-46}$$

According to [Lahey and Moody, 1993], the perturbation of the boundary can be expressed as:

$$\delta\lambda_1 = -\frac{\rho_A A_c u_{in}}{q^{"}P_h}\delta h(s,\lambda_1)$$

$$= \frac{1-\exp(-s\lambda_1 / u_{in})}{s}\delta u_{in} - \frac{\rho_A A_c u_{in}}{q^{"}P_h}\exp(-s\lambda_1 / u_{in})\delta h_{in} \tag{4-47}$$

$$\delta(\Delta p_1) = \Gamma_1 \delta u_{in} + \Gamma_2 \delta h_{in} \tag{4-48}$$

Where,

$$\Gamma_1 = \rho_A \lambda_1 s + \frac{f_1 \rho_A u_{in} \lambda_1}{D_e} + k_{in} \rho_A u_{in} + (\frac{f_1 \rho_A u_{in}^2}{2D_e} + \rho_A g)[\frac{1 - \exp(-s\lambda_1 / u_{in})}{s}]$$

$$\Gamma_2 = -\frac{\rho_A A_c u_{in}}{q^{"} P_h} \exp(-s\lambda_1 / u_{in})(\frac{f_1 \rho_A u_{in}^2}{2D_e} + \rho_A g)$$

(2-B) "Heavy and light fluid mixture" region

From the velocity divergence Equation (4-13), one can obtain:

$$u_m(z) = u_{in} + \Omega_1 (z - \lambda_1) \tag{4-49}$$

Thus,

$$\delta u_m(s, z) = \delta u_{in} - \Omega_1 \delta \lambda_1 \tag{4-50}$$

Using the same method as in the "Heavy fluid" region, the perturbation and Laplace transformation of energy Equation (4-15) yields:

$$\frac{d\delta h_m}{dz} + \frac{s - \Omega_1}{u_m} \delta h_m + \frac{q^{"} P_h}{G A_c u_m} \delta u_m = 0 \tag{4-51}$$

Again, this is a Bernoulli-type ordinary differential equation. After integration,

$$\delta h_m(s, z) = \frac{q^{"} P_h}{G A_c (\Omega_1 - s)} \delta u_m + C[u_{in} + \Omega_1 (z - \lambda_1)]^{\frac{\Omega_1 - s}{\Omega_1}} \tag{4-52}$$

Where C is the integration constant, which can be determined by boundary condition $\delta h_m(s,z) = \delta h(s,\lambda_1)$ at $z = \lambda_1$, then,

$$\delta h_m(s,z) = \frac{q'' P_h}{GA_c}\frac{1}{\Omega_1 - s}[1 - \frac{\Omega_1}{s}(1-\exp(-s\lambda_1/u_{in})) - \exp(-s\lambda_1/u_{in})(1+\frac{\Omega_1(z-\lambda_1)}{u_{in}})^{\frac{\Omega_1 - s}{\Omega_1}}]\delta u_{in}$$
$$+\frac{1}{\Omega_1 - s}\exp(-s\lambda_1/u_{in})[\Omega_1 - s(1+\frac{\Omega_1(z-\lambda_1)}{u_{in}})^{\frac{\Omega_1 - s}{\Omega_1}}]\delta h_{in} \tag{4-53}$$

The description of $\rho_m(z)$ can be obtained from:

$$G = \rho_m(z)u_m(z) \tag{4-54}$$

Combined with Equation (4-49), gives,

$$\rho_m(z) = G/[u_{in} + \Omega_1(z-\lambda_1)] \tag{4-55}$$

The perturbation at the boundary between the mixture and the light fluid region can be obtained by applying the method described in [Lahey and Moody, 1993].

$$\delta\lambda_2 = -\frac{GA_c}{q'' P_h}\delta h_m(s,\lambda_2) \tag{4-56}$$

Now, we integrate the momentum equation for region (2-B). In Equation (4-14), the acceleration term can be simplified as:

$$\frac{\partial}{\partial z}(G^2/\rho_m) = \frac{\partial G u_m}{\partial z} = G\frac{\partial u_m}{\partial z} = G\Omega_1 \tag{4-57}$$

The detail of equation (4-57) is:

$$\frac{\partial G u_m}{\partial z} = \frac{G_2 u_{m2} - G_1 u_{m1}}{\Delta z} = \frac{(G_1 + \Delta G) u_{m2} - G_1 u_{m1}}{\Delta z} \approx \frac{G_1 (u_{m2} - u_{m1})}{\Delta z} \tag{4-57A}$$

$$G \frac{\partial u_m}{\partial z} = G_1 \frac{(u_{m2} - u_{m1})}{\Delta z} \tag{4-57B}$$

Thus, the momentum Equation (4-14) can be written as:

$$-\frac{\partial p}{\partial z} = \frac{\partial G}{\partial t} + G\Omega_1 + \frac{f_2 \rho_m u_m^2}{2D_e} + \rho_m g \tag{4-58}$$

$$\begin{aligned}\delta(\Delta P_2) = & \int_{\lambda_1}^{\lambda_2} [(s + \Omega_1)\rho_m + \frac{f_2}{D_e} G] \delta u_m dz + \int_{\lambda_1}^{\lambda_2} [(s + \Omega_1) u_m + \frac{f_2}{2D_e} u_m^2 + g] \delta \rho_m dz \\ & - (G\Omega_1 + \frac{f_2}{2D_e} G u_{in} + \rho_f g) \delta \lambda_1 + [G\Omega_1 + \frac{f_2}{2D_e} G u_m(\lambda_2) + \rho_g g] \delta \lambda_2 \\ & = R_1 + R_2 + R_3 + R_4 \end{aligned} \tag{4-59}$$

(a) The first item of right hand side of Equation (4-59):

$$R_1 = [1 - \Omega_1 \frac{1 - \exp(-s\lambda_1 / u_{in})}{s}][\frac{G(s + \Omega_1)}{\Omega_1} \ln(1 + \frac{\Omega_1(\lambda_2 - \lambda_1)}{u_{in}}) + \frac{f_2}{D_e} G(\lambda_2 - \lambda_1)] \delta u_{in} + C_1 \delta h_{in} \tag{4-60}$$

(b) The second item of right hand side of equation (4-59):

$$\begin{aligned} R_2 = & \{-(s + \Omega_1) G \ln(1 + \frac{\Omega_1(\lambda_2 - \lambda_1)}{u_{in}}) \frac{1}{\Omega_1 - s} [1 - \frac{\Omega_1}{s}(1 - \exp(-s\lambda_1 / u_{in}))] \\ & + Gg[\frac{1}{u_{in} + \Omega_1(\lambda_2 - \lambda_1)} - \frac{1}{u_{in}}] \frac{1}{\Omega_1 - s} [1 - \frac{\Omega_1}{s}(1 - \exp(-s\lambda_1 / u_{in}))] \\ & - \frac{f_2}{2D_e} G\Omega_1(\lambda_2 - \lambda_1) \frac{1}{\Omega_1 - s} [1 - \frac{\Omega_1}{s}(1 - \exp(-s\lambda_1 / u_{in}))] \end{aligned}$$

$$+(s+\Omega_1)G\Omega_1\frac{1}{\Omega_1-s}[(1+\Omega_1(\lambda_2-\lambda_1)/u_{in})^{\frac{\Omega_1-s}{\Omega_1}}-1]\frac{1}{\Omega_1-s}\exp(-s\lambda_1/u_{in})$$

$$+Gg\Omega_1\frac{1}{u_{in}^{\frac{\Omega_1-s}{\Omega_1}}}(-\frac{1}{s})[(u_{in}+\Omega_1(\lambda_2-\lambda_1))^{-\frac{s}{\Omega_1}}-u_{in}^{-\frac{s}{\Omega_1}}]\frac{1}{\Omega_1-s}\exp(-s\lambda_1/u_{in})$$

$$+\frac{f_2}{2D_e}G\Omega_1\frac{1}{u_{in}^{\frac{\Omega_1-s}{\Omega_1}}}\frac{1}{2\Omega_1-s}[(u_{in}+\Omega_1(\lambda_2-\lambda_1))^{\frac{2\Omega_1-s}{\Omega_1}}-u_{in}^{\frac{2\Omega_1-s}{\Omega_1}}]\frac{1}{\Omega_1-s}\exp(-s\lambda_1/u_{in})\}\delta u_{in}$$

$$+C_2\delta h_{in} \tag{4-61}$$

(c) The third term of right hand side of Equation (4-59):

$$R_3=-(G\Omega_1+\frac{f_2}{2D_e}Gu_{in}+\rho_f g)\frac{1-\exp(-s\lambda_1/u_{in})}{s}\delta u_{in}+C_3\delta h_{in} \tag{4-62}$$

(d) The fourth term of right hand side of Equation (4-59):

$$R_4=-[G\Omega_1+\frac{f_2}{2D_e}G(u_{in}+\Omega_1(\lambda_2-\lambda_1))+\rho_g g]$$

$$\times\frac{1}{\Omega_1-s}[1-\frac{\Omega_1}{s}(1-\exp(-s\lambda_1/u_{in}))-\exp(-s\lambda_1/u_{in})(1+\frac{\Omega_1(\lambda_2-\lambda_1)}{u_{in}})^{\frac{\Omega_1-s}{\Omega_1}}]\delta u_{in}$$

$$+C_4\delta h_{in} \tag{4-63}$$

(2-C) "Light fluid" region

From the velocity divergence Equation (4-29), one can obtain:

$$u(z)=u_{in}+\Omega_1(\lambda_2-\lambda_1)+\Omega_2(z-\lambda_2) \tag{4-64}$$

Thus,

$$\delta u(s,z) = \delta u_{in} - \Omega_1 \delta\lambda_1 + (\Omega_1 - \Omega_2)\delta\lambda_2 \tag{4-65}$$

Applying the same method as in region (2-A) and (2-B), the perturbation and Laplace transformation of energy Equation (4-22) yields:

$$\frac{d\delta h}{dz} + \frac{s-\Omega_2}{u}\delta h + \frac{q^{"}P_h}{GA_c u}\delta u = 0 \tag{4-66}$$

Again, this is a Bernoulli-type ordinary differential equation. After integration,

$$\delta h(s,z) = \frac{q^{"}P_h}{GA_c(\Omega_2 - s)}\delta u + Du^{\frac{\Omega_2 - s}{\Omega_2}} \tag{4-67}$$

Where D is the integration constant, which can be determined by boundary condition: $\delta h(s,z) = \delta h_m(s,\lambda_2)$ at $z = \lambda_2$, thus,

$$D = \frac{q^{"}P_h}{GA_c}\frac{1}{\Omega_2 - s}[-\exp(-s\lambda_1/u_{in})(1+\frac{\Omega_1(\lambda_2-\lambda_1)}{u_{in}})^{\frac{\Omega_1 - s}{\Omega_1}}][u_{in}+\Omega_1(\lambda_2-\lambda_1)]^{\frac{s-\Omega_2}{\Omega_2}}\delta u_{in} + D_1\delta h_{in} \tag{4-68}$$

$$\begin{aligned}\delta h(s,z) = {} & \frac{q^{"}P_h}{GA_c(\Omega_2 - s)}[\delta u_{in} - \Omega_1\delta\lambda_1 + (\Omega_1 - \Omega_2)\delta\lambda_2] \\ & - \frac{q^{"}P_h}{GA_c}\frac{1}{\Omega_2 - s}\exp(-s\lambda_1/u_{in})(1+\frac{\Omega_1(\lambda_2-\lambda_1)}{u_{in}})^{\frac{\Omega_1 - s}{\Omega_1}}[1+\frac{\Omega_2(z-\lambda_2)}{u_{in}+\Omega_1(\lambda_2-\lambda_1)}]^{\frac{\Omega_2 - s}{\Omega_2}}\delta u_{in} \\ & + H\delta h_{in}\end{aligned}$$

$$\begin{aligned}= {} & \frac{q^{"}P_h}{GA_c(\Omega_2 - s)}\{1 - \Omega_1\frac{1-\exp(-s\lambda_1/u_{in})}{s} \\ & - \frac{\Omega_1 - \Omega_2}{\Omega_1 - s}[1 - \frac{\Omega_1}{s}(1-\exp(-s\lambda_1/u_{in})) - \exp(-s\lambda_1/u_{in})(1+\frac{\Omega_1(\lambda_2-\lambda_1)}{u_{in}})^{\frac{\Omega_1 - s}{\Omega_1}}]\end{aligned}$$

$$- \exp(-s\lambda_1 / u_{in})(1 + \frac{\Omega_1(\lambda_2 - \lambda_1)}{u_{in}})^{\frac{\Omega_1 - s}{\Omega_1}} [1 + \frac{\Omega_2(z - \lambda_2)}{u_{in} + \Omega_1(\lambda_2 - \lambda_1)}]^{\frac{\Omega_2 - s}{\Omega_2}} \} \delta u_{in}$$

$$+ H\delta h_{in} \tag{4-69}$$

From $(\frac{dv}{dh})_p = \frac{R}{pC_p}$ one can obtain:

$$\delta\rho(z) = -\rho^2 \frac{R}{pC_P} \delta h(z) \tag{4-70}$$

The description of $\rho(z)$ can be obtained from $G = \rho(z)u(z)$

Combined with Equation (4-64), yields:

$$\rho(z) = G / [u_{in} + \Omega_1(\lambda_2 - \lambda_1) + \Omega_2(z - \lambda_2)] \tag{4-71}$$

Now, we integrate the momentum Equation (4-21), and have it expressed as:

$$-\frac{\partial p}{\partial z} = \frac{\partial G}{\partial t} + G\Omega_2 + \frac{f_3 \rho u^2}{2D_e} + \rho g \tag{4-72}$$

$$\delta(\Delta P_3) = \int_{\lambda_2}^{L} [(s + \Omega_2)\rho + \frac{f_3}{D_e} G]\delta u dz + \int_{\lambda_2}^{L} [(s + \Omega_2)u + \frac{f_3}{2D_e} u^2 + g]\delta\rho dz$$

$$- (G\Omega_2 + \frac{f_3}{2D_e} G u_m(\lambda_2) + \rho_g g)\delta\lambda_2$$

$$= T_1 + T_2 + T_3 \tag{4-73}$$

(a) The first item of the right hand side of Equation (4-73):

$$T_1 = [\frac{G(s+\Omega_2)}{\Omega_2}\ln(1+\frac{\Omega_2(L-\lambda_2)}{u_{in}+\Omega_1(\lambda_2-\lambda_1)}) + \frac{f_2}{D_e}G(L-\lambda_2)]\delta u + C_5\delta h_{in}$$

$$= \{1-\Omega_1\frac{1-\exp(-s\lambda_1/u_{in})}{s}$$

$$-\frac{\Omega_1-\Omega_2}{\Omega_1-s}[1-\frac{\Omega_1}{s}(1-\exp(-s\lambda_1/u_{in}))-\exp(-s\lambda_1/u_{in})(1+\frac{\Omega_1(\lambda_2-\lambda_1)}{u_{in}})^{\frac{\Omega_1-s}{\Omega_1}}\}$$

$$\times[\frac{G(s+\Omega_2)}{\Omega_2}\ln(1+\frac{\Omega_2(L-\lambda_2)}{u_{in}+\Omega_1(\lambda_2-\lambda_1)}) + \frac{f_2}{D_e}G(L-\lambda_2)]\delta u_{in} + C_5\delta h_{in} \qquad (4\text{-}74)$$

(b) The second item of the right hand side of Equation (4-73):

$$T_2 = \{-(s+\Omega_2)G\ln(1+\frac{\Omega_2(L-\lambda_2)}{u_{in}+\Omega_1(\lambda_2-\lambda_1)})$$

$$\times\frac{1}{\Omega_2-s}\{1-\frac{\Omega_1}{s}(1-\exp(-s\lambda_1/u_{in}))-\frac{\Omega_1-\Omega_2}{\Omega_1-s}[1-\frac{\Omega_1}{s}(1-\exp(-s\lambda_1/u_{in}))-\exp(-s\lambda_1/u_{in})(1+\frac{\Omega_1(\lambda_2-\lambda_1)}{u_{in}})^{\frac{\Omega_1-s}{\Omega_1}}]\}$$

$$+Gg[\frac{1}{u_{in}+\Omega_1(\lambda_2-\lambda_1)+\Omega_2(L-\lambda_2)}-\frac{1}{u_{in}+\Omega_1(\lambda_2-\lambda_1)}]$$

$$\times\frac{1}{\Omega_2-s}\{1-\frac{\Omega_1}{s}(1-\exp(-s\lambda_1/u_{in}))-\frac{\Omega_1-\Omega_2}{\Omega_1-s}[1-\frac{\Omega_1}{s}(1-\exp(-s\lambda_1/u_{in}))-\exp(-s\lambda_1/u_{in})(1+\frac{\Omega_1(\lambda_2-\lambda_1)}{u_{in}})^{\frac{\Omega_1-s}{\Omega_1}}]\}$$

$$-\frac{f_3}{2D_e}G\Omega_2(L-\lambda_2)$$

$$\times\frac{1}{\Omega_2-s}\{1-\frac{\Omega_1}{s}(1-\exp(-s\lambda_1/u_{in}))-\frac{\Omega_1-\Omega_2}{\Omega_1-s}[1-\frac{\Omega_1}{s}(1-\exp(-s\lambda_1/u_{in}))-\exp(-s\lambda_1/u_{in})(1+\frac{\Omega_1(\lambda_2-\lambda_1)}{u_{in}})^{\frac{\Omega_1-s}{\Omega_1}}]\}$$

$$+(s+\Omega_2)G\Omega_2\frac{1}{\Omega_2-s}[(1+\frac{\Omega_2(L-\lambda_2)}{u_{in}+\Omega_1(\lambda_2-\lambda_1)})^{\frac{\Omega_2-s}{\Omega_2}}-1]$$

$$\times\frac{1}{\Omega_2-s}\exp(-s\lambda_1/u_{in})(1+\frac{\Omega_1(\lambda_2-\lambda_1)}{u_{in}})^{\frac{\Omega_1-s}{\Omega_1}}$$

$$+Gg\Omega_2\frac{1}{(u_{in}+\Omega_1(\lambda_2-\lambda_1))^{\frac{\Omega_2-s}{\Omega_2}}}(-\frac{1}{s})[(u_{in}+\Omega_1(\lambda_2-\lambda_1)+\Omega_2(L-\lambda_2))^{-\frac{s}{\Omega_2}}-(u_{in}+\Omega_1(\lambda_2-\lambda_1))^{-\frac{s}{\Omega_2}}]$$
$$\times\frac{1}{\Omega_2-s}\exp(-s\lambda_1/u_{in})(1+\frac{\Omega_1(\lambda_2-\lambda_1)}{u_{in}})^{\frac{\Omega_1-s}{\Omega_1}}$$

$$+\frac{f_3}{2D_e}G\Omega_2\frac{1}{(u_{in}+\Omega_1(\lambda_2-\lambda_1))^{\frac{\Omega_2-s}{\Omega_2}}}\frac{1}{2\Omega_2-s}[(u_{in}+\Omega_1(\lambda_2-\lambda_1)+\Omega_2(L-\lambda_2))^{\frac{2\Omega_2-s}{\Omega_2}}-(u_{in}+\Omega_1(\lambda_2-\lambda_1))^{\frac{2\Omega_2-s}{\Omega_2}}]$$
$$\times\frac{1}{\Omega_2-s}\exp(-s\lambda_1/u_{in})(1+\frac{\Omega_1(\lambda_2-\lambda_1)}{u_{in}})^{\frac{\Omega_1-s}{\Omega_1}}$$
$$\}\,\delta u_{in}$$

$$+C_6\delta h_{in} \tag{4-75}$$

(c) The third term of the right hand side of Equation (4-73):

$$T_3=[G\Omega_2+\frac{f_3}{2D_e}G(u_{in}+\Omega_1(\lambda_2-\lambda_1))+\rho_g g]$$
$$\times\frac{1}{\Omega_1-s}[1-\frac{\Omega_1}{s}(1-\exp(-s\lambda_1/u_{in}))-\exp(-s\lambda_1/u_{in})(1+\frac{\Omega_1(\lambda_2-\lambda_1)}{u_{in}})^{\frac{\Omega_1-s}{\Omega_1}}]\delta u_{in}$$
$$+C_7\delta h_{in} \tag{4-76}$$

(3) Non-heated part

(3-A) Lower non-heated part

Applying the conservation equations and assuming constant fluid density in this part, the relation between the pressure drop oscillation and the inlet flow oscillation can be expressed as:

$$\delta\Delta p_{nod}=(f_1/D_eL_{nod}G+s\rho_AL_{nod})\delta u_{in} \tag{4-77}$$

(3-B) Upper non-heated part

Applying the conservation equations in this part:

$$\delta\Delta p_{nou} = (f_3 / D_e L_{nou} \frac{u(L)^2}{2} + gL_{nou} + su(L)L_{nou})\delta\rho(L) + (f_3 / D_e L_{nou} G + s\rho(L)L_{nou})\delta u(L) \tag{4-78}$$

Where:

$$u(L) = u_{in} + \Omega_1(\lambda_2 - \lambda_1) + \Omega_2(L - \lambda_2)$$

$$\rho(L) = G / [u_{in} + \Omega_1(\lambda_2 - \lambda_1) + \Omega_2(L - \lambda_2)]$$

$$\delta u(L) =$$

$$\{1 - \Omega_1 \frac{1 - \exp(-s\lambda_1 / u_{in})}{s}$$

$$+ \frac{\Omega_2 - \Omega_1}{\Omega_1 - s}[1 - \frac{\Omega_1}{s}(1 - \exp(-s\lambda_1 / u_{in})) - \exp(-s\lambda_1 / u_{in})(1 + \frac{\Omega_1(L - \lambda_1)}{u_{in}})^{\frac{\Omega_1 - s}{\Omega_1}}]\}\delta u_{in}$$

$$\delta\rho(L) = -\rho(L)^2 \frac{R}{pC_P} \frac{q^{"}P_h}{GA_c(\Omega_2 - s)} \{1 - \Omega_1 \frac{1 - \exp(-s\lambda_1 / u_{in})}{s}$$

$$- \frac{\Omega_1 - \Omega_2}{\Omega_1 - s}[1 - \frac{\Omega_1}{s}(1 - \exp(-s\lambda_1 / u_{in})) - \exp(-s\lambda_1 / u_{in})(1 + \frac{\Omega_1(\lambda_2 - \lambda_1)}{u_{in}})^{\frac{\Omega_1 - s}{\Omega_1}}]$$

$$- \exp(-s\lambda_1 / u_{in})(1 + \frac{\Omega_1(\lambda_2 - \lambda_1)}{u_{in}})^{\frac{\Omega_1 - s}{\Omega_1}} [1 + \frac{\Omega_2(L - \lambda_2)}{u_{in} + \Omega_1(\lambda_2 - \lambda_1)}]^{\frac{\Omega_2 - s}{\Omega_2}}\}\delta u_{in}$$

(4) The characteristic equation

The perturbation of the total channel pressure can be expressed as:

$$\delta\Delta p_{total} = \delta\Delta p_{ori} + \delta\Delta p_1 + \delta\Delta p_2 + \delta\Delta p_3 + \delta\Delta p_{nou} + \delta\Delta p_{nod} = \Pi_1 \delta u_{in} + \Pi_2 \delta h_{in} \tag{4-79}$$

Setting $\delta h_{in} = 0$, the characteristic equation for this single channel is Π_1.

$$\Pi_1 =$$

$$\rho_f \lambda_1 s + \frac{f_1 \rho_f u_{in} \lambda_1}{D_e} + k_{in} \rho_f u_{in} + (\frac{f_1 \rho_f u_{in}^2}{2D_e} + \rho_f g)(\frac{1 - \exp(-s\lambda_1 / u_{in})}{s}$$

$$+[1 - \Omega_1 \frac{1 - \exp(-s\lambda_1 / u_{in})}{s}][\frac{G(s+\Omega_1)}{\Omega_1} \ln(1 + \frac{\Omega_1(\lambda_2 - \lambda_1)}{u_{in}}) + \frac{f_2}{D_e} G(\lambda_2 - \lambda_1)]$$

$$+\{-(s+\Omega_1) G \ln(1 + \frac{\Omega_1(\lambda_2 - \lambda_1)}{u_{in}}) \frac{1}{\Omega_1 - s}[1 - \frac{\Omega_1}{s}(1 - \exp(-s\lambda_1 / u_{in}))]$$

$$+ Gg[\frac{1}{u_{in} + \Omega_1(\lambda_2 - \lambda_1)} - \frac{1}{u_{in}}] \frac{1}{\Omega_1 - s}[1 - \frac{\Omega_1}{s}(1 - \exp(-s\lambda_1 / u_{in}))]$$

$$- \frac{f_2}{2D_e} G\Omega_1(\lambda_2 - \lambda_1) \frac{1}{\Omega_1 - s}[1 - \frac{\Omega_1}{s}(1 - \exp(-s\lambda_1 / u_{in}))]$$

$$+ (s+\Omega_1) G\Omega_1 \frac{1}{\Omega_1 - s}[(1 + \Omega_1(\lambda_2 - \lambda_1)/u_{in})^{\frac{\Omega_1 - s}{\Omega_1}} - 1] \frac{1}{\Omega_1 - s} \exp(-s\lambda_1 / u_{in})$$

$$+ Gg\Omega_1 \frac{1}{u_{in}^{\frac{\Omega_1 - s}{\Omega_1}}}(-\frac{1}{s})[(u_{in} + \Omega_1(\lambda_2 - \lambda_1))^{-\frac{s}{\Omega_1}} - u_{in}^{-\frac{s}{\Omega_1}}] \frac{1}{\Omega_1 - s} \exp(-s\lambda_1 / u_{in})$$

$$+ \frac{f_2}{2D_e} G\Omega_1 \frac{1}{u_{in}^{\frac{\Omega_1 - s}{\Omega_1}}} \frac{1}{2\Omega_1 - s}[(u_{in} + \Omega_1(\lambda_2 - \lambda_1))^{\frac{2\Omega_1 - s}{\Omega_1}} - u_{in}^{\frac{2\Omega_1 - s}{\Omega_1}}] \frac{1}{\Omega_1 - s} \exp(-s\lambda_1 / u_{in})\}$$

$$-(G\Omega_1 + \frac{f_2}{2D_e} G u_{in} + \rho_f g) \frac{1 - \exp(-s\lambda_1 / u_{in})}{s}$$

$$-[G\Omega_1 + \frac{f_2}{2D_e} G(u_{in} + \Omega_1(\lambda_2 - \lambda_1)) + \rho_g g]$$

$$\times \frac{1}{\Omega_1 - s}[1 - \frac{\Omega_1}{s}(1 - \exp(-s\lambda_1 / u_{in})) - \exp(-s\lambda_1 / u_{in})(1 + \frac{\Omega_1(\lambda_2 - \lambda_1)}{u_{in}})^{\frac{\Omega_1 - s}{\Omega_1}}]$$

$$+\{1-\Omega_1\frac{1-\exp(-s\lambda_1/u_{in})}{s}-\frac{\Omega_1-\Omega_2}{\Omega_1-s}[1-\frac{\Omega_1}{s}(1-\exp(-s\lambda_1/u_{in}))-\exp(-s\lambda_1/u_{in})(1+\frac{\Omega_1(\lambda_2-\lambda_1)}{u_{in}})^{\frac{\Omega_1-s}{\Omega_1}}\}$$

$$\times[\frac{G(s+\Omega_2)}{\Omega_2}\ln(1+\frac{\Omega_2(L-\lambda_2)}{u_{in}+\Omega_1(\lambda_2-\lambda_1)})+\frac{f_2}{D_e}G(L-\lambda_2)]$$

$$+\{-(s+\Omega_2)G\ln(1+\frac{\Omega_2(L-\lambda_2)}{u_{in}+\Omega_1(\lambda_2-\lambda_1)})$$

$$\times\frac{1}{\Omega_2-s}\{1-\frac{\Omega_1}{s}(1-\exp(-s\lambda_1/u_{in}))$$

$$-\frac{\Omega_1-\Omega_2}{\Omega_1-s}[1-\frac{\Omega_1}{s}(1-\exp(-s\lambda_1/u_{in}))-\exp(-s\lambda_1/u_{in})(1+\frac{\Omega_1(\lambda_2-\lambda_1)}{u_{in}})^{\frac{\Omega_1-s}{\Omega_1}}]\}$$

$$+Gg[\frac{1}{u_{in}+\Omega_1(\lambda_2-\lambda_1)+\Omega_2(L-\lambda_2)}-\frac{1}{u_{in}+\Omega_1(\lambda_2-\lambda_1)}]$$

$$\times\frac{1}{\Omega_2-s}\{1-\frac{\Omega_1}{s}(1-\exp(-s\lambda_1/u_{in}))$$

$$-\frac{\Omega_1-\Omega_2}{\Omega_1-s}[1-\frac{\Omega_1}{s}(1-\exp(-s\lambda_1/u_{in}))-\exp(-s\lambda_1/u_{in})(1+\frac{\Omega_1(\lambda_2-\lambda_1)}{u_{in}})^{\frac{\Omega_1-s}{\Omega_1}}]\}$$

$$-\frac{f_3}{2D_e}G\Omega_2(L-\lambda_2)$$

$$\times\frac{1}{\Omega_2-s}\{1-\frac{\Omega_1}{s}(1-\exp(-s\lambda_1/u_{in}))$$

$$-\frac{\Omega_1-\Omega_2}{\Omega_1-s}[1-\frac{\Omega_1}{s}(1-\exp(-s\lambda_1/u_{in}))-\exp(-s\lambda_1/u_{in})(1+\frac{\Omega_1(\lambda_2-\lambda_1)}{u_{in}})^{\frac{\Omega_1-s}{\Omega_1}}]\}$$

$$+(s+\Omega_2)G\Omega_2\frac{1}{\Omega_2-s}[(1+\frac{\Omega_2(L-\lambda_2)}{u_{in}+\Omega_1(\lambda_2-\lambda_1)})^{\frac{\Omega_2-s}{\Omega_2}}-1]\times\frac{1}{\Omega_2-s}\exp(-s\lambda_1/u_{in})(1+\frac{\Omega_1(\lambda_2-\lambda_1)}{u_{in}})^{\frac{\Omega_1-s}{\Omega_1}}$$

$$+Gg\Omega_2\frac{1}{(u_{in}+\Omega_1(\lambda_2-\lambda_1))^{\frac{\Omega_2-s}{\Omega_2}}}(-\frac{1}{s})[(u_{in}+\Omega_1(\lambda_2-\lambda_1)+\Omega_2(L-\lambda_2))^{-\frac{s}{\Omega_2}}-(u_{in}+\Omega_1(\lambda_2-\lambda_1))^{-\frac{s}{\Omega_2}}]$$

$$\times\frac{1}{\Omega_2-s}\exp(-s\lambda_1/u_{in})(1+\frac{\Omega_1(\lambda_2-\lambda_1)}{u_{in}})^{\frac{\Omega_1-s}{\Omega_1}}$$

$$+\frac{f_3}{2D_e}G\Omega_2\frac{1}{(u_{in}+\Omega_1(\lambda_2-\lambda_1))^{\frac{\Omega_2-s}{\Omega_2}}}\frac{1}{2\Omega_2-s}[(u_{in}+\Omega_1(\lambda_2-\lambda_1)+\Omega_2(L-\lambda_2))^{\frac{2\Omega_2-s}{\Omega_2}}-(u_{in}+\Omega_1(\lambda_2-\lambda_1))^{\frac{2\Omega_2-s}{\Omega_2}}]$$

$$\times\frac{1}{\Omega_2-s}\exp(-s\lambda_1/u_{in})(1+\frac{\Omega_1(\lambda_2-\lambda_1)}{u_{in}})^{\frac{\Omega_1-s}{\Omega_1}}\}$$

$$+[G\Omega_2+\frac{f_3}{2D_e}G(u_{in}+\Omega_1(\lambda_2-\lambda_1))+\rho_g g]$$

$$\times\frac{1}{\Omega_1-s}[1-\frac{\Omega_1}{s}(1-\exp(-s\lambda_1/u_{in}))-\exp(-s\lambda_1/u_{in})(1+\frac{\Omega_1(\lambda_2-\lambda_1)}{u_{in}})^{\frac{\Omega_1-s}{\Omega_1}}$$

$$+(f_1/D_eL_{nod}G+s\rho_fL_{nod})$$

$$+(f_3/D_eL_{nou}G+s\rho_fL_{nou})$$

$$\times\{1-\Omega_1\frac{1-\exp(-s\lambda_1/u_{in})}{s}+\frac{\Omega_2-\Omega_1}{\Omega_1-s}[1-\frac{\Omega_1}{s}(1-\exp(-s\lambda_1/u_{in}))-\exp(-s\lambda_1/u_{in})(1+\frac{\Omega_1(L-\lambda_1)}{u_{in}})^{\frac{\Omega_1-s}{\Omega_1}}]\}$$

$$-\{f_3/D_eL_{nou}\,[u_{in}+\Omega_1(\lambda_2-\lambda_1)+\Omega_2(L-\lambda_2)]^2/2+gL_{nou}+sL_{nou}\,[u_{in}+\Omega_1(\lambda_2-\lambda_1)+\Omega_2(L-\lambda_2)]\}$$

$$\times\{G/\,[u_{in}+\Omega_1(\lambda_2-\lambda_1)+\Omega_2(L-\lambda_2)]\}^2$$

$$\times\frac{R}{pC_P}\frac{q''P_h}{GA_c(\Omega_2-s)}\{1-\Omega_1\frac{1-\exp(-s\lambda_1/u_{in})}{s}-\frac{\Omega_1-\Omega_2}{\Omega_1-s}[1-\frac{\Omega_1}{s}(1-\exp(-s\lambda_1/u_{in}))-\exp(-s\lambda_1/u_{in})(1+\frac{\Omega_1(\lambda_2-\lambda_1)}{u_{in}})^{\frac{\Omega_1-s}{\Omega_1}}]$$

$$-\exp(-s\lambda_1/u_{in})(1+\frac{\Omega_1(\lambda_2-\lambda_1)}{u_{in}})^{\frac{\Omega_1-s}{\Omega_1}}[1+\frac{\Omega_2(L-\lambda_2)}{u_{in}+\Omega_1(\lambda_2-\lambda_1)}]^{\frac{\Omega_2-s}{\Omega_2}}\}\quad(4\text{-}80)$$

4.6 Static or Ledinegg Stability using characteristic equation

According to Ishii [1971], the Ledinegg type stability criterion can be expressed as:

$$\lim_{s\to 0}\frac{\delta\Delta p_{channel}}{\delta u_{in}}>0\Rightarrow\lim_{s\to 0}\Pi_1(s)>0\quad(4\text{-}81)$$

The perturbation of inlet velocity can be expressed as:

$$\delta u_{in}=\varepsilon e^{st}\quad(4\text{-}82)$$

Where, ε is an arbitrarily constant number and s is a complex number ($s = \sigma + j\omega$, where σ is amplification coefficient and ω is the frequency of oscillation). Thus, by taking the limit $s \to 0$, the perturbation becomes constant. Thus inequality (4-81) becomes the same as inequality (1-1).

$$\frac{\partial(\Delta p_{System})}{\partial u_{in}} > 0 \qquad (1\text{-}1)$$

For the U.S. reference SCWR design, and as previously defined hot channel ($k_{in} = 20.0$):

$$\lim_{s \to 0} \Pi_1(s) = 6.63e4 > 0 \qquad (4\text{-}83)$$

Similarly, at an average channel ($k_{in} = 115.0$):

$$\lim_{s \to 0} \Pi_1(s) = 1.47e5 > 0 \qquad (4\text{-}84)$$

Thus, there will be no Ledinegg type static instability in the U.S. reference SCWR design at steady-state operation conditions. This finding is the same as discussed in Section 4.4.

4.7 Stability map construction

The stability map that defines the onset of instability can be constructed by two methods. One is so called D-Partition method. The other one is decay ratio method by finding the condition that decay ratio equals 1.0 for the fundamental oscillation mode. These two methods will be discussed first, then, the stability map will be constructed by using the D-Partition method.

4.7.1 Stability map construction methods

As mentioned previously, the variables for the single channel system are: geometry, system pressure, inlet flow rate, inlet enthalpy and surface heat flux. Also, the characteristic equation includes the complex variable s. Thus,

$$\Pi_1 = f(Geometry, p, u_{in}, s, h_{in}, q'') = 0 \tag{4-85}$$

For a specific heated channel such as U.S. reference SCWR flow channel, the geometry is specified. If the system pressure and inlet flow rate are also specified, the remaining variables for the characteristic equation are: complex variable s, coolant inlet enthalpy h_{in} and surface heat flux q''. The system will be unstable if s has positive real part; or, the system will be stable if s has negative real part. Thus, the system will be neutrally stable if s has zero real part. If we set $s = j\omega$ in above Equation (4-85), the boundary value of h_{in} and q'' pair can be solved at a specific ω. Changing the ω, we can plot the stability boundary. Otherwise, if we give the q'' at a specific h_{in}, Equation (4-85) can be solved to find the decay ratio of the dominant oscillation mode. Increasing the q'' step by step until the decay ratio equals 1.0, the boundary value of q'' was obtained. Changing the h_{in} to repeat the calculation procedure, a stability boundary map can be plottd.

According to D-Partition method, we can construct the neutral stability boundary or the stability map by the procedure described below. One can find the details on the D-Partition method in [Porter, 1968].

(A) Setting boundary value $s = j\omega$.

(B) Solving the system of equations $\mathrm{Re}(\Pi_1) = 0, \mathrm{Im}(\Pi_1) = 0$ for a specific ω. This complicated system of equations is numerically solved by Newton's method. The boundary pair of h_{in} and q'' are obtained for this specific ω.

(C) Repeating procedure (B) by changing ω, the other boundary pairs of h_{in} and q'' are obtained.

(D) The pseudo subcooling number and expansion number are calculated based on above h_{in} and q'' pairs.

(E) Plotting the results on N_{psub} - $N_{\exp}$ plane.

If we use the decay ratio method instead, the calculation procedure will be:

(A) Setting specific inlet enthalpy h_{in}.

(B) Solving the system of equations $\mathrm{Re}(\Pi_1) = 0, \mathrm{Im}(\Pi_1) = 0$ at a given q'', the dominant root s can be found, then the decay ratio can be obtained corresponding to this dominant root. Increasing the q'' step by step until the decay ratio grows to 1.0, the boundary pair of h_{in} and q'' is obtained.

(C) Repeating procedure (B) by changing h_{in}, the other boundary pairs of h_{in} and q'' are obtained.

(D) The pseudo subcooling number and expansion number are calculated based on above h_{in} and q'' pairs.

(E) Plotting the results on N_{psub} - $N_{\exp}$ plane.

4.7.2 Stability maps for U.S. reference SCWR design at full power condition

Applying the above mentioned D-Partition method to the U.S. reference SCWR design, the stability maps were constructed for both the hot channel (with $k_{in} = 20.0$) and the average channel (with $k_{in} = 115.0$). These are shown in Figures 4-11 and 4-12, respectively.

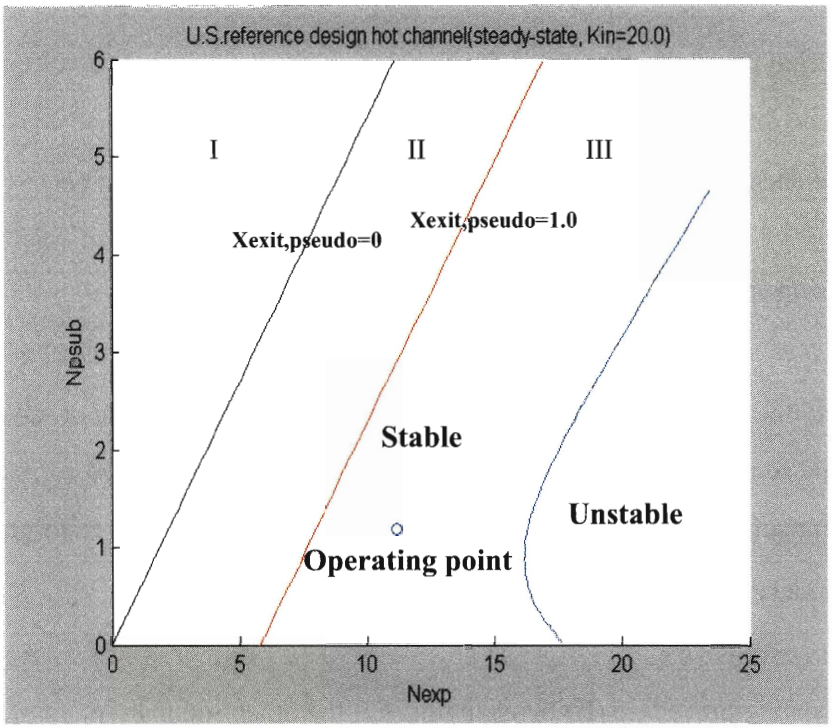

Fig. 4-11: Stability map for U.S. reference SCWR design for hot channel ($k_{in} = 20.0$)

In Figure 4-11, the operating condition in region I means that the coolant enthalpy at the channel exit is below the pseudo saturation fluid enthalpy h_A. The operating condition in region II means the coolant enthalpy at the channel exit is above the pseudo saturation fluid enthalpy h_A but below the pseudo saturation vapor enthalpy h_B. The operating

condition in region III means the coolant enthalpy at the channel exit is above the pseudo saturation vapor enthalpy h_B. Also, in the above figure, the "operating point" is the U.S. reference SCWR design at full power operation conditions.

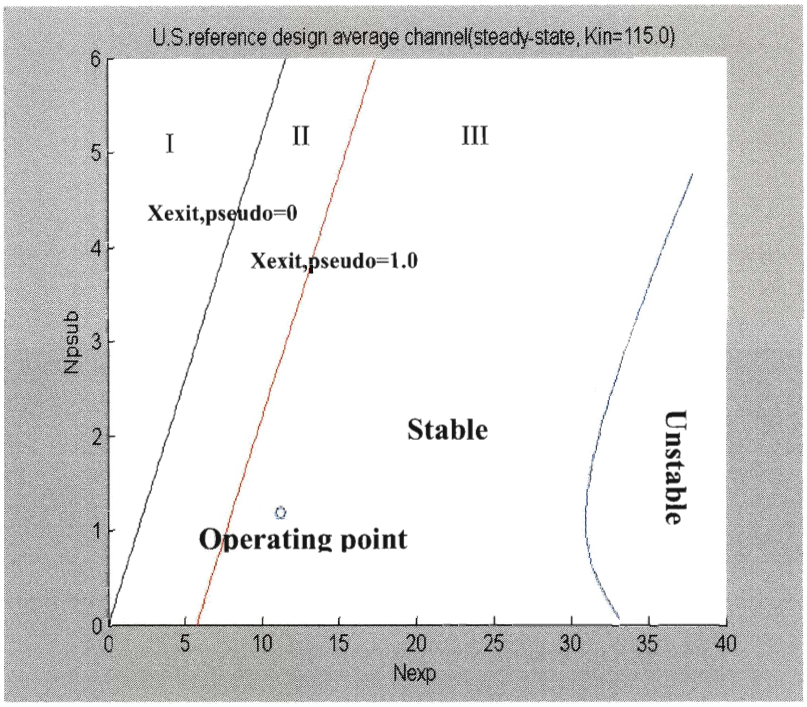

Fig. 4-12: Stability map for U.S. reference SCWR design for average channel ($k_{in}=115.0$)

From Fig. 4-11 and 4-12, it is easy to see that the U.S. reference design, with the inlet orifice coefficient specified here, will operate in a stable region both for the hot and the average channels with a large margin.

The stabilization effect of the inlet orifice is also shown in Figure 4-13, where the neutral stability boundaries for various values of the inlet orifice coefficients are plotted.

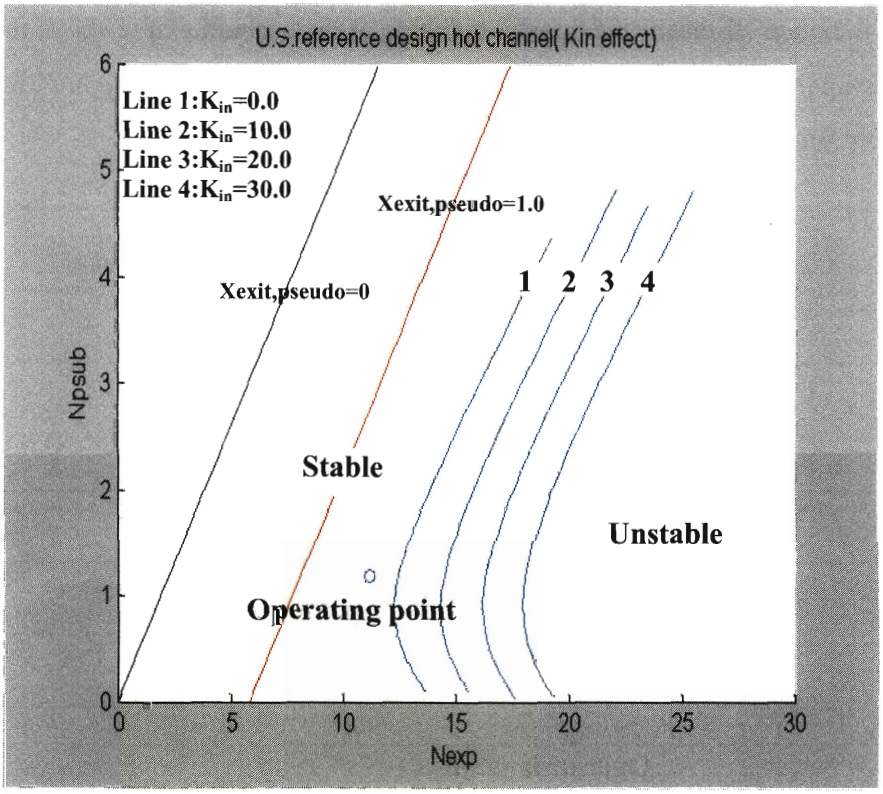

Fig. 4-13: The stability effects of inlet orifice coefficient for hot channel

It is seen from Fig. 4-13 that the stability boundary will move to the right with increasing value of the inlet orifice coefficients. Thus the stability margin increases for the same operating conditions. It is interesting to note that even for $k_{in} = 0.0$, the operating point is in the stable region. This is in agreement with the result shown in Fig. 3-5 where the decay ratio was around 0.55 for $k_{in} = 0.0$.

As mentioned previously, the characteristic equation is also a function of system pressure and inlet flow rate. During the stability map construction in the pseudo-subcooling number versus expansion number plane, the pressure and the inlet flow rate were pre-specified. To study the effects of inlet flow rate and system pressure on the stability boundary, the following maps have been constructed.

In the inlet flow effect analysis, the inlet flow in the hot channel of U.S. reference design was solely varied while keeping the other parameters unchanged. The results are shown in Fig. 4-14.

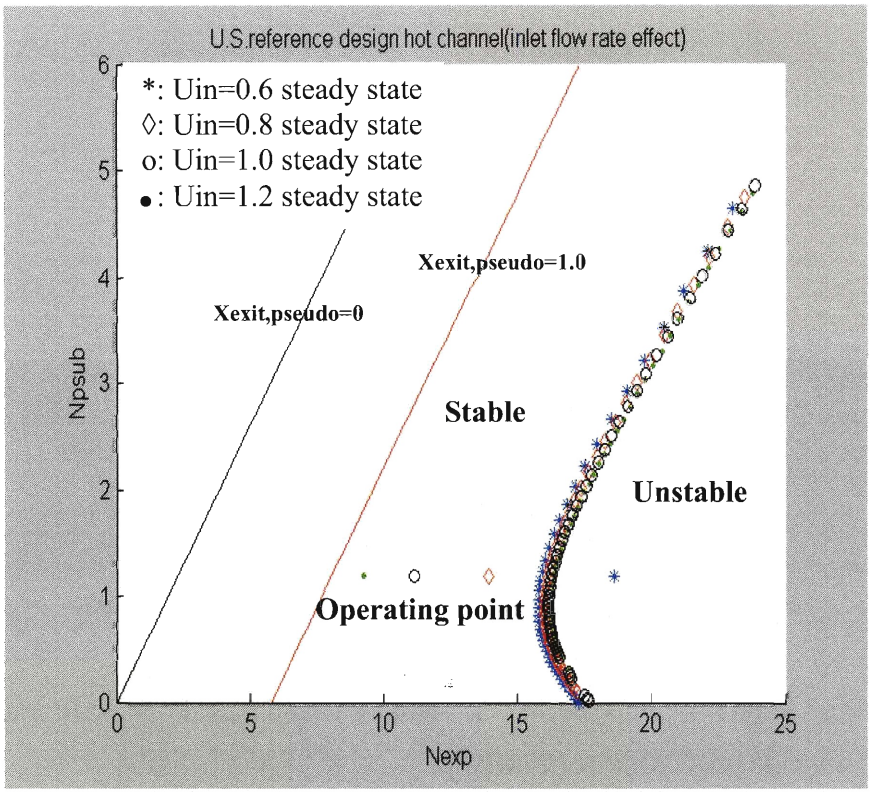

Fig. 4-14: The inlet flow effect to stability boundary

From Fig. 4-14 above, the inlet flow rate will not have much effect on the stability boundary in the pseudo subcooling number and expansion number plane. The operating point will move to the right if the inlet flow rate was reduced. If the inlet flow is reduced to 60% of the full power case, the operating point will move into the unstable region as shown by star point in Fig. 4-14.

Also, in the system pressure effect analysis, the system pressure for the U.S. reference design hot channel was solely varied while keeping the other parameters unchanged. The results are shown in Fig. 4-15.

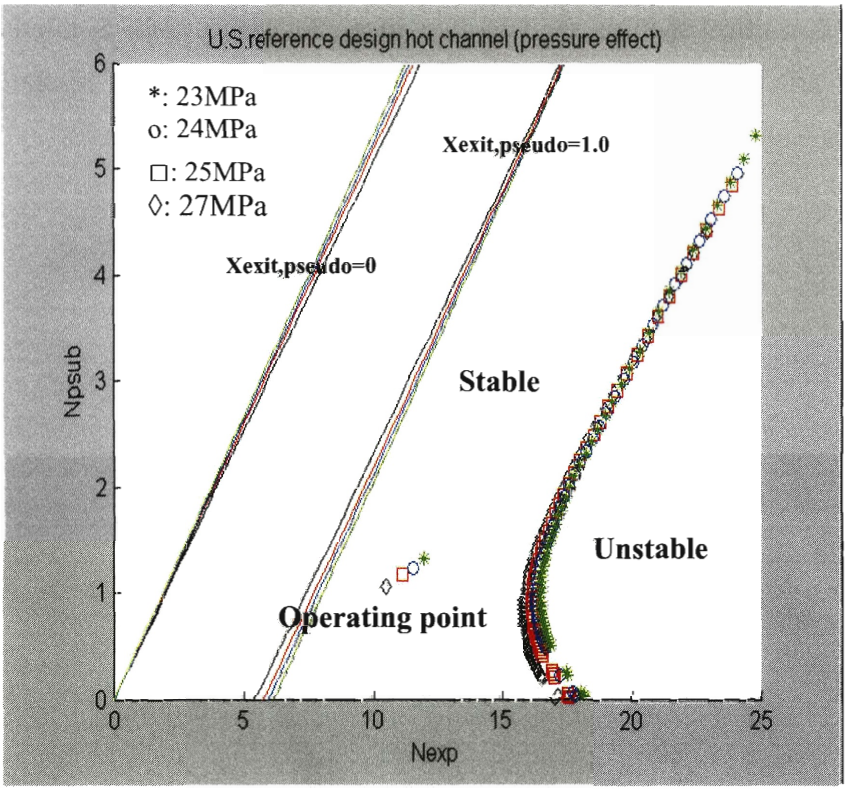

Fig. 4-15: The stability boundary effect of system pressure

It is seen from Figure 4-15 above that the stability boundaries do not shift much in the system pressure range of 23MPa to 27MPa.

From Figures 4-14 and 4-15 above, it is seen that both the inlet flow and system pressure effects on the stability boundary can be absorbed if the stability boundary is plotted on the pseudo-subcooling number versus expansion number plane. This means that once the stability map is constructed for a specific pressure and inlet flow rate, it is also applicable for a quick check of the stability features at other supercritical pressures and inlet flow rates.

Additionally, the inlet temperature effects on the channel stability could be read very easily on the stability map. If we change the inlet coolant temperature, say increasing, while keeping other parameters constant, the pseudo subcooling number will decrease

also while the expansion number is fixed. Then, a vertical line can be plotted in the stability map, the stability margins are ready to read. These are illustrated in Fig. 4-16.

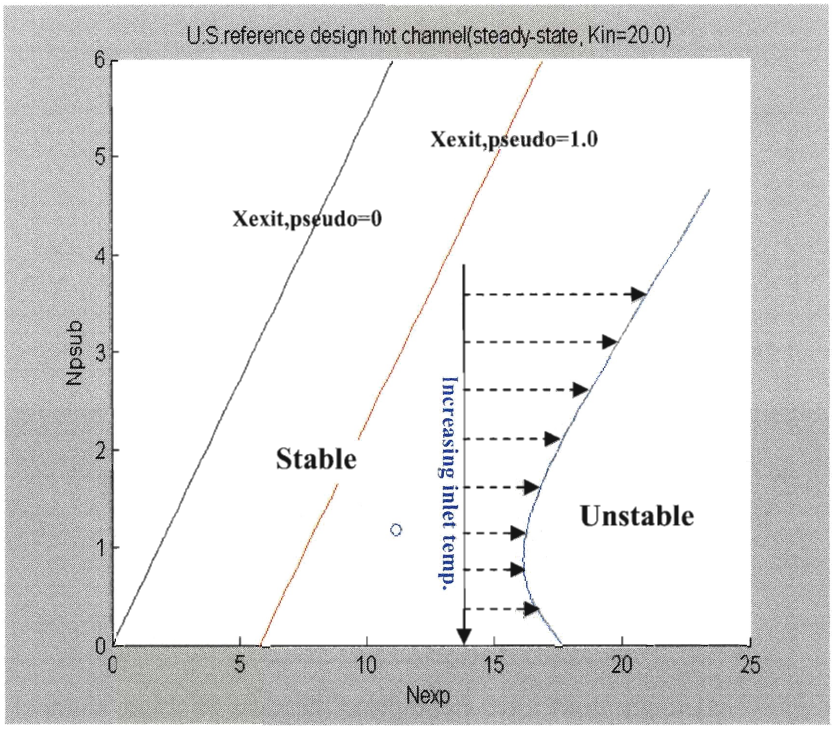

Fig. 4-16: Inlet temperature effects on stability

From above Fig. 4-16, it is easy to see that: at low pseudo subcooling numbers, increasing the inlet temperature will destabilize the channel; at the high pseudo subcooling numbers, increasing the inlet temperature will stabilize the channel. In fact, this total effect is the combination of two effects as increasing the inlet temperature. First, the higher inlet temperature means a higher average temperature and a lower average density in the whole core, therefore, the coolant is more compressible, which is a destabilization effect. Secondly, a higher inlet temperature will give a shorter first region length in our three-region model. Therefore, the oscillation amplitude in the boundary between the first region and the second region will be smaller, which is a stabilization effect. In the three region model, the first region (corresponding to single phase region in the BWR) can be assumed incompressible, and the second and third regions (corresponding to two phase region in the BWR) are the compressible part. These are illustrated in Fig. 4-17:

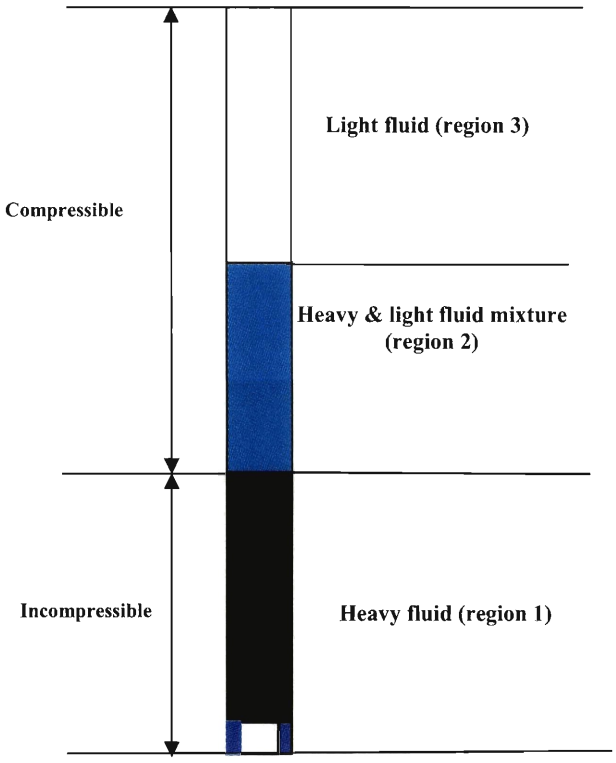

Fig. 4-17: Compressible and incompressible parts of single channel

During the density wave oscillations, the boundary oscillation of the incompressible part and the compressible part is in fact the inlet oscillation of the compressible part. A large inlet oscillation obviously will generate the large oscillation amplitude in the compressible region. Therefore, increasing the inlet temperature will generate smaller oscillation in the boundary and stabilize the system.

At higher pseudo subcooling number, the effect of increasing the inlet temperature is destabilization, since the first reason is dominant. At lower pseudo subcooling number, the effect of the increasing inlet temperature is stabilization, because the second reason is dominant. In fact, at very high inlet temperature, say above the pseudo saturation point 350°C, there will be no instability problem in the channel according to [Khabensky, V. B. and Gerliga, V. A., 1995].

4.8 Model evaluation

The single-channel stability model for the supercritical pressure has been validated using the experimental data presented in [Khabensky and Gerliga, 1995]. Although limited information was available regarding the details of the experiment [Yu, 1965], this was the only set of relevant data we could find on the stability boundary at supercritical pressure. The experiment was conducted in a long heated coil (12.6m high, 0.01m diameter) using water at 23 – 23.5MPa pressure. No information regarding the inlet and outlet restrictions was available. Thus, we had to neglect the effect of inlet and outlet restrictions during the model validation. The predicted stability boundary agreed with the experimental stability boundary within ±30% which is reasonable given the lack of detailed information on the experiment.

In this evaluation, the stable boundary heat flux was predicted based on the developed model and compared with that of the experimental value. The results are presented in Table 4-1.

Table 4-1: Comparison of experimental and predicted stability boundary

Pressure MPa	Inlet enthalpy kJ/kg	Inlet flow rate kg/m^2s	Experimental boundary heat flux kW/m^2	Predicted boundary heat flux kW/m^2	Experimental boundary N_{exp}	Predicted boundary N_{exp}	Relative error $\left\|\frac{N_{\exp,ex.} - N_{\exp,pre.}}{N_{\exp,ex.}}\right\|$
23	1200	180	81.3	81.3	14.1	14.1	0%
23	1200	150	69.5	78.5	14.4	16.3	13.2%
23	1590	300	116.0	154.0	12.1	16.0	32.2%
23	840	135	69.5	72.3	16.0	16.7	4.38%
23.5	1000	150	116.0	78.6	23.6	16.0	32.2%
23.5	1000	100	58.0	67.2	17.7	20.5	15.8%

It is seen that most of the data points are within ± 30% relative error range. The results have also been plotted in Figure 4-18.

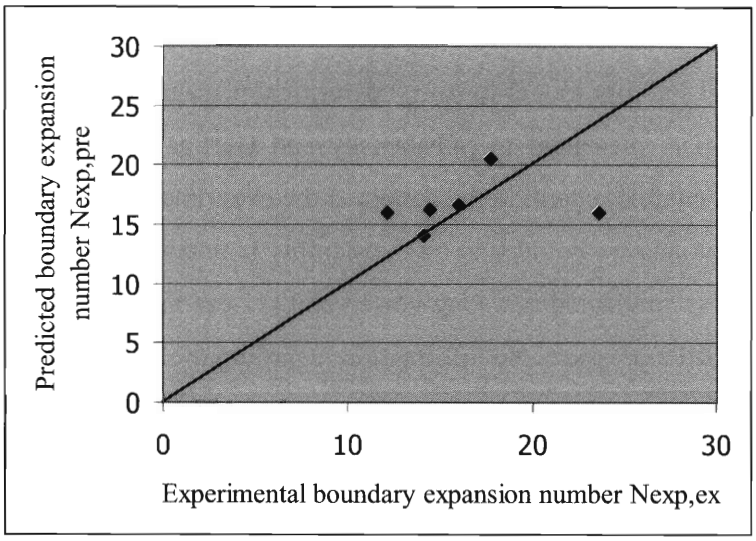

Fig. 4-18: Comparison of experimental and predicted boundary expansion number

4.9 The three-region model comparison with the response matrix method

To compare the three-region model developed in this chapter to the response matrix method described in the Chapter 3, the decay ratios for the hot channel at steady state were calculated by using these two methods. The decay ratios at different inlet orifice coefficients were calculated. The results are listed in Table 4-2 and plotted in Fig. 4-19. Again, eighty nodes were used for the response matrix method.

Table 4-2: Comparison of three-region model with the response matrix model

Inlet orifice coefficients	0	10	15	20
DR calculated by three-region model	0.5432	0.2394	0.1744	0.1323
DR calculated by response matrix method	0.5744	0.2184	0.1532	0.1132

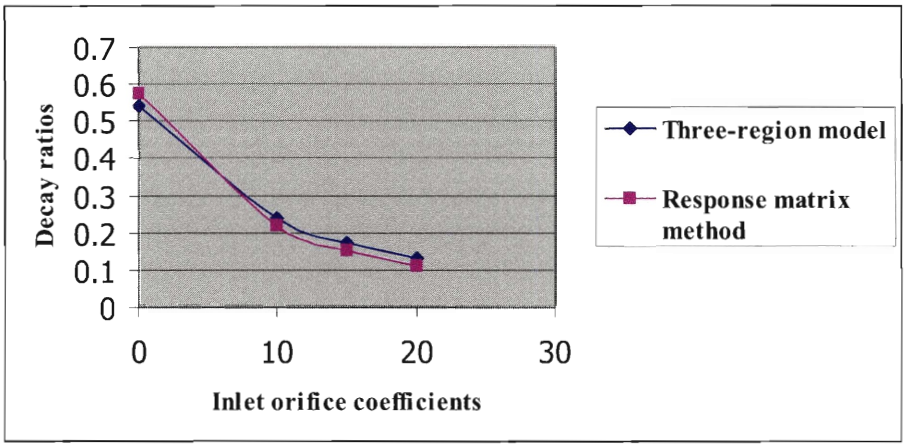

Fig. 4-19: Comparison between three region model and response matrix method

Therefore, the three-region model agrees with the response matrix method quite well.

Chapter 5

Stability map construction for subcritical Pressure

The governing parameters for stability in subcritical pressure are the Subcooling number and the Phase change number (also called as Zuber number). These are defined as: $N_{sub} = \frac{(h_f - h_{in})}{h_{fg}} \frac{\Delta\rho}{\rho_g}$ and $N_{pch} = \frac{v_{fg}}{h_{fg}} \frac{q'' P_h}{A_c} \frac{L}{u_{in}}$. These two governing parameters can be derived from nondimensional analysis of the conservation equations for subcritical pressure. The detailed discussion can be found in [Ishii, 1971]. The stability map will be constructed in the subcooling number versus phase change number plane.

Construction of stability maps for single heated channel at subcritical pressure has a long history. Using a non-homogenous drift flux model, Ishii [1971] had constructed a stability map in subcooling number versus phase change number plane. Later, Saha [1974] improved Ishii's model by including the effect of thermal non-equilibrium. But it was found to be too complicated to derive the characteristic equation analytically if one used a detailed vapor generation model such as an exponential distribution. Saha [1974] simplified the exponential distribution to a linear model so that the characteristic equation could be derived analytically. More recently, Podowski [2003] compared the stability boundary effects of different two phase flow models. But, all of his three models, i.e., HEM, Drift flux and Two-fluid model, were based on the assumption of thermal

equilibrium. In the present work, we use the non-homogenous and non-equilibrium model with a detailed exponential vapor generation distribution for two phase flow and the characteristic equation is derived numerically. Also, the effects of different two-phase flow models on the stability boundary are investigated. Thus, the stability boundary maps are constructed using four different models, namely, the Homogenous-Equilibrium model (HEM), the Homogenous-Nonequilibrium model (HNEM), the Nonhomogenous-Equilibrium model (NHEM) and the Nonhomogenous-NonEquilibrium model (NHNEM). The Non-equilibrium models account for the existence of subcooled boiling, whereas the Non-homogenous models incorporate the drift flux concepts.

In the subcritical pressure region, for some situations, the system may be unstable when the heat flux is high enough so that the channel exit thermodynamic equilibrium quality is above 1.0. In these cases, to investigate the onset of instability, a three region model is required. These three regions are: (1) single-phase liquid region, (2) two-phase mixture region, and (3) superheated vapor region. For the U.S. reference SCWR design, all operations normally occur at high pressures. Since the HEM model is a good simulation at high pressure, the three region model derived for the supercritical region based on the pseudo HEM model can be applied to the subcritical pressure as well. However, in the following subsections, we concentrate on two-region model which means that the channel exit equilibrium quality is constrained to remain below 1.0.

5.1 Non-homogenous Non-equilibrium model description

(1) Net vapor generation point and exponential vapor generation rate

The net vapor generation point that defines the boiling boundary was predicted by applying the widely used Saha and Zuber [1974] correlation:

$$\Delta h_\lambda = h_f - h_\lambda = 0.0022 \frac{q_w'' D_h C_{pf}}{k_f} \qquad P_e \le 70{,}000 \tag{5-1}$$

$$\Delta h_\lambda = h_f - h_\lambda = 154\frac{q_w^{"}}{\rho_f u_{in}} \qquad P_e \geq 70{,}000 \tag{5-2}$$

For vapor generation rate, an exponential distribution [Saha, 1974] along the channel is assumed:

$$\Gamma_g = \frac{q_w^{"} P_h}{A_c h_{fg}}[1 - \exp(-\frac{z - \lambda_1(t)}{\Delta l})] = \Gamma_{g,eq}[1 - \exp(-\frac{z - \lambda_1(t)}{\Delta l})] \tag{5-3}$$

Where,

λ_1 is the boiling boundary which is defined as:

$$\lambda_1 = \frac{GA_c(h_\lambda - h_{in})}{q_w^{"} P_h} \tag{5-4}$$

The characteristic length Δl was defined as:

$$\Delta l = \lambda_{eq} - \lambda_1 = \frac{GA_c(h_f - h_\lambda)}{q_w^{"} P_h} \tag{5-5}$$

The vapor generation rate model based on the exponential distribution and the thermal equilibrium assumption are illustrated in Fig. 5-1.

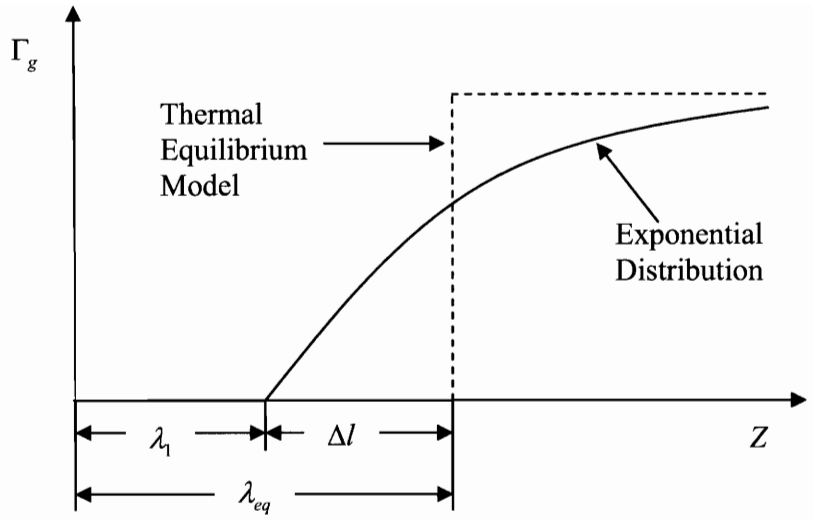

Fig. 5-1: Comparison of two vapor generation models

(2) Bestion drift-flux correlation

For the non-homogenous model, the Bestion [1985] drift-flux correlation was applied in this work. According to Coddington [2002], despite the simplicity of this correlation, it yields very good results for most of the experimental data. This correlation has the following form:

$$C_o = 1.0$$

$$V_{gj} = 0.188\sqrt{\frac{gD_e\Delta\rho}{\rho_g}} \tag{5-6}$$

Where,

C_o: The concentration parameter, which represents the global effect due to radial non-uniform void and velocity profiles

V_{gj}: The drift velocity of the vapor

(3) Subcooled flow quality and void fraction

Using the exponential vapor generation model defined in equation (106), Saha [1974] derived the flow quality in the following form:

$$x(z) = x_{eq} - x_{eq,\lambda} \exp(\frac{x_{eq}}{x_{eq,\lambda}} - 1) \tag{5-7}$$

The above formula follows that of Levy [1967] using the profile-fit approach.

The equilibrium quality in the above formula can be expressed as:

$$x_{eq} = \frac{q_w'' P_h \Delta l}{G A_c h_{fg}} (\frac{z - \lambda_1}{\Delta l} - 1) \tag{5-8}$$

And $x_{eq,\lambda}$ is the equilibrium quality at net vapor generation point $z = \lambda_1$. The void fraction may then be predicted from the drift flux model as:

$$\alpha(z) = \frac{x}{C_o (x \frac{\Delta\rho}{\rho_f} + \frac{\rho_g}{\rho_f}) + \frac{\rho_g V_{gj}}{G}} \tag{5-9}$$

5.2 Friction factor for subcritical pressure

For the subcritical pressure region, according to Todreas and Kazimi [1990]:

For $\mathrm{Re} = 3 \times 10^4 - 10^6$, the following McAdams relation can be applied:

$$f = 0.184\,\mathrm{Re}^{-0.2} \tag{5-10}$$

For $\mathrm{Re} < 3 \times 10^4$, the following Blasius relation can be applied:

$$f = 0.316\,\mathrm{Re}^{-0.25} \tag{5-11}$$

Using the above correlations, the friction factor calculations in the subcritical pressure region are carried out as follows:

(1) Single phase liquid region

The friction factor is assumed constant and equals f_s, which is the friction factor at the boiling boundary.

(2) Two phase mixture flow region

According to Ishii [1971], in the two phase mixture region at subcritical pressure, the friction factor could be assumed in the following form:

$$f_2 = C_m f_s \tag{5-12}$$

Where, the C_m is a constant number and f_s was calculated at the boiling boundary. For high system pressure and reasonably high exit qualities in a subcritical pressure system, C_m has a range from 1.5 to 2.5. Thus, $C_m = 2.0$ was taken both by Ishii [1971] and Saha [1974]. In this report, $C_m = 2.0$ is also taken. Thus, $f_2 = 2.0 f_s$

(3) Superheated vapor region

Again, the friction factor is assumed constant in this region, and the Reynolds number is calculated at the saturation vapor properties.

5.3 Characteristic equation for Non-homogenous Non-equilibrium model

The single flow channel of the SCWR core at subcritical pressure is also divided into four parts as in the supercritical pressure region. The four parts are the inlet orifice, the lower non-heated part, the heated part and the upper non-heated part.

(1) Inlet orifice

The momentum equation for the inlet orifice can be expressed as:

$$\Delta p_{ori} = k_{in} \frac{\rho_f u_{in}^2}{2} \tag{5-13}$$

Perturbation and Laplace transformation of the above equation, yields:

$$\delta\Delta p_{ori} = k_{in} \rho_f u_{in} \delta u_{in} \tag{5-14}$$

(2) Heated part

This part includes the single phase liquid region and the two phase mixture region.

(A) Liquid region

The conservation equations can be expressed as:

$$\frac{\partial u}{\partial z} = 0 \quad (\rho(z) = \rho_f = Const.) \tag{5-15}$$

$$\rho_f \frac{\partial h}{\partial t} + \rho_f u_{in} \frac{\partial h}{\partial z} = \frac{q'' P_h}{A_c} \tag{5-16}$$

$$-\frac{\partial p}{\partial z} = \rho_f \frac{du_{in}}{dt} + \frac{f_1 \rho_f u_{in}^2}{2D_e} + \rho_f g \tag{5-17}$$

In this region, the water density is assumed constant and equal to the saturated water density ρ_f. Perturbing and Laplace transforming the energy equation (5-16), one obtains:

$$\frac{d\delta h}{dz} + \frac{s}{u_{in}}\delta h + \frac{q^{"} P_h}{A_c \rho_f u_{in}^2}\delta u_{in} = 0 \tag{5-18}$$

Equation (5-18) is a Bernoulli-type ordinary differential equation that can be readily integrated from inlet to some axial point "z". Then, the enthalpy perturbation at the net vapor generation location is:

$$\delta h(s,\lambda_1) = \exp(-s\lambda_1 / u_{in})\delta h_{in} - \frac{q^{"} P_h}{\rho_f u_{in} A_c s}[1 - \exp(-s\lambda_1 / u_{in})]\delta u_{in} \tag{5-19}$$

For perturbation of the boiling boundary, there are two parts. The first part is due to the direct relationship of the inlet velocity to the enthalpy at the point of net vapor generation which may be obtained from the Saha-Zuber formula (5-1) and (5-2) as:

$$\delta h_1(s,\lambda_1) = \begin{cases} 0 & P_e \le 70{,}000 \\ 154\dfrac{q_w^{"}}{\rho_f u_{in}^2}\delta u_{in} & P_e \ge 70{,}000 \end{cases} \tag{5-20}$$

The other part is due to the influence of inlet velocity oscillation on the enthalpy at the boiling boundary or point of net vapor generation, which can be described as follows:

$$\delta h_2(s,\lambda_1) = -\frac{q^{"} P_h}{\rho_f u_{in} A_c s}[1 - \exp(-s\lambda_1 / u_{in})]\delta u_{in} \tag{5-21}$$

Then, the total enthalpy oscillation at the net vapor generation point is:

$$\delta h(s,\lambda_1) = \delta h_1(s,\lambda_1) + \delta h_2(s,\lambda_1)$$

Thus, the boiling boundary perturbation can be obtained as:

$$\delta\lambda_1 = -\frac{\rho_f A_c u_{in}}{q'' P_h}\delta h(s,\lambda_1) = \frac{1-\exp(-s\lambda_1/u_{in})}{s}\delta u_{in} \qquad \text{For Pe} \le 70{,}000 \quad (5\text{-}22)$$

$$= (154\frac{A_c}{P_h u_{in}} + \frac{1-\exp(-s\lambda_1/u_{in})}{s})\delta u_{in} \qquad \text{For Pe} \ge 70{,}000 \quad (5\text{-}23)$$

Saha [1974] and Saha and Zuber [1978] found that the boiling boundary fluctuation model described by Equation (5-22) was a better match to the experimental data for flow instability even for Pe ≥ 70,000. Thus, Equation (5-22) will be applied during this analysis for all Peclet numbers.

If the inlet enthalpy h_{in} in Equation (5-4) is higher than h_λ, the net vapor generation will occur right at the inlet of the channel. In that case, $\lambda_1 = 0$ and also $\delta\lambda_1 = 0$.

From integration of the momentum equation, the pressure drop perturbation in this region can be obtained as:

$$\delta(\Delta p_{liquid}) = \Gamma_1 \delta u_{in} + \Gamma_2 \delta h_{in} \qquad (5\text{-}24)$$

Where,

$$\Gamma_1 = \rho_f \lambda_1 s + \frac{f_1 \rho_f u_{in} \lambda_1}{D_e} + (\frac{f_1 \rho_f u_{in}^2}{2D_e} + \rho_f g)(\frac{1-\exp(-s\lambda_1/u_{in})}{s}) \qquad (5\text{-}25)$$

Since we assume no inlet enthalpy fluctuation, the derivation of Γ_2 is omitted.

(B) Two phase mixture region

This region starts from the net vapor generation point. The conservation equations for two phase flow provided in [Saha and Zuber, 1978] were applied:

$$\frac{\partial j}{\partial z} = \frac{\Gamma_g \Delta\rho}{\rho_g \rho_f} \tag{5-26}$$

$$\frac{\partial \rho_m}{\partial t} + C_k \frac{\partial \rho_m}{\partial z} + \rho_m \frac{\Gamma_g \Delta\rho}{\rho_g \rho_f} = 0 \tag{5-27}$$

$$\rho_m \left(\frac{\partial u_m}{\partial t} + u_m \frac{\partial u_m}{\partial z}\right) = -\frac{\partial P_m}{\partial z} - \frac{f_m}{2D_e}\rho_m u_m^2 - g\rho_m - \frac{\partial}{\partial z}\left[\frac{\rho_f - \rho_m}{\rho_m - \rho_g}\frac{\rho_f \rho_g}{\rho_m} V_{gj}^2\right] \tag{5-28}$$

$$\rho_m \left(\frac{\partial h_m}{\partial t} + u_m \frac{\partial h_m}{\partial z}\right) = \frac{q_w'' P_h}{A_c} + \frac{\partial P_m}{\partial t} - \frac{\partial}{\partial z}\left(\frac{\rho_f - \rho_m}{\rho_m}\frac{\rho_f \rho_g}{\Delta\rho} V_{gj} h_{fg}\right) \tag{5-29}$$

Where,

$$C_k = j + V_{gj} \tag{5-30}$$

$$u_m = j - \left(\frac{\rho_f}{\rho_m} - 1\right) V_{gj} \tag{5-31}$$

$$\rho_m = (1-\alpha)\rho_f + \alpha\rho_g \tag{5-32}$$

$$h_m = \frac{\alpha\rho_g}{\rho_m} h_g + \frac{(1-\alpha)\rho_f}{\rho_m} h_f \tag{5-33}$$

For the numerical characteristic equation derivation, this region was divided into N nodes. The above conservation equations were linearized, perturbed and Laplace transformed. The pressure drop oscillation at every node i was obtained by applying the above

conservation equations, and the total pressure drop oscillation across this region was obtained by adding up the oscillations of every node.

Linearization, perturbation and Laplace transformation of the velocity Equation (5-26) at node i, yields:

$$\delta j_{i+1} = \delta j_i + \frac{\Delta z \Delta \rho}{\rho_g \rho_f} \delta \Gamma_{g,i} \tag{5-34}$$

The volumetric flux oscillation at the first node ($z = \lambda_1$) should be the same as the inlet velocity oscillation. Therefore, $\delta j_1 = \delta u_{in}$.

From formula (5-3),

$$\delta \Gamma_{g,i} = -\Gamma_{g,eq} \exp(-\frac{(i-1)\Delta z}{\Delta l}) \frac{1}{\Delta l} \delta \lambda_1 \tag{5-35}$$

Linearization, perturbation and Laplace transformation of the density propagation Equation (5-27) at node i, yields:

$$\delta \rho_{m,i+1} = -\frac{\Delta z}{j_i + V_{gj}} (s + \frac{j_{i+1} - 2j_i - V_{gj}}{\Delta z}) \delta \rho_{m,i} - \frac{\rho_{m,i+1} - \rho_{m,i}}{j_i + V_{gj}} \delta j_i - \frac{\Delta z}{j_i + V_{gj}} \frac{\rho_{m,i} \Delta \rho}{\rho_g \rho_f} \delta \Gamma_{g,i} \tag{5-36}$$

The density oscillation at the first node ($z = \lambda_1$) should be zero, since the exponential vapor generation rate distribution will give a zero vapor generation rate at the boiling boundary.

Perturbation and Laplace transformation of identity (5-31) at node i, yields:

$$\delta u_{m,i} = \delta j_i + \frac{\rho_f V_{gj}}{\rho_{m,i}^2} \delta \rho_{m,i} \tag{5-37}$$

Now, we are ready for linearization, perturbation and Laplace transformation of the momentum Equation (5-28) at node i. The acceleration part of the momentum equation is only related to the inlet and outlet conditions of the region, and, it will be treated separately.

$$\begin{aligned} \delta \Delta p_i = {} & \rho_{m,i} u_{m,i} \delta u_{m,i+1} + (u_{m,i}(u_{m,i+1} - u_{m,i}) + f_2 \Delta z u_{m,i} / (2D_e) + 9.81 \Delta z) \delta \rho_{m,i} \\ & + (s \rho_{m,i} \Delta z + \rho_{m,i}(u_{m,i+1} - u_{m,i}) - \rho_{m,i} u_{m,i} + f_2 \Delta z \rho_{m,i} u_{m,i} / D_e) \delta u_{m,i} \end{aligned} \tag{5-38}$$

For the acceleration part,

$$\begin{aligned} \Delta p_{acc} &= \int_{\lambda_1 + \delta\lambda_1}^{L} \frac{\partial}{\partial z} \left(\frac{\rho_f - \rho_m}{\rho_m - \rho_g} \frac{\rho_f \rho_g}{\rho_m} V_{gj}^2 \right) dz \\ &= \frac{\rho_f - \rho_m(L)}{\rho_m(L) - \rho_g} \frac{\rho_f \rho_g}{\rho_m(L)} V_{gj}^2 \\ &\approx \frac{\rho_f - \rho_m(L)}{\rho_m(L)} \frac{\rho_f \rho_g}{\rho_m(L)} V_{gj}^2 \end{aligned} \tag{5-39}$$

It is easy to perturb and Laplace transform the above equation to obtain the total acceleration pressure drop oscillation as:

$$\delta \Delta p_{acc} = \frac{\rho_m(L) - 2\rho_f}{\rho_m^3(L)} \rho_f \rho_g V_{gj}^2 \delta \rho_m(L) \tag{5-40}$$

The nodalization is from λ_1 to L, but the real case should be from $\lambda_1 + \delta\lambda_1$ to L. Thus, the pressure drop oscillation due to boiling boundary oscillation should be deleted from the total oscillation. The pressure drop oscillation due to boundary oscillation can be expressed as:

$$\delta\Delta p_{\delta\lambda_1} = (G\frac{\partial u_m}{\partial z}\Big|_{z=\lambda_1} + f_2\rho_f u_{in}^2/(2D_e) + 9.81\rho_f)\delta\lambda_1 \tag{5-41}$$

From the identity (5-31):

$$u_m = j - (\frac{\rho_f u_m}{G} - 1)V_{gj} = j - (\frac{\rho_f u_m}{\rho_f u_{in}} - 1)V_{gj} == j - (\frac{u_m}{u_{in}} - 1)V_{gj} \tag{5-42}$$

Solving u_m from the above formula:

$$u_m = \frac{j + V_{gj}}{1 + \frac{V_{gj}}{u_{in}}} \tag{5-43}$$

Thus,

$$\frac{\partial u_m}{\partial z} = \frac{\partial j}{\partial z}\frac{u_{in}}{u_{in} + V_{gj}} = \frac{\Gamma_g \Delta\rho}{\rho_g \rho_f}\frac{u_{in}}{u_{in} + V_{gj}} \tag{5-44}$$

For the exponential vapor generation distribution, $\Gamma_g = 0.0$ at $z = \lambda_1$. Therefore $\frac{\partial u_m}{\partial z}\Big|_{z=\lambda_1} = 0.0$. Thus,

$$\delta\Delta p_{\delta\lambda_1} = (f_2\rho_f u_{in}^2/(2D_e) + 9.81\rho_f)\delta\lambda_1 \tag{5-45}$$

Now, the total pressure drop oscillation in the heated part can be expressed as:

$$\delta\Delta p_{heated} = \delta\Delta p_{liquid} + \sum_{i=1}^{N}\delta\Delta p_i + \delta\Delta p_{acc} - \delta\Delta p_{\delta\lambda_1} \tag{5-46}$$

(3) Non-heated gas plenum part

(A) Lower gas plenum

As mentioned in the supercritical region characteristic equation derivation, applying the conservation equations and assuming a constant density in this part, the relation between the pressure drop oscillation and the inlet flow oscillation can be expressed as:

$$\delta\Delta p_{nod} = (f_1 / D_e L_{nod} G + s\rho_f L_{nod})\delta u_{in} \tag{5-47}$$

(B). Upper gas plenum

Applying the conservation equations to this part:

$$\delta\Delta p_{nou} = (f_2 / D_e L_{nou} \frac{u_{m,n+1}^2}{2} + gL_{nou} + su_{m,n+1} L_{nou})\delta\rho_{m,n+1} + (f_2 / D_e L_{nou} G + s\rho_{m,n+1} L_{nou})\delta u_{m,n+1} \tag{5-48}$$

(4) Total pressure drop oscillation

Adding up all of above pressure drop oscillation parts, the total pressure drop oscillations can be obtained as:

$$\delta\Delta p_{Channel} = \delta\Delta p_{ori} + \delta\Delta p_{heated} + \delta\Delta p_{nou} + \delta\Delta p_{nod} \tag{5-49}$$

If we set the drift velocity $V_{gj} = 0.0$, the characteristic equation, derived for NHNEM will become that for the Homogenous Non-equilibrium model (HNEM).

5.4 The characteristic equation for the Non-homogenous Equilibrium Model

The characteristic equation based on the Non-homogenous Equilibrium model (NHEM) had been derived by Ishii [1971] analytically. In this report, we derive it based on a numerical method, since that for the Non-homogenous Non-equilibrium model (NHNEM) was derived numerically. Also, the numerical method avoids the complicated integration procedure that is needed in the analytical method.

The same procedure as adopted for NHNEM can be applied to NHEM. The vapor generation rate of exponential distribution needs to be change to a constant value corresponding to the equilibrium vapor generation rate $\Gamma_{g,eq}$, which has been defined in Equation (5-3). Also, the two phase region will start at $z = \lambda_{eq}$. Therefore, the volumetric flux conservation Equation (5-26) can be expressed as:

$$\frac{\partial j}{\partial z} = \frac{\Gamma_g \Delta\rho}{\rho_g \rho_f} = \frac{\Gamma_{eg} \Delta\rho}{\rho_g \rho_f} = \frac{v_{fg}}{h_{fg}} \frac{q_w'' P_h}{A_c} = \Omega_1 \tag{5-50}$$

$$j(z) = u_{in} + \Omega_1 (z - \lambda_{eq}) \tag{5-51}$$

$$\delta j = \delta u_{in} - \Omega_1 \delta\lambda_{eq} \tag{5-52}$$

Therefore, the perturbation of volumetric flux will be constant along the channel in the two phase region.

The density oscillation and mixture velocity oscillation will have the same scheme as NHNEM. However, the density oscillation of the boiling boundary for NHEM will be different from that of NHNEM, since the vapor generate rate at the boiling boundary is not zero for NHEM while it is zero for NHNEM. According to Saha [1974], the density oscillation at the boiling boundary for NHEM can be derived as:

$$\delta\rho_{m,1} = \frac{\rho_f \Omega_1}{u_{in} + V_{gj}} \delta\lambda_{eq} \tag{5-53}$$

The pressure drop oscillation scheme will also be the same as NHNEM.

Applying the same procedure as NHNEM, the characteristic equation based on NHEM can be derived easily.

Similarly, if we set the drift velocity $V_{gj} = 0.0$, the characteristic equation, derived for NHEM, will become that for the Homogenous Equilibrium model (HEM).

5.5 Stability map for U.S. reference SCWR design for subcritical pressure

Using the D-Partition method mentioned in Section 4.7, the stability map for subcritical pressure region was plotted in the Subcooling Number versus Phase Change Number plane.

To investigate the effects of different two-phase flow models (in the subcritical pressure region) on the stability boundary, stability boundary maps were constructed using the previously mentioned four different models, namely, the Homogenous Equilibrium model (HEM), the Homogenous Non-equilibrium model (HNEM), the Non-homogenous Equilibrium model (NHEM) and the Non-homogenous Non-equilibrium model (NHNEM). For U.S. reference SCWR design at 5.0MPa in the hot channel (with $k_{in} = 20.0$), the comparison of the above four models can be seen in Fig. 5-2.

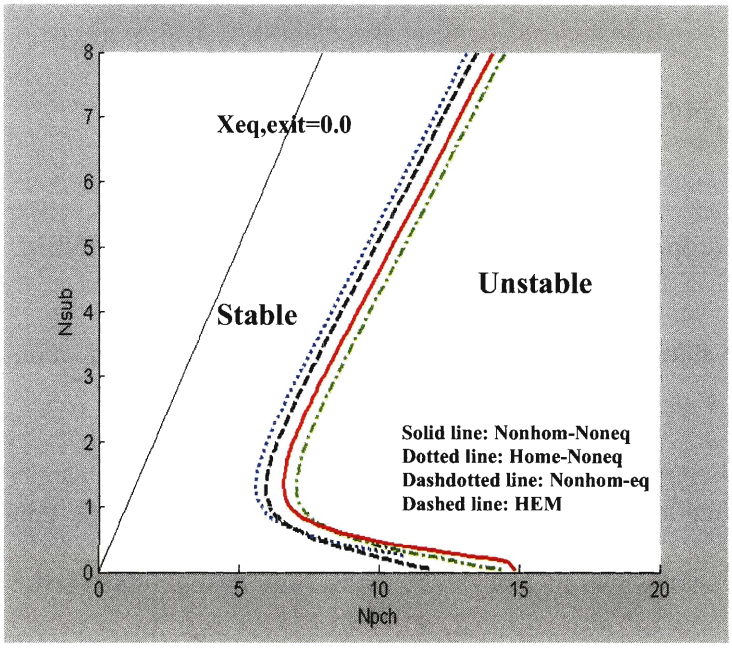

Fig. 5-2: Comparison of stability boundaries using four different two phase flow models at 5.0MPa

From Figure 5-2 above, it is found that the HNEM model predicts the most conservative stability boundary at high Subcooling numbers, whereas the HEM model yields the most conservative stability boundary at low Subcooling numbers. The Homogenous model will predict more conservative stability boundary both for thermal Equilibrium and thermal Non-Equilibrium conditions. This can be explained physically, because in the Non-Homogenous two phase flow model, the vapor phase always moves faster than the liquid phase. Thus, the Homogenous model always calculates a higher void faction and a less stable system compared to the Non-homogenous model. Therefore, the Homogenous model predicts a conservative stability boundary. On the other hand, at high subcooling numbers, the Non-Equilibrium model is found to be more conservative than the Equilibrium model both for Homgenous and Non-Homgenous models. Physically, the Non-Equilibrium model predicts higher void fraction since the subcooled boiling was accounted for in this model. However, at low subcooling number, the situation reverses, the Equilibrium model predicts conservative boundary. This can also be explained physically. At low subcooling numbers, the subcooled boiling is negligible compared to the saturation boiling. Thus, the Non-equilibrium model does not affect the void fraction

calculation much. But, at saturation boiling region, the Non-Equilibrium model with an exponential vapor generation asymptotically approaches the Equilibrium model, which makes the vapor generation rate of Non-Equilibrium model below the Equilibrium model. Therefore, the average void fraction for Non-Equilibrium model is less than Equilibrium model as the inlet subcooling number is below some value.

Physically, the stability boundary differences among the four different models will decrease as the pressure increases. This can be seen from Fig. 5-3 where various stability boundaries have been plotted at a pressure of 10MPa for the hot channel.

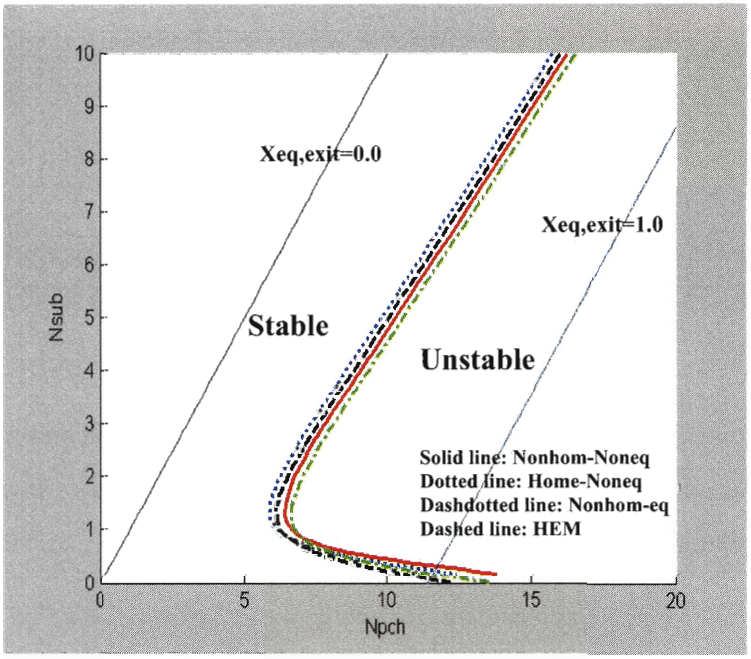

Fig. 5-3: Comparison of four two phase flow models at 10.0MPa

Therefore, at high pressures, the simple HEM model may be chosen for a quick check of the system stability boundary.

As mentioned previously, the value of multiplier C_m in the two phase friction factor was assumed to be 2.0. The effect of C_m on the stability boundary was evaluated by setting

C_m = 1.0,1.5,2.0,2.5,3.0 for the HEM model for the hot channel at pressure of 10MPa. The results are shown in Fig. 5-4 below.

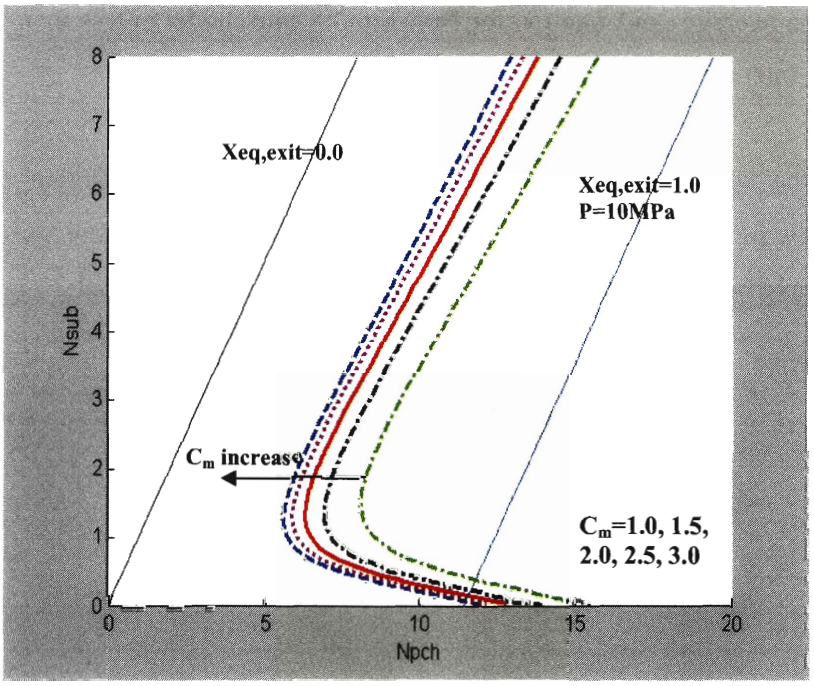

Fig. 5-4: Cm effects to stability boundary

From the above figure, it is seen that the stability boundary will move left as the Cm increases. The effects on stability boundary will decrease as the Cm increase. Also, it is seen that applying Cm=2.0 will give reasonable results since the Cm has range from 1.5 to 2.5.

5.6 Model evaluation

The stability boundary maps developed for the subcritical pressure region have been compared with the experimental data of Carver [1968] and Solberg [1966]. These two experimental results were found in [Ishii, 1971]. Both of these experiments used water as the working fluid. Solberg had used a circular tube as the heated channel with water at 80 atm pressure, whereas Carver used an annulus as the heated channel with water at 70 atm pressure.

Since the Equilibrium models are nothing new and had been evaluated in the literature such as [Ishii, 1971], only the Non-Equilibrium models are compared with the experimental data in this report.

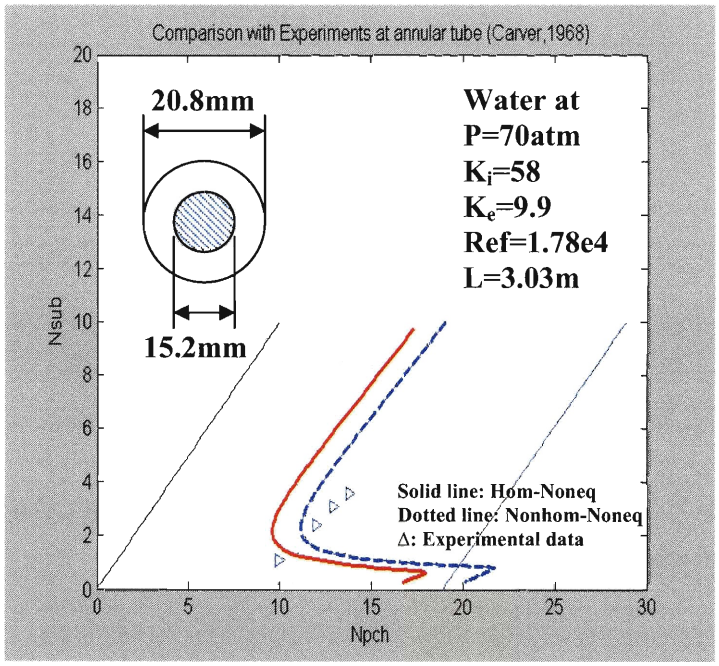

Fig. 5-5: Model evaluation with Carver's experimental data

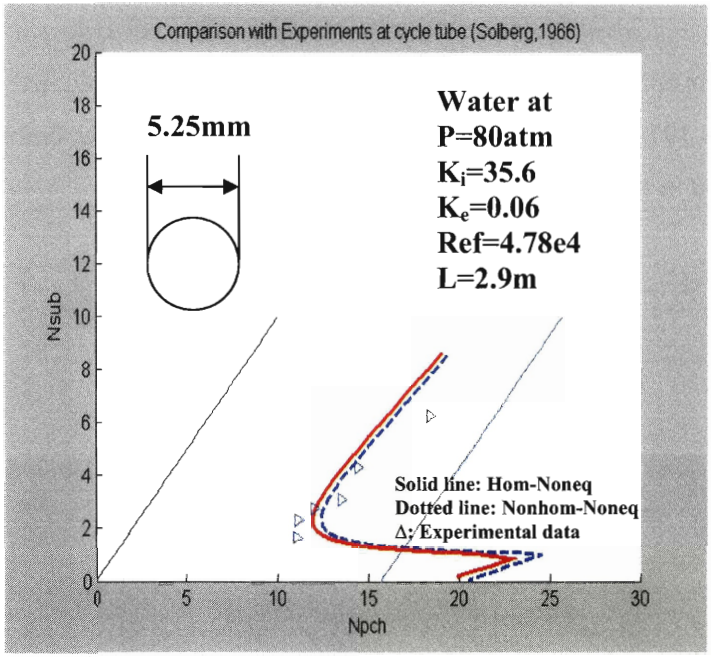

Fig. 5-6: Model evaluation with Solberg's experimental data

From Figures 5-5 and 5-6, it is seen that the Non-equilibrium models match the experimental data reasonably well.

5.7 Suggested SCWR sliding pressure startup procedure

There are two ways to start up a SCWR - one is a constant pressure startup and the other is the sliding pressure startup. During the constant pressure startup, the system will be pressurized to a supercritical pressure, say 25MPa, before the reactor starts nuclear heating. However, during the sliding pressure startup, the nuclear heating starts at subcritical pressure, and the system will be pressurized to supercritical pressure accompanied with the load increase. According to Nakatsuka, et al [2001], both the constant pressure and the sliding pressure startup procedures are feasible for SCWR. However, to simplify the plant system and to reduce the component sizes, a sliding pressure startup with a steam separator in the bypass line is desirable.

In the U.S. reference SCWR design, the sliding pressure startup was chosen and the startup procedure has been investigated at BREI (Burns & Roe Enterprises Inc.). In the following Table 5-1, the startup procedure was listed at different time points based on BREI's initial design [2004].

Table 5-1: Start-up parameters based on BREI's initial design

Time (hour)	System Pressure (MPa)	Core mass flow rate (kg/s)	% of steady-state (1843kg/s)	Inlet temp.(°C)	Core fission power (KW)	% of steady-state (3575MW)
0	0	0	0%	0	0	0%
1	0.25	470	25.5%	0	0	0%
2	2.7	518	28.11%	50	150000	4.2%
3	5.7	518	28.11%	115	150000	4.2%
4	8.3	518	28.11%	205	700000	19.58%
5 & 6	8.3	518	28.11%	271	827940	23.16%
7	14.9	518	28.11%	271	827940	23.16%
8	23	550	29.84%	271	858781	24.02%
9	24.7	825	44.76%	271	1504762	42.09%
10	24.7	1460	79.22%	271	2897029	81.04%
11 & 12	24.7	1832	99.4%	280	3553893	99.41%

From Table 5-1, it is seen that the supercritical condition is starting at the 8^{th} hour time point. The stability features of SCWR were checked for the above startup procedure by applying previously developed stability models for both supercritical and subcritical pressures. At a subcritical pressure, the stability boundaries were plotted on the Subcooling Number versus the Phase Change Number plane based on the NHNEM two phase flow model. At a supercritical pressure, the stability boundaries were plotted on the Pseudo subcooling number versus the Expansion number plane. The stability boundaries of the hot channel are shown since it limits the system as discussed before.

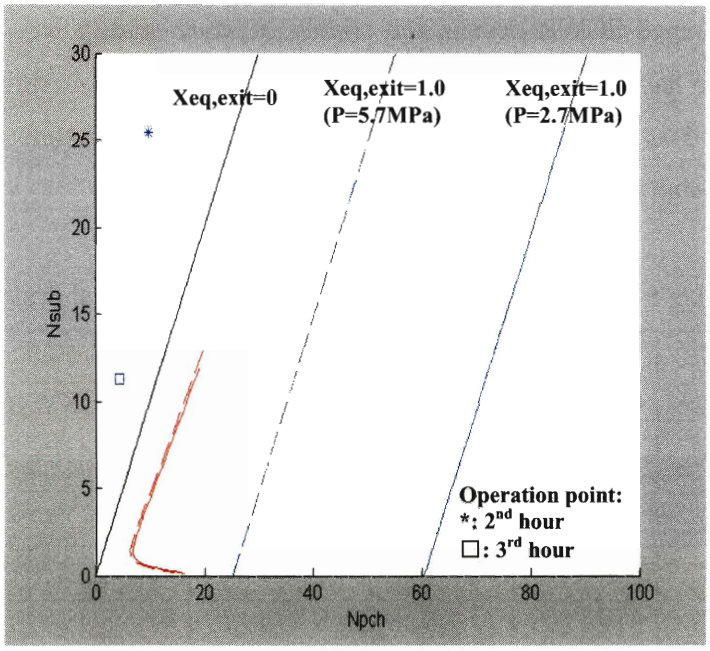

Fig. 5-7: Startup stability check (2nd & 3rd hour) at SCWR hot channel

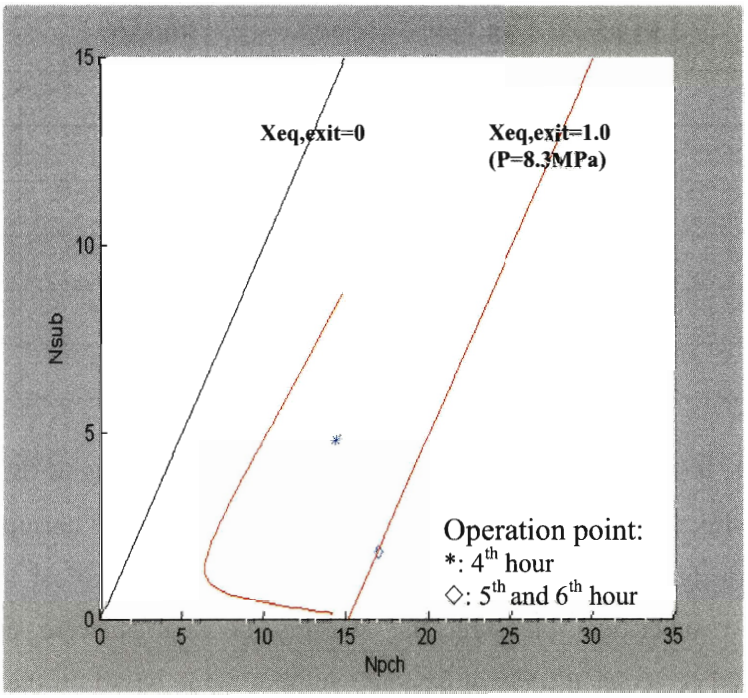

Fig. 5-8: Startup stability check (4th, 5th and 6th hour) at SCWR hot channel

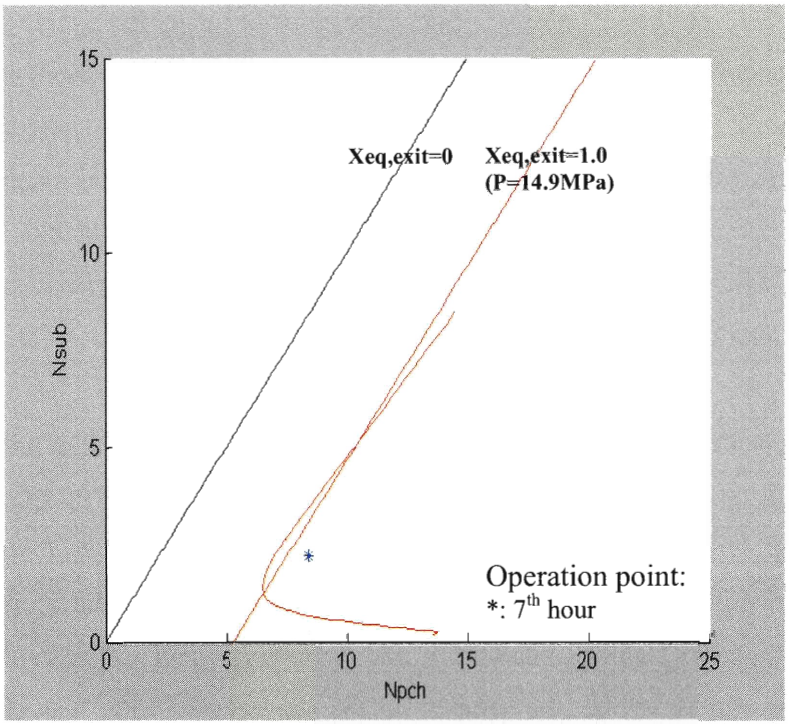

Fig. 5-9: Startup stability check (7th hour) at SCWR hot channel

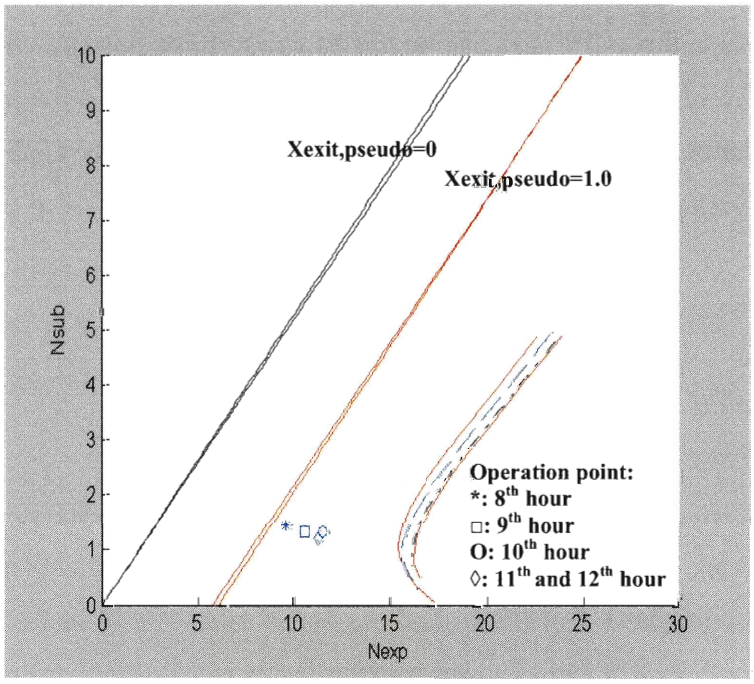

Fig. 5-10: Startup stability check (8th, 9th, 10th, 11th, and 12th hour) at SCWR hot channel

From Table 5-1, at the 2^{th} and 3^{rd} hour, the coolant is in the single liquid phase throughout the core (the core exit quality below 0.0), the system obviously is stable. And at the 8^{th}, 9^{th}, 10^{th}, 11^{th}, and 12^{th} hour, the system is in the supercritical conditions, it is also stable. However, at the 4^{th}, 5^{th}, 6^{th} and 7^{th} hour, the system is in the subcritical pressure two phase flow conditions, the BREI's initial design is not stable. Further work was done at MIT to modify the SCWR startup procedure so that no single channel instability or temperature excursion would occur.

According to Nakatsuka, et al [2001], the reactor power during a sliding pressure startup process would have to be limited due to peak cladding temperature (PCT). If burnout or dryout occurs, the PCT will greatly exceed the acceptable value. Therefore, the burnout must be avoided during startup. Also, the minimum core flow rate during pressurization will be determined by stability, coolability, and pump performance. The coolant flow rate of 28% of the full flow rate, the same as in the supercritical FPP, was chosen in this analysis. This was the same as that assumed by Nakatsuka, et al [2001].

For the critical heat flux (CHF) calculation, the Bowring correlation [Bowring, 1972] was selected because of its large applicable pressure range. The detailed expression of the Bowring correlation can be found in [Todreas and Kazimi, 1990]. The applicable range of the Bowring correlation is listed here.

$$D = 0.002 - 0.045m$$
$$L = 0.15 - 3.7m$$
$$p = 0.2 - 19.0MPa$$
$$G = 136 - 18{,}600kg/m^2s$$

Using the Bowring correlation, it was found that the Minimum Critical Heat Flux Ratio (MCHFR) of traditional GE BWR/6 [Todreas and Kazimi, 1990] in full power at hot channel is about 2.59. The radial power peaking factor is 1.5 according to [Todreas and Kazimi, 1990]. Uniform axial heat flux was assumed in the hot channel. If the same CHF margin is applied to SCWR as the GE BWR/6, it means that the hot channel of SCWR

would have MCHFR of 2.59 during pressurization and heating. Keeping the core flow rate at 28% of the full power flow rate during the pressurization process, the maximum allowable power can be determined. The maximum powers for different pressures at different inlet temperatures were calculated and are presented in Table 5-2. As previously mentioned, the hot channel of SCWR has a power peaking factor 1.3 and a uniform axial heat flux was assumed.

Table 5-2: Maximum reactor power (% of full power) to avoid CHF for different pressures at different inlet temperatures

Press. / Temp.	6MPa	8MPa	10 MPa	12 MPa	14 MPa	16 MPa	18 MPa	20 MPa	22 MPa
100°C	51.9%	40.8%	33.7%	29.0%	26.0%	24.0%	22.8%	22.3%	22.6%
200°C	46.1%	35.0%	28.0%	23.3%	20.2%	18.2%	17.0%	16.4%	16.7%
250°C	43.1%	31.9%	24.9%	20.2%	17.1%	15.1%	13.9%	13.3%	13.6%

The results shown in the above table are also plotted in Figure 5-11.

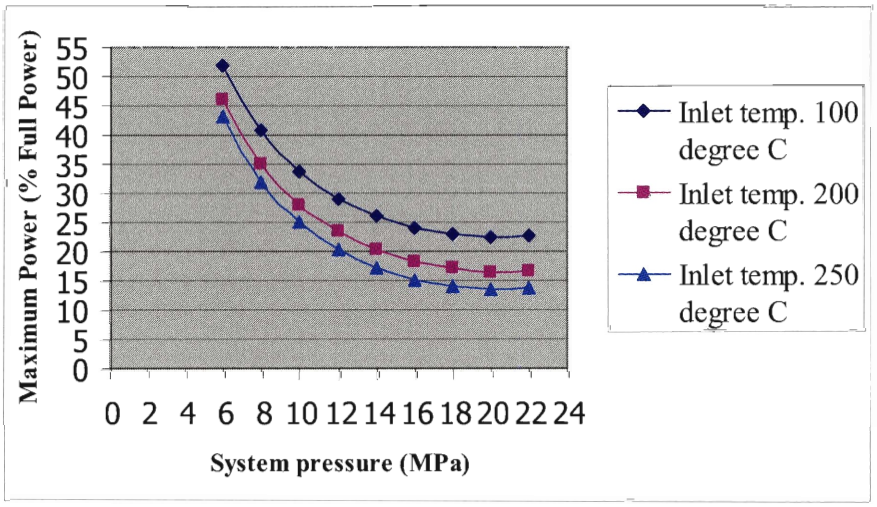

Fig. 5-11: Maximum power under CHF limitation

Based on BREI suggested design, and taking into account the CHF limitation and stability, the following start up procedure shown in Table 5-3 is suggested.

Table 5-3: The suggested SCWR sliding pressure startup procedure

Time (hour)	System Pressure (MPa)	Core mass flow rate (kg/s)	Core Inlet temp. (°C)	Core fission power (MWt)	Max. allowable power (MWt) from stability viewpoint	Max. allowable power (MWt) with MCHFR of 2.59
0	0	0	0	0		
1 (BREI)	0.25	470	0	0		
2 (BREI)	2.7	518	50	150		
3 (BREI)	5.7	518	115	150		
Revised 4 (MIT)	**8.3**	**518**	**205**	**400 (11.2% of full power)**	**610**	**1198**
Revised 5 (MIT)	**12.0**	**518**	**205**	**400 (11.2% of full power)**	**690**	**824**
Revised 6 (MIT)	**12.0**	**518**	**250**	**400 (11.2% of full power)**	**580**	**725**
Revised 7 (MIT)	**14.9**	**518**	**250**	**550 (15.4% of full power)**	**750**	**578**
8 (BREI)	23	550	271	859		
9 (BREI)	24.7	825	271	1505		
10 (BREI)	24.7	1460	271	2897		
11 &12 (BREI)	24.7	1832	280	3554		

The stability features for the new procedure at the above suggested time hours 4^{th}, 5^{th}, 6^{th} and 7^{th} are checked in Figures 5-12, 5-13 and 5-14.

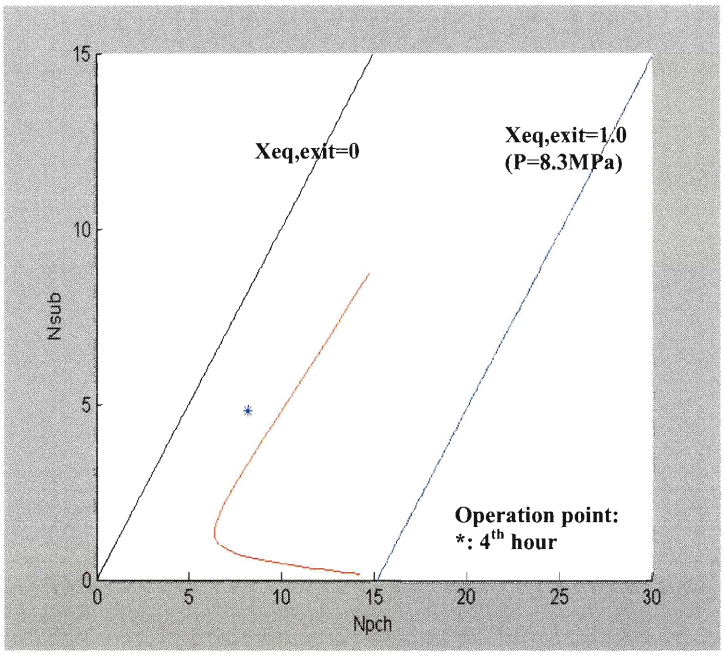

Fig. 5-12: Startup stability check (revised 4th hour) at SCWR hot channel

It is seen from Fig. 5-12, that at 4th hour, by decreasing the initial power from 700MWt to 400 MWt, the revised operation point is in the stable region.

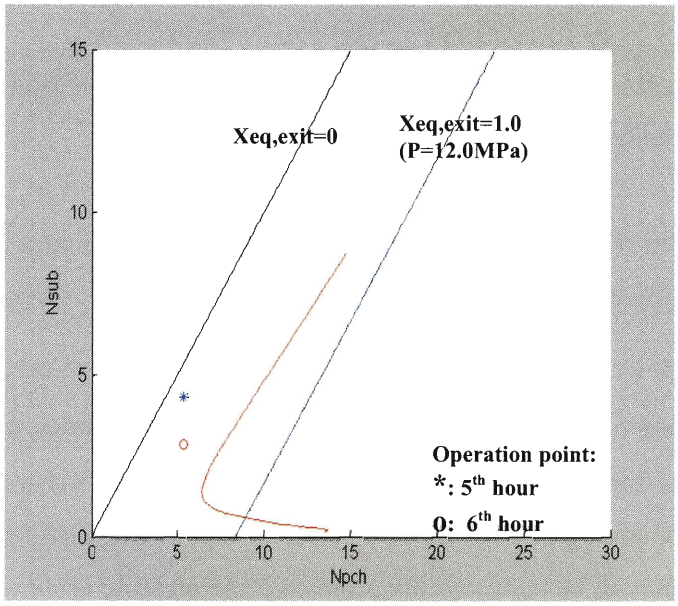

Fig. 5-13: Startup stability check (5th & 6th hour) at SCWR hot channel

By decreasing the initial power from 830MWt to 400 MWt and decreasing the inlet temperature from 271°C to 205°C for the 5th hour and from 271°C to 250°C for the 6th hour, while increasing the pressure from 8.3MPa to 12.0 MPa, the revised operation points fall in the stable region.

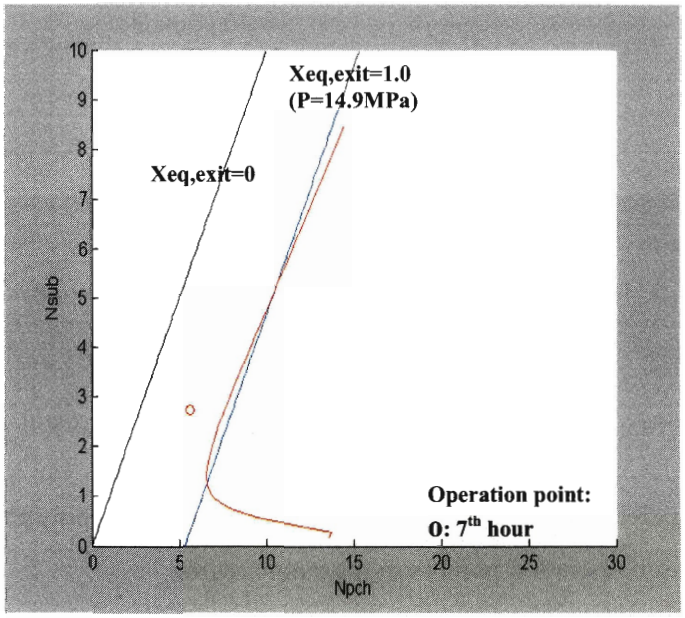

Fig. 5-14: Startup stability check (7th hour) at SCWR hot channel

For the 7th hour, again, the revised operation point is in the stable region corresponding to Fig. 5-14 by decreasing the power from 830MWt to 550MWt.

Also, it can be seen from the above subcritical region stability boundary maps, that even though the stability boundaries did not shift much in the $N_{sub} - N_{pch}$ plane during pressurization, the exit equilibrium quality $X_{eq,exit} = 1.0$ lines move towards left. In Figure 38 at pressure of 14.9MPa, the stability boundary almost moves to the three region case which means the instability will occur after the burnout occurs in the channel. Therefore, if the operating point is limited in the second or two phase mixture region to avoid burnout, there will be no instability problem if the pressure is above 14.9MPa.

The pressure effect can be absorbed if the stability boundary is plotted on the $N_{sub} - N_{pch}$ plane. This can be easily seen once all of the above boundaries are plotted in the same Figure 5-15.

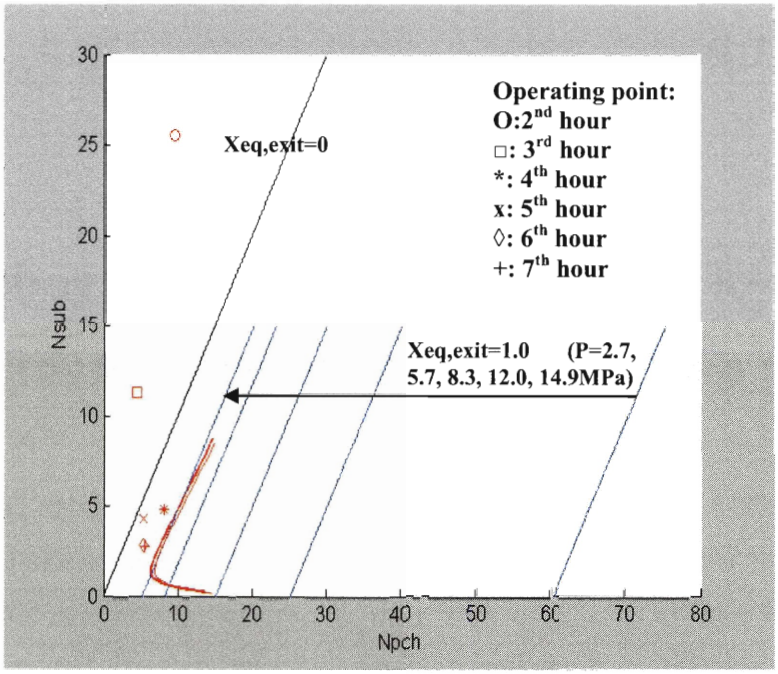

Fig. 5-15: The stability boundary for 2nd, 3rd, 4th, 5th, 6th and 7th hours

From all of the above stability checks, it is seen that the suggested start up procedure as presented in Table 5-3 will have no single channel instability and burnout problems at hot channel.

Chapter 6

Effects of fuel dynamics and water rods heating on SCWR single channel stability

According to the U.S. reference SCWR design, the feedwater splits into two parts after flowing into the reactor pressure vessel. The 90% of total inlet flow goes up to the upper dome, then flows down through the water rods. The remaining 10% inlet flow goes down through the downcommer. In the lower plenum, the water rods exit flow mixes with the downcommer flow. Then, the total flow is delivered to the coolant channels and flows up to remove the fission energy. The water rods may be insulated if it is required. But, how much insulation will be applied is still unknown at the current design stage. In this chapter, an analysis will be conducted for two conditions: (1) perfectly insulated water rods with no heat transfer to the water rods from the upward coolant flow; (2) water rods without insulation, there is heat transfer to water rods from the upward coolant flow, through the water rods wall.

During density wave oscillations, the fuel rods will be coupled with the coolant thermal-hydraulic dynamics through the fuel rods heat flux dynamics. In Chapters 3, 4 and 5, the fuel rods heat flux were assumed to be constant, therefore the fuel dynamics was decoupled from the coolant. To investigate the fuel dynamics effects on single channel stability, a fuel dynamics model was added to the above developed coolant thermal-hydraulics model.

The case without water rods heating was studied first, then, the case with water rods heating was addressed.

6.1 Fuel dynamics effects on SCWR single channel stability

As said above, the single channel can be illustrated as in Fig. 6-1 in the case without water rods heating.

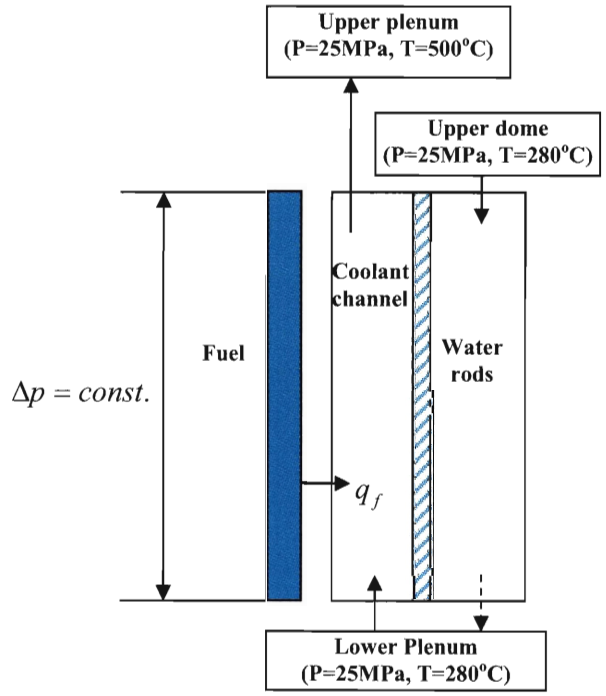

Fig. 6-1: SCWR single channel representation at steady state

From Fig. 6-1, it can be seen that the coolant temperature remained at 280°C in the lower plenum, which is the same as the RPV inlet.

6.1.1 Fuel dynamics model

The coupling of fuel dynamics with the coolant dynamic model can be illustrated as in Fig. 6-2.

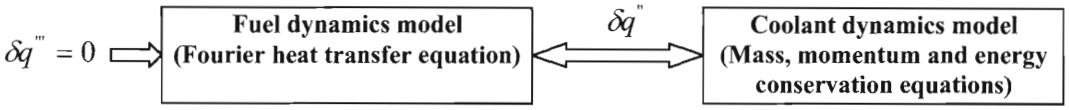

Fig. 6-2: Coupling of fuel and coolant dynamics models

1. The fuel dynamics model

A lumped fuel dynamics model with the temperature distribution in the fuel pin developed at BNL [] was applied. The temperature profile in the fuel, gas gap and cladding are illustrated in Fig. 6-3.

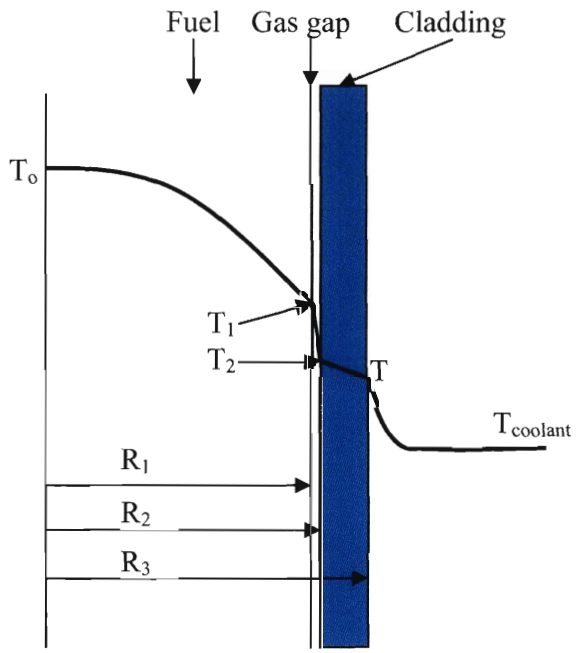

Fig. 6-3: Fuel pin temperature distribution profile

Assuming a power polynomial for temperature distribution in the fuel pellet, it can be given as:

$$T_f = T_o + b\xi + c\xi^2 \tag{6-1}$$

Where, $\xi = \frac{r}{R_1}$

Assuming a linear temperature distribution in the cladding:

$$T_c = T_2 + d\eta \tag{6-2}$$

Where, $\eta = \frac{r - R_2}{R_3 - R_2}$ $(R_2 < r < R_3)$

Solving the Fourier heat transfer equation with the above temperature distribution, one obtains:

$$\frac{d\overline{T}_{pin}}{dt} = \frac{2}{(R_3 - R_2)R_3} \frac{k_c}{(\rho c_p)_f} \frac{N_{Bi,c}}{[1 + (C_{gm} + F_{pr})N_{Bi,c}]} (T_\infty - \overline{T}_{pin}) + (\frac{R_1}{R_3})^2 \frac{q_v'''}{(\rho c_p)_f} \tag{6-3}$$

Where,

$\overline{T}_{pin}$: Average temperature of the fuel pin

$$N_{Bi,c} = \frac{\overline{h}(R_3 - R_2)}{k_c},$$

$$C_{gm} = (\frac{R_1}{R_3})^2 + [1 - (\frac{R_2}{R_3})^2][\frac{3(R_2 + R_3) - (R_3 - R_2)}{6(R_2 + R_3)}],$$

$$F_{pr} = \frac{R_1^3}{(R_3 - R_2)R_3^2} (\frac{k_c}{4k_f} + \frac{k_c}{R_1} \frac{1}{h_{gap}})$$

From Fig. 6-3, the fuel rods surface temperature, fuel pin average temperature and the coolant bulk temperature can be related as:

$$T_w - T_\infty = \frac{\overline{T}_{pin} - T_\infty}{[1 + (C_{gm} + F_{pr})N_{Bi,c}]} \tag{6-4}$$

2. The material properties

The thermal conductivity and specific heat of the fuel pellet were iteratively calculated since the properties are functions of temperatures, and the temperatures are also function of the properties.

$$\begin{aligned} k_f &= \frac{k_1}{k_2 + T} + k_3 \exp(k_4 T) \qquad 0 \le T \le 1650^o C \\ &= k_5 + k_3 \exp(k_4 T) \qquad 1650 \le T \le 2840^o C \end{aligned} \tag{6-5}$$

Where, $k_1 = 41.4, k_2 = 464, k_3 = 1.216 \times 10^{-4}, k_4 = 1.867 \times 10^{-3}, k_5 = 0.091$

$$c_{pf} = \frac{k_1 \theta^2 \exp(\theta / T)}{T^2 [\exp(\theta / T) - 1]^2} + k_2 T + \frac{k_3 E_D}{RT^2} \exp(-E_D / RT) \tag{6-6}$$

Where,

$R = 8.3143, \theta = 535.285, k_1 = 296.7, k_2 = 2.43 \times 10^{-2}, k_3 = 8.745 \times 10^7, E_D = 1.577 \times 10^5$

The cladding material is still under investigation. The thermal conductivity of stainless steel (type 316) at 500°C was applied: $k_c = 21.5 \times 10^{-3}$ (kW/m^oC).

3. The heat transfer coefficient correlation

The Dittus-Boelter correlation was applied in this analysis.

$Nu = 0.023\,\mathrm{Re}^{0.8}\,\mathrm{Pr}^{0.4}$, when the fluid is heated (6-7)

$Nu = 0.023\,\mathrm{Re}^{0.8}\,\mathrm{Pr}^{0.3}$, when the fluid is cooled (6-8)

6.1.2 Coupling of Fuel dynamics model to coolant thermal hydraulics model

The fuel dynamics model is coupled to the coolant thermal hydraulics model through the dynamics of the fluctuation of the fuel rods surface heat flux.

Perturbation, linearization and Laplace transformation of Equation (6-3) and combining it with Equation (6-4), one obtains:

$$s\delta\bar{T}_{pin} = (\frac{R_1}{R_3})^2 \frac{\delta q_v'''}{(\rho c_p)_f} - \frac{2}{R_3}\frac{\delta q_w''}{(\rho c_p)_f} \tag{6-9}$$

Perturbation, linearization and Laplace transformation of Equation (6-4), and combining it with $q_w'' = \bar{h}(T_w - T_\infty)$, one obtains:

$$\frac{\delta q_w''}{\bar{h}} - \frac{q_w''}{\bar{h}}\frac{\delta\bar{h}}{\bar{h}} + \frac{(C_{gm} + F_{pr})(R_3 - R_2)}{k_c}\delta q_w'' = \delta\bar{T}_{pin} - \delta T_\infty \tag{6-10}$$

Perturbation, linearization and Laplace transformation of the Dittus-Boelter correlation, which is Equation (6-7), one obtains:

$$\frac{\delta\bar{h}}{\bar{h}} = 0.8\frac{\delta\rho_\infty u_\infty + \rho_\infty \delta u_\infty}{\rho_\infty u_\infty} \tag{6-11}$$

Combining the above Equations (6-9), (6-10) and (6-11), after some rearrangement, one obtains:

$$[\frac{1}{\bar{h}}+\frac{2}{sR_3(\rho c_p)_f}+\frac{(C_{gm}+F_{pr})(R_3-R_2)}{k_c}]\delta q_w^{''}=\frac{q_w^{''}}{\bar{h}}\frac{\delta\bar{h}}{\bar{h}}+(\frac{R_1}{R_3})^2\frac{\delta q_v^{'''}}{(\rho c_p)_f}-\frac{\delta h_\infty}{c_{p,\infty}} \qquad (6\text{-}12)$$

Set $\delta q_v^{'''}=0$ in Equation (6-12), we can find the fluctuation of the fuel rods surface heat flux as function of coolant density, velocity and enthalpy oscillations. Plugging Equation (6-12) into the coolant thermal hydraulics dynamics model, the characteristic equation of coupled fuel dynamics model could be derived.

6.1.3 SCWR single channel stability map with fuel dynamics model

Once coupled with the fuel dynamics model, the characteristic equation will be too complicated to integrate analytically. A numerical method similar to that applied in the subcritical pressure NHNEM model construction was developed. The stability map for both the cases with and without the fuel dynamics model are plotted in Fig. 6-4. For fair comparison, the characteristic equation for without fuel model case also was integrated numerically.

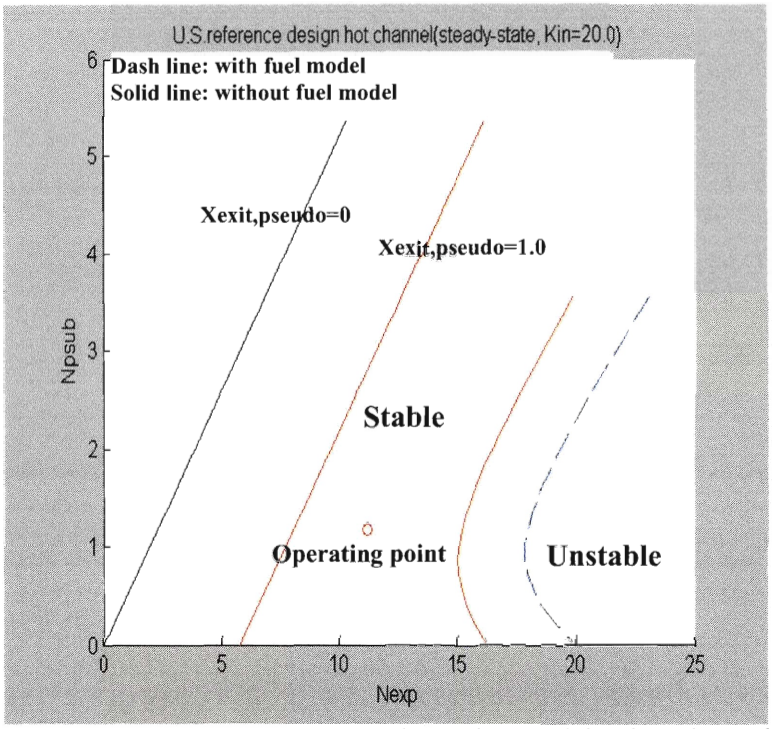

Fig. 6-4: The stability map for coupled fuel dynamics model at hot channel (Kin=20.0)

From Fig. 6-4, it is seen that the coupled fuel dynamics model reduces the region of instability. Physically, in the coupled fuel dynamics model, the fuel heat capacity will dampen the coolant oscillation amplitude by providing the negative feedback.

The decay ratios were calculated at different RPV inlet temperatures at the nominal condition as listed in Table 6-1.

Table 6-1: Fuel rods effect on single hot channel stability

RPV inlet (°C)	260	270	280	290
With fuel dynamics model	0.1016	0.1157	0.1296	0.1423
Without fuel dynamics model (constant fuel rods surface heat flux)	0.1581	0.1808	0.2031	0.2234

Table 6-1 can be shown graphically in Fig. 6-5:

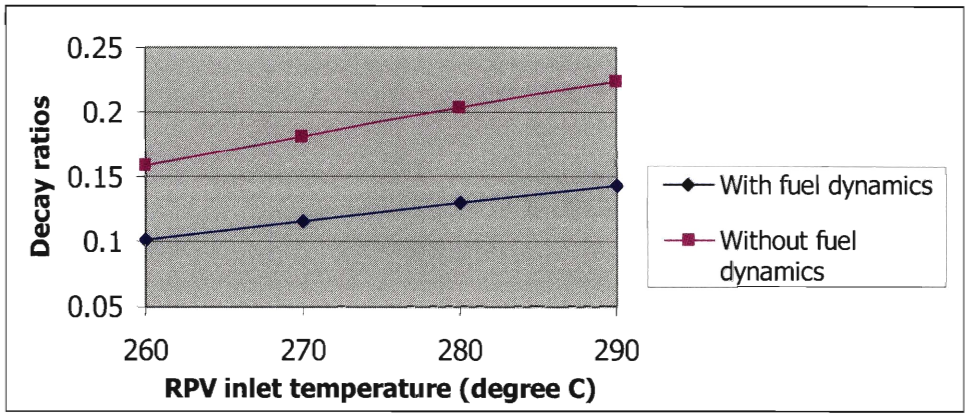

Fig. 6-5: Comparison between with and without fuel dynamics model

From Fig. 6-5 and Table 6-1, the stabilization effect of the fuel rods can also be seen.

6.2 Water rods heating effects on the SCWR single channel stability

The flow path and heat transfer in the reactor pressure vessel is illustrated in Fig. 6-6. The core was illustrated as two channels. Part of the fission energy was transferred into water rods through the water rods wall to warm up the water rods flow. Therefore, the temperature in the lower plenum will be higher than that without water rods heating. The flow coming from the water rods was assumed perfectly mixed with that from the downcommer in the lower plenum.

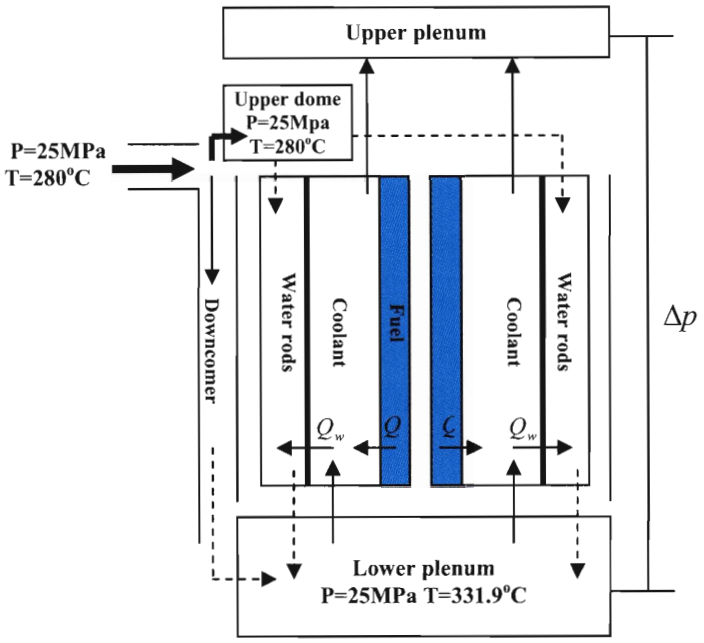

Fig. 6-6: Flow path and heat transfer in the reactor pressure vessel

For a single channel, the flow and the heat transfer can be illustrated as in Figure 6-7:

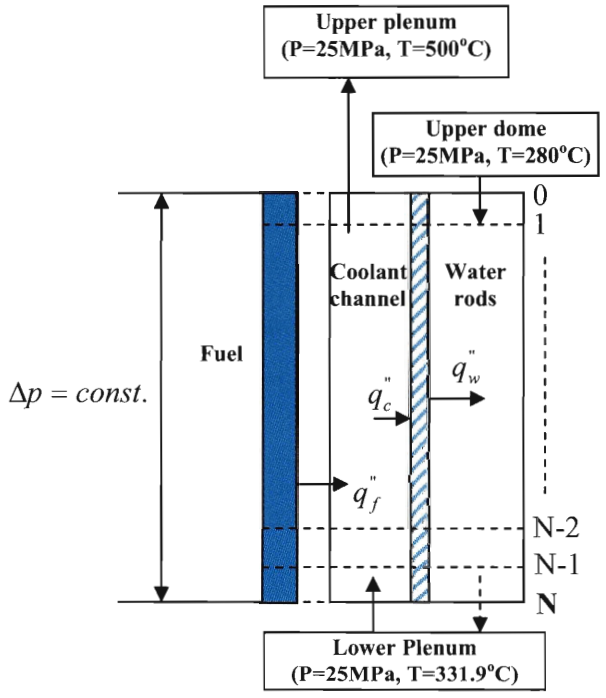

Fig. 6-7: Flow path and heat transfer in the single channel

6.2.1 The coolant channel inlet and water rods outlet temperatures calculation

To simulate the coolant and water rods flow by using previously described three-region model, the coolant channel inlet and water rods outlet temperatures must be calculated. This calculation was conducted numerically. The channel was discretized into N nodes axially. For a specific node i, applying the mass and energy conservation to the coolant channel and ignoring the pressure loss at steady state, one can obtain:

$$m_{c,i} = m_{c,i+1} \tag{6-13}$$

$$(q''_{f,i}P_h - q''_{c,i}P_{wo})\Delta z = m_{c,i}(h_{c,i} - h_{c,i+1}) \tag{6-14}$$

Where,

$m_{c,i}$: the coolant flow rate for the hot assembly at node i

$q''_{f,i}$: the fuel rods surface heat flux at node i

$q''_{c,i}$: the water rods outside surface heat flux at node i

P_h : the heating parameter of the fuel rods per assembly

P_{wo} : the heating parameter of the water rods outside per assembly

Similarly, applying the mass and energy conservation equations to water rods flow and ignoring the pressure loss at steady state, one can obtain:

$$m_{w,i} = m_{w,i+1} \tag{6-15}$$

$$q''_{w,i}P_{wi}\Delta z = m_{w,i}(h_{w,i+1} - h_{w,i}) \tag{6-16}$$

Where,

$m_{w,i}$: the water rods flow rate for the hot assembly at node i

$q''_{w,i}$: the water rods inside surface heat flux at node i

P_{wi}: the heating parameter of the water rods inside per assembly

At steady state, the water rods linear heat transfer rate can be calculated by:

$$q'_{w,i} = \frac{T_{c,i} - T_{w,i}}{R_{t,i}} \tag{6-17}$$

Where,

$q'_{w,i}$: the water rods linear heat transfer rate at node i

$T_{c,i}$: the coolant channel bulk flow temperature at node i

$T_{w,i}$: the water rods bulk flow temperature at node i

$R_{t,i}$: the total heat transfer resistance of the water rods wall at node i

$$R_{t,i} = \frac{1}{P_{wo}H_{wo,i}} + \frac{t_w}{P_{wo}K_w} + \frac{1}{P_{wi}H_{wi,i}} \tag{6-18}$$

Where,

t_w: Water rods wall thickness

$H_{wi,i}$ and $H_{wo,i}$: Heat transfer coefficients at node i inside and outside the water rods

Applying D-B correlations to the coolant flow and the water rods flow, the heat transfer coefficients for both outside and inside of the water rods can be calculated for the node i.

The inlet temperature of the reactor pressure vessel and the core outlet temperature are known for the average assembly. Also, the flow rate of the water rods and coolant channel are known. The downward flow is assumed uniformly distributed among the water rods for different assemblies. Applying the above Equations (164) to (169), the temperatures at every node can be calculated for both the coolant and the water rods for an average assembly. Therefore, the core inlet temperature is obtained for the average

assembly, which is the lower plenum temperature and is the same for the hot assembly inlet temperature. To obtain the water rods outlet temperature at the hot channel, the core outlet temperature at the hot channel is adjusted until the hot channel inlet temperature equals the previously calculated average channel inlet temperature. In Table 6-2, the hot channel water rods outlet and the coolant inlet temperatures are listed for different RPV inlet temperatures.

Table 6-2: The coolant channel inlet and the water rods outlet temperatures for the hot channel

RPV inlet (°C)	260	270	**280**	290
Water rods outlet (°C)	329	333.9	**339.3**	344.4
Coolant inlet (Lower plenum) (°C)	320.7	326.3	**331.9**	337.7
Water rods heat (% of total fuel heat)	12.5%	12.0%	**11.4%**	10.7%

6.2.2 The coolant and water rods flow modeling

From Table 6-2, it is seen that, as the RPV inlet temperatures are around nominal value 280°C, the water rods outlet flow temperature is below 350°C which is the boundary between region 1 &2 of the three region model. Therefore, the water rods flow can be simulated as the first region. The conservation equations can be described as:

$$\frac{\partial u_w}{\partial z} = 0 \quad (\rho_w(z) = \rho_A = Const.) \tag{6-19}$$

$$\rho_A \frac{\partial h_w}{\partial t} + \rho_A u_{w,in} \frac{\partial h_w}{\partial z} = \frac{q''_w P_{wi}}{A_w} \tag{6-20}$$

$$-\frac{\partial p_w}{\partial z} = \rho_A \frac{du_{w,in}}{dt} + \frac{f_1 \rho_A u^2_{w,in}}{2D_{w,e}} + \rho_A g \tag{6-21}$$

Where,

$D_{w,e}$: the equivalent diameter for downward water rods flow

A_w: the flow area for water rods flow

From Table 6-2, the inlet temperatures of the upward coolant flow are still in the first region. It is worth noting that, for the supercritical fluids, it is known that once the inlet temperature is above the pseudo-saturation temperature, i.e. 350°C, there will be no instability problem for the upward flow [Khabensky, 1995]. Therefore, only the water rods outlet temperatures bellow 350°C is of interest here. Therefore, the upward coolant still experiences three regions axially. The conservation equations can be described as:

For the first region:

$$\frac{\partial u_{c,H}}{\partial z} = 0 \quad (\rho_{c,H}(z) = \rho_A = Const.) \tag{6-22}$$

$$\rho_A \frac{\partial h_{c,H}}{\partial t} + \rho_A u_{c,in} \frac{\partial h_{c,H}}{\partial z} = \frac{q_f^{"} P_h - q_c^{"} P_{wo}}{A_c} \tag{6-23}$$

$$-\frac{\partial p_{c,H}}{\partial z} = \rho_A \frac{du_{c,in}}{dt} + \frac{f_1 \rho_A u_{c,in}^2}{2D_{c,e}} + \rho_A g \tag{6-24}$$

Where,

$D_{c,e}$: the equivalent diameter for upward coolant flow

A_c: the flow area for upward flow

For the second region:

$$\frac{\partial u_{c,m}}{\partial z} = \Omega_1 = \frac{v_{AB}}{h_{AB}} \frac{q_f^{"} P_h - q_c^{"} P_{wo}}{A_c} \tag{6-25}$$

$$\rho_{c,m} \frac{\partial h_{c,m}}{\partial t} + \rho_{c,m} u_{c,m} \frac{\partial h_{c,m}}{\partial z} = \frac{q_f^{"} P_h - q_c^{"} P_{wo}}{A_c} \tag{6-26}$$

$$-\frac{\partial p_{c,m}}{\partial z} = \frac{\partial G_{c,m}}{\partial t} + \frac{\partial}{\partial z}(G_{c,m}^2 / \rho_{c,m}) + \frac{f_2 \rho_{c,m} u_{c,m}^2}{2D_{c,e}} + \rho_{c,m} g \tag{6-27}$$

For the third region:

$$\frac{\partial u_{c,L}}{\partial z} = \Omega_2 = \frac{R}{pC_p}\frac{q_f^{"}P_h - q_c^{"}P_{wo}}{A_c} \tag{6-28}$$

$$\rho_{c,L}\frac{\partial h_{c,L}}{\partial t} + \rho_{c,L}u_{c,L}\frac{\partial h_{c,L}}{\partial z} = \frac{q_f^{"}P_h - q_c^{"}P_{wo}}{A_c} \tag{6-29}$$

$$-\frac{\partial p_{c,L}}{\partial z} = \frac{\partial G_{c,L}}{\partial t} + \frac{\partial}{\partial z}(G_{c,L}^2/\rho_{c,L}) + \frac{f_3\rho_{c,L}u_{c,L}^2}{2D_{c,e}} + \rho_{c,L}g \tag{6-30}$$

The Pseudo subcooling number and Expansion number at these conditions can be expressed as:

$$N_{psub} = \frac{(h_A - h_{c,in})}{h_{AB}}\frac{\rho_A - \rho_B}{\rho_B} \tag{6-31}$$

$$N_{\exp} = \frac{R}{pC_p}\frac{Q_f - Q_w}{A_c}\frac{1}{u_{c,in}} \tag{6-32}$$

Where,

Q_f : Channel total heat released from fuel rods

Q_w : Channel total heat transferred to water rods

$h_{c,in}$: Upward coolant flow inlet enthalpy

$u_{c,in}$: Upward coolant flow inlet velocity

During a single channel fluctuation, the upward coolant flow rate and properties will induce heat transfer oscillation between the upward coolant flow and the downward water rods flow. The water rods oscillations will be transferred into the lower plenum. However, since the single channel is only a small fraction of the core, the bulk flow is not disturbed and remains in steady state during a single channel oscillation. After mixing with the bulk flow, the small fluctuation in the oscillation channel will be absorbed by the steady state

bulk flow in the lower plenum. Therefore, upward coolant flow inlet enthalpy is assumed constant during a single channel oscillation.

The fluctuation of the water rods wall surface heat flux is neglected in this work. The following reasons make this possible:

(1) From Table 6-2, only about 10% of the total energy is transferred into water rods in the condition of without isolation completely. Therefore, the water rods heating is only a small fraction of the total energy,

(2) The water rods flow is in the heavy fluid region of the three region model. The density and other properties have very small fluctuations,

(3) Since the single channel stability analysis deals with the upward flow, the flow is disturbed at the inlet of the upward flow,

(4) From the conclusion of the fuel dynamics effect, neglecting the surface heat flux fluctuation will predict a conservative value of the decay ratio.

6.2.3 Water rods heating effect on single channel stability

The decay ratios and frequencies for a single hot channel are calculated at nominal power and flow for different RPV inlet temperature as described in Table 6-1. Both cases with water rods heating and without water rods heating are graphically shown in Fig. 6-8 and 6-9.

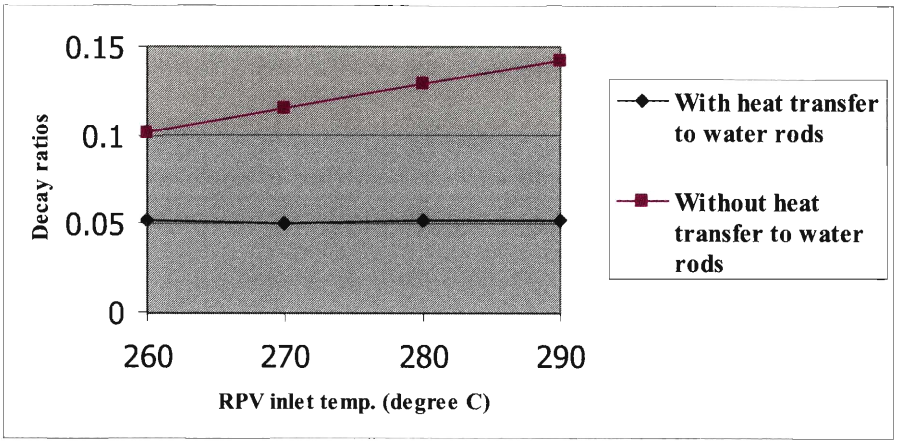

Fig. 6-8: Water rods heating effects on decay ratios of the single channel stability

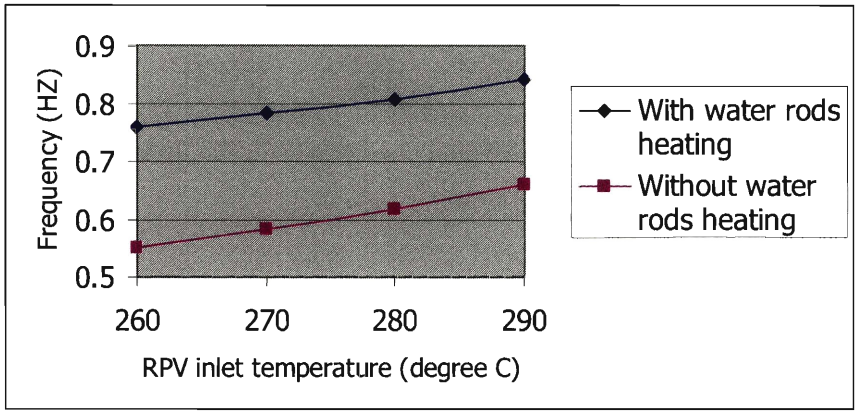

Fig. 6-9: Water rods heating effects on frequencies of the single channel stability

From Fig. 6-8, it is seen that the water rods heating will stabilize the channel. Two reasons make this possible:

(1) Water rods heating will increase the upward flow inlet temperature (from 280°C to 331.9°C at nominal condition). According to Fig. 4-15 in Chapter 4, at higher Psedo-subcooling number, increasing the inlet temperature will stabilize the system.

(2) Upward flow loses heat to water rods through the water rods heating. Smaller net heat addition to the upward flow means smaller expansion number, which will increase the stability margin, therefore stabilize the system.

From Fig. 6-9, it can be seen that the oscillation frequency will increase as the RPV inlet temperature increases. This can be explained since the oscillation period (reverse of the frequency) is proportional to the fluid transport time through the channel. The higher inlet temperature means lower average density and higher average velocity in the channel, which will provide a shorter time to transport through the core. Similarly, the higher frequency with water rods heating than without water rods heating can be explained, since with water rods heating will increase the upward flow inlet temperature as shown in Table 6-2.

6.2.4 Water rods flow rate sensitivity analysis

As mentioned previously, for the U.S. reference SCWR design, the water rods flow rate is about 90% of the total flow rate. The water rods flow rate effect on single hot channel stability is studied by varying the water rods flow rate to be 60%, 70%, 80% and 90% of the total flow. The upward coolant inlet and water rods outlet temperatures for different cases are listed in Table 6-3.

Table 6-3: Water rods flow rate effect on single hot channel stability

Water rods flow fraction	RPV inlet temp. (°C)	Coolant inlet temp. (°C)	Water rods outlet temp. (°C)	Water rods heat (% of total fuel heat)
60%	280	319.0	344.2	8.41%
70%	280	323.4	342.5	9.47%
80%	280	327.4	340.9	10.5%
90%	280	331.9	339.3	11.4%

It is seen that the water rods flow is in the first region for all the water rods flow fraction cases listed in Table 6-3. The decay ratios and the frequencies for the different cases listed in Table 6-3 are plotted in Fig. 6-10 and 6-11.

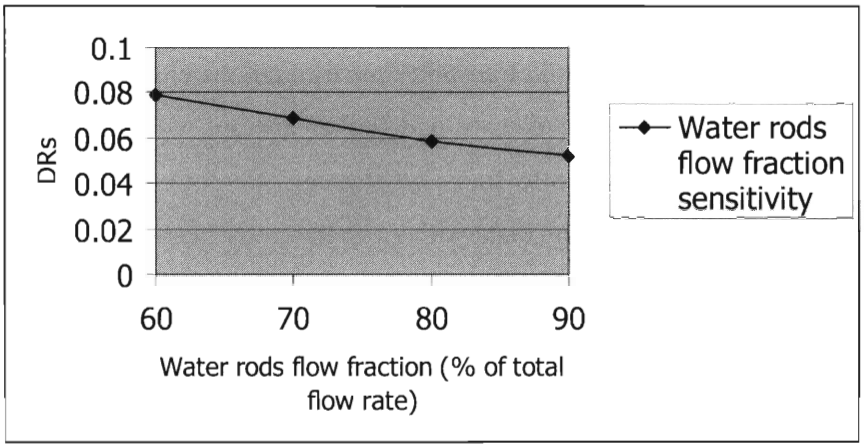

Fig. 6-10: Water rods flow rate effect on decay ratio

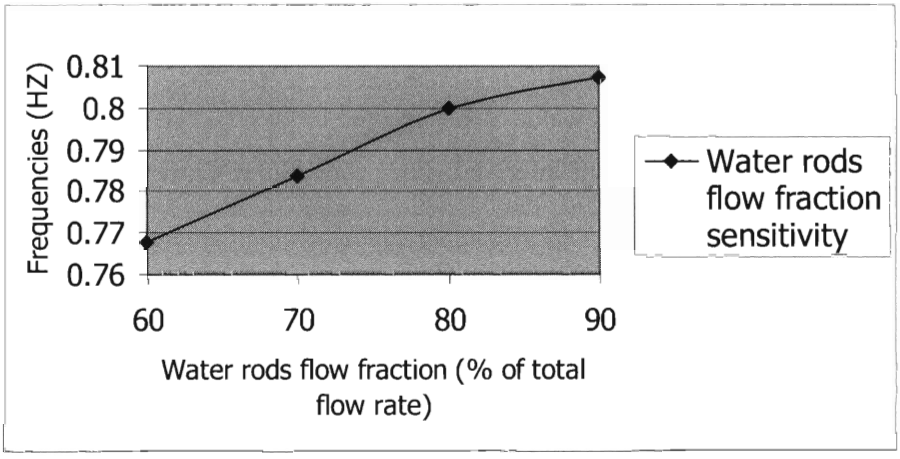

Fig. 6-11: Water rods flow rate effect on oscillation frequency

From Fig. 6-10, it is seen that increasing the water rods flow rate will enhance the single channel stability. The reason is that more power is extracted by the water rods flow at higher water rods flow rate, which means the upward coolant loses more energy. Further more, the increased energy transferred to water rods will increase the upward coolant flow inlet temperature, which stabilizes the system further. Since the inlet temperature is higher at larger water rods flow rate, the frequency will be higher as shown in Fig. 6-11.

Chapter 7

Single channel comparison between SCWR and BWR

The SCWR single channel stability features are compared to the BWR in this chapter. From Fig. 5-3, it is seen that the stability boundary is not sensitive to different two phase flow models at high system pressures, such as 10.0MPa. From Fig. 5-2, it is seen that the HEM model is the most conservative one among the four two phase flow models at low subcooling numbers. Since a typical BWR operates at high pressure (7.2 MPa) and low subcooling number (about 0.8), the HEM model is selected for the BWR single channel stability analysis.

The comparison between the SCWR and a typical BWR is made by hot a channel sensitivity analysis. The fuel dynamics model is included for both the SCWR and the BWR.

The design parameters of a typical 8x8 BWR were listed in Table 7-1.

Table 7-1: the design parameters of a typical BWR

Parameter	Value
CORE	
Thermal power	3293 MW
Core inlet pressure	7.24 MPa
Reactor core inlet/outlet temperature	275/286°C
Coolant flow rate in core	12915 kg/s
Number of fuel assemblies	764
Equivalent diameter	4.75 m
Hot channel factors	Max. relative assembly Power: 1.4 Local peaking factor: 1.24 Axial peaking factor: 1.5
Pressure drop across the core	0.152 MPa
FUEL PIN	
Fuel pin OD	12.52 mm
Cladding thickness	0.8636 mm
Fuel pellet OD	10.57 mm
Active length	3.66 m
Total fuel pin height	4.47 m
FUEL ASSEMBLY	
Fuel pin lattice	8x8 square
Assembly side	138x138 mm
Assembly wall thickness	2 mm
Inlet orifice coefficient	Central region: 31.1 Peripheral region: 205.0
Assembly flow rate	Central region average: 16.7 kg/s Peripheral region average:8.89 kg/s

Applying the radial power peaking factor 1.4 for the hot assembly channel, it is found that a flow rate of 15.9kg/s will generate a pressure drop of 0.152MPa across the hot channel if the inlet orifice coefficient is 31.1.

7.1 Single channel stability analysis for the BWR

Just like the SCWR single channel stability analysis, a constant fuel rods surface heat flux is applied first for the BWR, then the fuel dynamics effects is studied.

For a constant fuel rods surface heat flux, applying the models for subcritical pressure stability analysis developed in Chapter 5, the single channel stability map for the typical BWR described in Table 7-1 can be plotted in Fig. 7-1.

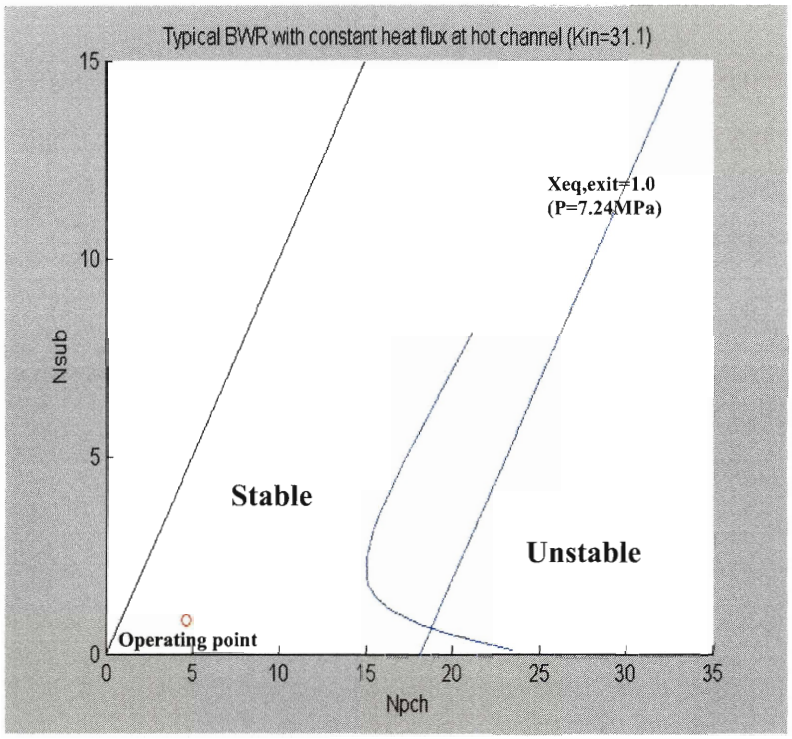

Fig. 7-1: Typical BWR single channel stability at constant heat flux

The fuel dynamics model described in Chapter 6 was applied to the BWR also. The Dittus-Boelter correlation was applied for single liquid region. For the two phase flow region, correlations such as Chen's correlation were formulated by including the effects of both nucleate boiling and convection heat transfer. Therefore, the surface heat flux will oscillate coupled with the fuel dynamics model during coolant density wave oscillations (DWO). Some correlations have simple forms and were frequently used for nucleate boiling region such as Thom's correlation, which is described as follows:

$$q'' = \frac{\exp(2p/8.7)}{(22.7)^2}(T_w - T_{sat})^2 \tag{183}$$

Where, $q^{"}$ is in MW/m^2, p is in MPa and T is in °C. From the above Thom's correlation, it is seen that the surface heat flux in the boiling region is not affected by flow and quality perturbations. Thus, the surface heat flux will be constant and decoupled from fuel dynamics during the coolant DWO in the two phase flow region.

To investigate the stability effects of the above two kinds of heat transfer correlations, both the Thom's and Chen's correlations were applied for BWR single hot channel stability analysis. The stability boundaries are plotted in the Fig. 7-2 together with the stability boundary without the fuel dynamics model.

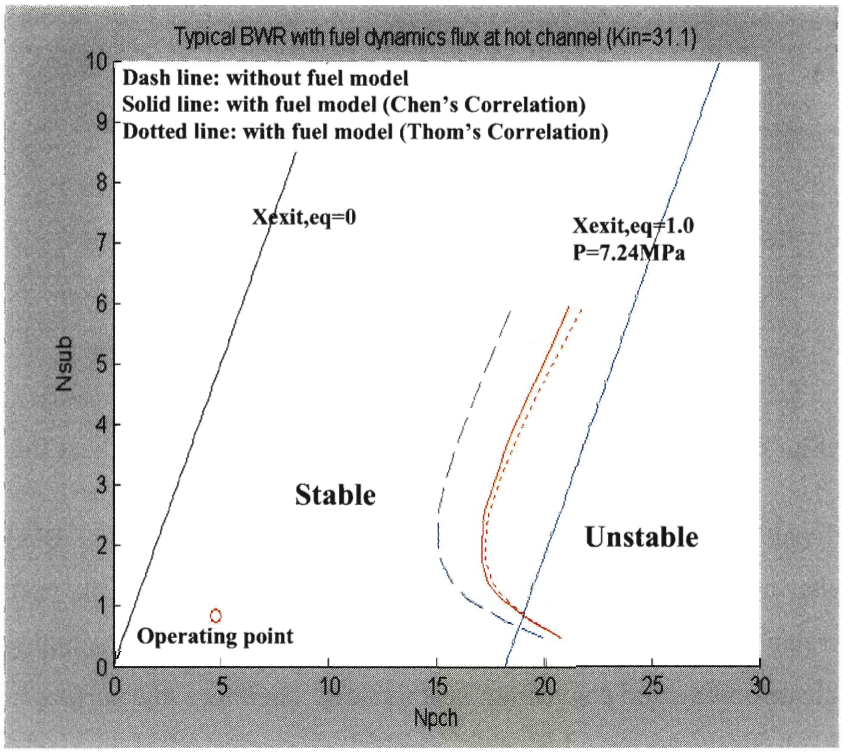

Fig. 7-2: The fuel dynamics effect on stability boundary for BWR at hot channel

From Fig. 7-2, it is seen that the two correlations are matched well. A simple correlation form such as Thom's correlation is applicable to this kind of stability analysis. It also can be seen that the fuel rods will also stabilize the system like SCWR. Since the coolant dynamics is decoupled with fuel dynamics in the two phase region according to Thom's correlation, the fuel stabilization effects is only through the single liquid region. The

length of the single phase region will decrease as the subcooling number increase. Therefore, the fuel effects becomes smaller at high subcooling numbers compared with the low subcooling number as shown in above Fig. 7-2.

7.2 Hot channel stability comparison between SCWR and BWR

The stability sensitivities to inlet orifice coefficient, system power and flow rate have also been analyzed and compared. The coupled fuel dynamics model was applied for both SCWR and BWR. For the SCWR, the case of without water rods heating is analyzed first, then the water rods heating effect is discussed follows. The usual BWR thermal-hydraulic stability criterion of decay ratio less than 0.5 is applied here also for the SCWR.

7.2.1 Sensitivity analysis for SCWR and BWR

The nominal operating conditions were taken as the reference for both SCWR and BWR in the following analysis.

7.2.1.1 Inlet orifice coefficient sensitivity

The inlet orifice coefficient plays a very important role in system stability characteristics. The decay ratios at different inlet orifice coefficient values for the hot channel are plotted in Fig. 7-3.

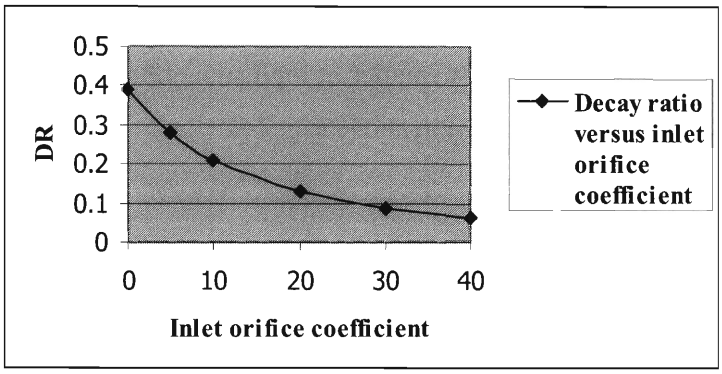

Fig. 7-3: SCWR hot channel decay ratios at different orifice coefficients

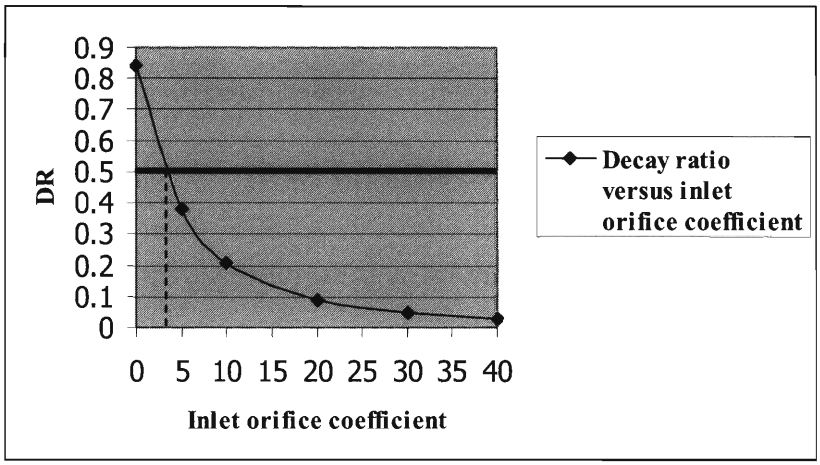

Fig. 7-4: BWR hot channel decay ratios at different orifice coefficients

From Fig. 7-3 and 7-4, it is seen that both the SCWR and BWR are sensitive to the inlet orifice coefficient. The BWR is more sensitive at low inlet orifice coefficient values. A minimum inlet orifice coefficient of about 4.0 is required to satisfy the stability criterion, i.e. below 0.5. It is well know that the single phase (incompressible) pressure drop has a significant role in the stability. The system is more stable at higher single phase pressure drop. For the typical BWR, the core inlet temperature is about 275°C, which is very close to saturation temperature 288°C. Therefore, the single phase pressure drop is mainly due to the inlet orifice pressure loss. Thus, the BWR stability is very sensitive to inlet orifice coefficient, especially at low values. For the U.S. reference SCWR design, the core inlet temperature is 280°C, the pseudo saturation temperature is about 350°C. Therefore, there is a significant pressure drop in the first region (incompressible) part, which decreases the

sensitivity of the inlet orifice coefficient on stability compared with the BWR, especially at low values.

7.2.1.2 Mass flow rate and power sensitivity analysis

The mass flow sensitivity was addressed by changing the mass flow rate, while keeping the power and the pressure at reference conditions. The power sensitivity was addressed by changing the system power, while keeping the mass flow rate and the system pressure at the reference conditions. The inlet orifice coefficient for SCWR is 20.0 and BWR is 31.1. The results are illustrated in Fig. 7-5 and 7-6.

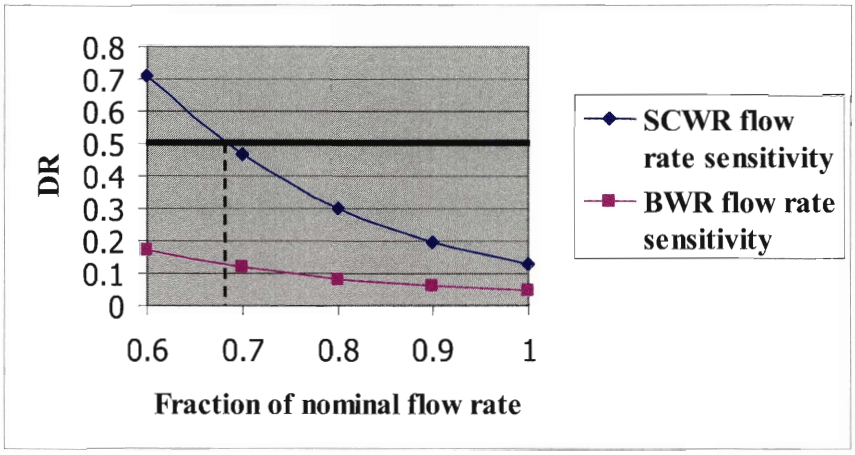

Fig. 7-5: Mass flow rate sensitivity analysis

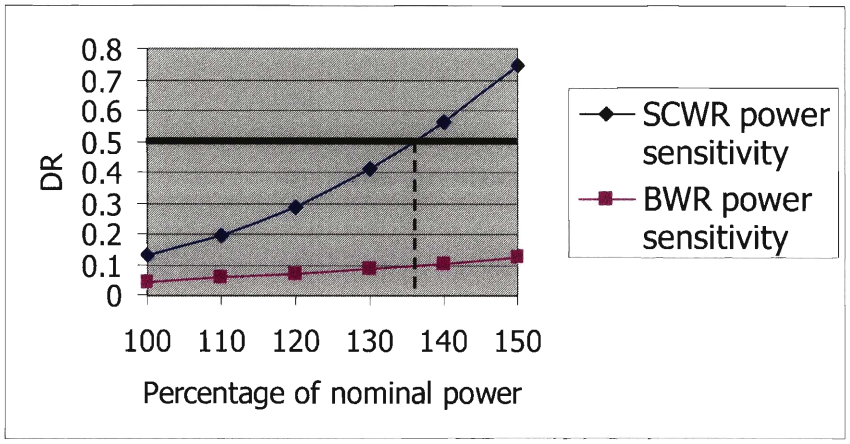

Fig. 7-6: Power sensitivity analysis

From above Fig. 7-5 and 7-6, it is seen that the stability criterion will be violated as the flow rate is decreased to 68% of the nominal value and power increased to 136% of the nominal power for the SCWR, while the typical BWR still satisfies the criterion at that power and flow level with large margins. Therefore, the SCWR is more sensitive to the flow rate and power changes even with the sophisticated inlet orifice scheme applied to obtain a uniform core enthalpy rise.

7.2.1.3 Mass flow rate and power sensitivity on stability maps

The stability sensitive feature of SCWR also can be illustrated by using stability map in following Fig. 7-7 and 7-8

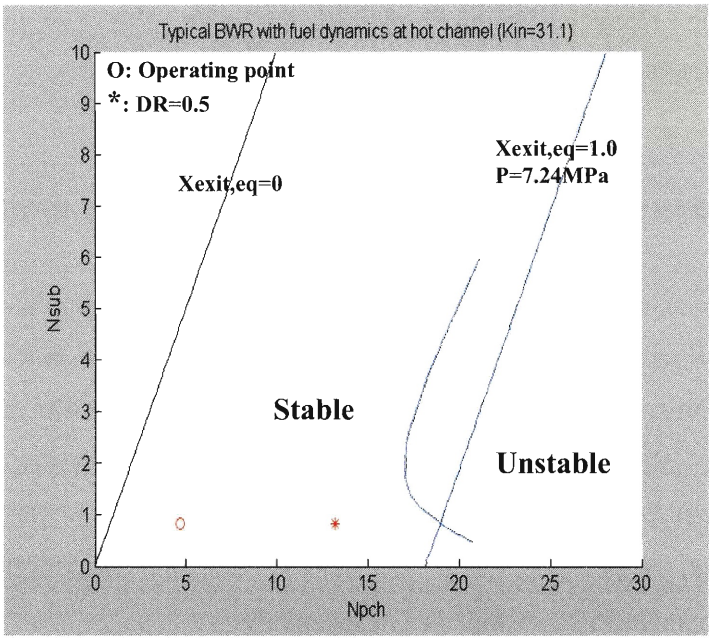

Fig. 7-7: BWR stability map for hot channel

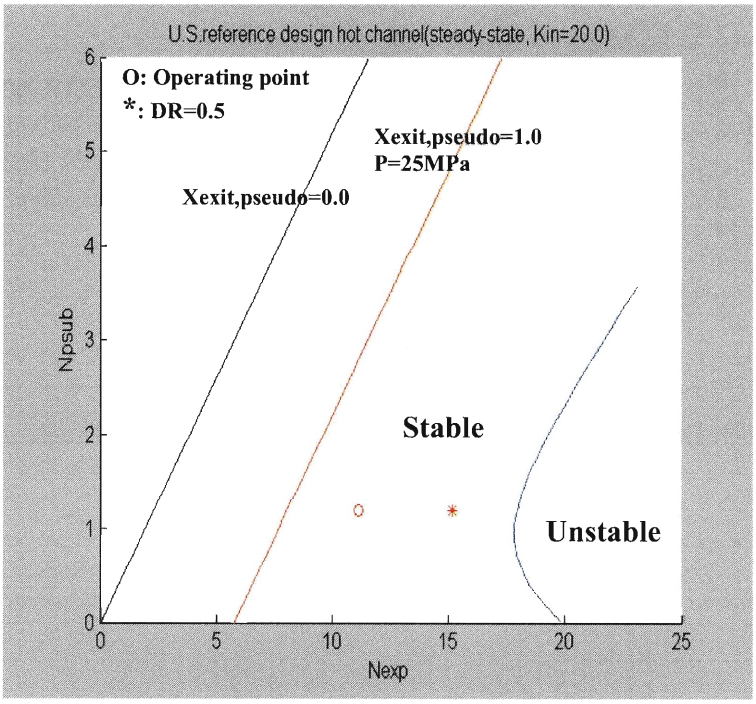

Fig. 7-8: SCWR stability map for hot channel

From above figures, the BWR operating point is at a low phase change number about 4.7 while the stability boundary value is about 13.2, and SCWR operating point is at a high

expansion number about 11.0 while the stability boundary value is about 15.0. Therefore, the SCWR is more sensitive to operating parameters than the BWR.

7.2.2 Adequacy of the use of decay ratio for stability monitoring

From the above sensitivity analysis, although the SCWR has a similar stability level to the typical BWR at nominal operating conditions (DR=0.13 for SCWR and DR=0.05 for BWR), the stability margin is much smaller than the typical BWR. To make it more comparable, the inlet orifice coefficient of the typical BWR should be reduced to 15.0, which will generate a decay ratio about 0.13, the same as the SCWR, at nominal conditions. Then, the power and flow sensitivity is compared between SCWR and BWR, which can be found in Fig. 7-9 and 7-10, respectively.

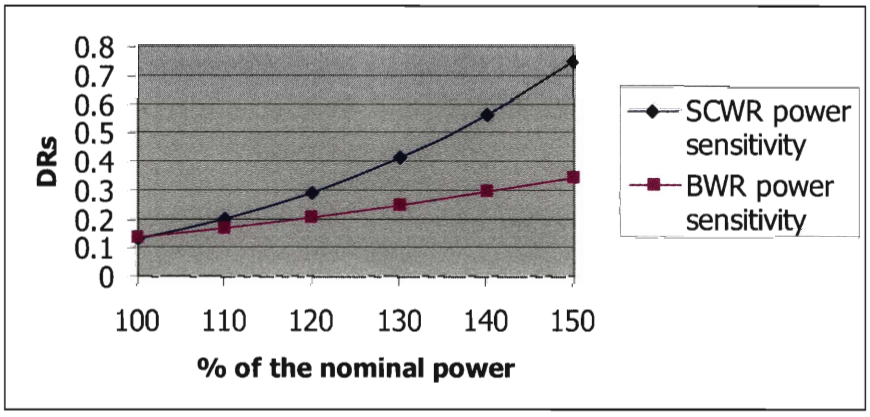

Fig. 7-9: Power sensitivity comparison at the same nominal stability level

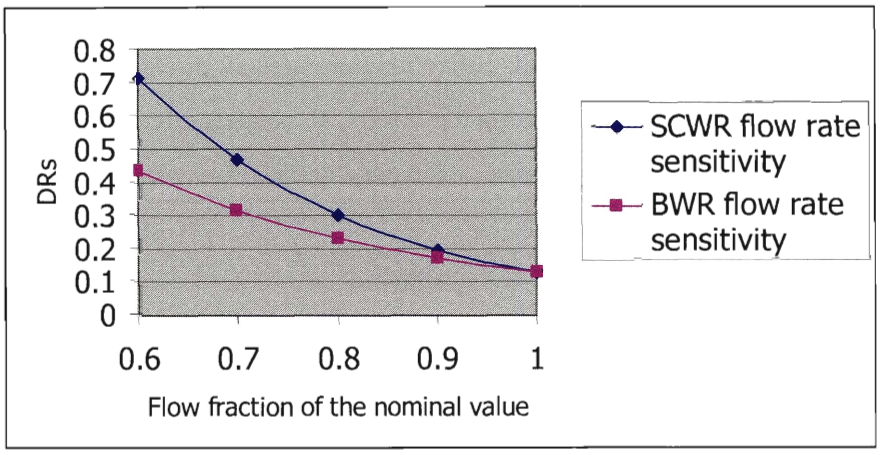

Fig. 7-10: Flow rate sensitivity comparison at the same nominal stability level

From Fig. 7-9 and 7-10, it is seen that the typical BWR is less sensitive to power and flow changes than the U.S. reference SCWR design. It is worth noting that the same power to flow ratio between the hot channel and the average channel was applied for the U.S. reference SCWR design, while the hot channel power to flow ratio is 1.4 of the average channel for the typical BWR. Thus, even in such "worse" condition, the hot channel of the BWR is still less sensitive than the SCWR. Therefore, the systems can have different stability margins even if the decay ratio is the same at the nominal condition. Van de Hagen et al (2003) did question the use of decay ratio in BWR stability monitoring. They mentioned that the DR can not give the stability margin which may misled the operator, since a small DR does not mean a high stability margin. They suggested that instead of merely focusing on DRs, it would be beneficial to compare the sensitivity of predicted DR-values to independent reactor variables.

7.2.3 Power and flow sensitivity with water rods heating

In the above part, it was found that the SCWR is sensitive to power and flow in the case of no water rods heating. The SCWR sensitivity feature is studied here with water rods heating.

With water rods heating, increasing the power or decreasing the flow rate, the inlet temperature of the upward flow and outlet temperature of the water rods will also increase. Beyond the pseudo saturation temperature, the supercritical flow will have no instability problem, increasing the power or decreasing the flow was conducted such that the outlet temperature of the water rods is below about 350°C. The upward flow inlet and water rods outlet temperatures are listed in Table 7-2.

Table 7-2: power sensitivity with water rods heating

Power (% nominal)	100	110	120	130
Water rods outlet temp. (°C)	339.3	344.1	350.1	355.4
Upward flow inlet temp. (°C)	331.9	334.4	338.0	342.7

The decay ratios sensitivity against to power is plotted in Fig. 7-11 for both cases with and without water rods heating.

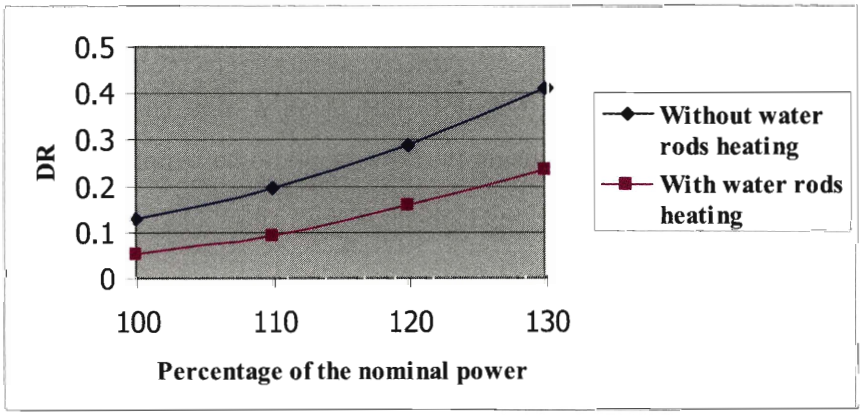

Fig. 7-11: SCWR power sensitivity with water rods heating

The flow rate sensitivity has also been analyzed and the upward flow inlet and water rods outlet temperatures are listed in Table 7-3.

Table 7-3: flow sensitivity with water rods heating

Flow rate (% nominal)	80	90	100
Water rods outlet temp. (°C)	354.3	346.5	339.3
Upward flow inlet temp. (°C)	342.3	335.6	331.9

The decay ratios sensitivity against flow rate is plotted in Fig. 7-12 for both cases with and without water rods heating.

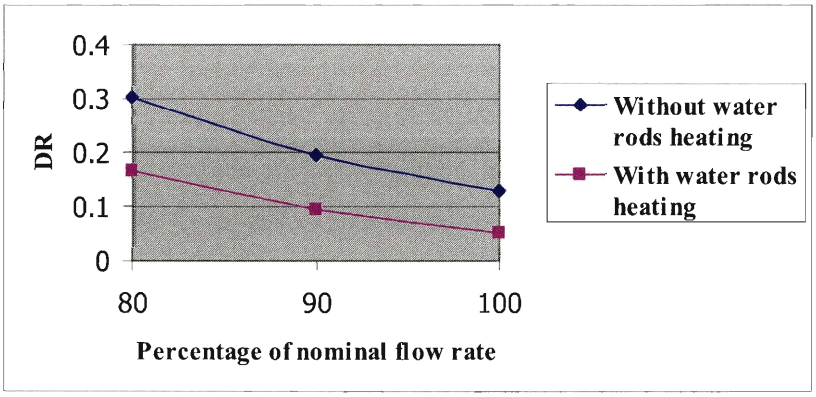

Fig. 7-12: SCWR velocity sensitivity with water rods heating

From Fig. 7-11 and Fig. 7-12, it is seen that with the water rods heating, although the system is more stable, the sensitivity feature can not be improved significantly for both power and flow rate.

Chapter 8

Coupled neutronic region-wide (out-of-phase) stability analysis

As mentioned by [Munoz-Cobo, et al, 1996], the out-of-phase oscillations have been observed in several BWRs during the stability tests or startup conditions. The out-of-phase oscillations have been reported in Leibstada, Cofrentes [Mata et al., 1992], Caorso [Gialdi et al., 1985], Ringhals [Van der Hagen et al., 1994], and other nuclear power plants [Brandes, 1990].

During the out-of-phase instability, half of the core rises in power while the power in the other half decrease to maintain an approximately constant total core power. In the tests described in [E. Gialdi et al., 1985], local power oscillations amplitude was as large as 70% while the average reactor power oscillated by only 12%. Since the automatic safety systems in BWRs rely on total power measurements to scram the reactor, large amplitude out-of-phase oscillations can occur without reactor scram. Therefore, it is necessary to design the reactors to avoid the out-of-phase instability problem. Also, the system adjusts flow from one half of the core to the other half while keeping the total flow rate almost constant.

During the out-of-phase oscillations, all of the channels will have the same but oscillating pressure drop [Munoz-Cobo, et al, 2002]. If both a constant pressure drop boundary condition and a constant total mass flow rate condition are simultaneously applied to the entire core, the system of differential equations will be overdetermined and only small variations in the inlet mass fluxes to the channels will be allowed. However, there is

empirical evidence [Takigawa, et al, 1987], that the inlet mass flux may have large oscillations during out of phase oscillation, therefore, the constant pressure drop boundary condition should be discarded.

The out-of-phase stability features of U.S. reference SCWR design are analyzed in this chapter. The linearized thermal-hydraulics model and point kinetics model were developed. To obtain the first subcritical neutronic dynamic mode, the modal expansion method for point kinetics equation based on λ modes was applied. Then, the radial lumping effects on SCWR stability was discussed. Similar to the single channel analysis, two models, without water rods heating and with water rods heating, were developed. Finally, the out-of-phase analysis model for a BWR was developed and the stability feature was compared with the SCWR.

8.1 The model description

The thermal-hydraulic and neutronic models were developed first, then, the characteristic equation was constructed for the out-of-phase stability mode. The thermal-hydraulic and neutronic models can be illustrated in the following Fig. 8-1.

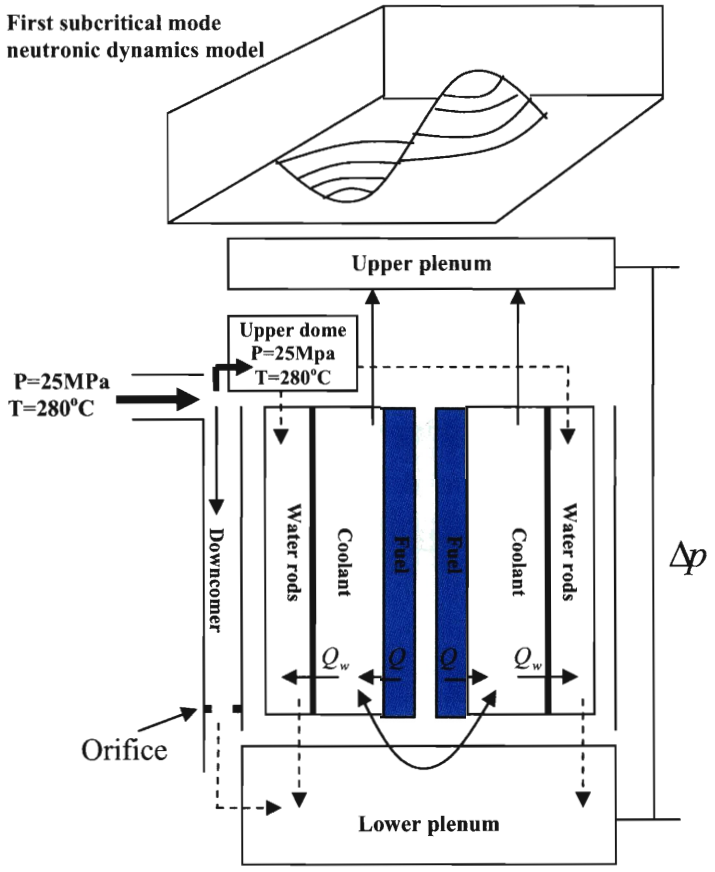

Fig. 8-1: The models illustration for out-of-phase stability

Without water rods heating, the water rods were isolated perfectly, the heat transfer between upward flow and the water rods downward flow is zero, i.e. $Q_w = 0$, therefore the temperature in the lower plenum remains equal to the RPV inlet temperature 280°C. With water rods heating, part of the fission energy is transferred into water rods, i.e. $Q_w \neq 0$, the lower plenum temperature will be above the RPV inlet temperature. As seen in Fig. 8-1, the core model includes two channels with one channel to represent each half of the core.

8.1.1 Thermal-hydraulic model descriptions

In the single channel stability analysis, the thermal hydraulic model was developed for a single channel. For investigating the coupled neutronic stability, the thermal hydraulic models must be developed for the whole core. The core thermal-hydraulic models without water rods heating are developed in this part for each different lumping strategy. For investigating the stability effects of different modes of lumping, each half of the core was lumped into one average channel, two channels or three channels, with an appropriate power distribution.

8.1.1.1 One channel model (half of the core)

In this mode of lumping, the whole core is represented by two identical channels, with each channel representing half of the core, as illustrated below:

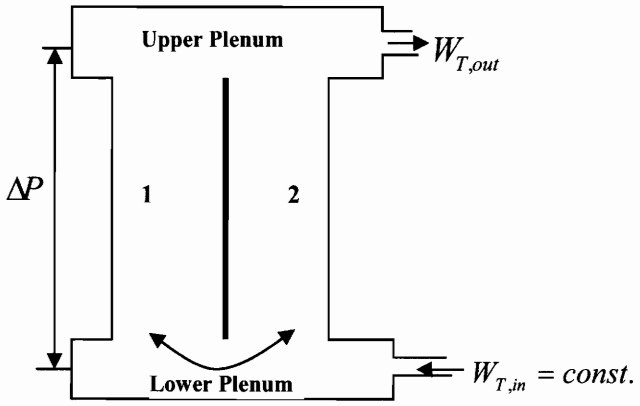

Fig. 8-2: The one channel lumping (half of the core)

During out-of-phase density wave oscillations, the input variables for a specific channel are: the inlet flow rate, inlet enthalpy and power. Therefore, output pressure drop oscillations across the channel 1 or 2 can be described as a function of the inlet flow rate oscillation, inlet enthalpy oscillation and power oscillation. Since the enthalpy in the lower plenum can be taken constant during the out-of-phase oscillation, the pressure drop oscillations are only functions of the inlet flow rate and power oscillations:

$$\delta\Delta p_1 = \Gamma_1 \delta w_1 + \pi_1 \delta q_1''' \tag{8-1}$$

$$\delta\Delta p_2 = \Gamma_2 \delta w_2 + \pi_2 \delta q_2''' \tag{8-2}$$

Solving the δw_1 and δw_2 from above equations (8-1) and (8-2), and applying the boundary condition:

$$\delta\Delta p_1 = \delta\Delta p_2 \tag{8-3}$$

The inlet flow response for an input pressure drop oscillation or power oscillation for channel 1 and 2 can be expressed as:

$$\delta w_1 = \frac{1}{\Gamma_1}\delta\Delta p - \frac{\pi_1}{\Gamma_1}\delta q_1''' \tag{8-4}$$

$$\delta w_2 = \frac{1}{\Gamma_2}\delta\Delta p - \frac{\pi_2}{\Gamma_2}\delta q_2''' \tag{8-5}$$

For this two parallel channels system, if the pressure drop or power oscillated in one channel, say channel 1, to maintain the total flow rate constant, the flow rate in the other channel would have the same amount of oscillation feedback but with an opposite sign. The feedback process can be illustrated as:

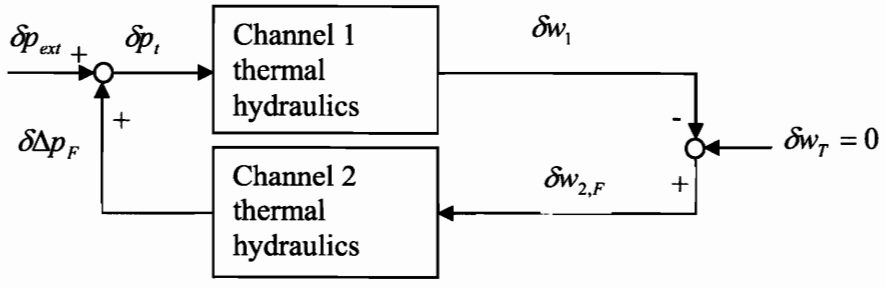

Fig. 8-3: Block diagram of the pressure feedback mechanism

From above Fig. 8-3,

$$\delta w_{2,F} = \frac{1}{\Gamma_2}\delta\Delta p_F - \frac{\pi_2}{\Gamma_2}\delta q_2''' \tag{8-6}$$

and,

$$\delta w_1 + \delta w_{2,F} = 0 \tag{8-7}$$

therefore,

$$\frac{1}{\Gamma_1}\delta\Delta p_t - \frac{\pi_1}{\Gamma_1}\delta q_1''' + \frac{1}{\Gamma_2}\delta\Delta p_F - \frac{\pi_2}{\Gamma_2}\delta q_2''' = 0 \tag{8-8}$$

Plusing the $\frac{1}{\Gamma_2}\delta\Delta p_{ext}$ in both sides of the above equation and applying:

$$\delta\Delta p_F + \delta\Delta p_{ext} = \delta\Delta p_t \tag{8-9}$$

Equation (8-8) can be re-written as:

$$\frac{1}{\Gamma_1}\delta\Delta p_t - \frac{\pi_1}{\Gamma_1}\delta q_1''' + \frac{1}{\Gamma_2}\delta\Delta p_t - \frac{\pi_2}{\Gamma_2}\delta q_2''' = \frac{1}{\Gamma_2}\delta\Delta p_{ext} \tag{8-10}$$

Also, during the out-of-phase oscillations, the power has the relation: $\delta q_1''' = -\delta q_2''' = \delta q_o'''$. Plugging Equation (8-1) into above Equation (8-10), after some rearrangement, one obtains:

$$\Gamma_t\delta w_1 + \pi_t\delta q_o''' = \frac{\Gamma_1+\Gamma_2}{\Gamma_2}\delta w_1 + \frac{\pi_1+\pi_2}{\Gamma_2}\delta q_o''' = \frac{1}{\Gamma_2}(\Gamma_1\delta w_{1,ext} + \pi_1\delta q_{o,ext}''') \tag{8-11}$$

This equation will be applied to construct the characteristic equation after coupling with the neutronic feedback relations. The coefficients Γ_1 , Γ_2 and π_1 , π_2 can be obtained from the single channel pressure response analysis, which had been described previously in the single channel stability analysis part.

8.1.1.2 Two channel model (half of the core)

For the case that half of the core was lumped by two channels, the whole core can be still treated as two large channels with each one has two subchannels. The core can be illustrated as shown in Fig. 8-4

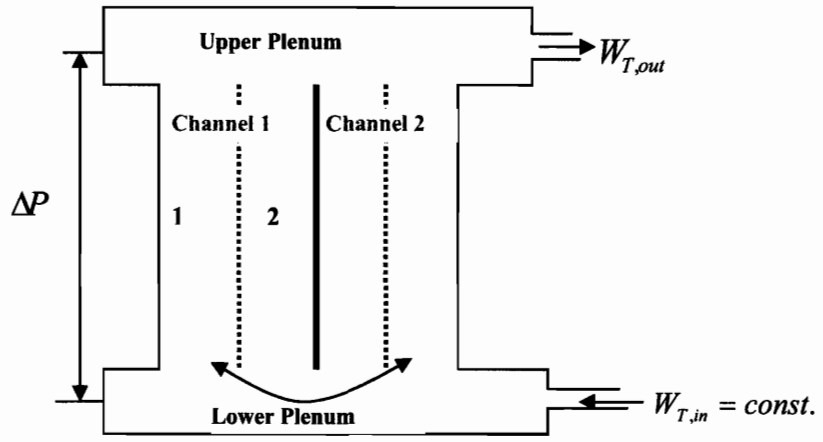

Fig. 8-4: The two channels lumping (half of the core)

In Fig. 8-4, the pressure drop oscillations for the large channel 1 and 2 can be described as:

$$\delta\Delta p_{1t} = \Gamma_{1t}\delta w_{1t} + \pi_{1t}\delta q'''_{1t} \tag{8-12}$$

$$\delta\Delta p_{2t} = \Gamma_{2t}\delta w_{2t} + \pi_{2t}\delta q'''_{2t} \tag{8-13}$$

Then, the procedure described in the one channel part can be applied here to derive a relation similar to Equation (8-11). For the large channel #1, the pressure responses for the individual subchannels 1 and 2 can be expressed as:

$$\delta\Delta p_1 = \Gamma_1 \delta u_1 + \pi_1 \delta q_1''' \tag{8-14}$$

$$\delta\Delta p_2 = \Gamma_2 \delta u_2 + \pi_2 \delta q_2''' \tag{8-15}$$

If the flow area of subchannel 1 and 2 are A_1 and A_2, respectively, and the volumetric powers of subchannels 1 and 2 have the relation with the core average volumetric power:

$$q_1''' = F_1 q_o''' \tag{8-16}$$

$$q_2''' = F_2 q_o''' \tag{8-17}$$

Then,

$$\delta\Delta p = [\Gamma_1 /(\rho_f A_1)]\delta w_1 + \pi_1 F_1 \delta q_o''' \tag{8-18}$$

$$\delta\Delta p = [\Gamma_2 /(\rho_f A_2)]\delta w_2 + \pi_2 F_2 \delta q_o''' \tag{8-19}$$

Therefore,

$$\delta w_1 = \frac{\rho_f A_1}{\Gamma_1}\delta\Delta p - \pi_1 F_1 \frac{\rho_f A_1}{\Gamma_1}\delta q_o''' \tag{8-20}$$

$$\delta w_2 = \frac{\rho_f A_2}{\Gamma_2}\delta\Delta p - \pi_2 F_2 \frac{\rho_f A_2}{\Gamma_2}\delta q_o''' \tag{203}$$

Then, the total flow rate oscillation for the large channel 1 can be described as:

$$\delta w_{1t} = \delta w_1 + \delta w_2 = (\frac{\rho_f A_1}{\Gamma_1} + \frac{\rho_f A_2}{\Gamma_2})\delta\Delta p - (\pi_1 F_1 \frac{\rho_f A_1}{\Gamma_1} + \pi_2 F_2 \frac{\rho_f A_2}{\Gamma_2})\delta q_o''' \tag{8-21}$$

Solving $\delta\Delta p$ from the above Equation (8-21), one can obtain:

$$\delta\Delta p = \frac{\Gamma_1\Gamma_2}{\rho_f A_1\Gamma_2 + \rho_f A_2\Gamma_1}\delta w_{1t} + \frac{\rho_f A_1\pi_1 F_1\Gamma_2 + \rho_f A_2\pi_2 F_2\Gamma_1}{\rho_f A_1\Gamma_2 + \rho_f A_2\Gamma_1}\delta q_o''' = \Gamma_{1t}\delta w_{1t} + \pi_{1t}\delta q_o''' \quad (8\text{-}22)$$

Similarly, for the large channel 2, one can obtain:

$$\delta\Delta p = \Gamma_{2t}\delta w_{2t} + \pi_{2t}\delta q_o''' \quad (8\text{-}23)$$

From Equations (8-22) and (8-23), applying the procedure of Part 1, Equation (8-24) that is similar to Equation (8-11) could be derived:

$$\Gamma_t\delta w_{1t} + \pi_t\delta q_o''' = \frac{\Gamma_{1t} + \Gamma_{2t}}{\Gamma_{2t}}\delta w_{1t} + \frac{\pi_{1t} + \pi_{2t}}{\Gamma_{2t}}\delta q_o''' = \frac{1}{\Gamma_{2t}}(\Gamma_{1t}\delta w_{1t,ext} + \pi_{1t}\delta q_{o,ext}''') \quad (8\text{-}24)$$

8.1.1.3 Three channels model (half of the core)

Using the same methodology described as in Part 2, similar equations to (8-11) and (8-24) can be found for the three channel model case (half of the core) illustrated in Fig. 8-5.

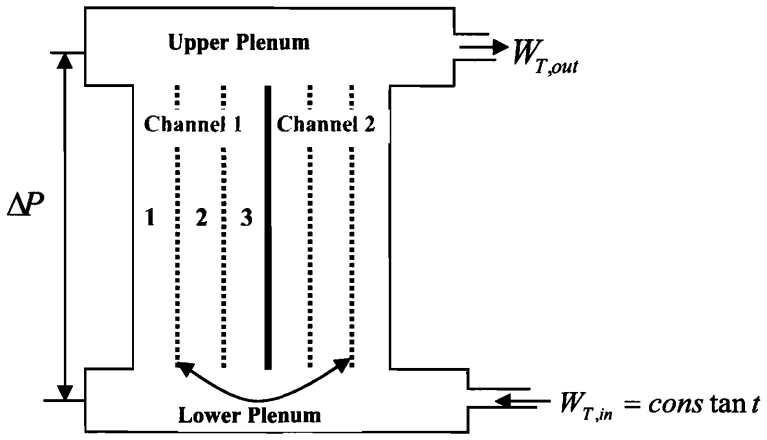

Fig. 8-5: Three channels lumping for half of the core

From above discussions for the different lumping case, it is seen that once the transfer functions from inlet flow rate and power oscillations to pressure drop oscillation was

developed for a specific single channel, the out-of-phase thermal hydraulic characteristic equation can be easily obtained just after some mathematic derivations.

8.1.2 Neutronic model descriptions

During an out-of-phase instability, the high harmonic neutron spacial distribution modes are excited even if the fundamental mode is stable. To obtain the dynamic features of the high harmonic modes, a modal expansion method is widely used. The basic idea of the modal expansion method is to approximate the unknown space and time related neutron flux function by a linear combination of known space functions with time-depended coefficients. Therefore, the modal expansion method includes two steps: (1) define the space functions (2) derive the time-dependent coefficients.

According to [Hashimoto, et. al., 1997], the basic neutron balance equation can be described as:

$$\frac{1}{V(E)}\frac{\partial\phi(r,E,t)}{\partial t} = -L(r,E,t)\phi(r,E,t) + M(r,E,t)\phi(r,E,t) - \sum_{i=1}^{6}\beta_i M_{di}(r,E,t)\phi(r,E,t) + \sum_{i=1}^{6}\chi_{di}(E)\lambda_i C_i(r,t) \tag{8-25}$$

$$\frac{\partial(\chi_{di}(E)C_i(r,t))}{\partial t} = \beta_i M_{di}(r,E,t)\phi(r,E,t) - \lambda_i\chi_{di}(E)C_i(r,t) \tag{8-26}$$

where,

$\phi(r,E,t)$: the space, energy and time dependent neutron flux,

$C_i(r,t)$: the space and time dependent concentration of ith-group precursors,

$L(r,E,t)$: the destruction operator,

$$M(r,E,t)\phi(r,E,t) = [(1-\beta)\chi_p(E) + \sum_{i=1}^{6}\beta_i\chi_{di}(E)]\int_0^{\infty}\nu\Sigma_f(r,E',t)\phi(r,E'.t)dE' ,$$

$$M_{di}(r,E,t)\phi(r,E,t) = \chi_{di}(E)\int_0^\infty \nu\Sigma_f(r,E',t)\phi(r,E'.t)dE' ,$$

$V(E)$: neutron velocity,

λ_i : decay constant of ith-group precursors,

β_i : fraction of neutrons in ith delayed group,

$\chi_{di}(E)$: ith-group delayed neutron spectra, and

$\chi_p(E)$: prompt neutron spectra.

We can decouple the above time-dependent operating factor: $L(r,E,t)$, $M(r,E,t)$ and $M_{di}(r,E,t)$ as a steady state part and a time dependent part:

$$L(r,E,t) = L^o(r,E) + \delta L(r,E,t)$$
$$M(r,E,t) = M^o(r,E) + \delta M(r,E,t)$$
$$M_{di}(r,E,t) = M^o_{di}(r,E) + \delta M_{di}(r,E,t) \qquad (8\text{-}27)$$

According to the modal expansion method, the space time dependent neutron flux can be described as:

$$\phi(r,E,t) = N_o\phi_o(r,E) + \sum_{k=0}^{\infty} n_k(t)\phi_k(r,E) \qquad (8\text{-}28)$$

Also, we can describe the time and space dependent precursors concentrations as:

$$C_i(r,t) = C_{i,o}\phi_o(r,E)/V(E) + \sum_{k=0}^{\infty} c_{i,k}(t)\phi_k(r,E)/V(E) \qquad (8\text{-}29)$$

There are several ways to choose the space functions $\phi_k(r,E)$, wide in used are so called λ modes (Reactivity modes) or ω modes (Period modes). In the following, these two expansion methods are described.

8.1.2.1 Lamda modes expansion

$$L^o\phi_m(r,E) = \frac{1}{\lambda_m} M^o\phi_m(r,E) \tag{8-30}$$

λ_m : m^{th} mode reactivity

ϕ_m : m^{th} neutron flux mode

For a bare homogenous cylindrical reactor with radius R and height H, it can be shown that the fundamental and first subcritical modes can be described as:

$$\phi_o(r,z,\theta) = J_o(2.40r/R)\sin(\pi z/H)$$
$$\phi_1(r,z,\theta) = J_1(3.83r/R)\sin(\pi z/H)\sin(\theta) \tag{8-31}$$

The shapes of these two modes are illustrated in Fig. 8-6.

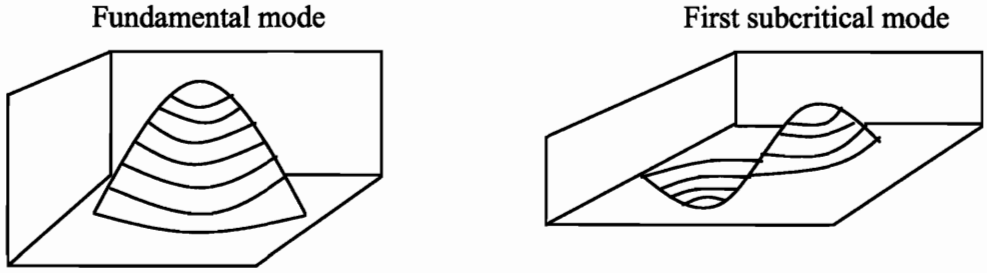

Fig. 8-6: Shapes of the fundamental and first subcritical modes

During out-of-phase oscillations, the excited first subcritical mode coupled to a stable fundamental mode generates an out-of-phase dynamics feature. The total neutron flux is the combination of these two dominant neutron flux modes and can be illustrated as:

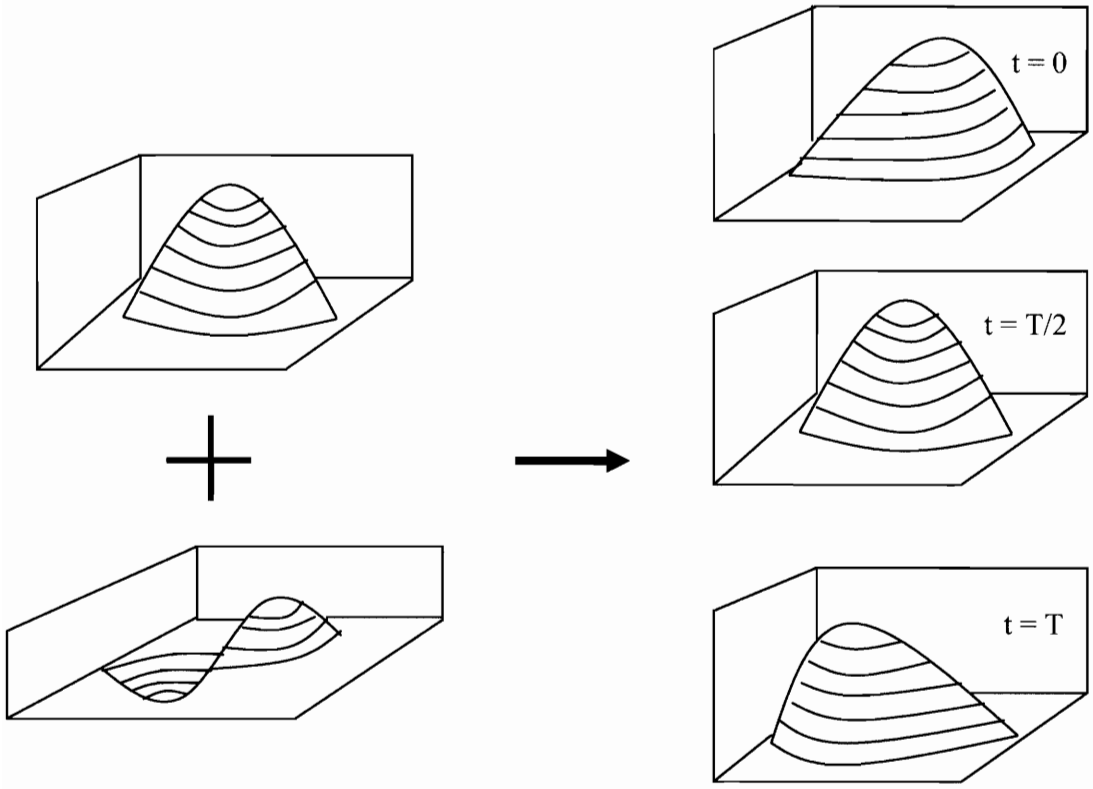

Fig. 8-7: Total neutron flux dynamics during out-of-phase oscillation

The adjoint equations of ϕ_m can be described as:

$$L^{oT}\phi_m^*(r,E) = \frac{1}{\lambda_m} M^{oT}\phi_m^*(r,E) \tag{8-32}$$

And the ϕ_m together with its adjoint eigenvectors ϕ_m^* have the relation:

$$< \phi_m^*, M^o\phi_k >= 0, \text{ for } m \neq k \tag{8-33}$$

Plugging Equations (8-27), (8-28), (8-29) and (8-30) into Equations (8-25) and (8-26), multiplying the adjoint eigenvectors ϕ_m^* on the left, and integrating over the whole space, the modal point kinetic equation, normalized by the steady state value N_o, can be obtained:

$$\frac{dn_m}{dt} = \frac{\rho_m^s - \beta}{\Lambda_m} n_m + \sum_{k=0}^{\infty} \frac{\rho_{mk}}{\Lambda_m} n_m + \frac{\rho_{m0}}{\Lambda_m} + \sum_{i=1}^{6} \lambda_i c_{i,m} - \sum_{i=1}^{6} \beta_i \frac{\rho_{m0}^{di}}{\Lambda_m} - \sum_{i=1}^{6} \beta_i \sum_{k=0}^{\infty} \frac{\rho_{mk}^{di}}{\Lambda_m} n_k \qquad (8\text{-}34)$$

$$\frac{dc_{i,m}}{dt} = \frac{\beta_i}{\Lambda_m} n_m - \lambda_i c_{i,m} + \beta_i \frac{\rho_{m0}^{di}}{\Lambda_m} + \beta_i \sum_{k=0}^{\infty} \frac{\rho_{mk}^{di}}{\Lambda_m} n_k \qquad (8\text{-}35)$$

Where,

ρ_m^s : the subcritical reactivity of the m[th] mode, which can be defined as:

$$\rho_m^s = 1 - 1/\lambda_m \qquad (8\text{-}36)$$

The subcritical reactivity ρ_m^s can be calculated using the formula derived by [March-Leuba and Blakeman, 1991]:

$$\rho_m^s = D\nabla B^2 / \nu\Sigma_f \qquad (8\text{-}37)$$

Where,

D: diffusion coefficient

Σ_f : fission cross section

ν : number of neutrons per fission

∇B^2 : the geometric buckling difference between the fundamental and m[th] mode

Let ρ_{mn} be the excitation reactivity of the m[th] mode, which is introduced by a net change in the n[th] mode reaction rate. It can be described as:

$$\rho_{mn} = < \phi_m^*, (\delta M - \delta L)\phi_n > / < \phi_m^*, M_o \phi_m > \qquad (8\text{-}38)$$

Λ_m : the neutron generation time of the m[th] mode, which can be described as:

$$\Lambda_m = < \phi_m^*, 1/V\phi_m > / < \phi_m^*, M_o\phi_m > \quad (8\text{-}39)$$

In Equation (8-34), the second and sixth terms on the right hand side are non-linear. In Equation (8-35), the fourth term on the right hand side is non-linear. In this analysis, the non-linear parts are neglected to obtain only linearized equations. Also, the fifth term on the right hand side of Equation (8-34) and the third term on the right hand side of Equation (8-35) are small. After neglecting these two small parts, the final linearized equations can be described as:

$$\frac{dn_m}{dt} = \frac{\rho_m^s - \beta}{\Lambda_m} n_m + \frac{\rho_{m0}}{\Lambda_m} + \sum_{i=1}^{6} \lambda_i c_{i,m} \quad (8\text{-}40)$$

$$\frac{dc_{i,m}}{dt} = \frac{\beta_i}{\Lambda_m} n_m - \lambda_i c_{i,m} \quad (8\text{-}41)$$

Applying Perturbation and Laplace transformations to the above equations, the so called zero-power transfer function of the mth harmonic mode can be derived:

$$\delta q''' = \Phi_m(s)\delta\rho_{m0} \quad (8\text{-}42)$$

$$\Phi_m(s) = q_o'''(s\Lambda_m - \rho_m^s + \sum_{i=1}^{6} \frac{\beta_i s}{s + \lambda_i})^{-1} \quad (8\text{-}43)$$

8.1.2.2 Omega modes expansion

For the ω modes expansion, the space functions $\phi_k(r, E)$ are chosen as the eigenvectors of the following equation:

$$(L^o - M^o)\phi_k(r) = \omega_k \phi_k(r) \quad (8\text{-}44)$$

The adjoint equations of ϕ_k can be described as:

$$(L^o - M^o)^T \phi_k^*(r) = \omega_k \phi_k^*(r) \quad (8\text{-}45)$$

And the ϕ_k function together with its adjoint eigenvector ϕ_k^* has the relation:

$$< \phi_m^*, 1/V(E)\phi_k >= 0 \text{, for } m \neq k \tag{8-46}$$

Using the same substitution and integration procedure described in the λ modes case, the modal point kinetics equation for the ω modes can be developed. Some more detailed ω modes expansion method can be found in [Karve, 1998].

The ω modes may be interpreted as the natural modes of the unperturbed reactor with no delayed neutrons while the λ modes are with delayed neutrons. Since the delayed neutrons are a small fraction of the total neutrons, there will be small differences between these two expansion methods for this out-of-phase stability analysis. In the out-of-phase stability analysis literature, the λ modes modal expansion is frequently applied, such as: [March-Leuba and Blakeman, 1991], [Munoz-Cobo, et. al., 1996, 2000, 2002], [Hashimoto, et. al., 1993, 1997], [Dokhane, et. al., 2003], etc. In fact, since in reactor physics calculations, the reactivity is always an interesting value, therefore it is natural to expand the modes by using the λ modes. The λ modes expansion method is used in this analysis.

8.1.3 Coupling of the thermal-hydraulic and neutronic models

During out-of-phase density wave oscillations, the flow rate and properties oscillations will induce oscillations at the core power through two paths for the neutronic feedbacks. First is the fuel temperature dynamics induced Doppler feedback. The second is the coolant density oscillation induced neutronic feedback in the SCWR case, or the voids feedback in the BWR case. The feedback loop can be described as shown in Fig. 8-8:

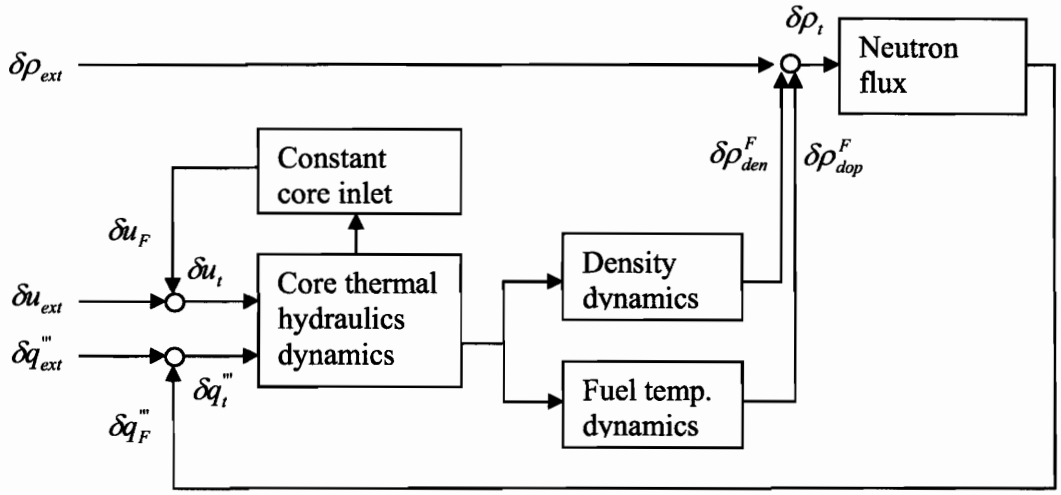

Fig. 8-8: Block diagram of the out-of-phase stability

If only the first subcritical harmonic mode was excited, using Fig. 8-8, the following relations can be obtained:

$$\delta q'''_t = \delta q'''_{ext} + \delta q'''_F \tag{8-47}$$

$$\delta q'''_F = \Phi_1(s)\delta\rho_t \tag{8-48}$$

Therefore,

$$\delta q'''_t - \Phi_1(s)\delta\rho_t = \delta q'''_{ext} \tag{8-49}$$

Also, the reactivity has the relation:

$$\delta\rho_t = \delta\rho_{ext} + \delta\rho_F \tag{8-50}$$

$$\delta\rho_F = \delta\rho^F_{den} + \delta\rho^F_{dop} \tag{8-51}$$

From Equation (8-38), the feedback reactivity can be described as:

$$\delta\rho^F_{mn} = < \phi^*_m, (\delta M - \delta L)\phi_n > / < \phi^*_m, M_o\phi_m > \tag{8-52}$$

If only the fundamental and first subcritical modes were interested, Equation (8-52) becomes:

$$\delta\rho_F = \delta\rho_{10}^F = <\phi_1^*, (\delta M - \delta L)\phi_0> / <\phi_1^*, M_o\phi_1> \tag{8-53}$$

It is worth noticing that the oscillation operator $(\delta M - \delta L)$ has an anti-symmetrical distribution similar to the first-harmonic neutronic mode during the out-of-phase oscillation. Imagining that the flow rate in one half of the core increases, the coolant density will increase and the fuel temperature will decrease in that half of the core, which will give a positive $(\delta M - \delta L)$ during the out-of-phase oscillation. Also, the first-harmonic neutronic mode has a positive sign in this half of the core. Therefore, the oscillation operator $(\delta M - \delta L)$ and the first-harmonic neutronic mode have the same sign in this half of the core, which will generate a positive reactivity feedback value from Equation (8-53). On the other hand, in the other half of the core, both the oscillation operator $(\delta M - \delta L)$ and the first-harmonic neutronic mode have negative signs, which also generate a positive reactivity feedback value from Equation (8-53). Adding up the feedback reactivity for the two halves of the core, the total feedback reactivity can be obtained.

For describing the feedback reactivity calculation procedure, the previously discussed model for half of the core simulated by an average channel was applied here. As mentioned before, the two channels were called channel 1 (left half of the core) and channel 2 (right half of the core). For channel 1, the reactivity feedback can be written as:

$$\delta\rho_{1,F} = \delta\rho_{1,den}^F + \delta\rho_{1,dop}^F = C_{1,den}\delta\widetilde{\rho}_{1,c} + C_{1,dop}\delta\widetilde{t}_{1,f} \tag{8-54}$$

For channel 2, the reactivity feedback can be written as:

$$\delta\rho_{2,F} = \delta\rho_{2,den}^F + \delta\rho_{2,dop}^F = C_{2,den}\delta\widetilde{\rho}_{2,c} + C_{2,dop}\delta\widetilde{t}_{2,f} \tag{8-55}$$

Taking the SCWR as symmetric, one can obtain: $\delta\widetilde{\rho}_{1,c} = -\delta\widetilde{\rho}_{2,c}$, $\delta\widetilde{t}_{1,f} = -\delta\widetilde{t}_{2,f}$. Also, we define:

$$C_{den} = C_{1,den} - C_{2,den} \tag{8-56}$$

$$C_{dop} = C_{1,dop} - C_{2,dop} \tag{8-57}$$

Recalling that $C_{1,den}$ and $C_{2,den}$, $C_{1,dop}$ and $C_{2,dop}$ have opposite signs, if we take $C_{1,den}$ and $C_{1,dop}$ as positive, the $C_{2,den}$ and $C_{2,dop}$ will be negative, which leads to positive C_{den} and C_{dop}. Therefore,

$$\delta\rho_F = \delta\rho_{1,F} + \delta\rho_{2,F} = C_{den}\delta\widetilde{\rho}_{1,c} + C_{dop}\delta\widetilde{t}_{1,f} \tag{8-58}$$

Where,

$\delta\widetilde{\rho}_{1,c}$: the average density oscillation in channel 1

$\delta\widetilde{t}_{1,f}$: the average fuel temperature in channel 1

To obtain the average density and fuel temperature oscillations in a channel, the oscillations in axial node i was weighted by a factor W_n and added up together axially. The weighting factor is usually taken in the form [Wulff et al., 1984]:

$$W_n = \frac{P_n^2}{\sum_{n=1}^{N} P_n^2} \tag{8-59}$$

Where,

P_n : the power at node n.

Therefore,

$$\delta\tilde{\rho}_{1,c} = \sum_{n=1}^{N} W_n \delta\rho_{1,c}^n \tag{8-60}$$

$$\delta\tilde{t}_{1,f} = \sum_{n=1}^{N} W_n \delta t_{1,f}^n \tag{8-61}$$

For the density and fuel temperature oscillation in the node *n*, one can express it to be the function of the inlet flow rate oscillation and power oscillation as:

$$\delta\rho_{1,c}^n = U_{1,den}^n \delta w_1 + Q_{1,den}^n \delta q_1''' \tag{8-62}$$

$$\delta t_{1,f}^n = U_{1,f}^n \delta w_1 + Q_{1,f}^n \delta q_1''' \tag{8-63}$$

Plugging the above equations (8-62) and (8-63) into the equations (8-60) and (8-61), one obtains:

$$\delta\tilde{\rho}_{1,c} = \delta w_1 \sum_{n=1}^{N} W_n U_{1,den}^n + \delta q_1''' \sum_{n=1}^{N} W_n Q_{1,den}^n = U_{1,den} \delta w_1 + Q_{1,den} \delta q_1''' \tag{8-64}$$

$$\delta\tilde{t}_{1,f} = \delta w_1 \sum_{n=1}^{N} W_n U_{1,f}^n + \delta q_1''' \sum_{n=1}^{N} W_n Q_{1,f}^n = U_{1,f} \delta w_1 + Q_{1,f} \delta q_1''' \tag{8-65}$$

Substituting the above two equations into Equation (8-58), one can obtain:

$$\begin{aligned} \delta\rho_F &= C_{den}\delta\tilde{\rho}_{1,c} + C_{dop}\delta\tilde{t}_{1,f} \\ &= (C_{den}U_{1,den} + C_{dop}U_{1,f})\delta w_1 + (C_{den}Q_{1,den} + C_{dop}Q_{1,f})\delta q_1''' \end{aligned} \tag{8-66}$$

Substituting the above Equation (8-66) into Equation (8-50), one obtains:

$$\delta\rho_t - C_{den}(U_{1,den} + U_{1,f})\delta w_1 - C_{dop}(Q_{1,den} + Q_{1,f})\delta q_o''' = \delta\rho_{ext} \tag{8-67}$$

8.1.4 Characteristic equation for coupled neutronics out-of-phase stability

To obtain the characteristic equation for the coupled neutronics out-of-phase oscillation, the one channel model (half of the core) was applied again. For the more detailed lumping, the same procedure can be used except the more complicated properties combinations.

In section 8.1.1, the characteristic equation that governing the thermal hydraulics dynamics was derived as equation (8-11), for recalling, this equation is listed here:

$$\Gamma_t \delta w_1 + \pi_t \delta q_o''' = \frac{\Gamma_1 + \Gamma_2}{\Gamma_2} \delta w_1 + \frac{\pi_1 + \pi_2}{\Gamma_2} \delta q_o''' = \frac{1}{\Gamma_2} (\Gamma_1 \delta w_{1,ext} + \pi_1 \delta q_{ext}''') \tag{8-11}$$

In section 8.1.2, the neutronic dynamics model was constructed and the transfer function from the reactivity oscillation to power oscillation was derived as Equations (8-42) and (8-43). Therefore, we come up with the power and reactivity relation as Equation (8-68):

$$\delta q_t''' - \Phi_1(s) \delta \rho_t = \delta q_{ext}''' \tag{8-68}$$

Noting that $\delta q_t''' = \delta q_o'''$ and for a nuclear reactor system $\delta q_{ext}''' = 0$.

In Section 8.1.3, the thermal hydraulics and neutronics model are coupled, the coupling equation of (8-67) was derived.

$$\delta \rho_t - (C_{den} U_{1,den} + C_{dop} U_{1,f}) \delta w_1 - (C_{den} Q_{1,den} + C_{dop} Q_{1,f}) \delta q_1''' = \delta \rho_{ext} \tag{8-67}$$

The above stability governing Equations (8-11), (8-67) and (8-68) can be written in matrix form as:

$$A(s)\delta x_t = B(s)\delta x_{ext} \tag{8-69}$$

Where,

$$\delta x_t = (\delta w_1, \delta q_o''', \delta \rho_t) \tag{8-70}$$

$$\delta x_{ext} = (\delta w_{1,ext}, \delta q_{ext}''', \delta \rho_{ext}) \tag{8-71}$$

$$A(s) = \begin{bmatrix} \Gamma_t & \pi_t & 0 \\ 0 & 1 & -\phi_1(s) \\ -(C_{den}U_{1,den} + C_{dop}U_{1,f}) & -(C_{den}Q_{1,den} + C_{dop}Q_{1,f}) & 1 \end{bmatrix}, \text{ and} \tag{8-72}$$

$$B(s) = \begin{bmatrix} \Gamma_1/\Gamma_2 & \pi_1/\Gamma_2 & 0 \\ 0 & 1 & 0 \\ 0 & 0 & 1 \end{bmatrix} \tag{8-73}$$

Therefore, the characteristic equation for the out-of-phase stability of a SCWR system can be derived from,

$$\det[A(s)] = 0 \tag{8-74}$$

Thus, the characteristic equation is:

$$\Gamma_t[1 - \phi_1(s)\,(C_{den}Q_{1,den} + C_{dop}Q_{1,f})] + \pi_t\,(C_{den}U_{1,den} + C_{dop}U_{1,f}) = 0 \tag{8-75}$$

For more detailed lumping, say two channels or three channels (half of the core), the characteristic equations similar to Equation (8-75) can be derived.

8.2 SCWR out-of-phase stability analysis and comparison with BWR

An out-of-phase stability analysis for the U.S. reference SCWR design is conducted in this section. First, the analysis without water rods heating is presented, and then with water rods heating case will be addressed in the next section. For comparison, the typical BWR out-of-phase stability was also analyzed.

To represent the SCWR core flow and power by a few channels, the detailed flow and power distributions should be obtained. By using 3-D thermal-neutronic coupled calculation, Yamaji et al (2003) provided the power and flow distributions for Japan SCWR design. In their analysis, the coolant flow rate distribution is matched to the radial power distribution through adjusting the inlet orifice in their design. Therefore, the enthalpy rise for the assemblies is about the same through the core. Four orifices were applied for a specific assembly. Since the core and assembly designs of the U.S. reference SCWR design were similar to the Japanese design, also the power densities were also pretty close for these two designs (69.4 kW/l for U.S. reference SCWR design and 61.5 kW/l for Japanese design). The core power and flow distributions of the U.S. reference SCWR design were assumed in our work to be the same as Japan design. The detailed power and flow distributions can be found in [Yamaji et al, 2003]. The U.S. reference SCWR core design was lumped into one average channel, two channels and three channels for each half of the core based on the radial power distribution.

Since every assembly has its own individual inlet orifice, the equivalent inlet orifice coefficients for the lumped channels will be different due to different lumping. The equivalent inlet orifice coefficient was calculated for every lumped channel based on the following conditions:

(1). The same enthalpy rise and pressure drop across every channel.
(2). The hot assembly has an inlet orifice coefficient of 20.0

The U.S. reference SCWR design can be lumped into three channels based on above mentioned methodology. The detailed lumping parameters are listed in the following Table 8-1:

Table 8-1: Parameters of the three lumped channel model for SCWR (half of the core)

Lumped channel number	Power range (Relative to average channel)	Assembly number (half core)	Power (MW)	Flow rate (kg/s)	Equivalent inlet orifice coefficient
1	Above 1.2	7	221.6	114.25	22.7
2	0.9~1.19	45.5	1176.5	606.5	93.0
3	Below 0.9	20	398.0	205.15	241.1

The typical BWR was lumped into three channels also, and the lumped parameters can be found in Table 8-2.

Table 8-2: Parameters of the three channel model for a typical BWR (half of the core)

Lumped channel	Power (relative to core average)	Assembly Number (half core)	Flow rate per assembly (kg/s)	Kin
1	1.3	30	16.1	31.1
2	1.037	306	16.76	31.1
3	0.565	46	8.89	205.0

In the following, a reactivity sensitivity study is conducted for both the SCWR and BWR. Then, the effect of different core thermal hydraulic lumping model is studied for the SCWR and compared with the BWR. Finally, the power and flow sensitivities were compared for the SCWR and BWR.

8.2.1 Reactivity sensitivity analysis for both the SCWR and the BWR

Yang and Zavaljevski (2003) calculated the feedback coefficients for U.S. reference SCWR design. At steady state full power conditions, they obtained the Doppler coefficient as $-1.4\times10^{-5}/^{o}K$ for the average fuel temperature, and the coolant density

coefficient as $1.0\times10^{-5}/(kg/m^3)$. In Table 8-3, the coefficients of a typical BWR were compared with those of the SCWR.

Table 8-3: Reactivity coefficients comparison between BWR and SCWR

Reactor	Doppler coefficient	Density/void coefficient
BWR	-2.3e-5($\frac{\Delta k}{k}/^oC$)	-0.124 $\frac{\Delta k}{k}$ For a HEM, the void coefficient can be translated to average density coefficient by using: $\Delta\alpha = -\Delta\rho/\rho_{fg}$ =1.77e-4[$\frac{\Delta k}{k}/(kg/m^3)$]
SCWR	-1.4e-5($\frac{\Delta k}{k}/^oC$)	1.0e-5[$\frac{\Delta k}{k}/(kg/m^3)$]

From Table 8-3, it is seen that the Doppler coefficient of the SCWR is comparable to that of the BWR. The slightly smaller value is due to the higher SCWR fuel enrichment. However, the SCWR density coefficient is quite small compared with the typical BWR, because most of the moderation power is provided by the water rods. It was assumed that no water rods heating is present, therefore the water density is constant and no neutronic feedback is provided by the water rods. The water rods heating effects will be addressed in Section 8.3.

The Doppler feedback effect in the BWR stability is usually small compared with the void coefficient effect. Lahey (1993) ignored the Doppler feedback during the coupled neutronic stability analysis. In this analysis, a constant Doppler feedback coefficient is applied for both the SCWR and BWR.

From Table 8-3, it is seen that the coolant density coefficient of the SCWR is very small, only about 5% of that for a typical BWR. Therefore, the density coefficient effect is also small for the SCWR. The sensitivity analysis was conducted by multiplying a factor F to the steady state value for both the SCWR and the BWR, and keeping the constant

Doppler feedback coefficient. The decay ratios for the three lumped channels model were calculated and plotted in Figure 8-9.

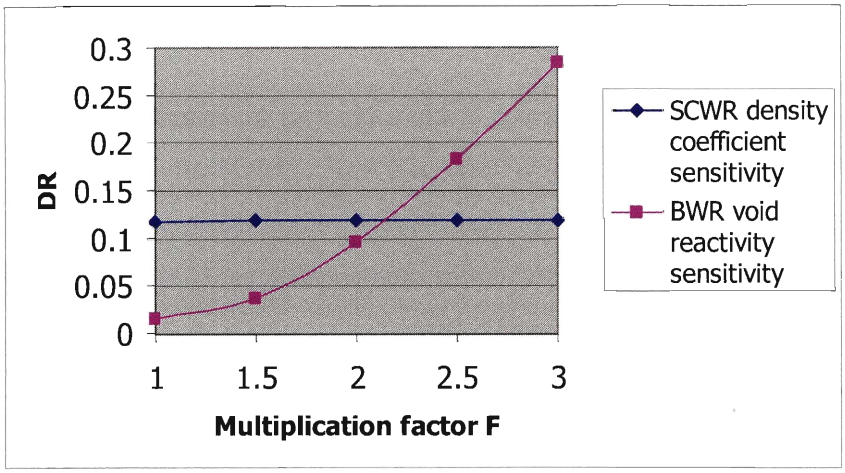

Fig. 8-9: SCWR and BWR reactivity coefficient sensitivity

From Fig. 8-9, it is seen that the SCWR was not sensitive to the density coefficient. Therefore, the neutronic coupling during out-of-phase oscillation is very weak for the SCWR. It is worth noting that even after multiplying by a Factor of 3 in above Fig. 8-9, the density coefficient of the SCWR is $3.0e-5\frac{\Delta k}{k}/kg/m^3$, which is still much lower than the BWR steady state value $1.77e-4\frac{\Delta k}{k}/kg/m^3$. Therefore, the U.S. reference SCWR design out-of-phase oscillation is dominated by the thermal hydraulic characteristics. Besides the low level of the density reactivity coefficient for the SCWR, the subcriticality of the first subcritical dynamics mode is about $\rho^s_{1,SCWR}=-1.72\$$, while a typical BWR is about $\rho^s_{1,BWR}=-1.18\$$. Therefore, the SCWR has a much larger subcriticality and the first subcritical neutronic dynamic mode will decay much faster during the oscillation than the BWR. Thus, the neutronic coupling of the SCWR during the out-of-phase oscillation is very weak compared with the typical BWR.

In fact, even with the water rods heating, only about 10% of the total fission energy is transferred into water rods from previous single channel stability analysis. Therefore, the

density change in the water rods is not significant. We simulated the water rods flow as constant density "heavy fluid region" model in the single channel stability analysis. Therefore, the neutronic feedback in the case of with water rods heating will be also weak compared with the typical BWR.

From the above reactivity sensitivity discussion, it is reasonable to take a constant Doppler coefficient for both the SCWR and BWR. For the density coefficient, a constant value was assumed for the SCWR. It will be not a good assumption to take a constant value for the BWR since it is sensitive to the void coefficient. Therefore, a quadratic form described as follows was taken for the BWR.

$$C_v = C_1 + C_2\overline{\alpha} + C_3\overline{\alpha}^2 \tag{8-76}$$

Where $\overline{\alpha}$ is the core average void fraction.

It is difficult to find the appropriate factors for C_1, C_2, C_3 in the above formula for this typical reactor. However, the value for Ringhals NPP can be found as: $C_1 = -0.143, C_2 = 0.12005, C_3 = -0.1755$ in (Munoz-Cobo, 2002), and the Ringhals NPP has a similar core size as the typical BWR mentioned in this analysis.

Table 8-4: Core size comparison of the typical BWR and the Rignghals NPP

	Core size	Assembly number
Ringhals	4.39m (diameter) 3.65m (height)	648 (8x8 type)
Typical BWR	4.75m (diameter) 3.66m (height)	764 (188 8x8 type, 576 7x7 type)

Also, the fuel enrichments of these two power plants are similar. Therefore, the factors C_1, C_2, C_3 for this typical reactor was taken as that of the Ringhals NPP.

The core average void fraction is calculated by the formula:

$$\overline{\alpha} = \frac{\rho_f - \overline{\rho}_m}{\rho_{fg}} \tag{8-77}$$

Where,

$\overline{\rho}_m$: the core average water density

8.2.2 Core lumping sensitivity analysis for both SCWR and BWR

The core thermal hydraulic lumping effect on the stability was analyzed for both the SCWR and BWR.

8.2.2.1 SCWR lumping effect

For analyzing the core lumping effect on stability, the SCWR was modeled by one channel, two channels and three channels. The previously described lumping methodology was applied also. The detailed lumping parameters can be found in Table 8-5, as:

Table 8-5: Parameters of various channels for modeling the SCWR (half of the core)

Number of channels		Power range (Relative to average channel)	Assembly number (half core)	Power (MW)	Flow rate (kg/s)	Equivalent inlet orifice coefficient
One lumped channel		1.0	72.5	1787.5	921.5	115.0
Two lumped channels	1	Above 1.0	40.5	1110.0	572.0	70.0
	2	Below 1.0	32	677.5	349.5	198.0
Three lumped channels	1	Above 1.2	7	221.6	114.25	22.7
	2	0.9~1.19	45.5	1176.5	606.5	93.0
	3	Below 0.9	20	398.0	205.15	241.1

Based on the above lumping, the three lumping models described in the Table 8-5 were compared by the decay ratios calculated at different RPV inlet temperatures around the full power operating temperature 280°C, while keeping the other parameters at steady state. The results can be found in the following Fig. 8-10:

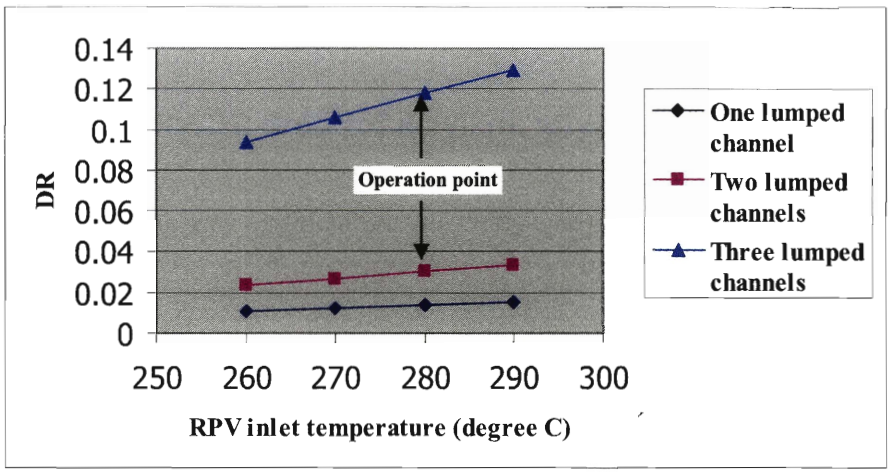

Fig. 8-10: the SCWR out-of-phase stability for different lumping

From Fig. 8-10, it is seen that the out-of-phase stability is sensitive to the approach to core lumping. From Table 8-5, the equivalent inlet orifice coefficient for the hottest group of the different lumping decreases, say 115.0 for one lumped channel, 70.0 for two lumped channels and 22.7 for three lumped channels. The phenomenon of decay ratio increase as the lumped channel number increase could be explained, if the SCWR out-of-phase stability is dominated by the hottest channel group.

To check if the hottest group dominates stability, the hottest channel group, for which the relative power is above 1.20 in Table 8-5, was kept for different lumping. And the remaining of the core was lumped into one channel and two channels as described by Table 8-6.

Table 8-6: Parameters of lumped channels for SCWR (half of the core) with the same hottest group

Channel		Power range (Relative to average channel)	Assembly number (half core)	Power(MW)	Flow rate (kg/s)	Inlet orifice coefficient
Two lumped channels	1	Above 1.2	7	221.6	114.25	22.7
	2	Below 1.2	65.5	1574.5	811.65	126.6
Three lumped channels	1	Above 1.2	7	221.6	114.25	22.7
	2	0.9~1.19	45.5	1176.5	606.5	93.0
	3	Below 0.9	20	398.0	205.15	241.1

Again, the two lumping models were compared by the decay ratios calculation. The results can be found in the following Fig. 8-11:

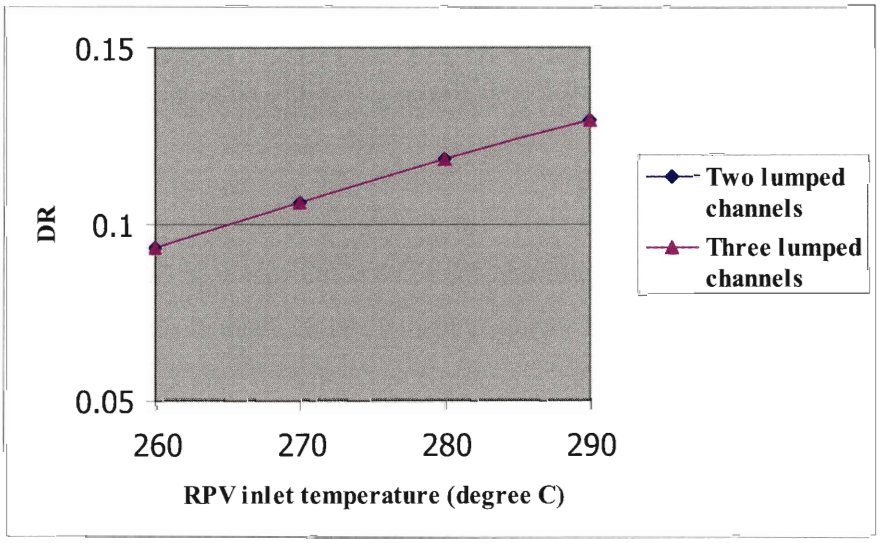

Fig. 8-11: SCWR out-of-phase stability for the different lumping at the same hottest group

Therefore, once the hottest group was separated, the SCWR out-of-phase stability would not be sensitive to the lumping of the remaining assemblies.

Using the three lumped channels model, the SCWR out-of-phase stability boundary map was constructed in the Fig. 8-12, as follows:

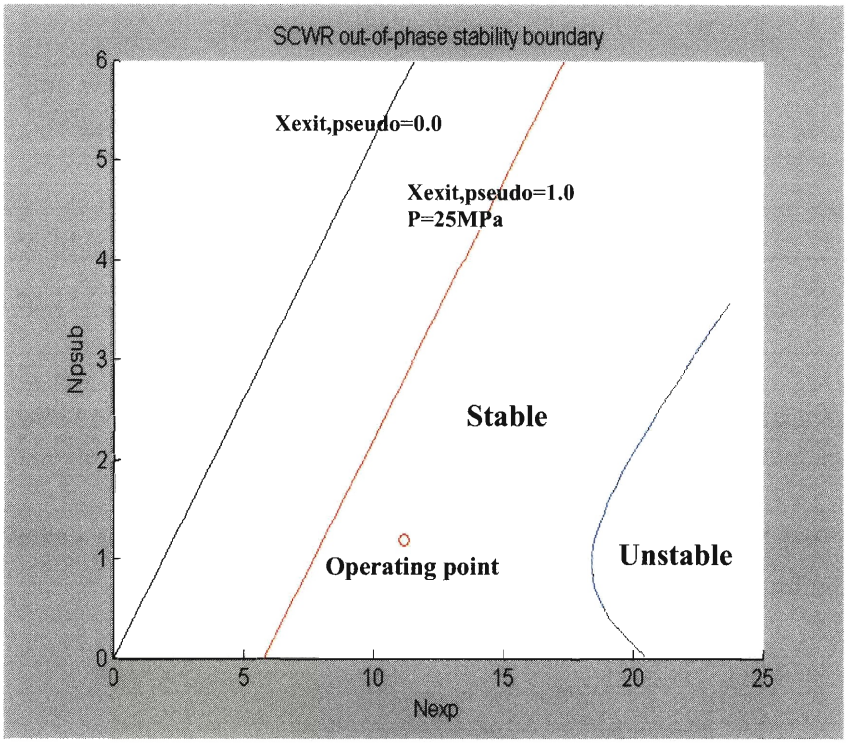

Fig. 8-12: SCWR out-of-phase stability boundary

8.2.2.2 BWR core lumping effect

From the above analysis, it is found that the SCWR out-of-phase stability is sensitive to different core representation approaches, and the hottest channel dominates the stability limits. For a typical BWR, as described in the Chapter 7, the core is divided into a peripheral region and a central region. The assemblies in the central region have the same inlet orifice coefficient with a value about 31.1 and the assemblies in the peripheral region have an inlet orifice coefficient with a value about 205.0.

Therefore, a typical BWR core was represented here by two channels according to the two zones. One channel stands for the peripheral region and the other one for the central region. To check if the hottest group also dominates the BWR out-of-phase stability, the hottest channel group is separated from the central region to generate a three channels model. The parameters for the three channels for this model of a typical BWR are listed in the Table 8-7.

Table 8-7: Parameters of the lumped channels for a typical BWR (half of the core)

Channel		Power (relative to core average)	Assembly Number (half core)	Flow rate per assembly (kg/s)	Kin
Two lumped channels	Central region (channel 1)	1.06	336	16.7	31.1
	Peripheral region (channel 2)	0.565	46	8.89	205.0
Three lumped channels	Hottest group (channel 1)	1.3	30	16.1	31.1
	Central region remaining (channel 2)	1.037	306	16.76	31.1
	Peripheral region (channel 3)	0.565	46	8.89	205.0

Just like the SCWR case, the two models are compared by the decay ratios calculated at different RPV inlet temperatures while keeping the other parameters at steady state. The results can be found in Fig. 8-13:

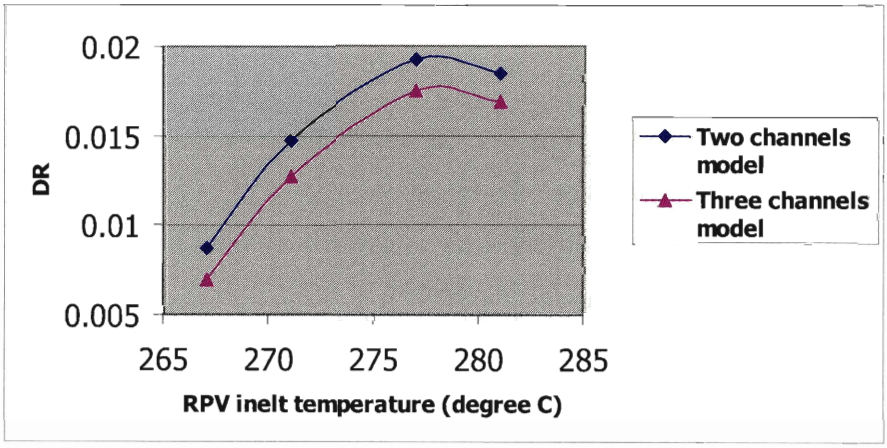

Fig. 8-13: BWR out-of-phase stability for different lumping

From Fig. 8-13, it can be seen that the BWR out-of-phase stability is not so sensitive as the SCWR cases shown in Fig. 8-10. By using the TRAC/BF1 code, Akitoshi Hotta, et al

(2001) analyzed the lumping effect on the BWR out-of-phase stability. They also found the stability is not sensitive to the lumped channel numbers.

8.2.2.3 Summary of the core thermal hydraulic lumping effect

From the preceding analysis of the core thermal hydraulic lumping, it was found that:

1. The SCWR out-of-phase stability is sensitive to different core thermal hydraulic lumping. The stability feature is dominated by hottest channel (channel group).

2. The BWR out-of-phase stability is not sensitive to different core thermal hydraulic lumping.

As mentioned previously, the neutronic feedback is very weak for the SCWR during out-of-phase oscillation. Additionally, the oscillation of the first neutronic subcritical mode will decay very fast due to its high subcriticality. Therefore, the SCWR out-of-phase oscillation is dominated by the thermal hydraulic features. The different core lumping will change the thermal hydraulic feature significantly through the equivalent inlet orifice coefficients changing.

For the BWR, it can be seen from Fig. 8-9, the out-of-phase oscillation is sensitive to the reactivity feedback coefficient. Since the neutronic feedback is controlled by the whole core average properties, and the different core thermal hydraulic lumping approach will not change the core average properties, the BWR out-of-phase stability is not sensitive to the different lumping. Moreover, since the BWR only applies two inlet orifice zones, unlike the SCWR case, the BWR different core lumping will not change the inlet orifice coefficients of the different lumped channels.

8.2.3 SCWR power and flow rate sensitivity analysis and comparison with BWR

Just like the sensitivity analysis conducted for the single channel stability analysis, the power and flow sensitivities are also analyzed for SCWR and BWR out-of-phase stability. The previously discussed three lumped channels model are used for both the SCWR and the BWR.

Again, the nominal operating conditions were taken as the reference for both the SCWR and the BWR during the analysis. The mass flow sensitivity was addressed by changing the mass flow rate, while keeping the power and the pressure at reference conditions. And the power sensitivity was addressed by changing the system power, while keeping the mass flow rate and the system pressure at reference conditions. The results are illustrated in Fig. 8-14 and 8-15.

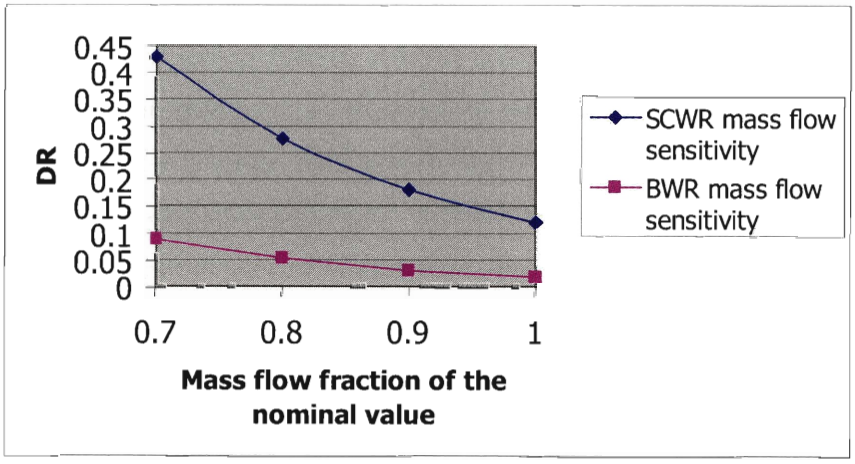

Fig. 8-14: Mass flow rate sensitivity for out-of-phase stability

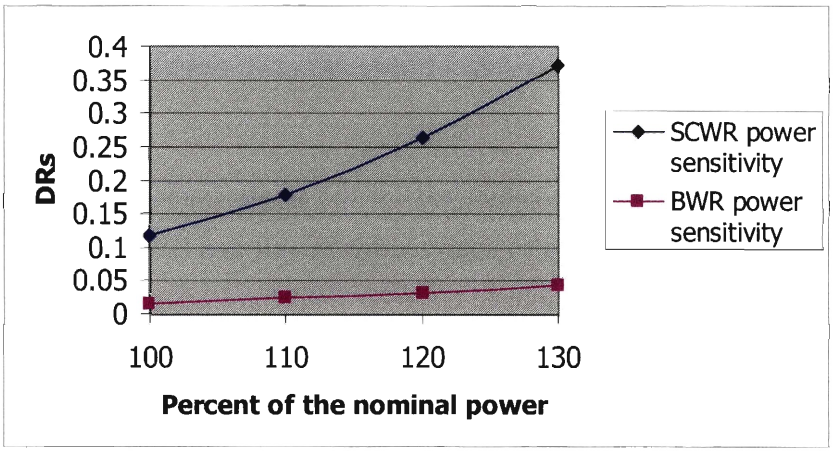

Fig. 8-15: Power sensitivity for out-of-phase stability

The same as the single channel stability, from Fig. 8-15, it can be seen that the SCWR is much more sensitive to the power and flow rate than the BWR.

8.3 Water rods effects on SCWR out-of-phase stability

As mentioned previously, for the U.S. reference SCWR design, about 90% of the RPV inlet water is delivered into the water rods and flows downward into the low plenum to mix with the other 10% of the RPV inlet flow which comes from the downcomer. The water rods heating effect was investigated by comparing with and without heating cases. The water rods flow sensitivity was also analyzed by varying the water rods flow rate.

8.3.1 Water rods heating effect

With the water rods heating, the $Q_w \neq 0$ in above Fig. 8-1, the temperature in the lower plenum will be above the RPV inlet temperature since part of the heat was transferred into water rods to increase the water temperature. The same as the single channel stability analysis, to simulate the water states in both the water rods and the upward coolant flow by using the three region model, the temperatures should be calculated in the upward coolant flow inlet (lower plenum) and the water rods outlet temperatures for different lumped channels.

The upward coolant inlet temperature had been calculated in section 6.2.1 during the water rods effect for single channel stability, the results can be found in Table 6-2. Since the water rods flow and the downcomer flow mix in the lower plenum, the upward flow should have the same inlet temperature for different lumped channels for the perfect mixing assumption.

The water rods outlet flow temperatures should be different for different lumped channels since the flow velocity and the power are different. The steady state temperatures values for upward flow inlet and water rods outlet for different lumped channels are calculated and listed in Table 8-8. The previously described three lumped channels model is applied here.

Table 8-8: Temperatures for the upward flow inlet and the water rods outlet

RPV inlet (°C)		260	270	280	290
Water rods outlet (°C)	1	328.8	333.7	339.1	344.4
	2	326.4	331.3	336.7	342
	3	323.1	328	333.4	338.7
Coolant inlet (°C)		320.7	326.3	331.9	337.7

From Table 8-8, it is seen that the water rods outlet temperatures are below 350 °C for all of the three lumped channels at the RPV inlet temperatures around 280 °C, the nominal value of the U.S. reference SCWR design. Therefore, the same as in the single channel stability, the water rods flow is in the first region of the three region model.

During an out-of-phase oscillation, the water rods outlet enthalpy oscillations have about the same amplitude but with the opposite sign for the two halves of the core. After mixing in the lower plenum, the enthalpy oscillations from the two half of the core will be canceled, a constant enthalpy can be assumed for the lower plenum (upward flow inlet) during this analysis. Like the single channel stability analysis, the heat flux fluctuation of the water rods wall is neglected.

The decay ratios and frequencies of the SCWR out-of-phase oscillation were calculated based on the conditions described in Table 8-9 and plotted in the following Fig. 8-16 and 8-17:

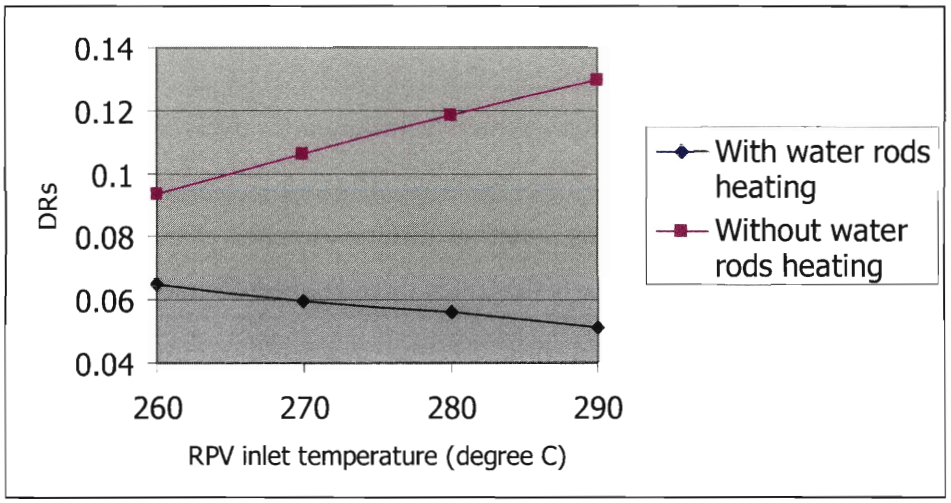

Fig. 8-16: Water rods effects on decay ratios of the SCWR out-of-phase stability

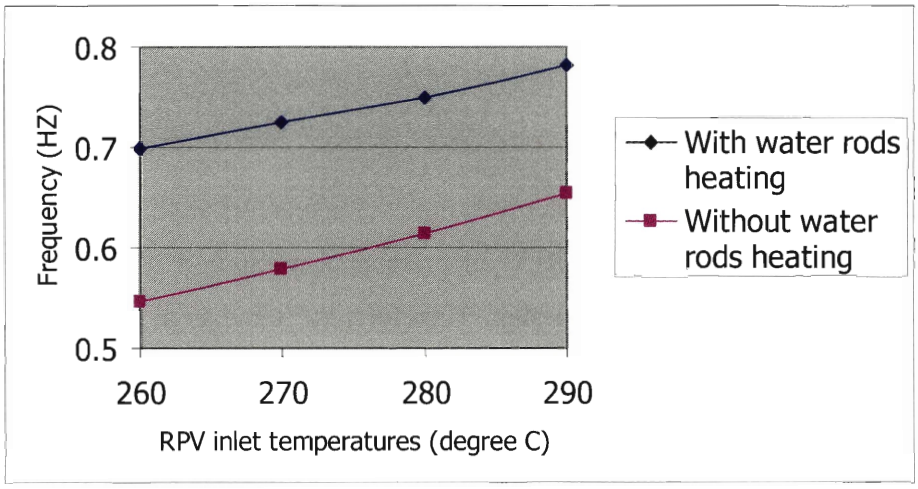

Fig. 8-17: Water rods effects on frequencies of the SCWR out-of-phase stability

From Fig. 8-16, it is seen that the water rods heating will stabilize the SCWR out-of-phase stability mode, the same as the single channel stability mode discussed in the chapter 6.

From Fig. 8-17, with water rods heating will increase the out-of-phase oscillation frequencies, since the upward inlet temperatures are increased.

The same reasons for explanation of the water rods heating effect on the single channel stability could be used to explain out-of-phase stability. The explanation can be found in Chapter 6.

8.3.2 Water rods flow rate sensitivity analysis

Just like in the single channel analysis, the water rods flow rate effect on out-of-phase stability was studied by varying the water rods flow rate to be 60%, 70%, 80% and 90% of the total flow. The three lumped channel model was applied again. The core inlet and water rods outlet temperatures for different cases are listed in the Table 8-9.

Table 8-9: Temperatures for the upward flow inlet and the water rods outlet at different water rods flow fractions

Water rods flow fraction	RPV inlet temp. (°C)	Upward flow inlet temp. (°C)	Water rods outlet temp. (°C)		
			Chan. 1	Chan. 2	Chan. 3
60%	280	319.0	344.0	342.0	339.1
70%	280	323.4	342.3	340.1	337.0
80%	280	327.4	340.7	338.3	335.1
90%	280	331.9	339.1	336.7	333.4

The decay ratios and the frequencies for the different water rods flow rate listed in Table 8-9 are plotted in Fig. 8-18 and 8-19.

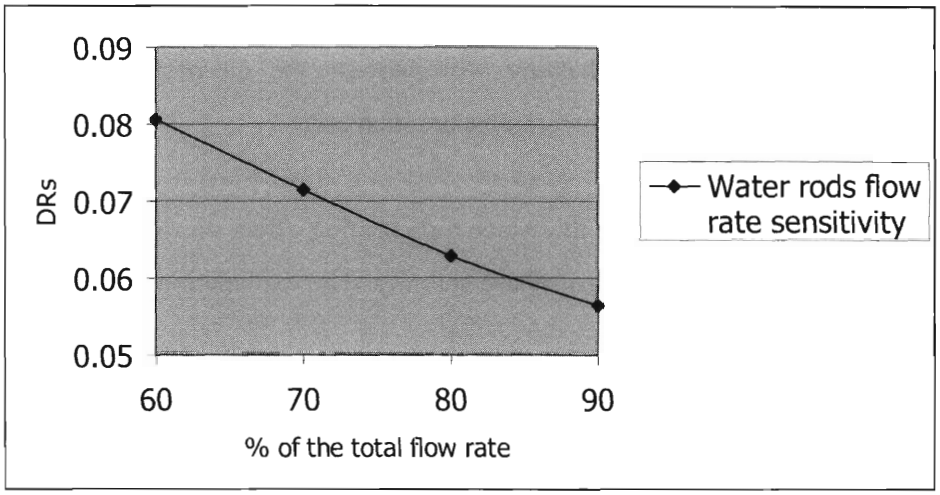

Fig. 8-18: The water rods flow effect on decay ratios of the out-of-phase stability

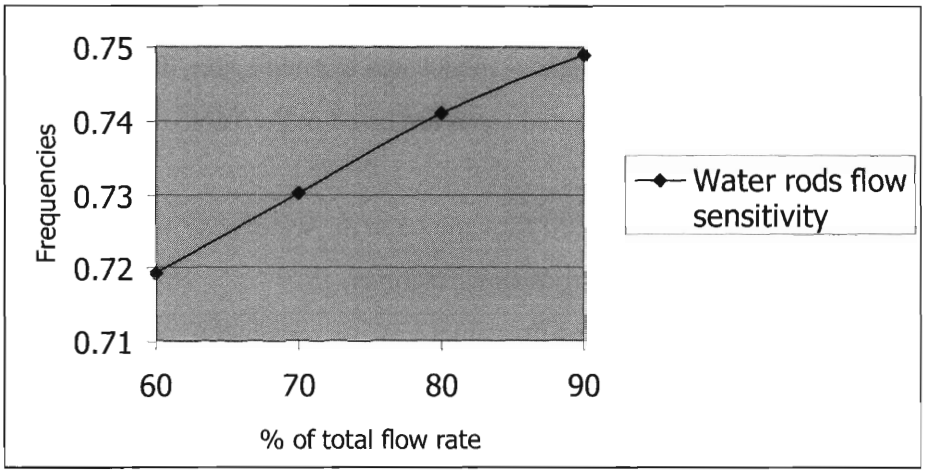

Fig. 8-19: The water rods flow effect on frequencies of the out-of-phase stability

From Fig. 8-18 and 8-19, it is seen that the water rods flow fraction has the same effect on out-of-phase stability as the single channel stability. Larger water rods flow has a stabilization effect. And the larger water rods flow will increase the out-of-phase frequency through increasing the upward flow inlet temperature.

8.3.3 Power and flow sensitivity with water rods heating

In this section, the power and flow sensitivity analysis is conducted for the SCWR out-of-phase stability with water rods heating. The upward flow inlet and water rods outlet temperatures at different power levels are listed in Table 8-10.

Table 8-10: Power sensitivity with water rods heating

Power (% nominal)		100	110	120
Water rods outlet temp. (°C)	Channel 1	339.1	342.5	347.2
	Channel 2	336.7	339.6	342.7
	Channel 3	333.4	334.8	338.7
Upward flow inlet temp. (°C)		331.9	334.4	338.0

The decay ratios sensitivity against power for both with water rods heating and without water rods heating was plotted in Fig. 8-20.

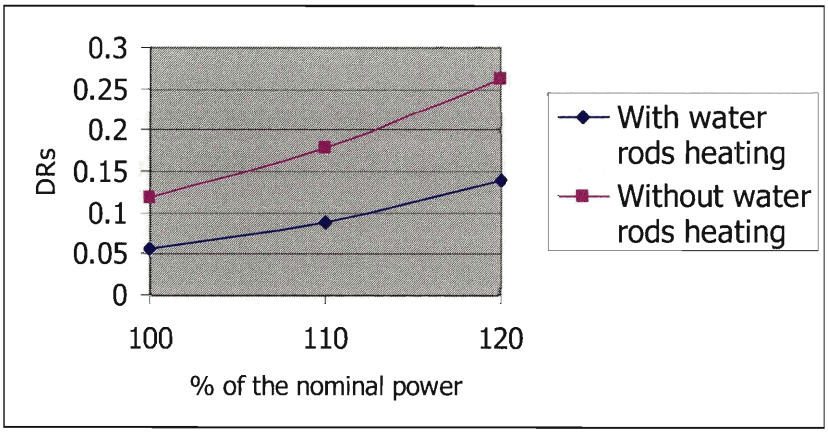

Fig. 8-20: SCWR power sensitivity for out-of-phase stability with water rods heating

The flow rate sensitivity was also analyzed and the upward flow inlet and water rods outlet temperatures are listed in the following Table 8-12.

Table 8-12: Flow rate sensitivity with water rods heating

Flow rate (fraction of the nominal)		0.8	0.9	1
Water rods outlet temp. (°C)	Channel 1	352.2	343.4	339.1
	Channel 2	347.4	340.3	336.7
	Channel 3	342.9	336.7	333.4
Upward flow inlet temp. (°C)		342.3	335.6	331.9

The decay ratios sensitivity against flow rate was plotted in the following Fig. 8-21 for both with and without water rods heating.

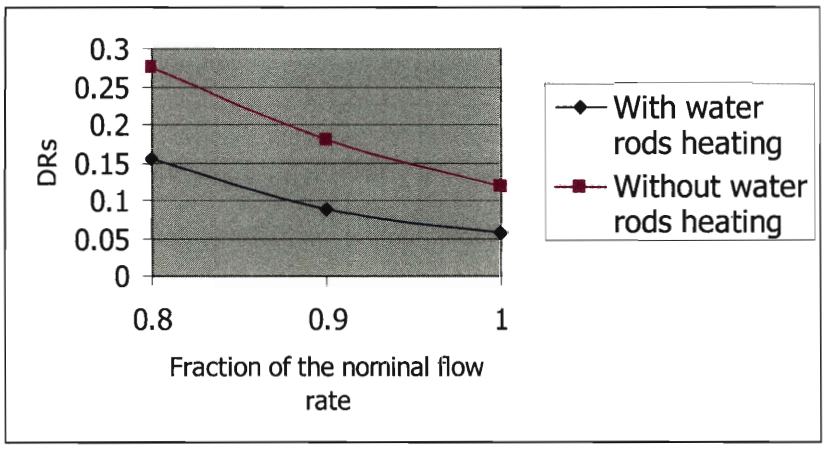

Fig. 8-21: SCWR flow rate sensitivity for out-of-phase stability with water rods heating

From above Fig. 8-20 and 8-21, it is seen that with the water rods heating, although the system is more stable, the sensitivity feature can not be improved significantly for both power and flow rate.

Chapter 9

Coupled neutronic core wide (in-phase) stability analysis

In this chapter, the coupled neutronic core wide in-phase stability will be analyzed for the SCWR and compared with the BWR. Just as the procedure applied in the single channel and out-of-phase stability analysis, the case for the SCWR without water rods heating will be addressed first, the case with the water rods heating effect will be discussed after that.

During the core in-phase oscillation, the whole core oscillates in the same phase and the fundamental mode of neutronic dynamics is excited. Unlike the single channel oscillation mode which is restricted by a constant pressure drop across the single oscillation channel, the core pressure drop during the core wide in-phase oscillation will fluctuate, and the magnitude is constrained by the out-of-core components. Also, unlike the region wide out-of-phase oscillation which adjusts the flow between two halves of the core to maintain an almost constant total inlet flow rate, the core inlet flow rate will oscillate during the in phase oscillation, and the feedback of the inlet flow rate is conducted by the flow dynamics in the out-of-core components. Both the single channel and the out-of-phase stability modes deal with the parallel channel system. For a BWR or SCWR system, every assembly can be taken as an isolated channel. Therefore, all of the assemblies in the reactor core are constituents of a parallel channel system. The in-phase stability mode

affects all of the components in the flow path. The reactor core is just one of the components in the flow path.

For a typical BWR system, the two phase mixture exits from the reactor core and flows through the upper plenum and riser, then the steam is separated from the two phase mixture in the steam separator and dryer region. The separated saturated water mixes with the feedwater and flows down through the downcomer. After flowing through the jet pumps and recirculation loops, the water finally is collected in the lower plenum and flows up through the core to finish the closed flow loop. The boundary condition of this closed loop is the total of pressure drops for all the components in the flow path is zero. A constant feedwater flow rate can be assumed, since the feedwater flow rate is not affected by the loop fluctuation and is a small fraction of the total flow (about 13% at the steady state). A typical BWR reactor flow path is illustrated in Fig. 9-1.

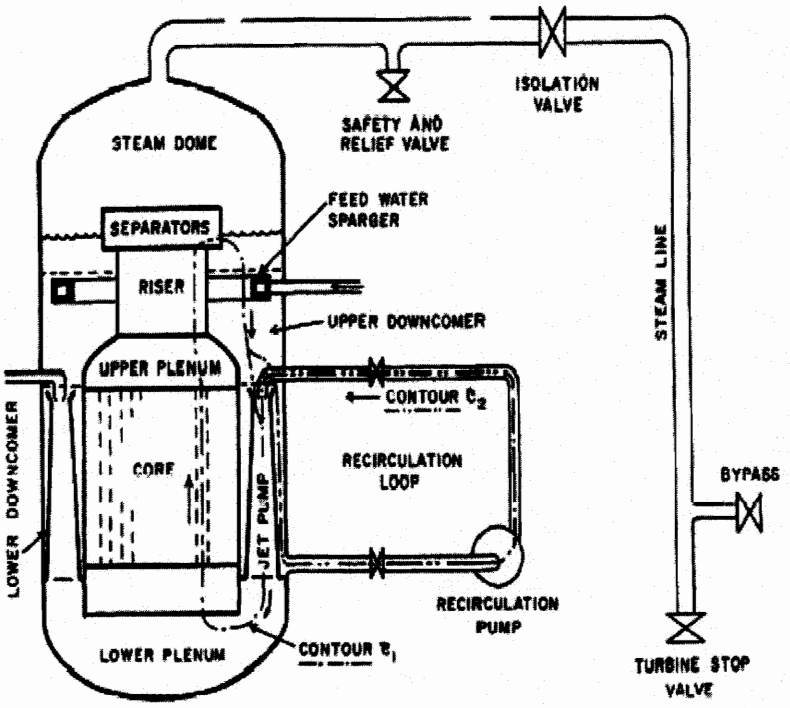

Fig. 9-1: BWR coolant flow path illustration (Hanggi, 2001)

The U.S. reference SCWR design is a once through cycle. After having heated through the core, the high temperature (500°C) and low density (90kg/m^3) supercritical water

flows directly into the turbine through the turbine control valve. Between the turbine control valve and the feedwater pump, the components such as the turbine, condenser and heaters, are very complicated, the oscillation energy will be dumped away through the friction very quickly. Both the feedwater pump and the turbine control valve are good oscillation dampers. Therefore, it was assumed that no flow oscillation occur in the components which are not located between the feedwater pump and the turbine control valve. Thus, a constant pressure drop boundary can be imposed on the components between the turbine valve and the feedwater pump. The flow path of the U.S. reference SCWR design is illustrated in Fig. 9-2.

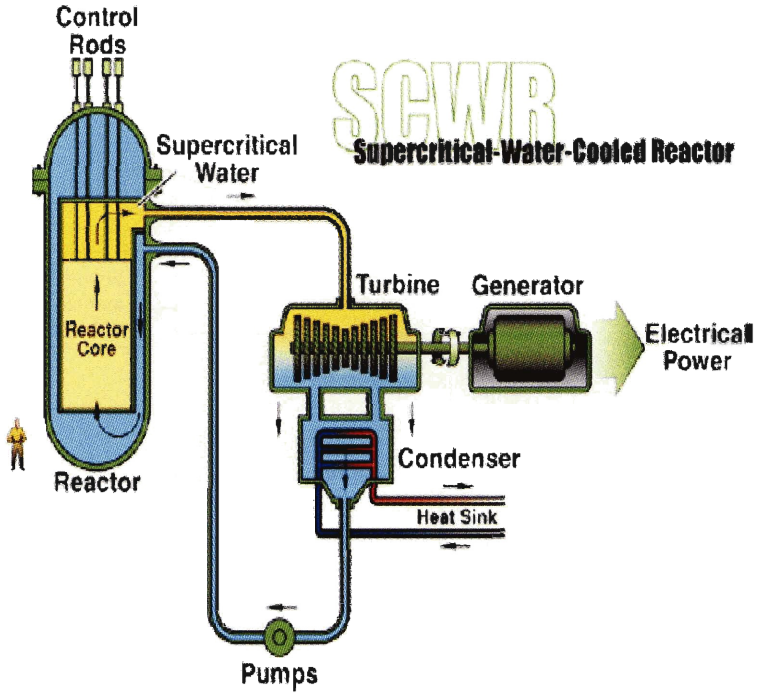

Fig. 9-2: Coolant flow path for the U.S. reference SCWR design (Buongiorno, 2003)

9.1 The model description

The thermal hydraulic models for all of the components in the flow path will be described for both the SCWR and the BWR in this section. The thermal hydraulic dynamics control equations are also developed.

9.1.1 Thermal-hydraulic model descriptions for the SCWR

As mentioned before, the SCWR in phase stability can be studied by imposing a constant pressure drop boundary condition on the components between the feedwater pump and the turbine inlet valve. Based on Fig. 9-2, the main components in the flow path that can be simulated are: feedwater pump, feedwater pipe, reactor core, steam line with exit valve and turbine control valve. A simplified diagram, together with the neutronic dynamics model, for in-phase oscillation of the U.S. reference SCWR design is illustrated in Fig. 9-3.

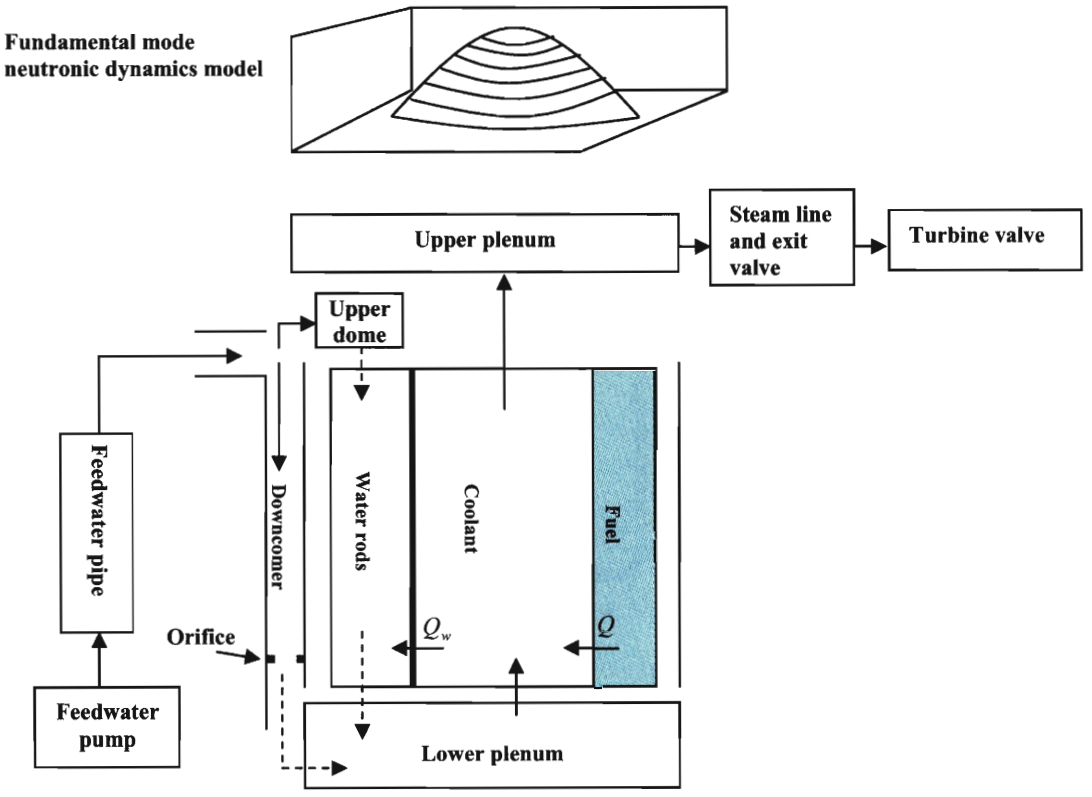

Fig.9-3: SCWR in-phase stability model illustration

In the above figure, the core is simulated as one channel. For more clear description, the flow path in the above figure was expanded as shown in Fig. 9-4. The flow velocity in the specific components is also indicated.

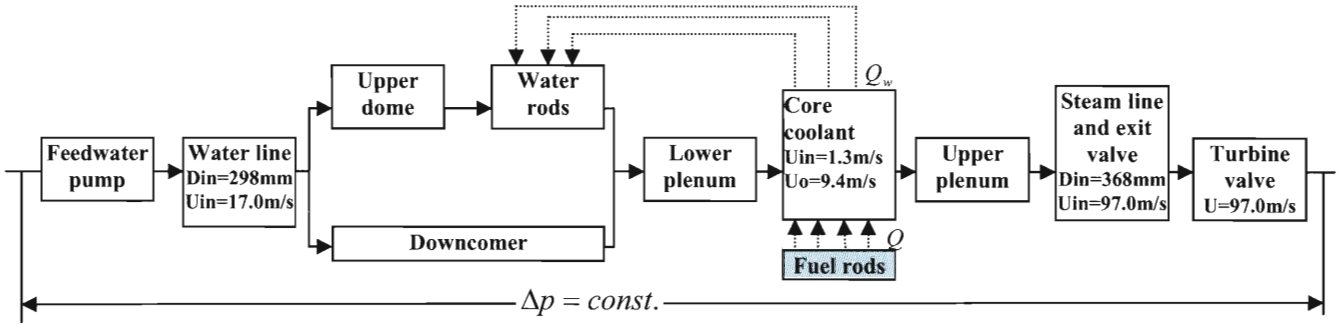

Fig. 9-4: Expanded SCWR flow path

Before the water flows into the reactor core, there is no energy added to the water for the case of no water rods heating. Therefore, the water in all components at the reactor core inlet can be simulated as the first region of the three region model. The water was heated up in the core from the first region to the third regions. Therefore, the core is simulated by a three region model as described previously. At the reactor core outlet, the water in the components will be in the third region.

At the reactor core inlet, the flow conservation equations have been described previously in Chapter 4. For easier reference, the first region conservation equations are listed here again.

$$\frac{\partial u}{\partial z} = 0 \quad (\rho(z) = \rho_A = Const.) \tag{9-1a}$$

$$\rho_f \frac{\partial h}{\partial t} + \rho_f u_{in} \frac{\partial h}{\partial z} = \frac{q'' P_h}{A_c} \tag{9-1b}$$

$$-\frac{\partial p}{\partial z} = \rho_f \frac{du_{in}}{dt} + \frac{f_1 \rho_f u_{in}^2}{2D_e} + \rho_f g \tag{9-1c}$$

Applying these conservation equations to an individual component, the thermal hydraulic models and the pressure drop oscillations for these components can be derived as given below.

9.1.1.1 Feedwater Pump

A linear relation of the pump head and volumetric flow rate can be assumed for the feedwater pump. Thus,

$$\Delta p_{pump} = C_{pump} Q_{pump} = C_{pump} \frac{w_{in}}{\rho_f} \tag{9-2}$$

where,

C_{pump} : pump coefficient, which is assumed a constant value

Q_{pump} : the volumetric flow rate

w_{in} : pump inlet mass flow rate

Perturbation and Laplace transformation of the above Equation (9-1), yields an equation for the pressure drop oscillation induced by inlet flow rate oscillation for the pump:

$$\delta\Delta p_{pump} = C_{pump} \frac{\delta w_{in}}{\rho_f} = \Gamma_{pump} \delta w_{in} \tag{9-3}$$

9.1.1.2 Feedwater pipe model

Applying the conservation equation for a pipe, perturbation and Laplace transformation of the momentum equation, yields:

$$\delta\Delta p_{pipe} = \rho_f s L_{pipe} \frac{\delta w_{in}}{\rho_f A_{pipe}} + f_{pipe} \frac{L_{pipe}}{D_{e,pipe}} \frac{w_{in}}{A_{pipe}} \frac{\delta w_{in}}{\rho_f A_{pipe}} = \Gamma_{pipe} \delta w_{in} \tag{9-4}$$

9.1.1.3 Downward flow

As mentioned before, the RPV inlet flow splits into two parts, one part flows downward through the downcomer and the other part through the water rods. Ignoring the friction pressure drop in the upper dome, the downward flow path can be illustrated in Fig. 9-5:

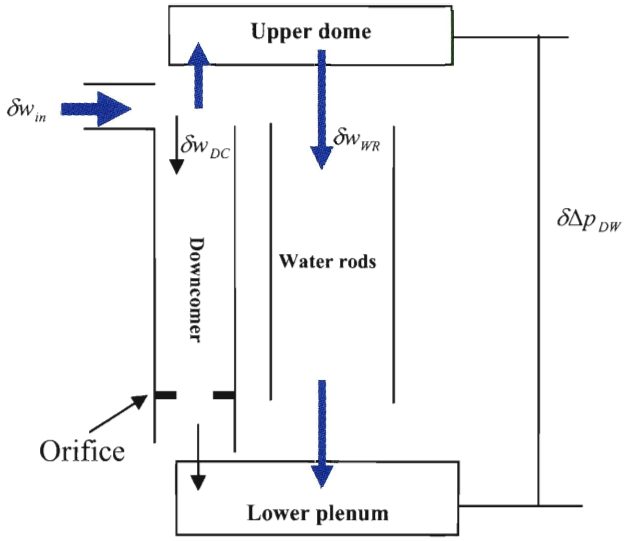

Fig. 9-5: Flow path of the downward flow

An orifice is located at the flow path of the downcomer. The water rods flow fraction can be adjusted by changing the pressure loss coefficient of the orifice. The orifice coefficient can be estimated through the condition of equal pressure drop across the downcomer and the water rods. The estimated orifice coefficients at different water rods flow fractions are listed in Table 9-1.

Table 9-1: Orifice coefficients at different water rods flow rate

Water rods flow rate (% of total core flow rate)	60%	70%	80%	90%
Orifice coefficients (at downcomer)	14.8	34.9	99.9	494.0

Applying the conservation equations to both the downcomer flow and the water rods flow, after perturbation and Laplace transformation, provides a relation for the pressure drop oscillation of the downcomer and water rods as:

$$\delta \Delta p_{WR} = \rho_f s L_{WR} \frac{\delta w_{WR}}{\rho_f A_{WR}} + f_{WR} \frac{L_{WR}}{D_{e,WR}} \frac{w_{WR}}{A_{WR}} \frac{\delta w_{WR}}{\rho_f A_{WR}} = \Gamma_{WR} \delta w_{WR} \tag{9-5}$$

$$\delta\Delta p_{DC} = \rho_f s L_{DC} \frac{\delta w_{DC}}{\rho_f A_{DC}} + (f_{DC} \frac{L_{DC}}{D_{e,DC}} + K_{DC}) \frac{w_{DC}}{A_{DC}} \frac{\delta w_{DC}}{\rho_f A_{DC}} = \Gamma_{DC} \delta w_{DC} \tag{9-6}$$

Also, from the boundary conditions:

$$\Delta p_{WR} = \Delta p_{DC},\ \delta\Delta p_{WR} = \delta\Delta p_{DC} \tag{9-7}$$

$$w_{in} = w_{WR} + w_{DC},\ \delta w_{in} = \delta w_{WR} + \delta w_{DC} \tag{9-8}$$

After some rearrangement, the pressure drop oscillation of the downward flow can be described as a function of the total RPV inlet flow oscillation as:

$$\delta\Delta p_{DW} = (\frac{1}{\Gamma_{WR}} + \frac{1}{\Gamma_{DC}})^{-1} \delta w_{in} = \Gamma_{DW} \delta w_{in} \tag{9-9}$$

9.1.1.4 Upward flow in the reactor core

Ignoring the lower plenum, the next component in the flow path is the upward flow in the reactor core. We shall also ignore the enthalpy oscillation feedback for the SCWR once through system as described previously, in other words only the inlet flow oscillation feedback is considered through the constant pressure drop boundary condition. Since the enthalpy oscillations were neglected for the non-heating region components before the inlet of the upward flow, i.e. feedwater pump, feedwater pipe, downward flow and lower plenum, a constant enthalpy condition can be imposed at the inlet of the upward flow. Just as mentioned in Chapter 8, the core can be lumped into N parallel channels. All of the lumped channels have the same pressure drop. Adding up the inlet flow rate for all channels, the total flow rate can be obtained. If the pressure drop response to the inlet flow rate and power oscillations for every specific lumped channel is calculated, the pressure drop response for the total flow rate of the whole core and power oscillations can be obtained. This methodology is illustrated as follows, assuming the core is lumped into N channels,

$$\delta\Delta p_1 = \Gamma_1 \delta w_{1,in} + \pi_1 \delta q_1'''$$

$$\delta\Delta p_2 = \Gamma_2 \delta w_{2,in} + \pi_2 \delta q_2'''$$

$$\vdots$$

$$\delta\Delta p_N = \Gamma_N \delta w_{N,in} + \pi_N \delta q_N''' \tag{9-10}$$

Solving the above equations for inlet flow rate oscillations and applying the boundary condition:

$$\Delta p_1 = \Delta p_2 \ldots = \Delta p_N = \Delta p_{core}$$

$$\delta\Delta p_1 = \delta\Delta p_2 \ldots = \delta\Delta p_N = \delta\Delta p_{core} \tag{9-11}$$

One obtains:

$$\delta w_{1,in} = \frac{1}{\Gamma_1}\delta\Delta p_{core} - \frac{\pi_1}{\Gamma_1}\delta q_1'''$$

$$\delta w_{2,in} = \frac{1}{\Gamma_2}\delta\Delta p_{core} - \frac{\pi_2}{\Gamma_2}\delta q_2'''$$

$$\vdots$$

$$\delta w_{N,in} = \frac{1}{\Gamma_N}\delta\Delta p_{core} - \frac{\pi_N}{\Gamma_N}\delta q_N''' \tag{9-12}$$

Applying the inlet flow boundary condition gives:

$$w_{1,in} + w_{2,in} \ldots + w_{N,in} = w_{in}, \qquad \delta w_{1,in} + \delta w_{2,in} \ldots + \delta w_{N,in} = \delta w_{in} \tag{9-13}$$

The volumetric power of the lumped channels can be related to the core average volumetric power as:

$$q_1''' = F_1 q_o'''$$

$$q_2''' = F_2 q_o'''$$

$$\vdots$$

$$q_N''' = F_N q_o''' \tag{9-14}$$

After some manipulations, one obtains,

$$\delta w_{in} = (\frac{1}{\Gamma_1} + \frac{1}{\Gamma_2} + \cdots + \frac{1}{\Gamma_N})\delta\Delta p_{core} - (\pi_1 F_1 \frac{1}{\Gamma_1} + \pi_2 F_2 \frac{1}{\Gamma_2} + \cdots + \pi_N F_N \frac{1}{\Gamma_N})\delta q_o''' \tag{9-15}$$

Solving the core upward flow pressure drop oscillation from Equation (9-15), one obtains:

$$\delta\Delta p_{core} = \Gamma_{core}\delta w_{in} + \pi_{core}\delta q_o''' \tag{9-16}$$

Where,

$$\Gamma_{core} = (\frac{1}{\Gamma_1} + \frac{1}{\Gamma_2} + \cdots + \frac{1}{\Gamma_N})^{-1}$$

$$\pi_{core} = (\pi_1 F_1 \frac{1}{\Gamma_1} + \pi_2 F_2 \frac{1}{\Gamma_2} + \cdots + \pi_N F_N \frac{1}{\Gamma_N})\,(\frac{1}{\Gamma_1} + \frac{1}{\Gamma_2} + \cdots + \frac{1}{\Gamma_N})^{-1}$$

Therefore, once the transfer functions of the single channel are developed, the total transfer functions for the whole core can be obtained.

Besides the pressure drop response should be related to the whole core flow rate and power as discussed above, the density and fuel temperature oscillations for every axial node should also be related to the whole core flow rate and power since the reactivity feedback related to the whole core properties. For a specific parameter oscillation such as enthalpy at axial node *i* for a specific channel *n*, the oscillation can be related to the inlet flow rate and power oscillations just like the pressure drop as:

$$\begin{aligned}\delta h_{n,i} &= W_{n,i}\delta w_{n,in} + Q_{n,i}F_n\delta q_o''' \\ &= W_{n,i}\left(\frac{1}{\Gamma_n}\delta\Delta p_{core} - \frac{\pi_n F_n}{\Gamma_n}\delta q_o'''\right) + Q_{n,i}F_n\delta q_o''' \\ &= W_{n,i}\frac{1}{\Gamma_n}\Gamma_{core}\delta w_{in} + \left[W_{n,i}\frac{1}{\Gamma_n}(\pi_{core} - \pi_n F_n) + Q_{n,i}F_n\right]\delta q_o''' \\ &= H_{n,i}^{w}\,\delta w_{in} + H_{n,i}^{q}\,\delta q_o''' \end{aligned} \tag{9-17}$$

Similarly, change in the flow rate, density and fuel temperature can be derived for a specific channel *n* at axial node *i* as:

$$\delta w_{n,i} = W_{n,i}^{w}\,\delta w_{in} + W_{n,i}^{q}\,\delta q_o''' \tag{9-18}$$

$$\delta \rho_{n,i} = D_{n,i}^{w}\,\delta w_{in} + D_{n,i}^{q}\,\delta q_o''' \tag{9-19}$$

$$\delta T_{n,i} = T_{n,i}^{w}\,\delta w_{in} + T_{n,i}^{q}\,\delta q_o''' \tag{9-20}$$

At the core exit, the water from all the lumped channels flows into and is mixed in the upper plenum. It was assumed that the mixing is perfect. From the mass and energy conservations:

$$\begin{aligned}\overline{w}_m &= w_{1,ex} + w_{2,ex} + \cdots + w_{N,ex} \\ \overline{w}_m\overline{h}_m &= w_{1,ex}h_{1,ex} + w_{2,ex}h_{2,ex} + \cdots + w_{N,ex}h_{N,ex}\end{aligned} \tag{9-21}$$

Where,

$\overline{h}_m$: the mixed enthalpy at the core exit

$\overline{w}_m$: the mixed flow rate at the core exit

$h_{1,ex}, h_{2,ex} \cdots h_{N,ex}$: the exit enthalpy for lumped channels

$w_{1,ex}, w_{2,ex} \cdots w_{N,ex}$: the exit flow rate for lumped channels

Perturbation and Laplace transformation Equation (9-21) and recalling that the channels have the same enthalpy rise at steady state, the mixed enthalpy and flow rate oscillations can be obtained:

$$\begin{aligned}\delta\overline{w}_m &= \delta w_{1,ex} + \delta w_{2,ex} + \cdots + \delta w_{N,ex} \\ &= (W^w_{1,ex} + W^w_{2,ex} + \cdots + W^w_{N,ex})\,\delta w_{in} + (W^q_{1,ex} + W^q_{2,ex} + \cdots + W^q_{N,ex})\,\delta q'''_o \\ &= W^w_{m,ex}\,\delta w_{in} + W^q_{m,ex}\,\delta q'''_o \end{aligned} \tag{9-22}$$

$$\begin{aligned}\delta\overline{h}_m &= w_{1,in}/w_{in}\delta h_{1,ex} + w_{2,in}/w_{in}\delta h_{2.ex} + \cdots + w_{N,in}/w_{in}\delta h_{N,ex} \\ &= \frac{1}{w_{in}}(w_{1,in}H^w_{1,ex} + w_{2,in}H^w_{2,ex} + \cdots + w_{N,in}H^w_{N,ex})\,\delta w_{in} \\ &\quad + \frac{1}{w_{in}}(w_{1,in}H^q_{1,ex} + w_{2,in}H^q_{2,ex} + \cdots + w_{N,in}H^q_{N,ex})\,\delta q'''_o \\ &= H^w_{m,ex}\,\delta w_{in} + H^q_{m,ex}\,\delta q'''_o \end{aligned} \tag{9-23}$$

Also, applying the relation between the enthalpy oscillation and density oscillation described in Chapter 4 for the third region, the mixed density oscillation in the core exit can be derived as,

$$\delta\overline{\rho}_m = -\frac{R}{pC_p}\overline{\rho}^2_{m,o}\delta\overline{h}_m \tag{9-24}$$

From the mixed flow rate and density oscillations, the mixture velocity oscillations at the core exit can be derived as:

$$\begin{aligned}\overline{w}_m &= \overline{\rho}_m\overline{u}_m A_{core} \\ \delta\overline{u}_m &= (\delta\overline{w}_m - w_{in}/\overline{\rho}_{m,o}\delta\overline{\rho}_m)/(A_{core}\overline{\rho}_{m,o}) \end{aligned} \tag{9-25}$$

Where,

A_{core} : total core flow area

$\overline{\rho}_{m,o}$: the steady state mixed density at core exit

Since the mixture oscillations at the core exit are now developed, we are ready to derive the pressure drop oscillations for the components at the core exit end.

9.1.1.5 Upper plenum

The upper plenum modeling and the oscillation derivations follow from those of [Lahey, 1993]. Since the cross section area of the upper plenum is much larger than its height, a lumped parameter model can be applied. Assuming adiabatic conditions, the mass, energy and momentum conservation equations are:

$$V_{up}\frac{d\overline{\rho}_{up}}{dt} = w_{up,in} - w_{up,ex} \tag{9-26}$$

$$V_{up}\frac{d(\overline{\rho}_{up}\overline{h}_{up} - p_{up})}{dt} = w_{up,in}\overline{h}_{up,in} - w_{up,ex}\overline{h}_{up,ex} \tag{9-27}$$

$$\Delta p_{up} = \frac{d}{dt}\int_0^{L_{up}} G_{up}dz + \int_0^{L_{up}} \frac{1}{A_{up}} \times \frac{\partial}{\partial z}\left(\frac{G_{up}^2 A_{up}}{\overline{\rho}_{up}}\right)dz + g\int_0^{L_{up}} \overline{\rho}_{up}dz \tag{9-28}$$

Where,

V_{up} : Upper plenum volume

A_{up} : Upper plenum flow area

$\overline{\rho}_{up}$: Volume averaged upper plenum density

$\overline{h}_{up}$: Volume averaged upper plenum enthalpy

Assuming perfect mixing, then, $\overline{\rho}_{up} = \overline{\rho}_{up,ex}$, and $\overline{h}_{up} = \overline{h}_{up,ex}$. Assuming the pressure at the upper plenum is constant, applying perturbation and Laplace transformation to Equations (9-26) and (9-27), after some rearrangement, leads to the following relation:

$$\delta\overline{\rho}_{up,ex} = (1+\tau_{up}s)^{-1}\delta\overline{\rho}_{up,in} \tag{9-29}$$

$$\delta u_{up,ex} = \frac{A_{up,in}}{A_{up,ex}}\delta u_{up,in} \tag{9-30}$$

Where,

τ_{up} : the mixing time constant in the upper plenum, $\tau_{up} = \frac{M_{up,o}}{w_{up,o}}$.

$M_{up,o}$: the water mass in the upper plenum at the steady state

$w_{up,o}$: the water flow rate in the upper plenum at the steady state

Integrating the momentum Equation (9-28), and ignoring the friction pressure drop, the pressure drop oscillation for the upper plenum can be derived as:

$$\begin{aligned}\delta\Delta p_{up} &= [A_{up,ex}\frac{L_{up}}{A_{up}}\overline{\rho}_{m,o}s + (1-\frac{A_{up,ex}^2}{A_{up,in}^2})G_{up,ex}]\delta u_{up,ex} \\ &+ [sA_{up,ex}\frac{L_{up}}{A_{up}}w_{in}/(A_{up,ex}\overline{\rho}_{m,o}) + \frac{1}{2}(\frac{w_{in}}{A_{up,ex}\overline{\rho}_{m,o}})^2(1-\frac{A_{up,ex}^2}{A_{up,in}^2}) + 9.81L_{up}]\delta\overline{\rho}_{up,ex}\end{aligned} \tag{9-31}$$

Recalling that the core exit is the upper plenum inlet, plugging Equations (9-24), (9-25), (9-29) and (9-30) into Equation (9-31), the pressure drop response of the upper plenum can be derived as:

$$\delta\Delta p_{up} = \Gamma_{up}\delta w_{in} + \pi_{up}\delta q_o''' \tag{9-32}$$

9.1.1.6 Steam line

As described in Chapter 4, the conservation equations for the third region flow can be expressed as:

$$\frac{\partial u_{st}}{\partial z} = \Omega_{2,st} = \frac{R}{pc_p}\frac{q_{st}^{"} P_{h,st}}{A_{st}} \tag{9-33}$$

$$\rho_{st}\frac{\partial h_{st}}{\partial t} + \rho_{st} u_{st}\frac{\partial h_{st}}{\partial z} = \frac{q_{st}^{"} P_{h,st}}{A_{st}} \tag{9-34}$$

$$-\frac{\partial p_{st}}{\partial z} = \frac{\partial G_{st}}{\partial t} + \frac{\partial}{\partial z}(G_{st}^{\ 2} / \rho_{st}) + \frac{f_{st}\rho_{st} u_{st}^{\ 2}}{2D_{e,st}} + \rho_{st} g \tag{9-35}$$

Assuming an adiabatic model for the steam line, integrating Equation (9-33), after perturbation and Laplace transformation, we get:

$$\frac{\partial u_{st}}{\partial z} = 0$$

$$\delta u_{st}(s,z) = \delta u_{st,in}(s) \tag{9-36}$$

Also, from the mass conservation, we have:

$$\frac{\partial \rho_{st}}{\partial t} + \frac{\partial}{\partial z}(\rho_{st} u_{st}) = 0 \tag{9-37}$$

Perturbation, Laplace transformation and integration of the above equation, yields:

$$\delta\rho_{st}(s,z) = \exp(-s / u_{st,o} z)\delta\rho_{st,in}(s) \tag{9-38}$$

Since both the velocity and density oscillations for the steam line had been developed, it is possible to integrate the momentum Equation (9-35). Recalling that the upper plenum exit is the steam line inlet, one obtains:

$$\begin{aligned}\delta\Delta p_{st} &= (s\overline{\rho}_{m,o} L_{st} + f_{st} L_{st} / D_{st}\frac{w_{in}}{A_{st}})\delta u_{up,ex} \\ &+ (f_{st} /(2D_{st}) u_{st,o}^2 + s u_{st,o})\frac{u_{st,o}}{s}[1 - \exp(-s / u_{st,o} L_{st})]\delta\rho_{up,ex}\end{aligned} \tag{9-39}$$

Plugging Equations (9-29) and (9-30) into Equation (9-39), the pressure drop oscillation in the steam line can be derived as:

$$\delta\Delta p_{st} = \Gamma_{st}\delta w_{in} + \pi_{st}\delta q_o''' \tag{9-40}$$

9.1.1.7 Exit valve

The pressure loss across the exit valve can be expressed as:

$$\Delta p_v = k_v \frac{\rho_v u_v^2}{2} \tag{9-41}$$

Perturbation and Laplace transformation the above equation, one obtains:

$$\begin{aligned}\delta\Delta p_v &= k_v \frac{w_{in}}{A_{st}}\delta u_{up,ex} + k_v \frac{u_{st,o}^2}{2}\exp(-s/u_{st,o}L_{st})\delta\rho_{up,ex} \\ &= \Gamma_v\delta w_{in} + \pi_v\delta q_o'''\end{aligned} \tag{9-42}$$

9.1.1.8 Turbine control valve

The hydraulic characteristic of the turbine control valve is similar to a pump. Therefore, the pump model developed above is applied to the turbine control valve also.

$$\Delta p_{tv} = C_{tv}Q_{tv} = C_{tv}\rho_{st}u_{st} \tag{9-43}$$

Hence, the pressure drop oscillation for the turbine control valve can be derived as:

$$\begin{aligned}\delta\Delta p_{tv} &= C_{tv}\overline{\rho}_{m,o}\delta u_{up,ex} + C_{tv}u_{st,o}\exp(-s/u_{st,o}L_{st})\delta\rho_{up,ex} \\ &= \Gamma_{tv}\delta w_{in} + \pi_{tv}\delta q_o'''\end{aligned} \tag{9-44}$$

9.1.1.9 Total pressure drop oscillation across the flow path

The pressure drop oscillations for all the components along the flow path have now been developed. Adding up all of them, the total pressure drop oscillations across the flow path can be written as:

$$\begin{aligned}\delta\Delta p_t &= (\Gamma_{pump} + \Gamma_{pipe} + \Gamma_{DW} + \Gamma_{core} + \Gamma_{up} + \Gamma_{st} + \Gamma_v + \Gamma_{tv})\delta w_{in} \\ &\quad + (\pi_{core} + \pi_{up} + \pi_{st} + \pi_v + \pi_{tv})\delta q_o''' \\ &= \Gamma_t \delta w_{in} + \pi_t \delta q_o''' \end{aligned} \tag{9-45}$$

The supercritical water in the flow path can be categorized into a compressible part and non-compressible part. Assuming the first region of the three region model is non-compressible, the non-compressible part includes the feedwater pump, feedwater pipe, downward flow and part of the core flow. Assuming the second and third regions are compressible, the compressible part includes part of the core, the upper plenum, steam line together with its associated exit valve and turbine control valve. During in-phase oscillation, a pressure drop fluctuation in the compressible part will generate an opposite sign feedback in the non-compressible part with the same amplitude to maintain the constant pressure drop boundary condition. The feedback loop can be represented in Fig. 9-6 as follows:

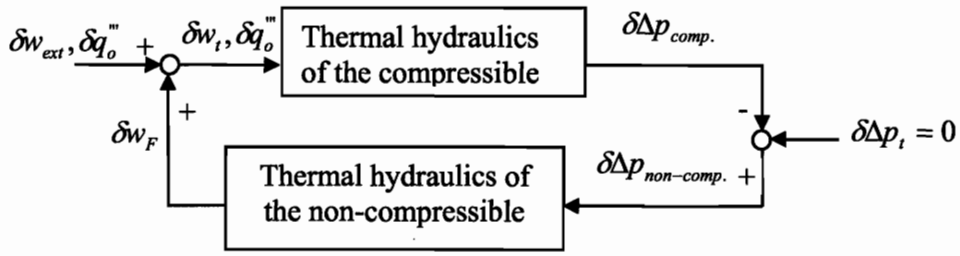

Fig. 9-6: thermal hydraulic feedback of the SCWR in phase stability

From the above diagram, the pressure drop oscillation in the compressible part can be expressed as:

$$\delta\Delta p_{comp.} = \Gamma_{comp.}\delta w_t + \pi_{comp.}\delta q_o''' \tag{9-46}$$

To maintain a constant total pressure drop,

$$\delta\Delta p_{comp.} + \delta\Delta p_{non-comp.} = 0 \tag{9-47}$$

Getting rid of the pressure drop oscillation due to the power fluctuation, the remaining pressure drop oscillation of the non-compressible part will generate an inlet flow feedback. Therefore,

$$\delta\Delta p_{non-comp.} = \Gamma_{non-comp.}\delta w_F + \pi_{non-comp.}\delta q_o''' \tag{9-48}$$

Plugging the equations (9-46) and (9-48) into (9-47), after some arrangement, one obtains,

$$\Gamma_t\delta w_t + \pi_t\delta q_o''' = \Gamma_{non-comp.}\delta w_{ext} \tag{9-49}$$

9.1.2 Thermal-hydraulic model description for the BWR

For a typical BWR, during the in phase oscillation, the density wave transits in a closed loop as illustrated in Fig. 9-1. The flow path and components can be represented by a block diagram as shown in Fig. 9-7.

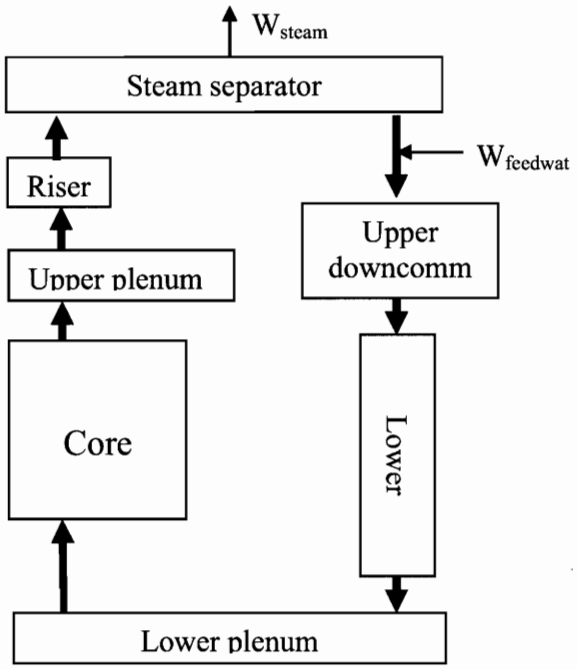

Fig. 9-7: BWR flow path loop for the in-phase stability

The controlled boundary condition for a dynamic loop is the total pressure drop oscillation for all of the components along the path is zero. To derive a governing equation like Equation (9-49), the pressure drop oscillation for every component should be derived. Since the loop is closed, it is worth noting that the core inlet enthalpy can not maintain constant for a BWR system. The enthalpy fluctuation associated with the flow oscillation will be transferred to the core inlet. The pressure drop oscillation for the specific component along the path is derived in the following section.

9.1.2.1 BWR reactor core

Simulating the core by N lumped parallel channels, for every lumped channel, the pressure drop oscillation can be described as:

$$\delta\Delta p_1 = \Gamma_1 \delta w_{1,in} + \pi_1 F_1 \delta q_o''' + H_1 \delta h_{in}$$

$$\delta\Delta p_2 = \Gamma_2 \delta w_{2,in} + \pi_2 F_2 \delta q_o''' + H_2 \delta h_{in}$$

$$\vdots$$

$$\delta\Delta p_N = \Gamma_N \delta w_{N,in} + \pi_N F_N \delta q_o''' + H_N \delta h_{in} \tag{9-50}$$

Applying the same methodology described in the SCWR analysis, the final pressure drop oscillation across the core can be expressed as a function of the inlet flow rate oscillation, power oscillation and inlet enthalpy oscillation as:

$$\delta\Delta p_{core} = \Gamma_{core} \delta w_{in} + \pi_{core} \delta q_o''' + H_{core} \delta h_{in} \tag{9-51}$$

Where,

$$\Gamma_{core} = (\frac{1}{\Gamma_1} + \frac{1}{\Gamma_2} + \cdots + \frac{1}{\Gamma_N})^{-1}$$

$$\pi_{core} = (\frac{1}{\Gamma_1} + \frac{1}{\Gamma_2} + \cdots + \frac{1}{\Gamma_N})^{-1} (\pi_1 F_1 \frac{1}{\Gamma_1} + \pi_2 F_2 \frac{1}{\Gamma_2} + \cdots + \pi_N F_N \frac{1}{\Gamma_N})$$

$$H_{core} = (\frac{1}{\Gamma_1} + \frac{1}{\Gamma_2} + \cdots + \frac{1}{\Gamma_N})^{-1} (H_1 \frac{1}{\Gamma_1} + H_2 \frac{1}{\Gamma_2} + \cdots + H_N \frac{1}{\Gamma_N})$$

And the oscillations for enthalpy, density, fuel temperature and the flow rate at every node i can be expressed as:

$$\delta w_{n,i} = W_{n,i}^{w} \delta w_{in} + W_{n,i}^{q} \delta q_o''' + W_{n,i}^{h} \delta h_{in} \tag{9-52}$$

$$\delta \rho_{n,i} = D_{n,i}^{w} \delta w_{in} + D_{n,i}^{q} \delta q_o''' + D_{n,i}^{h} \delta h_{in} \tag{9-53}$$

$$\delta h_{n,i} = H^{w}_{n,i}\,\delta w_{in} + H^{q}_{n,i}\,\delta q'''_{o} + H^{h}_{n,i}\,\delta h_{in} \tag{9-54}$$

$$\delta T_{n,i} = T^{w}_{n,i}\,\delta w_{in} + T^{q}_{n,i}\,\delta q'''_{o} + + T^{h}_{n,i}\,\delta h_{in} \tag{9-55}$$

As mentioned in the SCWR analysis, the mixed properties oscillations at the core exit need to be derived to analyze the components at the core exit. Again, it is assumed that mixing is perfect in the upper plenum. Perturbation and Laplace transformation of the mass and energy conservation, Equation (9-21), lead to the mixed enthalpy and flow rate oscillations for the BWR as:

$$\begin{aligned}
\delta \overline{w}_{m} &= \delta w_{1,ex} + \delta w_{2,ex} + \cdots + \delta w_{N,ex} \\
&= (W^{w}_{1,ex} + W^{w}_{2,ex} + \cdots + W^{w}_{N,ex})\,\delta w_{in} + (W^{q}_{1,ex} + W^{q}_{2,ex} + \cdots + W^{q}_{N,ex})\,\delta q'''_{o} \\
&+ (W^{h}_{1,ex} + W^{h}_{2,ex} + \cdots + W^{h}_{N,ex})\,\delta h_{in} \\
&= W^{w}_{m,ex}\,\delta w_{in} + W^{q}_{m,ex}\,\delta q'''_{o} + W^{h}_{m,ex}\,\delta h_{in}
\end{aligned} \tag{9-56}$$

$$\begin{aligned}
\delta \overline{h}_{m} &= [(h_{1,ex,o}\delta w_{1,ex} + w_{1,ex,o}\delta h_{1,ex}) + (h_{2,ex,o}\delta w_{2,ex} + w_{2,ex,o}\delta h_{2,ex}) + \cdots \\
&\quad + (h_{N,ex,o}\delta w_{N,ex} + w_{N,ex,o}\delta h_{N,ex}) - \overline{h}_{m,o}\delta \overline{w}_{m}]/\,w_{in} \\
&= H^{w}_{m,ex}\,\delta w_{in} + H^{q}_{m,ex}\,\delta q'''_{o} + H^{h}_{m,ex}\,\delta h_{in}
\end{aligned} \tag{9-57}$$

Applying the relation between the enthalpy oscillation and density oscillation described in Chapter 4 for the two phase mixture, the mixed density oscillation at the core exit can be derived as:

$$\delta \overline{\rho}_{m} = -\frac{v_{fg}}{h_{fg}}\,\overline{\rho}^{2}_{m,o}\,\delta \overline{h}_{m} \tag{9-58}$$

Also, the mixture velocity oscillation at the core exit can be derived by following the same procedure described in the SCWR analysis.

9.1.2.2 BWR upper plenum

Applying the same model as that developed for the SCWR analysis, the pressure drop oscillation for the BWR upper plenum can be described as:

$$\delta\Delta p_{up} = \Gamma_{up}\delta w_{in} + \pi_{up}\delta q_o''' + H_{up}\delta h_{in} \tag{9-59}$$

9.1.2.3 BWR riser

By using the two phase flow HEM model, and assuming an adiabatic condition, the conservation equations for the riser can be described as,

$$\frac{\partial u_{rs}}{\partial z} = \Omega_1 = \frac{v_{fg}}{h_{fg}}\frac{q'' P_{h,rs}}{A_{rs}} = 0 \tag{9-60}$$

$$\rho_{rs}\frac{\partial h_{rs}}{\partial t} + \rho_{rs}u_{rs}\frac{\partial h_{rs}}{\partial z} = \frac{q'' P_{h,rs}}{A_{rs}} \tag{9-61}$$

$$-\frac{\partial p_{rs}}{\partial z} = \frac{\partial G_{rs}}{\partial t} + \frac{\partial}{\partial z}(G_{rs}^2/\rho_{rs}) + \frac{f_2\rho_{rs}u_{rs}^2}{2D_{e,rs}} + \rho_{rs}g \tag{9-62}$$

Using the same methodology described in the steam line analysis of the SCWR, and the riser inlet is that of the upper plenum outlet, one obtains,

$$\delta u_{rs}(s,z) = \delta u_{up,ex}(s) \tag{9-63}$$

$$\delta\rho_{rs}(s,z) = \exp(-s/u_{rs,o}z)\delta\rho_{up,ex}(s) \tag{9-64}$$

The velocity and density oscillations at the upper plenum outlet can be related to the core exit through Equations (9-29) and (9-30). Integrating the momentum Equation (9-62), one obtains:

$$\delta\Delta p_{rs} = \frac{w_{in}}{A_{core}}(sL_{rs}/u_{rs,o} + f_{rs}L_{rs}/D_{e,rs} + K_{rs,in} + K_{rs,ex})\frac{A_{core}A_{up,ex}}{A_{rs}^2}\delta u_{up,ex}$$
$$+\frac{w_{in}}{A_{core}}\{(f_{rs}/(2D_{e,rs}))u_{rs,o}^2 + 9.81)\frac{w_{in}}{A_{core}u_{rs,o}s}[1-\exp(-s/u_{rs,o}L_{rs})]$$
$$+\frac{1}{2}\frac{w_{in}}{A_{core}}(K_{rs,in} + K_{rs,ex}\exp(-sL_{rs}/u_{rs,o}))\}\frac{A_{core}^2}{A_{rs}^2}\frac{1}{\overline{\rho}_{m,o}^2}\delta\rho_{up,ex}$$
$$= \Gamma_{rs}\delta w_{in} + \pi_{rs}\delta q_o''' + H_{rs}\delta h_{in} \tag{9-65}$$

9.1.2.4 BWR steam separator

The pressure loss of the steam separator is lumped into the form loss with a coefficient of K_{sep}. Therefore, the steam separator pressure drop model is described as:

$$\Delta p_{sep} = K_{sep}\frac{\overline{\rho}_{m,o}u_{sep}^2}{2} \tag{9-66}$$

According to [Marcelles and Ballesteros, 1997], for a typical BWR, the pressure drop of the cyclone-type separators is about 0.28 Kg/cm^2 at the rated condition. Based on this pressure drop, the loss coefficient can be found about 5.3. Then, the pressure drop oscillation can be derived as,

$$\delta\Delta p_{sep} = K_{sep}\frac{u_{sep}^2}{2}\delta\rho_{sep} + K_{sep}G_{sep}\delta u_{sep} \tag{9-67}$$

From the boundary condition, one obtains:

$$\delta u_{sep}(s) = \frac{A_{rs}}{A_{sep}}\delta u_{rs}(s) \tag{9-68}$$

$$\delta\rho_{sep}(s) = \delta\rho_{rs,ex}(s) = \exp(-s/u_{rs,o}L_{rs})\delta\rho_{up,ex}(s) \tag{9-69}$$

Finally, the pressure drop oscillation for the steam separator can be written as:

$$\delta\Delta p_{sep} = \Gamma_{sep}\delta w_{in} + \pi_{sep}\delta q_o''' + H_{sep}\delta h_{in} \tag{9-70}$$

9.1.2.5 The feedwater and the separated saturated water mixing region

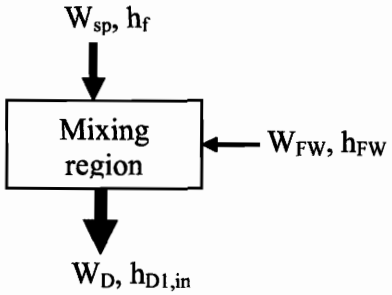

Fig. 9-8: Separated water and feedwater mixing region

Ignoring the storage dynamics in this region, the mass and energy conservation equations can be written as:

$$w_D = w_{sp} + w_{FW} \tag{9-71}$$

$$w_D h_{D1,in} = w_{sp} h_f + w_{FW} h_{FW} \tag{9-72}$$

As mentioned before, assuming the feedwater flow rate and enthalpy are constant, one obtains,

$$\delta h_{D1,in} = \frac{(h_f - h_{FW}) w_{FW}}{w_{D,o}^2} \delta w_D \tag{9-73}$$

Assuming non-compressible in the single phase region, the flow rate oscillations in the single phase region will be the same and equal to the core inlet flow rate oscillation, i.e. $\delta w_D = \delta w_{in}$.

9.1.2.6 The downcomer region

The downcomer region can be divided into an upper downcomer, a lower downcomer and the jet pump regions as illustrated in Fig. 9-9.

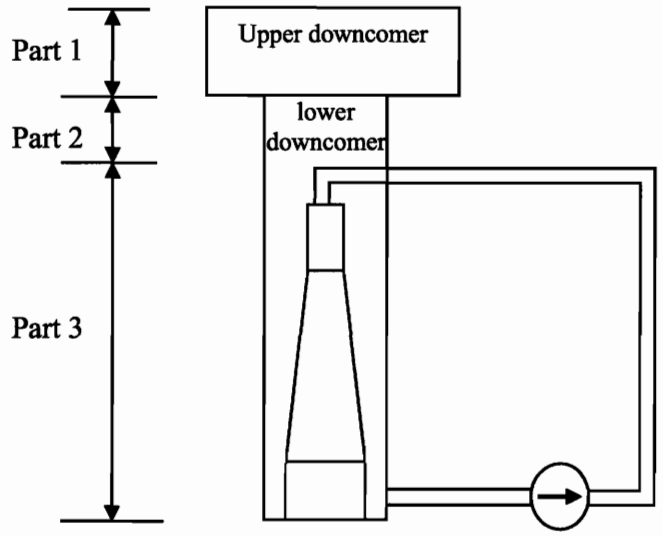

Fig. 9-9: The downcomer region

According to [Lahey, 1993], the energy conservation equation for the upper downcomer can be written as:

$$\rho_f A_{D1} \frac{\partial(h_{D1} - p/\rho_f)}{\partial t} + w_D \frac{\partial h_{D1}}{\partial z} = q''_{V1} P_{h,D1} \tag{9-74}$$

Where,

q''_V : heat flux between the downcomer water and the vessel wall. It can be written as:

$$q''_{V1} = H_{D1}(T_{V1} - T_{D1}) . \tag{9-75}$$

Perturbation and Laplace transformation of Equation (9-75), neglecting the heat transfer coefficient fluctuation, yields:

$$\delta q''_{V1} = H_{D1}(\delta T_{V1} - \delta T_{D1}) \tag{9-76}$$

Applying a lumped parameter model to the reactor vessel and neglecting the heat loss to the ambient and the heat generation in the vessel wall, the temperature dynamics of the vessel wall can be written as,

$$M_{V1}C_{p,V}\frac{dT_{V1}}{dt} = -q''_{V1}A_{V1} \tag{9-77}$$

Where,

M_{V1}: Upper plenum part vessel mass

A_{V1}: Total vessel heating area at the upper plenum part

Perturbation and Laplace transformation of Equation (9-77), yields:

$$\delta T_{V1}(s) = -A_{V1}/(M_{V1}C_{p,V}s)\delta q''_{V1} \tag{9-78}$$

Perturbation and Laplace transformation of Equation (9-74), and plugging Equations (9-76) and (9-78) into Equation (9-74), after integrating and rearrangement, the relation of the enthalpy oscillations between the inlet and the outlet of the upper downcomer can be obtained as:

$$\begin{aligned}\delta h_{D1,ex} &= \exp\{-L_{D1}[\frac{A_{D1}\rho_f s}{w_{D,o}} + \frac{P_{h,D1}H_{D1,o}}{w_{D,o}C_{pf}(1+H_{D1,o}A_{V1}/(M_{V1}C_{p,V}s))}]\}\delta h_{D1,in} \\ &= D_1\delta h_{D1,in}\end{aligned} \tag{9-79}$$

Similarly, for the lower downcomer at part 2, the enthalpy transaction can be described as:

$$\delta h_{D2,ex} = \exp\{-L_{D2}[\frac{A_{D2}\rho_f s}{w_{D,o}} + \frac{P_{h,D2}H_{D2,o}}{w_{D,o}C_{pf}(1+H_{D2,o}A_{V2}/(M_{V2}C_{p,V}s))}]\}\delta h_{D2,in}$$

$$= D_2 \delta h_{D1,ex} \tag{9-80}$$

Also, from the momentum equation, the pressure drop oscillation in the upper and low downcomers can be derived as,

$$\begin{aligned} \delta \Delta p_D &= \{I_D s + f_{D1} / \rho_f [w_{in} L_{D1} / (D_{e,D1} A_{D1}^2)] + f_{D2} / \rho_f [w_{in} L_{D2} / (D_{e,D2} A_{D2}^2)]\} \delta w_{in} \\ &= \Gamma_D \delta w_{in} \end{aligned} \tag{9-81}$$

Where,

I_D : Momentum of inertia of the downcomer

$I_D = L_{D1} / A_{D1} + L_{D2} / A_{D2}$

9.1.2.7 The jet pump part in the downcomer region

The jet pump includes the throat, diffuser and discharge as illustrated in Fig. 9-10. At steady state, the recirculation loop flow is only about 30% of the total flow rate (M ratio is about 1.96) for a typical BWR. The recirculation loop is a long flow path (about 60 meters) and the pump and valves associated with it. Therefore, the oscillations in the recirculation loop can be assumed smoothed away. In this analysis, only the jet pump dynamics model is included.

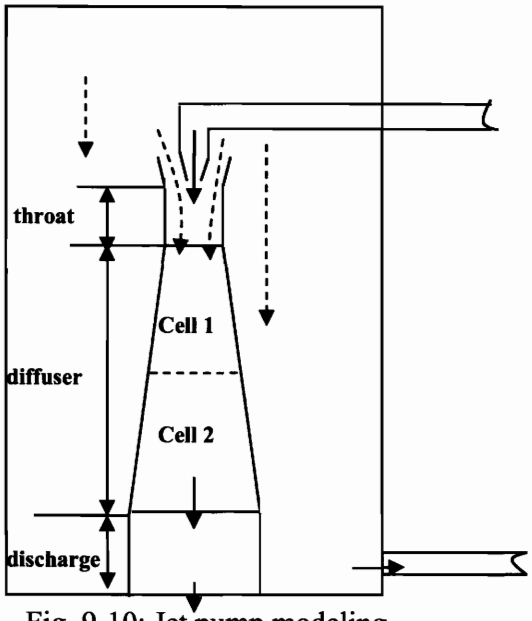

Fig. 9-10: Jet pump modeling

From the form loss model in the suction region, the pressure drop oscillation was derived as:

$$\delta\Delta p_{suction} = K_{suction} G_{suction} / (\rho_f A_{suction}) \delta w_{in} \tag{9-82}$$

Where,

$K_{suction}$: Pressure loss coefficient of the jet pump suction region

$G_{suction}$: Mass flux of the jet pump suction region

According to [Kao, 1996], the pressure loss coefficient of the jet pump suction region, $K_{suction}$, is about 0.35 for a typical BWR.

Applying the momentum conservation equation to the throat region, the pressure drop oscillation in this region can be found as:

$$\delta\Delta p_{throat} = L_{throat} / A_{throat} s + f_{throat} / \rho_f [w_{in} L_{throat} / (D_{e,throat} A_{throat}^2)] \delta w_{in} \tag{9-83}$$

For the diffuser region, the whole region is divided by two cells. For each of the cells, an equivalent diameter is applied,

$$D_{e,c1} = (D_{c1,inlet} + D_{c1,outlet})/2$$
$$D_{e,c2} = (D_{c2,inlet} + D_{c2,outlet})/2 \tag{9-84}$$

Then, the pressure drop oscillation is,

$$\begin{aligned}\delta\Delta p_{diffuser} &= \delta\Delta p_{c1} + \delta\Delta p_{c2} \\ &= L_{c1}/A_{c1}s + f_{c1}/\rho_f[w_{in}L_{c1}/(D_{e,c1}A_{c1}^2)]\delta w_{in} \\ &\quad + L_{c2}/A_{c2}s + f_{c2}/\rho_f[w_{in}L_{c2}/(D_{e,c2}A_{c2}^2)]\delta w_{in}\end{aligned} \tag{9-85}$$

And for the discharge part,

$$\delta\Delta p_{discharge} = L_{discharge}/A_{discharge}s + f_{discharge}/\rho_f[w_{in}L_{discharge}/(D_{e,discharge}A_{discharge}^2)]\delta w_{in} \tag{9-86}$$

Adding up all of the pressure drop oscillations, the total pressure drop oscillation for the jet pump can be obtained as,

$$\delta\Delta p_{jet} = \Gamma_{jet}\delta w_{in} \tag{9-87}$$

Now, let us derive the enthalpy transfer function for the jet pump part. From Chapter 4, the enthalpy oscillation transfer from the inlet to the outlet for an insulated flow can be expressed as,

$$\delta h_{outlet} = \exp(-sL/u_{inlet})\delta h_{inlet} \tag{9-88}$$

Applying the above relation to the jet pump, the final enthalpy transfer function can be expressed as:

$$\delta h_{jet,ex} = \exp[-s(L_{throat}/u_{throat} + L_{diffuser}/u_{diffuser} + L_{discharge}/u_{discharge})]\delta h_{jet,in} \quad (9\text{-}89)$$

And, the jet pump inlet enthalpy oscillation can be expressed as:

$$\delta h_{jet,in} = w_{suction}/w_{in}\delta h_{D2,ex} = \frac{M}{M+1}\delta h_{D2,ex} \quad (9\text{-}90)$$

Where,

M : M ratio of the recirculation loop, $M = \frac{w_{suction}}{w_{recirculation}}$

9.1.2.8 Lower plenum

Just as for the upper plenum, the lumped model was applied to the lower plenum. From the mass, momentum and energy Equations (9-26, 27 and 28), one obtains:

$$\delta h_{LP,ex} = (1+\tau_{LP}s)^{-1}\delta h_{LP,in} \quad (9\text{-}91)$$

Where,

τ_{LP} : the mixing time constant in the lower plenum, $\tau_{LP} = \frac{M_{LP,o}}{w_{in}}$.

$M_{LP,o}$: the water mass in the lower plenum at steady state

Recalling that the jet pump outlet is the lower plenum inlet, and the lower plenum outlet is the core inlet, from Equations (9-73), (9-79), (9-80), (9-89), (9-90) and (9-91), one obtains a relation for the core inlet flow rate oscillation and the core inlet enthalpy oscillation as:

$$\delta h_{in} = (1+\tau_{LP}s)^{-1} \times \exp[-s(L_{throat}/u_{throat} + L_{diffuser}/u_{diffuser} + L_{discharge}/u_{discharge})]$$
$$\times \frac{M}{M+1} \times \exp\{-L_{D2}[\frac{A_{D2}\rho_f s}{w_{D,o}} + \frac{P_{h,D2}H_{D2,o}}{w_{D,o}C_{pf}(1+H_{D2,o}A_{V2}/(M_{V2}C_{p,V}s))}]\}$$
$$\times \exp\{-L_{D1}[\frac{A_{D1}\rho_f s}{w_{D,o}} + \frac{P_{h,D1}H_{D1,o}}{w_{D,o}C_{pf}(1+H_{D1,o}A_{V1}/(M_{V1}C_{p,V}s))}]\} \times \frac{(h_f - h_{FW})w_{FW}}{w_{D,o}^2}\delta w_{in}$$
$$= T_{hw}\delta w_{in} \tag{9-92}$$

Plugging Equation (9-92) into Equations (9-51), (9-59), (9-65) and (9-70), one obtains,

$$\delta\Delta p_{core} = (\Gamma_{core} + H_{core}T_{hw})\delta w_{in} + \pi_{core}\delta q_o''' \tag{9-93}$$

$$\delta\Delta p_{up} = (\Gamma_{up} + H_{up}T_{hw})\delta w_{in} + \pi_{up}\delta q_o''' \tag{9-94}$$

$$\delta\Delta p_{rs} = (\Gamma_{rs} + H_{rs}T_{hw})\delta w_{in} + \pi_{rs}\delta q_o''' \tag{9-95}$$

$$\delta\Delta p_{rs} = (\Gamma_{sep} + H_{sep}T_{hw})\delta w_{in} + \pi_{sep}\delta q_o''' \tag{9-96}$$

The total core pressure drop responses can be obtained by adding up Equations (9-92), (9-93), (9-94), (9-80) and (9-86).

$$\delta\Delta p_{loop} = [(\Gamma_{core} + \Gamma_{up} + \Gamma_{rs} + \Gamma_D + \Gamma_{jet}) + (H_{core} + H_{up} + H_{rs})T_{hw}]\delta w_{in}$$
$$+ (\pi_{core} + \pi_{up} + \pi_{rs})\delta q_o'''$$
$$= \Gamma_{loop}\delta w_{in} + \pi_{loop}\delta q_o''' \tag{9-97}$$

Noting that the above Equation (9-97) has the same form as Equation (9-45) which is derived for the SCWR, following the same methodology as the SCWR, the thermal hydraulic dynamics control equation can be derived for the BWR. It is worth emphasizing that the compressible part for the BWR is the two phase flow region, which includes the two phase flow part in the reactor core, upper plenum, riser and steam separator and dryer. The non-compressible part is the single phase flow region, which includes the downcomer, jet pump, lower plenum and the single phase part of the reactor core.

$$\Gamma_{loop}\delta w_{in,t} + \pi_{loop}\delta q_o''' = \Gamma_{non-comp.}\delta w_{in,ext} \tag{9-98}$$

9.2 Coupling of the thermal-hydraulic model with the neutronic model

The neutronic dynamics transfer function had been derived in Chapter 8 by using a λ modes expansion of the point kinetic equation. According to Equations (8-42) and (8-43), the transfer function for the fundamental mode can be described as:

$$\delta q_F''' = \Phi_0(s)\delta\rho_t \tag{9-99}$$

$$\Phi_0(s) = q_o'''(s\Lambda_0 + \sum_{i=1}^{6}\frac{\beta_i s}{s+\lambda_i})^{-1} \tag{9-100}$$

Similar to the out-of-phase case, for the in-phase stability mode, the neutronic feedback is through the fuel Doppler effects and density or void feedback. As mentioned in Chapter 8, the fuel temperature and water properties during the out-of-phase oscillation are asymmetric and, associated with the asymmetric pattern of the first subcritical neutron dynamics mode, will generate a reactivity feedback with the same sign for the two halves of the core. For the in-phase oscillation, the fuel temperature and the water properties are of a symmetric pattern, and the fundamental neutron dynamics mode is also symmetric. Therefore, the reactivity feedbacks in the whole core are in the same phase obviously. In one word, both the out-of-phase and in-phase reactivity feedback are in-phase throughout the core.

As mentioned in Chapter 8, the control variable for the out-of-phase oscillation is the constant total inlet flow rate. For the in-phase stability, the control variable is the constant total pressure drop oscillation throughout of the whole closed loop ($\delta\Delta p_{loop} = 0$). While the BWR has a closed loop, the loop for the SCWR is not closed for the in-phase stability analysis. However, since we assumed a constant pressure drop boundary condition, if

considering the pressure drop for the remaining part of the loop as also constant, the loop can be closed and the total pressure drop oscillation throughout of the closed loop is also zero ($\delta\Delta p_{analyzed} + \delta\Delta p_{remainng} = \delta\Delta p_{loop} = 0$).

Similar to the out-of-phase case, the feedback loop for the in-phase stability can be described in Fig. 9-11.

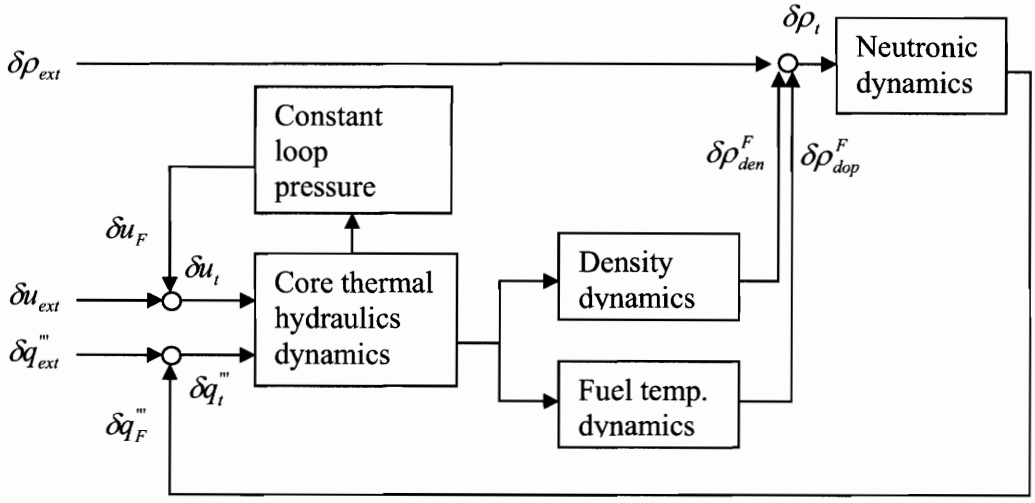

Fig. 9-11: Block diagram of the in-phase stability

Just as the out-of-phase case, the oscillations of the whole core average properties are obtained by adding up the weighted contributions for all of the nodes, radial and axially through out of the core. If the core has N channels and one channel has M nodes axially, the average core density and temperature oscillations can be expressed as:

$$\delta\tilde{\rho}_c = \delta w_{in}\sum_{j=1}^{N}\sum_{i=1}^{M} W_{j,i}U_{den}^{j,i} + \delta q_o'''\sum_{j=1}^{N}\sum_{i=1}^{M} W_{j,i}Q_{den}^{j,i} = U_{den}\delta w_{in} + Q_{den}\delta q_o''' \qquad (9\text{-}101)$$

$$\delta\tilde{t}_f = \delta w_{in}\sum_{j=1}^{N}\sum_{i=1}^{M} W_{j,i}U_f^{j,i} + \delta q_o'''\sum_{j=1}^{N}\sum_{i=1}^{M} W_{j,i}Q_f^{j,i} = U_f\delta w_{in} + Q_f\delta q_o''' \qquad (9\text{-}102)$$

Therefore, the reactivity feedback oscillation can be obtained as:

$$\begin{aligned}\delta\rho_F &= C_{den}\delta\tilde{\rho}_c + C_{dop}\delta\tilde{t}_f \\ &= (C_{den}U_{den} + C_{dop}U_f)\delta w_{in} + (C_{den}Q_{den} + C_{dop}Q_f)\delta q_o'''\end{aligned} \tag{9-103}$$

Then, the total reactivity oscillation equation can be written as:

$$\delta\rho_t - C_{den}(U_{den} + U_f)\delta w_{in,t} - C_{dop}(Q_{den} + Q_f)\delta q_o''' = \delta\rho_{ext} \tag{9-104}$$

And the total power oscillation equation can be expressed as:

$$\delta q_t''' - \Phi_0(s)\delta\rho_t = \delta q_{ext}''' \tag{9-105}$$

Similar to the out-of-phase stability analysis, the governing Equations (9-98), (9-104) and (9-105) can be described in a matrix form as:

$$A(s)\delta x_t = B(s)\delta x_{ext} \tag{9-106}$$

where,

$$\delta x_t = (\delta w_{in,t}, \delta q_o''', \delta\rho_t), \tag{9-107}$$

$$\delta x_{ext} = (\delta w_{in,ext}, \delta q_{ext}''', \delta\rho_{ext}) \tag{9-108}$$

$$A(s) = \begin{bmatrix} \Gamma_{loop} & \pi_{loop} & 0 \\ 0 & 1 & -\phi_o(s) \\ -(C_{den}U_{den} + C_{dop}U_f) & -(C_{den}Q_{den} + C_{dop}Q_f) & 1 \end{bmatrix}, \text{ and} \tag{9-109}$$

$$B(s) = \begin{bmatrix} \Gamma_{non-comp.} & 0 & 0 \\ 0 & 1 & 0 \\ 0 & 0 & 1 \end{bmatrix} \tag{9-110}$$

Therefore, the characteristic equation for the in-phase stability can be derived from

$$\det[A(s)] = 0 \tag{9-111}$$

Thus, the characteristic equation is:

$$\Gamma_{loop}[1-\phi_o(s)\,(C_{den}Q_{den}+C_{dop}Q_f)]+\pi_t\,(C_{den}U_{den}+C_{dop}U_f)=0 \tag{9-112}$$

9.3 In-phase stability model evaluations

The above developed models for the in-phase stability analysis were evaluated by comparison to the Peach Bottom flow stability tests. In 1977, a series of stability tests were conducted at the Peach Bottom Atomic Power Station Unit 2 at the end of the fuel cycle 2 by using a pressure perturbation technique. These tests provided a significant quantity of high quality operating plant stability data. Then, the cycle 3 stability tests at Peach Bottom-2 were performed by following the cycle 2 test in 1978. The tests results and conditions for cycle 2 can be found in [Carmichael and Niemi, 1978] and for cycle 3 in [Woffindon and Niemi, 1981]. The tests results and important parameters are listed in Table 9-2 for cycle 2 tests and in Table 9-3 for cycle 3 tests.

Table 9-2: Peach Bottom test results and conditions at cycle 2

Tests number		Core Pressure (MPa)	Power (% rated)	Flow rate (% rated)	Core inlet enthalpy (kJ/kg)	Experimental	
						Freq. (*HZ*)	DR*
Cycle 2	PT1	7.06	60.6	52.3	1184.6	0.439	0.259
	PT2	7.01	51.7	43.8	1187.7	0.441	0.303
	PT3	7.098	59.2	40.4	1184.6	0.424	0.331
	PT4	7.056	43.5	40.3	1183.8	0.383	0.271

*: Decay ratio

Table 9-3: Peach Bottom test results and conditions at cycle 3

Tests number		Core Pressure (MPa)	Power (% rated)	Flow rate (% rated)	Core inlet enthalpy (kJ/kg)	Experimental	
						Freq. (*HZ*)	DR*
Cycle 3	1PT1	6.936	39.7	47.8	1197.2	0.427	0.236
	1PT2	6.936	46.7	47.6	1188.9	0.403	0.314
	2PT2	6.977	52.0	45.5	1181.0	0.433	0.435
	2PT3	6.943	61.7	44.6	1165.6	0.433	0.509
	3PT2	6.922	52.1	47.1	1172.3	0.408	0.391
	3PT3	6.950	61.6	46.2	1154.2	0.407	0.504
	4PT1	6.922	50.7	47.5	1177.2	0.392	0.355
	4PT2	6.964	44.0	48.0	1188.6	0.382	0.293
	4PT3	6.846	38.4	48.1	1191.6	0.376	0.210

*: Decay ratio

The void reactivity coefficients are not available publicly for this stability test. A quadratic formula mentioned in Chapter 8 can be used to represent these reactivity coefficients reasonably.

An in-phase stability analysis code named SABS was developed, where SABS stands for Stability Analysis of BWR and SCWR.

9.3.1 Model evaluation against Peach Bottom-2 cycle 2 tests

In the fuel cycle 2 of Peach Bottom-2, 92 assemblies with 7x7 fuel rods loading are in the peripheral region. In the central region, 188 assemblies of the 8x8 type and 484 of the 7x7 types were loaded. A model with three lumped channels was applied during this evaluation according to the different fuel types and regions. The peripheral region assemblies (7x7 fuel type) were lumped into one channel. The 8x8 fuel assemblies in the central region were lumped into one channel. The last lumped channel was the 7x7 fuel assemblies in the central region. The detailed reactor core design for the cycle 2 of Peach

Bottom-2 could be found in [Solis, et. al, 2001]. Comparison of the SABS predicted results and the experimental data is given in Table 9-4.

Table 9-4: Comparison of experimental data and the predicted results for cycle 2

Tests number		Experimental Data		SABS predicted Data	
		Freq. (*HZ*)	Decay ratios	Freq. (*HZ*)	Decay ratios
Cycle 2	PT1	0.439	0.259	0.478	0.295
	PT2	0.440	0.303	0.501	0.327
	PT3	0.424	0.331	0.465	0.349
	PT4	0.383	0.271	0.457	0.329

The experimental data and predicted results can also be graphically illustrated as shown in Fig. 9-12 and 9-13.

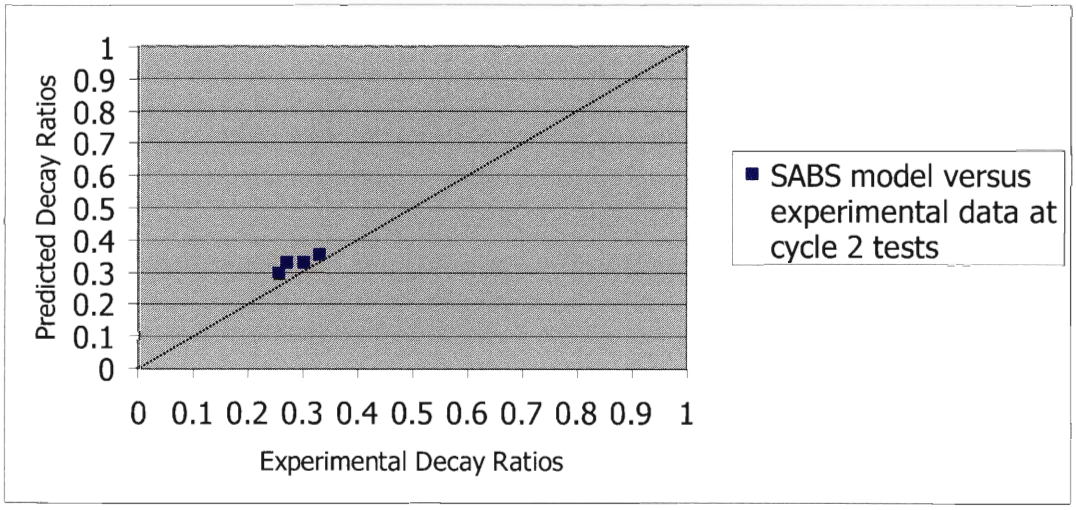

Fig. 9-12: The DRs evaluation for Peach Bottom fuel cycle 2 tests

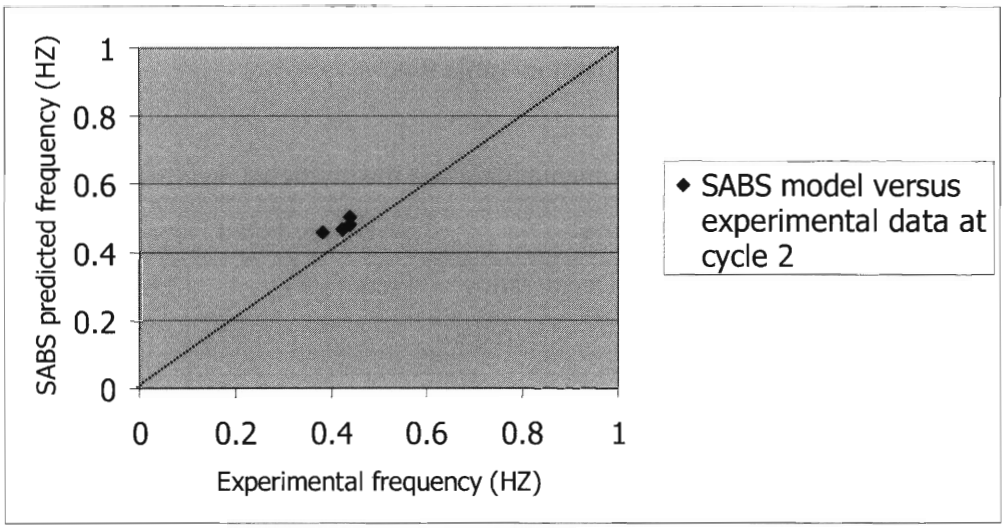

Fig. 9-13: The frequencies evaluation for Peach Bottom fuel cycle 2 tests

Defining the mean errors for the decay ratios and frequencies as:

$$\widetilde{E}_{DR} = \frac{\sum_{n=1}^{n_{\exp.}} \left| DR_{pre.} - DR_{\exp.} \right|_n}{n_{\exp.}} \tag{9-113}$$

$$\widetilde{E}_{Frq.} = \frac{\sum_{n=1}^{n_{\exp.}} \left| F_{pre.} - F_{\exp.} \right|_n}{n_{\exp.}} \tag{9-114}$$

Where,

$n_{\exp.}$: Number of the experimental data

It can be found that the mean errors for the predicted decay ratio and frequency are about 0.03 and 0.05 respectively.

Kao (1996) developed a BWR stability simulator and benchmarked his model by using Peach Bottom-2 stability test data. The comparison of SABS with Kao's model is graphically shown in Fig. 9-14 and 9-15 along with the experimental results.

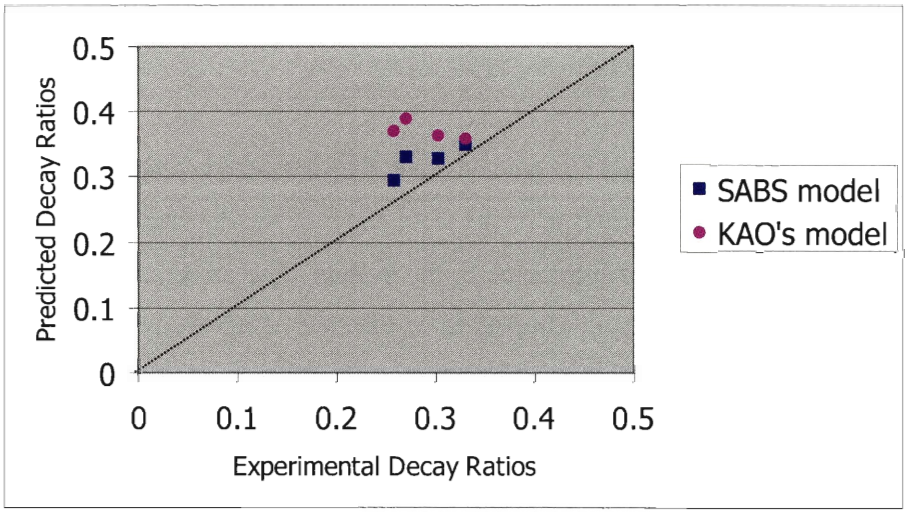

Fig. 9-14: Decay ratio comparison between Kao's model and SABS at cycle 2

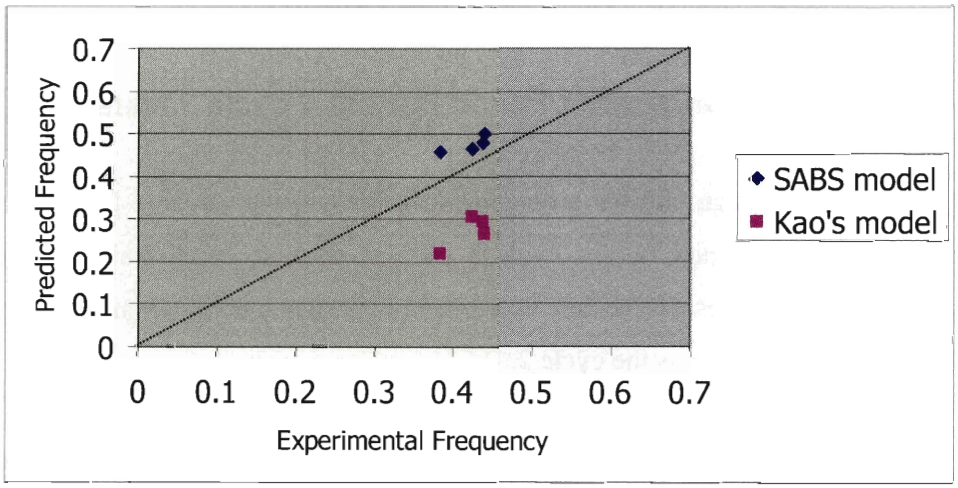

Fig. 9-15 Frequency comparison between Kao's model and SABS at cycle 2

From the above Fig. 9-14, Kao's model overestimated the decay ratio compared with the experimental value. One of the reasons may be due to his choice of the void reactivity coefficient. Since the void coefficients are not available for the experimental condition, Kao conducted a void coefficient sensitivity analysis for the test number PT3. It was found that the predicted value is close to the experimental data at a void coefficient equals -12 cents for the test PT3. Then, this value was applied for the other tests. From Table 9-1, it can be found that the test PT3 has a high power to flow ratio condition (59.2% power versus 40.4% flow). At this condition, the void coefficient is high. Since a

high void coefficient will destabilize the system, the higher void coefficient applied to the test will result in a larger decay ratio as predicted by Kao.

Also, from Fig. 9-15, the SABS predicted a higher frequency compared with Kao's model. Physically, the period (reverse of the frequency) of the density wave oscillation is the time of two phase flow transport time in the system. The current analysis lumps the steam separator and dryer pressure drop to the form loss of the riser exit. Therefore the time of the two phase flow transport in the separator and dryer was erased, which gives a shorter total transport time, therefore a higher frequency.

Therefore, the current BWR in-phase stability analysis model matches the experimental data reasonably well and is comparable to the other stability prediction models.

9.3.2 Model evaluation against Peach Bottom-2 cycle 3 tests

While the assembly design and the arrangement in the core is available for the cycle 2 tests, it can not be obtained for the cycle 3 stability tests at Peach Bottom-2. It was assumed that the cycle 3 tests have the same assembly design and arrangement along with the same inlet orifice design as the cycle 2.

Comparison of the SABS predicted results and the experimental data is given in Table 9-5 for the cycle 3 tests.

Table 9-5: Comparison of experimental data and the predicted results for cycle 3

Tests number		Experimental Data		SABS predicted Data	
		Freq. (*HZ*)	Decay ratios	Freq. (*HZ*)	Decay ratios
Cycle 3	1PT1	0.427	0.236	0.433	0.268
	1PT2	0.403	0.314	0.432	0.283
	2PT2	0.433	0.435	0.518	0.329
	2PT3	0.433	0.509	0.507	0.349
	3PT2	0.408	0.391	0.532	0.332
	3PT3	0.407	0.504	0.521	0.350
	4PT1	0.392	0.355	0.538	0.328
	4PT2	0.382	0.293	0.433	0.278
	4PT3	0.376	0.210	0.433	0.267

The above table 9-4 was graphically shown in Fig. 9-16 and 9-17 along with Kao's model predicted results.

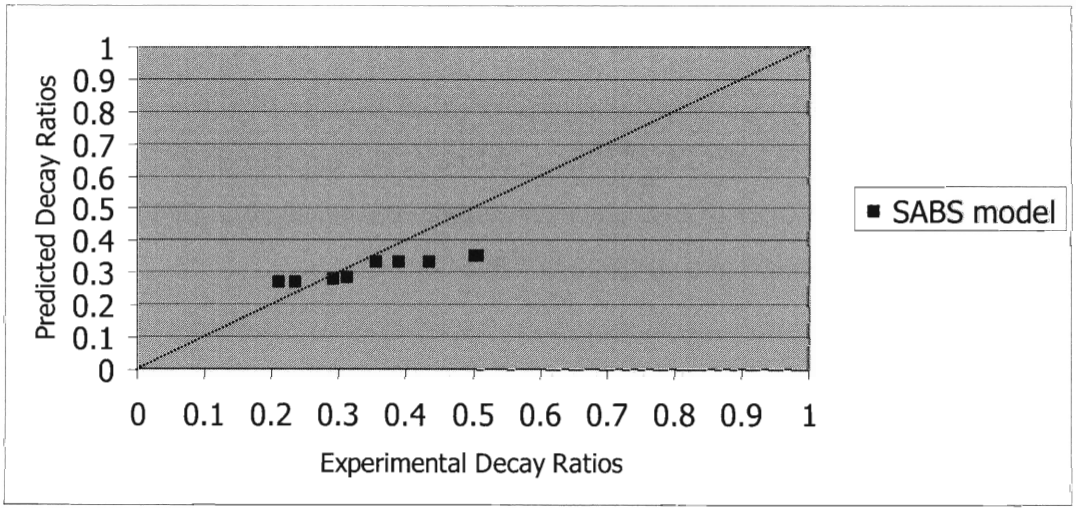

Fig. 9-16: The DRs evaluation for Peach Bottom fuel cycle 3 tests

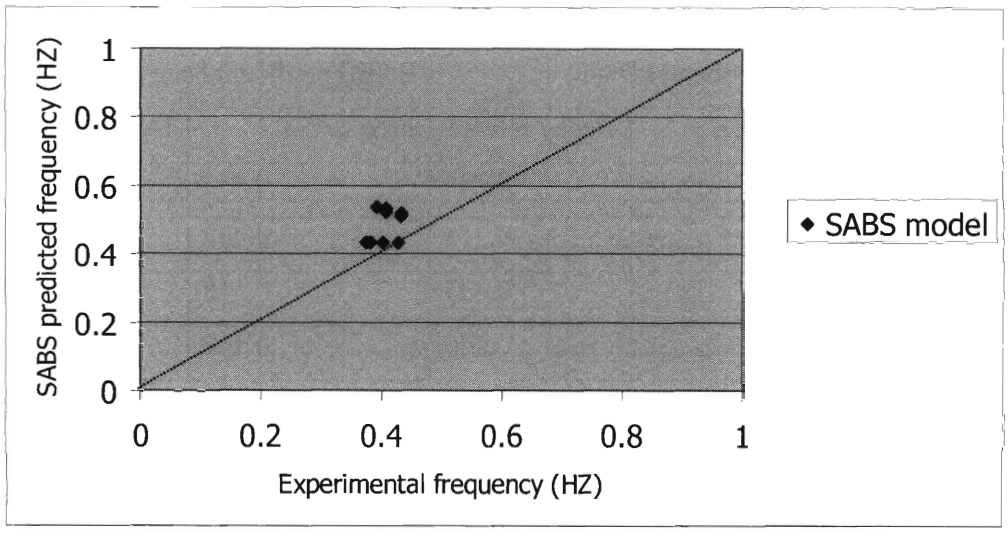

Fig. 9-17: The DRs evaluation for Peach Bottom fuel cycle 3 tests

Using formulas (9-113) and (9-114), it can be found that the mean errors for the SABS predicted decay ratio and frequency are about 0.07 and 0.08 respectively. Therefore, the SABS matches the experimental reasonably well recalling that the actual assembly design is unknown for the cycle 3.

Examining the Table 9-4 and Fig. 9-16 further, it is found that the SABS underestimated decay ratios for the cycle 3, especially at tests 2PT2, 2PT3 and 3PT3. Comparing Table 9-1 and 9-2, it is found that the test PT2 in cycle2 has a similar condition to test 2PT2 in cycle 3, and tests 2PT3 & 3PT3 in cycle 3 have similar conditions to test PT3 in cycle 2. The comparison of these test pairs is given in Table 9-5.

March-Leuba (1990) also analyzed the tests by using the stability code LAPUR-IV. For comparison, the predictions of SABS and LAPUR-IV are listed in Table 9-6 together with the experimental data.

Table 9-6: Stability predictions at similar tests conditions

Tests number	Core Pressure (MPa)	Power (% rated)	Flow rate (% rated)	Core inlet enthalpy (kJ/kg)	DR (Exp.)	DR (SABS)	DR (LAPUR)
PT2 (cycle 2)	7.01	51.7	43.8	1187.7	0.303	0.327	0.21
2PT2 (cycle 3)	6.977	52.0	45.5	1181.0	0.435	0.329	0.15
PT3 (cycle 2)	7.098	59.2	40.4	1184.6	0.331	0.349	0.35
2PT3 (cycle 3)	6.943	61.7	44.6	1165.6	0.509	0.349	0.27
3PT3 (cycle 3)	6.950	61.6	46.2	1154.2	0.504	0.350	0.35

From Table 9-6, both SABS and LAPUR-IV predict reasonable decay ratios at similar conditions. However, SABS is closer to the experimental data than LAPUR-IV. Therefore, the underestimation of the SABS and LAPUR-IV may be from lacking of the actual assembly design in cycle 3.

From the above model evaluation of cycle 2 and 3, it can be concluded that the SABS matches the experimental reasonably well.

9.4 SCWR In-phase stability analysis and comparison with the BWR

Applying the above developed model, the U.S. reference SCWR design is analyzed in this section. For comparison, the typical BWR described in Chapter 5 is also analyzed. The model with three lumped core channels mentioned in Chapter 8 is used for both the SCWR and the BWR. It was assumed that no water rods heating occurred during the current analysis. The water rods heating effects will be addressed later. The detailed parameters of three lumped channels are listed in Table 9-7 for SCWR and Table 9-8 for BWR, respectively.

Table 9-7: Parameters of the three lumped channel model for SCWR (whole core)

Lumped channel number	Power range (Relative to average channel)	Assembly number	Power (MW)	Flow rate (kg/s)	Equivalent inlet orifice coefficient
1	Above 1.2	14	443.2	228.5	22.7
2	0.9~1.19	91	2353.0	1213.0	93.0
3	Below 0.9	40	796.0	410.3	241.1

Table 9-8: Parameters of the three channel model for a typical BWR (whole core)

Lumped channel number	Power (relative to core average)	Assembly Number	Flow rate per assembly (kg/s)	Kin
1	1.3	60	16.1	31.1
2	1.037	612	16.76	31.1
3	0.565	92	8.89	205.0

9.4.1 Exit valve and turbine valve coefficients sensitivity analysis for SCWR

From Fig. 9-4, the flow velocity in the steam line is as high as 97.0 m/s. At such high velocity, a small velocity or density fluctuation may cause large pressure drop oscillation in the compressible flow region. Therefore, it is clear that the flow restrictions in the steam line will have large impact on system stability.

The exit valve pressure drop is proportional to the square of the flow velocity, as illustrated in the following formula,

$$\Delta p_v = k_v \frac{\rho_v u_v^2}{2} \tag{9-115}$$

The water density in the steam line is about 88.1kg/m^3 at steady state. The pressure drop across the exit valve at steady state was calculated at different exit valve coefficients as listed in the Table 9-9. For comparison, the core pressure drop at steady state is also listed.

Table 9-9: Exit valve pressure drop at different coefficients

Exit valve coefficient k_v	Velocity (m/s)	Density (kg/m^3)	Core pressure drop (MPa)	Exit valve pressure drop (MPa)
0.2	97.0	88.1	0.163	0.083
0.4				0.166
0.6				0.249
0.8				0.332
1.0				0.414

From Table 9-9, even for an exit valve coefficient as low as 0.4, the pressure drop across the exit valve is already larger than the core pressure drop. Therefore, the exit valve should be carefully chosen to provide a small pressure loss coefficient. One way to solve this problem is to use larger steam line diameter since this will decrease the flow velocity. However, the steam line flow is at supercritical pressure, a larger diameter pipe requires much thicker wall to assure the structural strength. The stability features are studied at different exit valve coefficients through the decay ratio calculations, which can be found in Fig. 9-18.

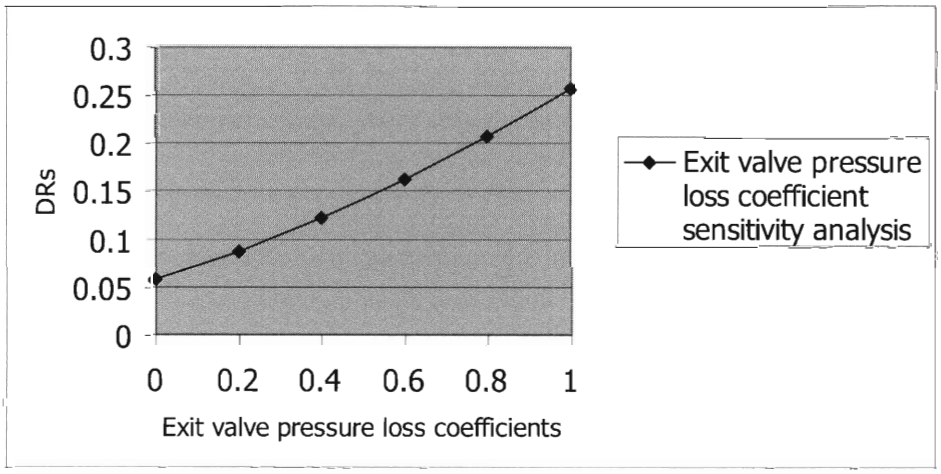

Fig. 9-18: Decay ratio dependence on exit valve pressure loss coefficient

As predicted, the system stability is very sensitive to the exit valve pressure loss coefficient. To make the system stable, the loss coefficient of the exit valve must be small. In the following analysis, it was assumed the loss coefficient is 0.25.

Unlike the exit valve, the turbine control valve has a hydraulic characteristic like a pump. Therefore, the pressure drop can be written as a function of the volumetric flow rate as,

$$\Delta p_{tv} = C_{tv} Q_{tv} = C_{tv} A_{st} u_{tv} \tag{9-116}$$

Therefore, the pressure drop of the turbine control valve is proportional to velocity instead of velocity square of exit valve. Thus, the effect of the turbine control valve coefficient on stability is small. Just like the inlet feedwater pump, a flat feature was assumed, i.e. $C_{tv} = 0$.

9.4.2 SCWR in-phase stability at exit valve coefficient 0.25

With an exit valve pressure loss coefficient 0.25, the decay ratios and oscillation frequencies for U.S. reference SCWR design in-phase stability mode were calculated and plotted in Fig. 9-19 and 9-20.

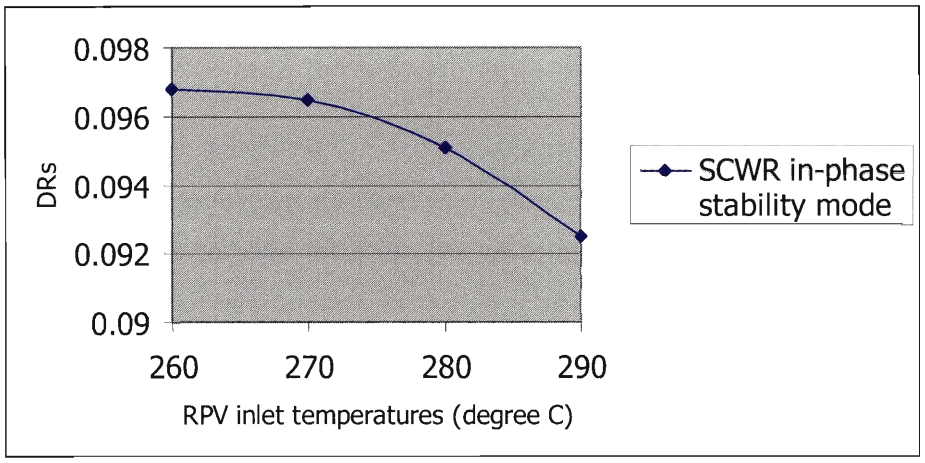

Fig. 9-19: DRs for the SCWR in-phase stability mode

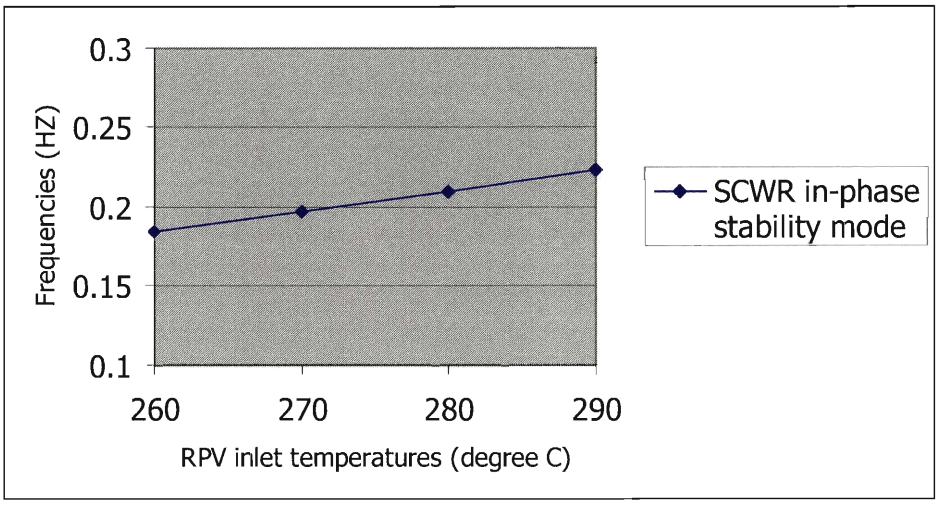

Fig. 9-20: Frequencies for the SCWR in-phase stability mode

From Fig. 9-19, it is seen that the SCWR will be very stable at exit valve coefficient 0.25 and an increase in the inlet temperature will further stabilize system. Like the single channel and out-of-phase mode, the oscillation frequencies of the in-phase stability mode will increase as the RPV inlet temperature increases.

9.4.3 Reactivity coefficient sensitivity analysis for both the SCWR and the BWR

As mentioned in Chapter 8, the density coefficient sensitivity has been studied for both the SCWR and the BWR in phase stability. Following the procedure discussed in Chapter 8, the density coefficient was multiplied by a factor F for both the SCWR and the BWR while keeping the Doppler coefficient at its constant value. The results can be found in Fig. 9-21.

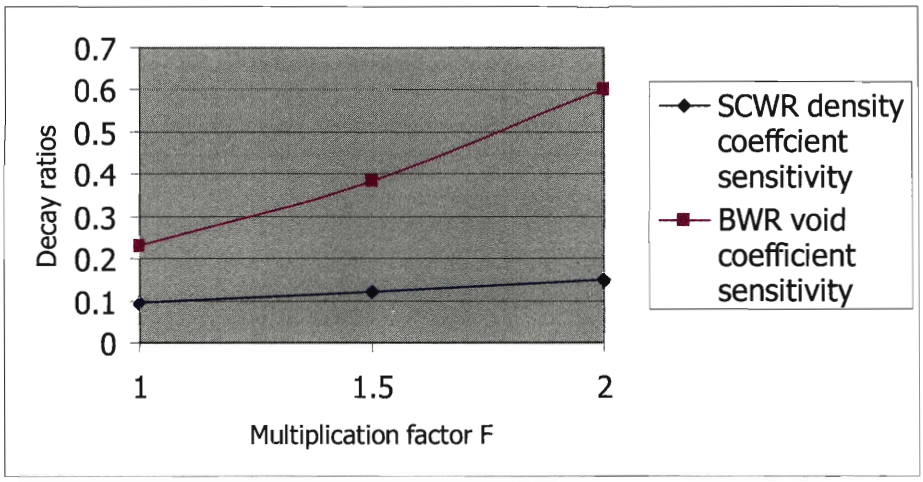

Fig. 9-21: Reactivity coefficient sensitivity analysis for in phase stability

From Fig. 9-21, it is seen that the BWR is more sensitive to the density reactivity coefficient than the SCWR. The same feature could be found in the out-of-phase stability case. As in the out-of-phase case, the reduced reactivity coefficient sensitivity of the SCWR is due to most of the moderation power is provided by the water rods, which has small or no density fluctuation. Also, it is seen that the reactivity coefficient has much more significant effect on the in-phase stability than on the out-of-phase stability for both the SCWR and the BWR. The reason is that the subcriticality of the first subcritical neutronic dynamics mode in the out-of-phase oscillation will smooth away part of the reactivity feedback during the oscillation.

9.4.4 Comparison of three SCWR stability modes

The decay ratios and oscillation frequencies for three SCWR stability modes (the single hot channel, out-of-phase and in-phase) are graphically shown in Fig. 9-22 and 9-23.

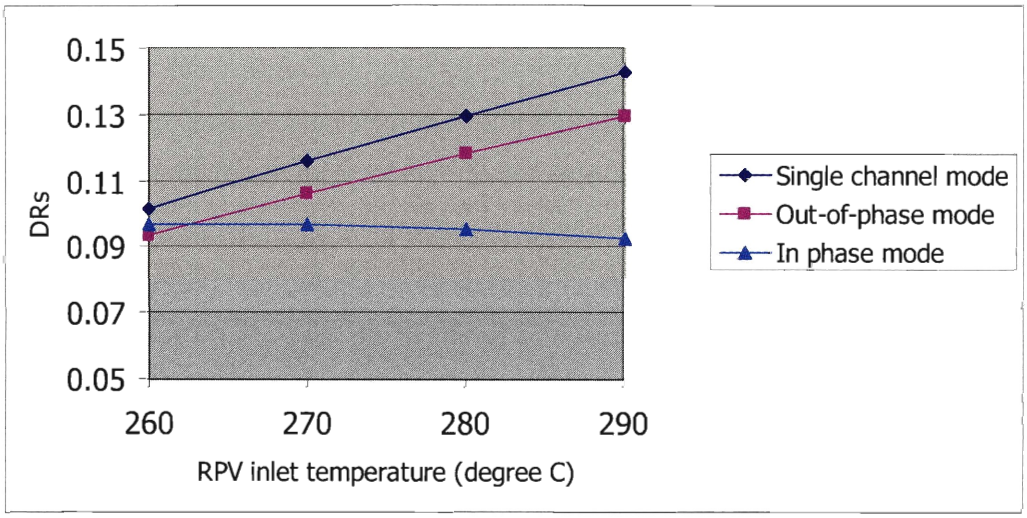

Fig. 9-22: Decay ratios comparison for the SCWR three stability modes

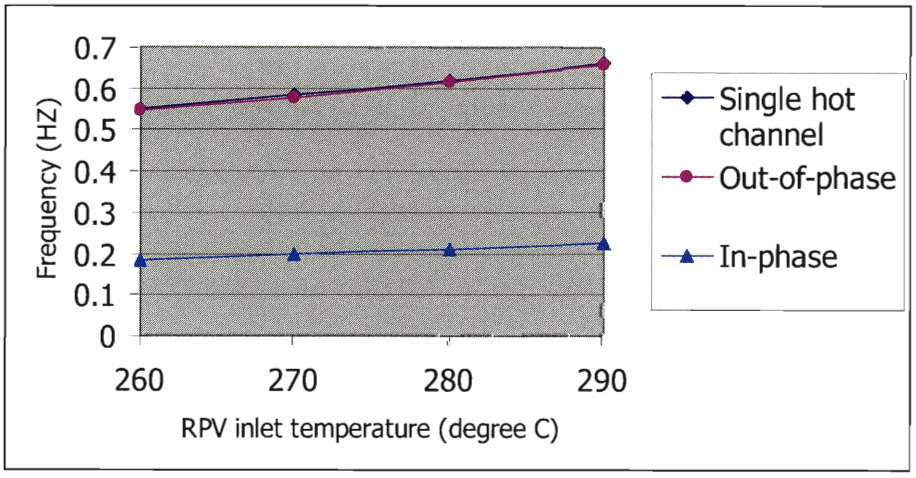

Fig. 9-23: Frequency comparison for the SCWR three stability modes

From Fig. 9-22, it is seen that the single channel mode limits the SCWR stability feature at the nominal conditions. The most stable mode is the in-phase stability mode. Without the riser and the steam separator, the pressure drop in the compressible fluid part of the

SCWR is significantly reduced. Additionally, the pressure drop in the incompressible fluid part, such as the feedwater line and water rods, will enhance the in-phase stability. Therefore, these two reasons combined together give the SCWR stable in-phase oscillation feature. However, the pressure loss in the steam line, such as the exit valve, must be kept small enough.

From Fig. 9-23, the frequency of the in-phase stability is seen as much lower than the out-of-phase and single channel stability. While both the single channel and out-of-phase oscillations deal with the parallel channel system, the in-phase oscillation deals with the whole flow path. The length of the feedwater line for the U.S. reference SCWR design is about 32.0 m. Therefore, it requires much more time for the fluid to transport through the system during the in-phase oscillation, which results in the lower oscillation frequency.

9.4.5 Power and flow sensitivity analysis for the SCWR and comparison to the BWR

The power and flow sensitivities of both the SCWR and the BWR are analyzed and compared for the in-phase stability mode in this section.

The power sensitivity is plotted in Fig. 9-24 for both the SCWR and the BWR.

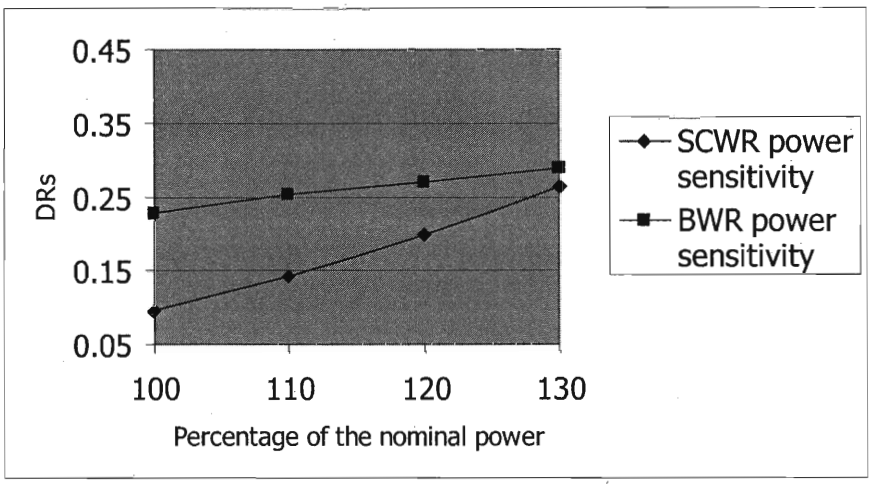

Fig. 9-24: Power sensitivity of the SCWR and the BWR in-phase stability

From Fig. 9-24, it is seen that although the BWR has a higher decay ratio at the nominal state than the SCWR, the slope of the power sensitivity line is quite smaller than the SCWR, which means that the BWR is less sensitive to power than the SCWR.

The flow sensitivity is plotted in Fig. 9-25 for both the SCWR and the BWR.

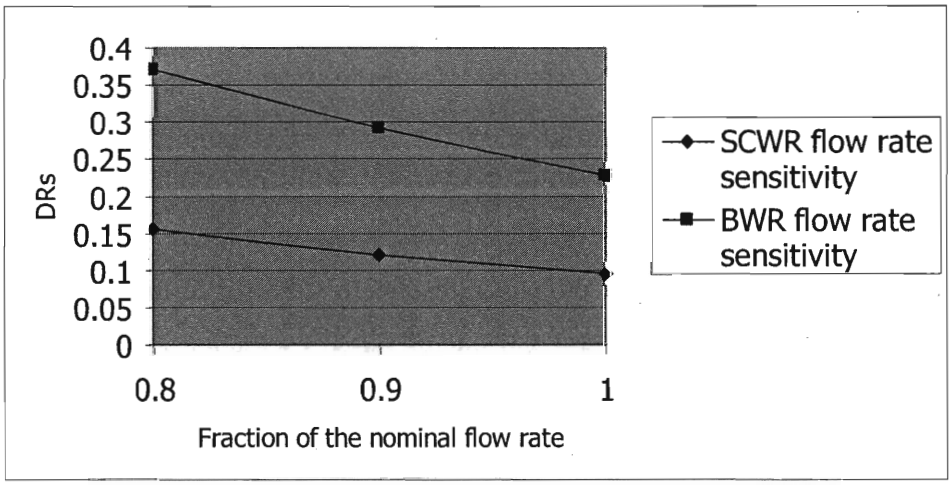

Fig. 9-25: Flow rate sensitivity of the SCWR and the BWR in-phase stability

From Fig. 9-25, it is seen that both the SCWR and the BWR are sensitive to the flow rate. Changing the flow rate has a larger effect on in-phase stability for the BWR. Unlike the

SCWR, the BWR has the enthalpy feedback to the core inlet. Decreasing the flow rate of the BWR, the enthalpy oscillation feedback will be more delay, which gives a destabilization effect. Therefore, changing the flow rate has a larger effect on the BWR.

9.5 Water rods heating effects on the SCWR in-phase stability

The water rods heating effects on SCWR in-phase stability was analyzed in this section.

Although, from the dynamics view point, the out-of-phase and in-phase stabilities are different modes, the steady state condition will be the same for these two stability modes. Therefore, the steady state calculation and results described in the out of phase analysis is applied for the in phase stability analysis. For the lumped three channels case, the core inlet temperature and water rods outlet temperatures for individual lumped channel can be found in Table 8-9. Since the water rods flow is in the first region of the three region model when the RPV inlet temperature is around the steady state temperature, the water rods flow was simulated by the first region model just like in the out of phase case. The technique applied for the water rods density reactivity feedback in the out of phase case is also applied for the in phase stability case.

It is assumed that the core inlet enthalpy is constant during both the single channel and out of phase stability. This assumption is reasonable for single channel stability analysis since the single channel enthalpy oscillation will be absorbed in the lower plenum by the majority constant flow rate from the remaining channels. Also, it is reasonable for the out of phase stability analysis because the out of phase oscillation is an anti-symmetric feature, the enthalpy oscillations will be counteracted after mixing in the lower plenum. However, for the in phase stability, the core inlet enthalpy oscillation must be taken into account just like the BWR in phase stability analysis. Like in the single channel and out-of-phase stability analysis, the heat flux fluctuation of the water rods wall is neglected.

W. S. Yang and N. Zavaljevski (2003) calculated the water rods density reactivity feedback coefficients for the U.S. reference SCWR design. At full power steady state,

they obtained water rods density coefficient of about $C_{den,w} = 7.5 \times 10^{-5} /(kg/m^3)$. Although the water rods feedback coefficient is larger than the coolant density coefficient which is about $1.0 \times 10^{-5} /(kg/m^3)$, the water density oscillation in the water rods is small since only about 10% of the total energy is transferred into the water rods. Therefore, the majority density feedback will be due to the upward coolant flow. The oscillation of the water rods density was calculated through the following procedure. For a specific node *i:*

$$\rho_w^i = \rho_w^i(P, h_w^i) \tag{9-117}$$

therefore,

$$\delta\rho_w^i = (\frac{d\rho_w}{dh_w})_P \delta h_w^i + (\frac{d\rho_w}{dP})_h \delta P \tag{9-118}$$

Since the pressure oscillation contribution to the density oscillation is small compared with the enthalpy contribution, above equation can be simplified as:

$$\delta\rho_w^i = (\frac{d\rho_w}{dh_w})_P \delta h_w^i \tag{9-119}$$

Then, the average density oscillation can be obtained by applying the weighting method described in the section 8.1, as:

$$\delta\widetilde{\rho}_w = \sum_{i=1}^{N} W_i \delta\rho_w^i \tag{9-120}$$

Therefore, the water rods reactivity feedback can be calculated as:

$$\delta\rho_{den,w} = C_{den,w}\delta\widetilde{\rho}_w \tag{9-121}$$

Adding the water rods density feedback up to the upward flow density feedback, the total density reactivity feedback can be obtained.

9.5.1 Water rods heating effect

The decay ratios and oscillation frequencies at different RPV inlet temperatures around the steady state value, i.e. 280°C, were calculated and plotted in the following Fig. 9-26 and Fig. 27. For comparison, both with the water rods heating and without water rods heating are plotted.

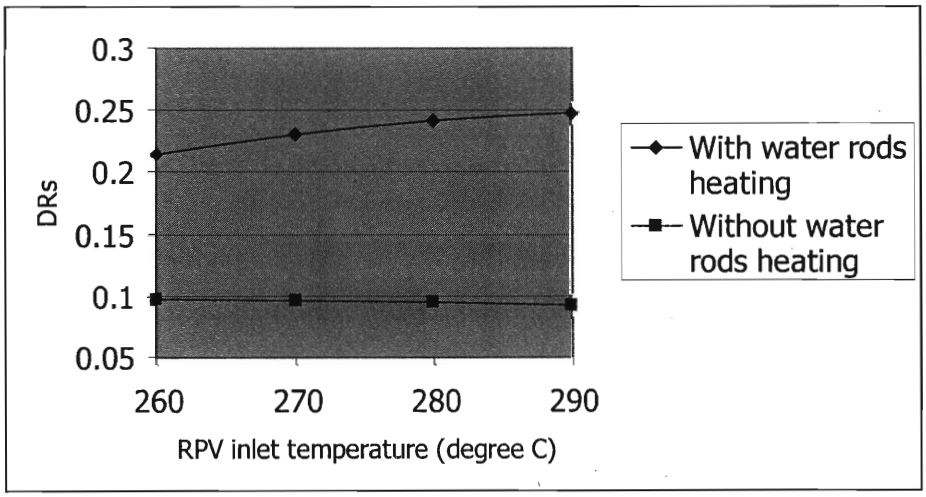

Fig. 9-26: Water rods effects on the decay ratio of the SCWR in phase stability

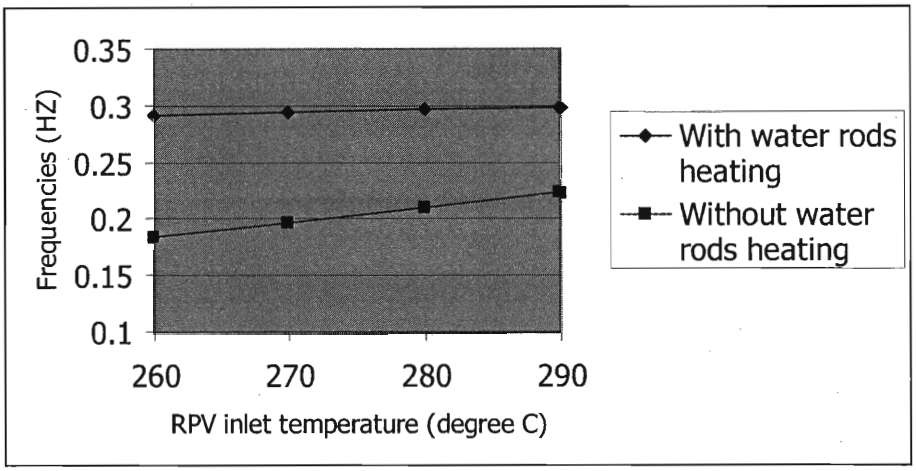

Fig. 9-27: Water rods effects on oscillation frequency of the SCWR in phase stability

From Fig. 9-26, it is seen that the water rods heating will decrease the in-phase stability significantly, while it will enhance the single hot channel and out-of-phase stability. Like the single hot channel and out-of-phase, the water rods heating will increase the oscillation frequencies.

Both the single channel oscillation and the out-of-phase oscillation deal with the parallel upward flow channels. With the water rods heating, the upward flow loses the energy. At the same time, the inlet temperature of the upward flow is increased. Both of them are stabilization effects.

However, the in-phase oscillation deals with the whole flow path. With the water rods heating, it is just that some of the energy added to the other part of the flow path (water rods part). There is no heat loss for this whole flow path. Adding more energy in the upstream part of the flow path will generate the following two effects:

1. A larger fluctuation at the boundary between the incompressible fluid part and the compressible fluid part.
2. Increasing the flow length of the compressible fluid part.

Both of above two factors are destabilization effects. Therefore, the water rods heating will destabilize the in-phase stability mode.

9.5.2 Water rods flow rate sensitivity analysis

As in the single channel and out-of-phase stability analysis, the water rods flow rate effect on in-phase stability was studied by varying the water rods flow rate from 70% to the total flow. The decay ratios and the frequencies for the different water rods flow rate are plotted in Fig. 9-28 and 9-29.

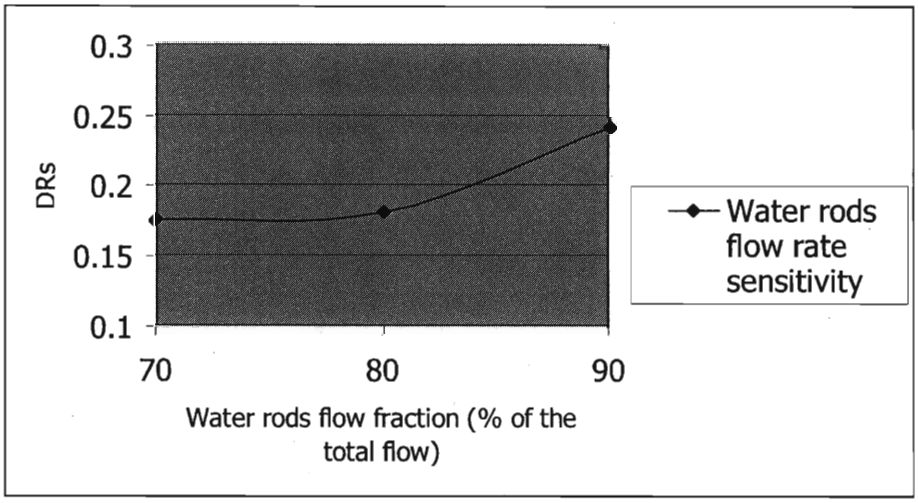

Fig. 9-28: The water rods flow effect on decay ratios of the in-phase stability

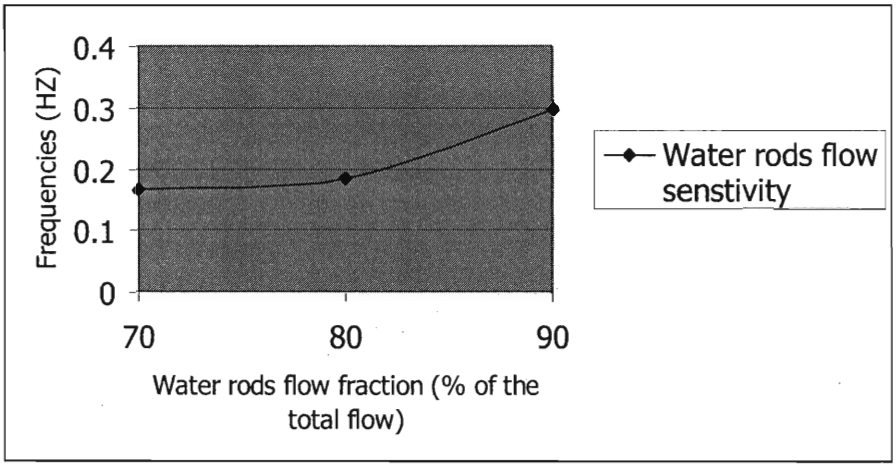

Fig. 9-29: The water rods flow effect on frequencies of the in-phase stability

From Fig. 9-28, it is seen that a larger water rods flow fraction will diminish the in-phase stability. The larger water rods flow fraction will extract more energy from the upward flow to generate a larger fluctuation of the boundary between incompressible and compressible part, therefore, the larger water rods flow will make the system more unstable.

From Fig. 9-29, the larger water rods flow rate will increase the oscillation frequency. Since the flow velocity is higher in the water rods, the transport time of the fluid in the system is reduced. Therefore, the frequency is increased.

9.5.3 Power and flow sensitivity with water rods heating

In this section, the power and flow sensitivity analysis is conducted for the SCWR in-phase stability with water rods heating. The upward flow inlet and water rods outlet temperatures at different power levels and different flow rates for in-phase stability are the same with the out-of-phase stability as listed in Table 8-11 and 8-12.

The decay ratios sensitivity against power and flow rate for both with water rods heating and without water rods heating were plotted in Fig. 9-30 and Fig. 31, respectively.

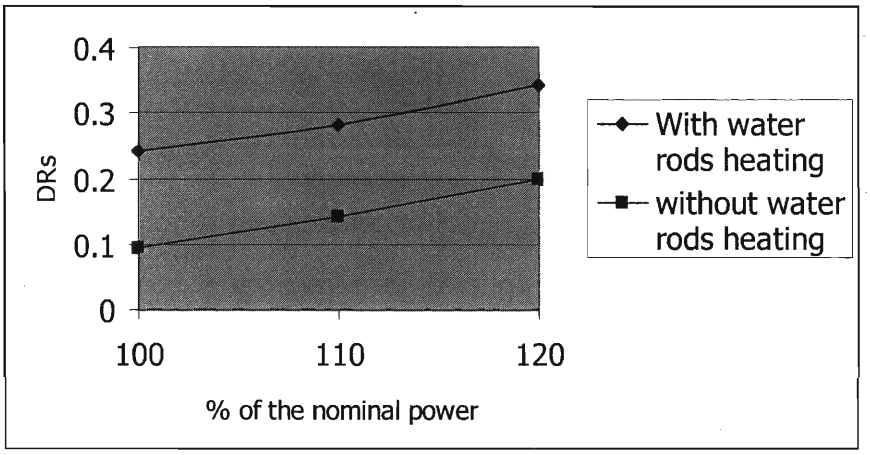

Fig. 9-30: SCWR power sensitivity for in-phase stability with water rods heating

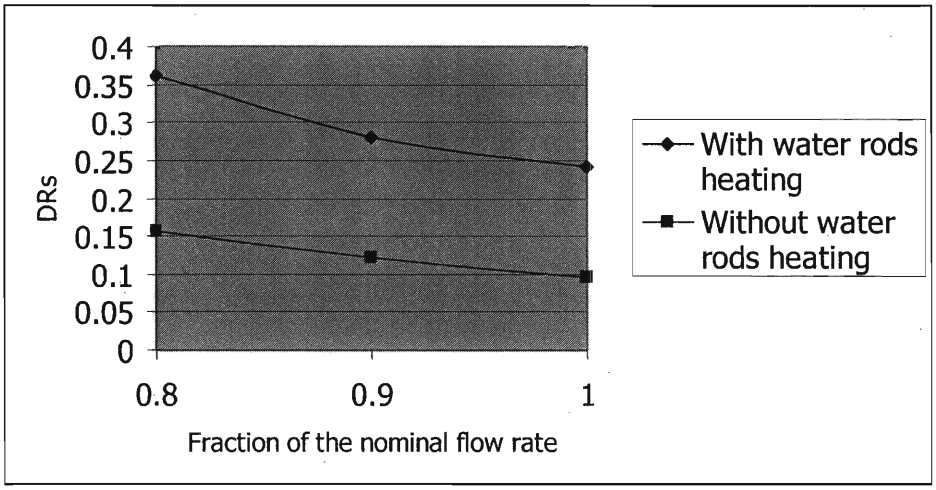

Fig. 9-31: SCWR flow rate sensitivity for in-phase stability with water rods heating

From Fig. 9-30 and 9-31, it is seen that the SCWR in-phase stability is sensitive to power and flow rate for with the water rods heating, the same as without water rods heating case.

Chapter 10

Summary and Conclusions

10.1 Summary of Conclusions

At steady state, the U.S. reference SCWR can be designed to be stable for all of the three density wave oscillation modes, i.e. the single channel mode, and neutronically coupled region-wide and core-wide modes. The stability depends on the choice of the core inlet orifice and the exit valve at the hot fluid line. As long as they have appropriate coefficient values, the design will be stable. The most limiting stability mode among the three modes, for the nominal operating conditions analyzed in this thesis, is the single hot channel oscillation mode. In our design, the hot channel has an inlet orifice coefficient of 20.0 and the exit valve has a coefficient of 0.25.

The U.S. reference SCWR design can also be made stable during a sliding pressure startup, once a proper startup procedure is chosen with the flow and power increasing at steps compatible with the pressure steps.

For the Ledinegg type instability, it was found that the U.S. reference SCWR design would not experience such an instability problem at normal operating conditions.

Through a sensitivity analysis of the operating parameters, such as power and flow, it was concluded that the SCWR is more sensitive to changes in these parameters than the typical BWR. The traditional stability measures of the oscillation decay ratio may not be sufficient for the SCWR, since a small decay ratio does not capture the extent to which a stability margin exist in a particular design of the SCWR. The robustness of stability can be assessed by finding the sensitivity of the decay ratio to the operating conditions, and ensuring an accommodation of the potential variation and/or uncertainty about these conditions.

The presence of water rods in the US SCWR design plays an important role in stability. The SCWR is less sensitive to the coolant density neutronic reactivity coefficient than the typical BWR, since most of the neutronic moderation function is provided by the water rods, which have no density oscillation (if the water rods are insulated) or small density oscillation (with water rods heating). The water rods heating will enhance the single channel stability and the out-of-phase (regional) stability, but it will diminish the in-phase (core-wide) stability.

Without the two-phase flow riser, the steam separator and the dryer, which lead to instability by increasing the pressure drop of the two phase (compressible) region in a typical BWR, the SCWR in-phase stability is improved. However, other flow restrictions such as exit valve in the hot fluid line may destabilize the system significantly due to the high velocity in that line. To make the system stable, flow restrictions in the hot fluid line should be made as small as possible.

10.2 Single channel stability analysis

The single channel stability was analyzed first through a system response matrix decay ratio calculation. It was found that for the U.S. reference SCWR design, an inlet orifice coefficient of 1.0 would be required for the hot channel to satisfy the stability criterion of a perturbation decay ratio of 0.5. However, a higher inlet orifice coefficient should be used to provide margin against uncertainties in core operating conditions, and partial

power or off-normal operations. A core pressure drop of 0.163MPa yields an inlet orifice coefficient of 20.0 for the hot channel, and an inlet orifice coefficient of 115.0 for the average channel. At this core pressure drop, both the hot and average channels will be very stable at full power normal operating conditions. A sensitivity analysis was conducted. It was found that the perturbation decay ratio in the SCWR hot channel is sensitive to mass flow rate, power level and system pressure (to a lesser degree). The hot channel, with an inlet orifice coefficient of 20.0, will be stable for a mass flow rate above 83% of the nominal flow rate and power level less than 121% of the nominal power level.

A stability analysis was also conducted by using the traditional frequency domain method, i.e. linearization and Laplace transformation of the mass, energy and momentum conservation equations. The supercritical water was simulated by using a three region model. A non-dimensional analysis of the conservation equations for the three regions under supercritical pressure was performed. It was found that the governing parameters for single channel instability are the Pseudo Subcooling number ($N_{psub} = \frac{(h_B - h_{in})}{h_{AB}} \frac{\rho_{AB}}{\rho_B}$) and the Expansion number ($N_{esp} = \frac{R}{pC_p} \frac{q'' P_h}{A_c} \frac{L}{u_{in}}$). A stability boundary map was plotted in the domain of the Pseudo Subcooling number and the Expansion number. It was found that the U.S. reference design would operate in a stable region with a large margin. The three region model was evaluated using the only open experimental data for a supercritical boiler, but the inlet and outlet restrictions for the experiment were unavailable. It was assumed that there were no inlet and outlet restrictions during the model evaluation. The divergence of the predicted values was within about 30% of the experimental data.

The stability results calculated by the response matrix method were compared with those of the traditional frequency domain method, and the results calculated by the two methods matched quite well.

The fuel dynamics effect was studied by adding a lumped parameter fuel dynamics model to the constant fuel surface heat flux model. It was found that the fuel heat capacity will smooth the water oscillation therefore stabilize the system, which is consistent with the literature findings, i.e. a larger fuel diameter pin usually stabilizes the system more than a thinner fuel pin.

The power and flow rate sensitivity of the single channel stability was analyzed for the U.S. reference SCWR design and compared with a typical BWR. It was found that the SCWR is more sensitive to power and flow rate changes than the typical BWR.

Also, the water rods heating effect was analyzed. It was found that although the water rods heating will improve the single channel stability, it can not significantly improve the power and flow sensitivity of the SCWR stability.

Finally, a model for the subcritical pressure conditions was developed and applied to the SCWR startup stability analysis. In the subcritical pressure region, a comparison of four different two phase flow models was made. It was found that the homogeneous non-equilibrium model (HNEM) would predict the most conservative stability boundary at high Subcooling Numbers, whereas the homogeneous equilibrium model (HEM) would yield the most conservative stability boundary at low Subcooling Numbers. Also, the stability boundary differences between the four different models will decrease as the pressure increases. At high pressures, the simple HEM model is suitable for a quick check of the stability features. Many experiments have been conducted in the subcritical pressure region. Comparison of the Non-homogenous Non-equilibrium model (NHNEM) and the Homogenous Non-equilibrium model (HNEM) with some of the experimental data revealed that both of these models show good agreement with the data. By taking CHF avoidance and stability assurance into account, a sliding pressure startup procedure for the U.S. reference SCWR design has been suggested.

10.3 Coupled neutronic out-of-phase stability analysis

An out-of-phase stability method was developed through different core lumping methods and applied to both the SCWR and the BWR. It was found that the SCWR was very sensitive to the core lumping approach since the different core lumping approaches generate different equivalent inlet orifice coefficients for the lumped channels. Since the SCWR was assumed to have the same enthalpy rise for all assemblies, the different lumping methods do not change the water properties in the individual channel. The stability effect comes from the different equivalent inlet orifice coefficients for different lumping strategies. It was also found that the SCWR out-of-phase stability is dominated by the hottest channel (channel group). Once the hottest channel (channel group) is separated, the stability analysis results were not affected much by the details of lumping the remaining assemblies. The same lumping effect was also analyzed for the BWR. It was found that the BWR is not as sensitive to the different lumping approaches as the SCWR. Also, the stability was not as dominated by the hottest channel as the SCWR. The reason is that the BWR has a quite larger void reactivity feedback coefficient and the stability is sensitive to the void coefficient which is related to the core average condition.

Through power and flow sensitivity comparison between the SCWR and the BWR, it was found that the SCWR is much more sensitive to both the power and flow rate than the typical BWR.

Like the single channel stability, the water rods heating will stabilize the out-of-phase stability mode, through increasing the upward flow inlet temperature and decreasing the net heat deposition into the upward flow.

10.4 Coupled neutronic in-phase stability analysis

For the U.S. reference SCWR design, the flow velocity in the hot fluid line is as high as 97.0m/s (40.5m/s for typical BWR). At such high flow velocity, the SCWR in-phase stability is very sensitive to the flow restrictions in that line. Through a sensitivity analysis, it was found that the stability is very sensitive to the exit valve coefficient. To make the system stable, a very small coefficient must be used. A coefficient of 0.25 was

assumed during the current analysis. The stability is not sensitive to turbine control valve coefficient since the turbine control valve has a pump-like pressure loss characteristic, which is independent on velocity if a flat feature was assumed i.e. the coefficient equals zero.

Through a sensitivity analysis of the density reactivity feedback coefficients, it was found that both the SCWR and the BWR are sensitive to the density coefficients and the SCWR is less sensitive than the BWR. The sensitivity of the coupled fundamental mode of the in-phase oscillation is much larger than the coupled first subcritical mode of the out-of-phase stability.

Through a comparison of all of the three density wave oscillation modes, it was found that the single hot channel stability mode is the most limiting one at the nominal operating state for the U.S. reference SCWR design.

Power and flow rate sensitivity analysis was also conducted for both the SCWR and the BWR in-phase stability. Although the BWR is less sensitive to the power than the SCWR, both of them are sensitive to the flow rate.

Also, the water rods heating was found to have a destabilization effect on the SCWR in-phase stability.

10.5 Combined Stability Envelop

10.5.1 Steady state conditions

At steady state condition, the single channel and core wide in-phase decay ratios for SCWR, typical BWR and ESBWR are combined in Fig. 10-1. As mentioned in Chapter 8, the out-of-phase stability of SCWR is dominated by single hot channel, once the system is stable for single hot channel, the out-of-phase will also be stable. Therefore, only the decay ratios for the single channel and in-phase stability are listed in Fig. 10-1. This

figure is typically used in the representation of BWR stability limits and operating conditions [Shiralkar, 2005]. The ESBWR decay ratios are taken from [Shiralkar, 2005].

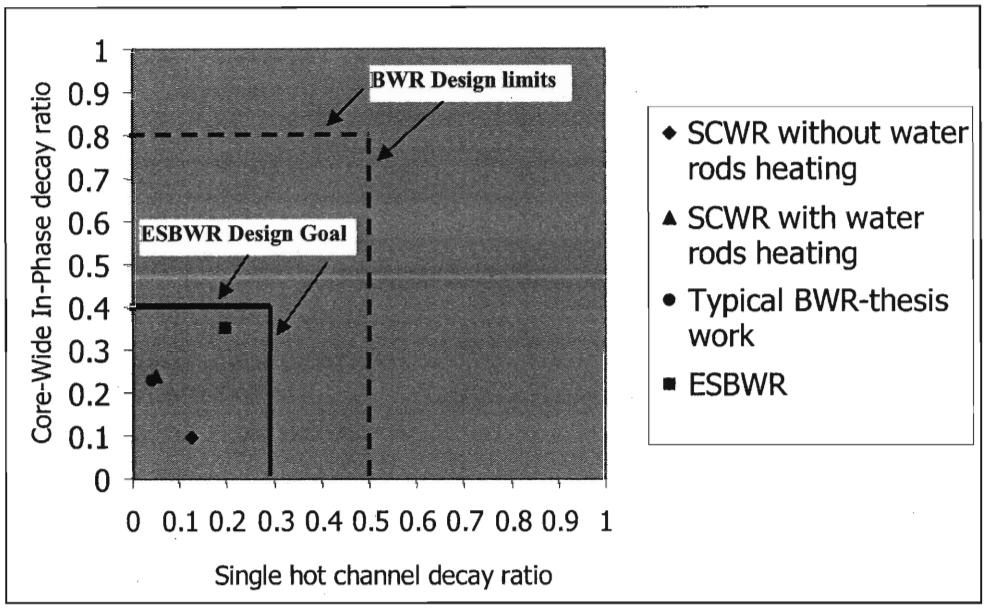

Fig. 10-1: Combined decay ratios for SCWR and BWR

It can be seen that the U.S. reference SCWR design is far away from the design limits. Water rods heating improves the single channel stability while deteriorates the core wide in-phase stability. However, the proximity of the operating points of the SCWR and the BWR do not imply the same robustness to variations in operating conditions.

10.5.2 Power sensitivity (120% of the steady state power)

To assess the power stability margin, the decay ratios at 120% of the steady state power conditions were calculated and are plotted in Fig. 10-2 for both the SCWR and the typical BWR.

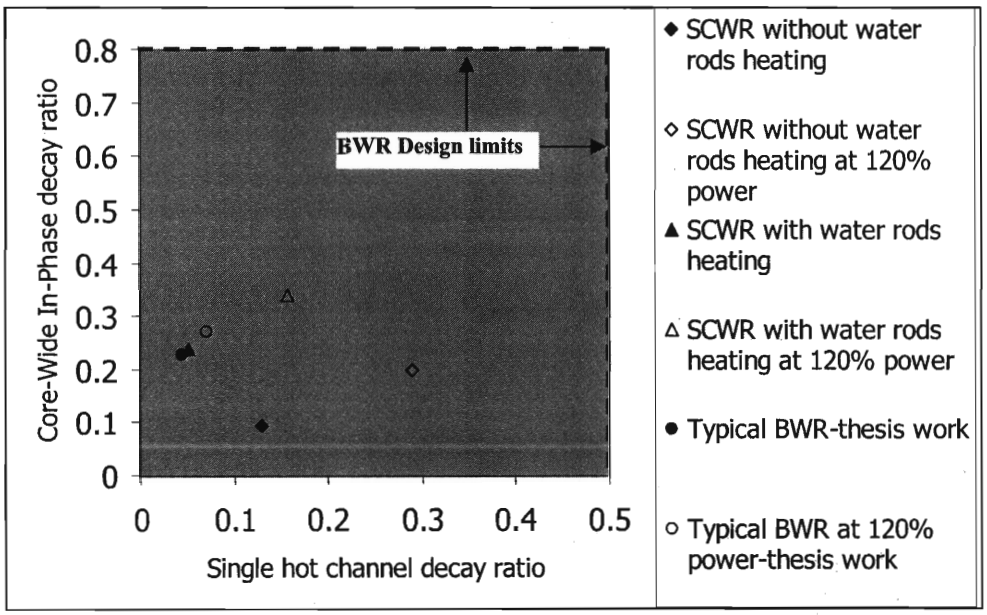

Fig. 10-2: Combined decay ratios for SCWR and BWR at 120% power

From Fig. 10-2, it is seen that the SCWR is more sensitive to power for both single hot channel and core-wide in-phase stabilities.

10.5.3 Flow sensitivity (80% of the steady state flow)

To investigate the flow sensitivity, the decay ratios at 80% of the steady state flow conditions have been calculated and are plotted in Fig. 10-3 for both the SCWR and the typical BWR.

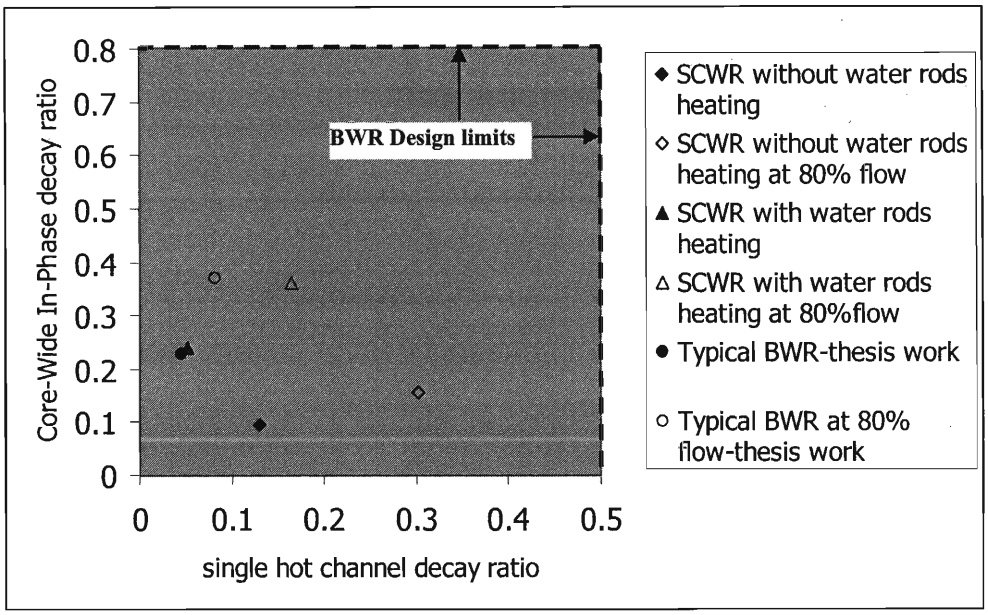

Fig. 10-3: Combined decay ratios for SCWR and BWR at 80% flow

From Fig. 10-3, it is seen that although the SCWR flow sensitivity is comparable to the BWR for in-phase stability, it is more sensitive to flow for single channel stability.

From the above sensitivity comparisons, it can be seen that the SCWR is much more sensitive to single channel stability for all cases. Since it is very difficult to detect, the single channel oscillation may cause serious damage. Therefore, the SCWR must be designed with a large margin to single channel instability.

Through the comparison of the U.S. reference SCWR design and the typical BWR, it can be found that the SCWR experiences more drastic thermal-hydraulic properties changes through the core. This gives the benefit to BWR in comparison with the SCWR. However, from a neutronic perspective, most of the moderation power of the SCWR is provided by the water rods, which have no density oscillation (without water rods heating) or small density oscillation (with water rods heating). This gives the benefit to SCWR. Therefore, the comparison of the stability feature of the SCWR and BWR when the combination of these two kinds of effects, i.e. thermal-hydraulic perspective versus neutronic perspective, does not yield full advantage to a single reactor.

10.6 Recommendations for Future work

The following issues are recommended for future investigation:

1. Experiments for supercritical single channel stability should be carried out to evaluate the proposed three region stability model, since the existing experimental data is very limited in this area.

2. The stability effects of other assumptions about heat transfer should be investigated. For example, the different heat transfer coefficient correlations, such as Jackson's correlation should be evaluated. The stability effects of the axial fuel surface heat flux distributions, such as a cosine shape or bottom peaked shape, should be investigated.

3. More studies for off-normal conditions including startup are needed. A power-flow map defining the regions for stable SCWR operations (like BWR) should be developed. The oscillating effects may not be as limiting as the heat transfer effects. Both of these should be investigated for the startup procedure.

4. The robustness of the decay ratio with respect to changes in operating conditions should be pursued as another approach to map the margins for stability. A new design limits map that captures the sensitivity of power and flow changes is needed.

5. As the SCWR design is evolving, stability analysis should be done for the updated designs. The methods developed here can also be applied to designs from international origins.

References

Antoni, O. and Dumaz, P., "Preliminary Calculations of a Supercritical Light Water Reactor Concept using the CATHARE Code", Proceedings of ICAPP'03 Cordoba, Spain, May 4-7, 2003.

ASME, ASME Steam Properties for Industrial Use Based on IAPWS-IF97, Professional version 1.0.1, 1998.

Bestion, D., "The physical closure laws in the CATHARE code," Nuclear Engineering and Design, Vol. 124, pp. 229-245, 1990.

Bowring, R. W., "A simple but accurate round tube, uniform heat flux, dryout correlation for pressure in the range 0.7-17MN/m^2". AEEW-R789, 1972.

Brandes, L.P. and Waschull W., Workshop B. W. R. stability, Holtsville, New York, p 87, OECD/IAEA, 1990

Buongiorno, Jacopo and MacDonald, Philip E., "Supercritical Water Reactor (SCWR) Progress Report for the FY-03 Generation-IV R&D Activities for the Development of the SCWR in the U.S.", INEEL/EXT-03-01210, INEEL, September 30, 2003.

Burns & Roe Enterprises Inc., "Startup Study for SCWR-Generation IV," Draft 4-5-2004.

Carmichael, L.A. and Niemi, R.O., "Transient and Stability Tests at Peach Bottom Atomic Power Station Unit 2 at end of Cycle 2", EPRI NP-564, Electric Power Research

Institute, 1978

Carver, M. B., "An Analytical model for the prediction of Hydro-dynamic instability in Parallel heated channels," A.E.C.L., 2681, Atomic Energy Canada Limited, 1968.

Cheng, X. and Schulenberg, T., "Heat transfer at supercritical pressure-literature review and application to an HPLWR", Forschungszentrum Karlsruhe GmbH, Karlsruhe, 2001

Coddington , P., and Macian, R., "A study of the performance of void fraction correlations used in the context of drift-flux two-phase flow models", Nuclear Engineering and Design 215, 199–216, 2002

Dokhane, A., et. al, "Nuclear-Coupled thermal-hydraulics nonlinear stability analysis using a novel BWR reduced order model", 11th International Conference on Nuclear Engineering, Tokyo, Japan, April 20-23, 2003

Dyadyakin, B.V., and Popov, A.S., "Heat transfer and thermal resistance of tight seven-rod bundle, cooled with water flow at supercritical pressures," Trans. VTI (11), pp. 244–253 (in Russian), 1977.

Etter, D. et al., Introduction to Matlab 6, Prentice Hall, 2002.

Filonenko, G.K., "Hydraulic resistance of the pipelines". Thermal Engineering (4), pp. 40–44 (in Russian), 1954.

Gialdi, E., et al, Prog. Nucl. Energy 15, 447, 1985.

Golub, G. F., and van Loan, Ch. F., Matrix Computations, The Johns Hopkins University Press, 1996.

Hanggi, P., "Investigating BWR Stability with a New Linear Frequency-Domain Method and Detailed 3D Neutronics," a Ph.D. dissertation submitted to the Swiss Federal Institute of Technology, Zurich, 2001.

Hashimoto, K., "Linear modal analysis of out-of-phase instabilities in boiling water reactor cores", Ann. Nucl. Energy, 20, pp. 789-797, 1993

Hashimoto, K., et. al, "Neutronic model for modal multichannel analysis of out of phase instabilities in boiling water reactor cores", Ann. Nucl. Energy, 24, pp. 99-111, 1997

Holman, J. P., "Experimental Methods for Engineers", 7th Edition, pp 291-295, Boston: McGraw-Hill, 2001

Ilse C. F. Ipsen, "Computing an eigenvector with inverse iteration", SIAM Review, Vol. 39, No.2, 254-291, Jun., 1997.

Ishii, M., and Zuber, N., "Thermally Induced Flow Instabilities in Two Phase Mixtures," Paper No. B 5.11, 4th International Heat Transfer Conference, Paris, 1970.

Ishii, M., "Thermally induced flow instabilities in two-phase mixtures in thermal equilibrium", Ph.D. Thesis, School of Mechanical Engineering, Georgia Institute of Technology, Atlanta, Georgia, June, 1971.

Kao, C., "A Boiling Water Reactor Simulator for Stability Analysis", Ph.D. Dissertation, MIT, 1996

Karve, A. A., "Nuclear-Coupled Thermal-Hydraulic Stability Analysis of Boiling Water Reactors", Ph.D. Dissertation, University of Virginia, 1999

Kelley, C.T., "Solving non-linear equations with Newton's method", North Carolina State University, SIAM, 2003

Khabensky, V. B. and Gerliga, V. A., Hydrodynamic Flow Instabilities in Power Equipment Components, CBS Publishers & Distributors, New Delhi, India, 1995.

Kirillov, P.L., Yur'ev, Yu.S., Bobkov, V.P., 3.2. Flow hydraulic resistance of the working fluids with significantly changing properties, pp. 66–67. 8.4. Working fluids at nearcritical state, pp. 130–132. In: Handbook of Thermal-Hydraulics Calculations. Energoatomizdat Publ. House, Moscow, Russia, 1990

Koshizuka, S., Oka, Y., and Suhwan, J., 2003, "Stability Analysis of a High Temperature Reactor Cooled by Supercritical Light Water," Paper No. 1166, GENES4/ANP2003, Kyoto, Japan.

Lahey, R. T. Jr. and Podowski, M.Z., "Two Phase Flow Instabilities", Multiphase Science and Technology, 4, pp. 183-371, 1989.

Lahey, R. T., Jr., and Moody, F. J., The Thermal Hydraulics of a Boiling Water Nuclear Reactor, Chapter 7, La Grange Park, Ill., USA: American Nuclear Society, 1993.

Levy, S., "Forced convection subcooled boiling-prediction of vapor volumetric fraction," Int. J. Heat Mass Transfer, Vol.10, p. 951, 1967.

Marcelles, I. and Ballesteros, A., "EFFECT OF IRRADIATION ON WATER REACTORS INTERNALS", Volume 2, General Review of Reactor Vessel Internals: Boiling Water Reactors, May 1997

March-Leuba, J., "LAPUR benchmark against in-phase and out-of-phase stability tests", NUREG/CR-5605, ORNL/TM-11621, Oct., 1990

March-Leuba, J. and Blakeman, E.D., "A Mechanism for Out-of-Phase Power Instabilities in Boiling Water Reactors", Nuclear Science and Engineering: 107, 173-179, 1991

March-Leuba, J., and Rey, J.M., "Coupled Thermohydraulic-Neutronic instabilities in boiling water nuclear reactors: a review of the state of the art", Nuclear Engineering and Design, Vol. 145, No. 1-2, pp. 97-111, Nov., 1993.

Mata, P., et al, "Analysis of Cofrentes abnormal plant transients with RETRAN-02 and RETRAN-03", Nuclear Technology, Vol. 100, n 2, p. 203-215, 1992

Munoz-Cobo, J.L., et. al, "Non linear analysis of out of phase oscillations in boiling water reactors", Ann. Nucl. Energy, Vol. 23, No. 16, pp.1301-1335, 1996

Munoz-Cobo, J.L., et. al, "Coupling of density wave oscillations in parallel channels with high order modal kinetics: application to BWR out of phase oscillations", Ann. Nucl. Energy, 27, pp.1345-1371, 2000

Munoz-Cobo, J. L., Podowski, M.Z., and Chiva, S., "Parallel channel instabilities in boiling water reactor systems: boundary conditions for out of phase oscillations", Annals of Nuclear Energy, 29, pp.1891-1917, 2002.

Nakatsuka, T., Oka, Y., and Koshizuka S., "Startup Thermal Considerations for Supercritical-Pressure Light Water-Cooled Reactors", Nuclear Technology, Volume 134, Number 3, pp. 221-230, June 2001.

Peters, G. and Wilkinson, J. H., "Inverse iteration, ill-conditioned equations and Newton's method", SIAM Review, Vol. 21, No.3, pp. 339-360, July 1979.

Pioro, I. L., Duffey, R. B., and Dumouchel, T. J., "Hydraulic resistance of fluids flowing in channels at supercritical pressures (survey)", Nuclear Engineering and Design, Vol. 231, pp. 187–197, 2004.

Podowski, M. Z. and Lahey, R. T. Jr., and Clausse, A., "Modeling and analysis of channel to channel instabilities in boiling systems", Chem. Eng. Comm. Vol. 93, pp. 75-92, 1990.

Podowski, M. Z., "Modeling and analysis of two-phase flow instabilities", NURETH-10, Seoul, Korea, October 5-9, 2003.

Porter, B., "Stability Criteria for Linear Dynamical Systems", Academic press, New York, 1968.

Saha, P., "Thermally Induced Two-Phase Flow Instabilities, Including the Effect of Thermal Non-Equilibrium Between the Phases", Ph.D. Thesis, School of Mechanical Engineering, Georgia Institute of Technology, Atlanta, Georgia, 1974

Saha, P. and Zuber, N., "Point of net vapor generation and vapor void fraction in subcooled boiling," Paper No. B4.7, Proceedings of the Fifth International Heat Transfer Conference. Tokyo, Japan, Vol. IV. JSME and SCEJ, Tokyo, 1974.

Saha, P., Ishii, M. and Zuber, N., "An experimental investigation of the thermally induced flow oscillations in two-phase systems", J. Heat Mass Transfer, Vol. 98C, p. 616, 1976.

Saha, P., and Zuber, N., "An Analytical Study of Thermally Induced Two-Phase Flow Instabilities Including the Effect of Thermal Non-Equilibrium", Int. J. Heat Mass Transfer, Vol. 21, pp.415-426, 1978

Shiralkar, B., "ESBWR design and performance", Presentation for MIT Nuclear Plant Safety Course, June 22, 2005

Solberg, K., "Resulats des Essais d'Instabilites sur la Boucle 'Culine' et Comparisons avec un Code de Cakcykm" C.E.N.G., Note 225, Centre d'Etudes Nucleaires de Grenoble, France, 1966

Solis, J., Ivanov, K.N. and Sarikaya, B., "BOILING WATER REACTOR TURBINE TRIP (TT) BENCHMARK", Volume I: Final Specifications, Nuclear Engineering Program, the Pennsylvania State University, 2001

Takigawa, Y., Takeuchi, Y., Tsunoyama, S., Ebata, S., Chan, K., Tricoli, C., "Caorso limit cycle oscillation analysis with three-dimensional transient code TOSDYN-2", Nuclear Technology, V. 79, pp. 210–227, 1987.

Todreas, N. E., and Kazimi, M. S., Nuclear System I, Thermal Hydraulic Fundamentals, Chapter 1, Hemisphere Publishing Corporation, 1990.

Van der Hagen, T.H.J.J., et al, Nuclear Technology, 107, p. 193-214, 1994.

Van der Hagen, T.H.J.J., Zboray, R. and Kruijf, W.J.M. de, "Questioning the use of the decay ratio in BWR stability monitoring", Annals of Nuclear Energy 27 (2000) p727-732

Wagner, W., et al, "The IAPWS Industrial Formulation 1997 for the Thermodynamic Properties of Water and Steam," ASME J. Eng. Gas Turbines and Power, Vol. 122, pp. 150-182, 2000.

Wang, Fu-Shin, et al, "Thermal and Stability Analysis of a Two-Phase Natural Circulation Loop", Nuclear Science and Engineering: 117, 33-46, 1994

Woffindon, F.B. and Niemi, R.O., "Low-Flow stability tests at Peach Bottom atomic power station Unit 2 during cycle 3", EPRI NP-972, April, 1981

W. Wulff et al., "High-Speed BWR Power Plant Simulations on the Special-Purpose Peripheral Processor AD10," BNL-NUREG-34167, International Conference on Simulation for Nuclear Reactor Technology, Cambridge, England, April 9-11, 1984

Yamaji, A., Oka, Y. and Koshizuka, S., "Three-dimensional Core Design of SCLWR-H with Neutronic and Thermal-hydraulic Coupling", Proc. of Global 2003, New Orleans, LA, Nov. 16-20, 2003

Yang, W.S. and Zavaljevski, N., "Preliminary stability analysis for Supercritical Water Reactor," Proc. of Global 2003, New Orleans, LA, Nov. 16-20, 2003

Yang, W.S. and Zavaljevski, N., "Effects of water rods on Supercritical Water Reactor stability," Proc. of ICAPP'05, Seoul, Korea, May 15-19, 2005

Yi, T.T., et al, "A linear stability analysis of supercritical water reactors, (I) thermal-hydraulic stability", Journal of Nuclear Science and Technology, Vol. 41, No. 12, p. 1166-1175, 2004

Yi, T.T., et al, "A linear stability analysis of supercritical water reactors, (II) coupled neutronic thermal-hydraulic stability", Journal of Nuclear Science and Technology, Vol. 41, No. 12, p. 1176-1186, 2004

Yu, K. L. and Glusker B.N., "Flow stability investigation in parallel coils with upflow-downflow of the fluid at subcritical and supcritical pressures", CKTI Proceeding, Leningrad, issue 59, pp. 198-217, 1965.

Zhao, J., Saha, P. and Kazimi, M. S., "One Dimensional Thermal-Hydraulic Stability Analysis of Supercritical Fluid Cooled Reactors", ICONE 12-49075, Arlington, Virginia USA, 2004

Zhao, J., Saha, P. and Kazimi, M. S., "Stability of Supercritical Water-cooled Reactor during Steady-State and Sliding Pressure Start-up", NURETH-11, October 2-6, 2005

Zuber, N., "An Analysis of Thermally Induced Flow Oscillations in the Near-Critical and Super-Critical Thermodynamic region", Final Report Nas8-11422, May 25, 1966

Appendix A

Nomenclature

English

A_s : System matrix

$A_{general}$: Generalized system matrix

A_c : Fuel assembly cross sectional flow area (m^2)

A_w : Flow area for water rods flow (m^2)

C_{den} : Density reactivity coefficient

C_{dop} : Doppler reactivity coefficient

C_k : Kinematic wave velocity (m/s), $C_k = j + V_{gj}$

C_o : Void distribution parameter

c_p : Specific heat at constant pressure [kJ/(kg K)]

D_e : Hydraulic Diameter (m)

$D_{w,e}$: the equivalent diameter for downward water rods flow (m)

e_i : Eigenvectors

f_1 : Friction factor at liquid or "heavy fluid" region

f_2 : Friction factor at two phase mixture or "heavy & light fluid mixture" region

f_3 : Friction factor at vapor or "light fluid" region

G : Mass flux (kg/m^{2}s)

h : Enthalpy (kJ/kg)

$H_{wi,i}$ and $H_{wo,i}$: Water rods inside and outside heat transfer coefficients at node i

j : Volumetric flux density (m/s)

K_{in} : Inlet orifice coefficient

$K_{orifice}$: Orifice coefficient

k_f : Liquid thermal conductivity [W/(m K)]

L : Length of fuel rod heated region (m)

L_{nod} : Length of fuel rod lower gas plenum (m)

L_{nou} : Length of fuel rod upper gas plenum (m)

Δl : Characteristic length for subcooled boiling, $\Delta l = \lambda_{eq} - \lambda_1$, (m)

M : M ratio of the recirculation loop, $M = \dfrac{w_{suction}}{w_{recirculation}}$

$m_{c,i}$: Coolant flow rate for the hot assembly at node i, (kg/s)

$m_{w,i}$: Water rods flow rate for the hot assembly at node i, (kg/s)

N_{sub} : Subcooling Number

N_{pch} : Phase Change Number

N_{psub} : Pseudo Subcooling Number

$N_{\exp}$: Expansion Number

Δp : Pressure drop (MPa)

Δp_{system} : Channel pressure drop (MPa)

$\Delta p_{external}$: External pressure drop imposed on the channel (MPa)

p : Pressure (MPa)

p_{cr} : Water critical pressure (22.1MPa)

P_e : Peclet number $P_e = \dfrac{GD_e c_{pf}}{k_f}$

P_h : Fuel rod outside perimeter per fuel assembly (m)

P_h : Heating parameter of the fuel rods per assembly (m)

P_{wo} : Heating parameter of the water rods outside per assembly (m)

P_{wi} : Heating parameter of the water rods inside per assembly (m)

$q'_{w,i}$: Water rods linear heat transfer rate at node i (kW/m)

q'' : Surface heat flux (kW/m^2)

q'''_v : Volumetric heat flux (kW/m^3)

$q''_{f,i}$: Fuel rods surface heat flux at node i (kW/m^2)

$q''_{c,i}$: Water rods outside surface heat flux at node I (kW/m^2)

$q''_{w,i}$: Water rods inside surface heat flux at node i (kW/m^2)

Q_f : Channel total heat released from fuel rods (kW)

Q_w : Channel total heat transferred to water rods (kW)

r : Radius of the fuel pin (m)

R : Ideal gas constant [J/(mol K)]

R_1 : Fuel pellet radius (m)

R_2 : Fuel cladding inside radius (m)

R_3 : Fuel cladding outside radius (m)

s : Variable of Laplace Transformation

T_o : Fuel centerline temperature (K)

T_f : Fuel temperature (K)

T_c : Fuel cladding temperature (K)

$\overline{T}_{pin}$: Average temperature of the fuel pin (K)

T_w : Wall temperature (K)

$T_{c,i}$: Coolant channel bulk flow temperature at node i (K)

$T_{w,i}$: Water rods bulk flow temperature at node i (K)

$R_{t,i}$: Total heat transfer resistance of the water rods wall at node i

T_∞ : Bulk fluid temperature (K)

t : Time (s)

t_w : Water rods wall thickness (m)

u : Coolant velocity (m/s)

v : Specific volume (m^3/kg)

V_{gj} : Vapor drift velocity (m/s)

w : Flow rate (kg/s)

$x(t)$: Vector of state variables

x : Flow quality

x_{eq} : Equilibrium quality

$x_{eq,exit}$: Equilibrium quality at channel exit

$x_{exit,pseudo}$: Pseudo quality at channel exit

$y(t)$: Vector of constitutive variables.

Greek letters

ρ : Coolant density (kg/m^3)

$\Delta\rho$: Density difference between liquid and vapor at saturation (kg/m^3)

δ : Perturbation

ξ : Fuel pin non-dimensional radius, $\xi = \frac{r}{R_1}$

η : Fuel cladding non-dimensional radius, $\eta = \frac{r - R_2}{R_3 - R_2}$

ξ_i : Derivative of coolant density to enthalpy at constant pressure for axial node i

η_i : Derivative of coolant density to pressure at constant enthalpy for axial node i

σ : Real part of eigenvalue

ϖ : Imaginary part of eigenvalue

λ_i : Eigenvalues

λ_1 : Boundary between liquid region and mixture region (m)

λ_2 : Boundary between mixture region and vapor region (m)

λ_{eq} : Boiling boundary in the thermal equilibrium model (m)

Ω_1 : Two phase mixture or "Heavy & Light fluid mixture" phase change frequency

$$\Omega_1 = \frac{v_{AB}}{h_{AB}} \frac{q^{"} P_h}{A_c}, \text{(rad/s)}$$

Ω_2 : Superheated vapor or "light fluid" expansion frequency $\Omega_2 = \frac{R}{pC_p} \frac{q^{"} P_h}{A_c}$, (rad/s)

α : Vapor void fraction

Γ_g : Actual vapor generation rate (kg/m^{3}s)

$\Gamma_{g,eq}$: Vapor generation rate in the thermal equilibrium model (kg/m^{3}s)

Γ : Velocity to pressure transfer function

π_1 : Heat generation rate to pressure transfer function

Π : Transfer function of the inlet flow oscillation to the total pressure drop oscillation across the channel

ε : An arbitrarily constant number

λ_i : Decay constant of ith-group precursors,

β_i : Fraction of neutrons in ith delayed group,

$\chi_{di}(E)$: ith-group delayed neutron spectra, and

$\chi_p(E)$: Prompt neutron spectra.

λ_m : m^{th} mode reactivity

ϕ_m : m^{th} neutron flux mode

Σ_f : Fission cross section

ν : Number of neutrons per fission

Λ_m : Neutron generation time of the mth mode, which can be described as:

Subscripts

in : Channel inlet

exit : Channel outlet

f : Saturated Liquid

g : Saturated vapor

fg : Difference between values of vapor and liquid at saturation

A : Pseudo saturated liquid

B : Pseudo saturated vapor

AB : Difference between values of Pseudo saturated liquid and vapor

ext : External

m : Two phase mixture

λ : Properties at net vapor generation point

i : Axial node number

1: First region of the three region model

2: Second region of the three region model

3: Third region of the three region model

t : Total fluctuation

F : Feedback fluctuation

ori : Orifice

c : Coolant

w : Water rods

nod : Lower non-heating fuel part

nou : Upper non-heating fuel part

o : Steady state value

Superscripts

*: Dimensionless

o : Steady state value

T : Matrix transport

s : Subcritical reactivity

Acronyms

SCWR: Supercritical water-cooled reactor

LWR: Light water reactor

FPP: Fossil Power Plant

DNB: Departure from Nucleate Boiling

BWR: Boiling Water Reactor

DWO: Density wave oscillations

HEM: Homogenous-Equilibrium model

HNEM: Homogenous-Nonequilibrium model

NHEM: Nonhomogenous-Equilibrium model

NHNEM: Nonhomogenous-Nonequilibrium model

DR: Decay ratio

RPV: Reactor Pressure Vessel

IAPWS-IF97: International Association for Properties of Water and Steam – Industrial Formulation 1997

ASME: American Society of Mechanical Engineers

INEEL: Idaho National Engineering and Environmental Laboratory

BREI: Burns & Roe Enterprises Inc.

PCT: Peak cladding temperature

CHF: Critical heat flux

MCHFR: Minimum Critical Heat Flux Ratio

WR: Water rods

DC: Downcomer

DW: Downward

UP: Upper plenum

LP: Lower plenum

st: Steam line

v: Exit valve

tv: Turbine control valve

rs: Riser

sep: Steam separator

FW: Feed water

SABS: code for Stability Analysis of BWR and SCWR

Appendix B

Program description

The models described in the thesis are programmed in MATLAB compiler. The characteristic equations are solved numerically by a Newton Solver developed by Kelley (2003). The source code of this SCWR and BWR analysis is named SABS, which stands for Stability Analysis for BWR and SCWR. The source code is submitted to the department together with the thesis.

The source code for the SCWR single channel with fuel dynamics analysis is presented here. The code for the coupled neutronic out-of-phase and in-phase stability analysis has the similar scheme as the single channel analysis. Since coupled neutronic ones are very long, they are not listed here. The code for BWR stability analysis has the same scheme as the SCWR.

B.1 Source code description for the SCWR single channel analysis

For this stability analysis package, six subroutines, named diffjac.m, dirder.m, nsol.m, DRSCWR.m, DRSCWR_input.m and DRSCWRf.m can be found. Among them, first three is the Newton solver which can be found in the reference mentioned above. The remaining three are described as follows:

1. DRSCWR.m is the main code which reads the input data from input file DRSCWR_input.m, and calls the Newton solver nsol.m which will solve the characteristic equation described in the file DRSCWRf.m. Then, the dominant root, the decay ratio and the oscillation frequency are calculated and output.

2. DRSCWR_input.m is the input file. The input file includes: the steady state water properties, the geometric data of the fuel assembly, the coolant inlet properties, the inlet orifice coefficient and the original guess of the dominant root. Since the Newton method is local converge, it is important to have reasonable initial guess to make the code converge to dominant root. Since the frequency of the density wave oscillation in the typical reactor is around *0.5 HZ*, one can find that "$-1+3j$" is a good initial guess in the most of the cases.

3. DRSCWRf.m decribes the characteristic equation. This file numerically integrates the conservation equations to develop the characteristic equation. It includes steady state parameters calculations and dynamic parameters calculations.

B.2 DRSCWR_input.m listing

```
% Matlab script for calculating the Decay Ratios of the SCWR single channel stability.
% A three region model is applied
%
%Input file
%
%Written by Jiyun Zhao, Feb. 7, 2004

%%%%%%%%% Beginning of the input file
%Supercritical water properties
P = 25*1.0e6; %Pa, system pressure
```

```
vf = 0.0016015; %kg/m^3, heavy fluid specific volume at pseudo saturation point
vg = 0.0063973; %kg/m^3, light fluid sepcific volume at pseudo quality 1.0
hf = 1626.1591493; %kJ/kg, heavy fluid specific enthalpy at pseudo saturation point
hg = 2627.7339952; %kJ/kg, light fluid specific enthalpy at pseudo quality 1.0
dvisc1 = 0.00007262; %pa*s, heavy fluid dynamic viscocity at pseudo saturation point
dvisc3 = 0.00002883; %pa*s, light fluid dynamic viscocity at pseudo quality 1.0
Prf = 1.07275418; % heavy fluid Prandtl number at pseudo saturation point
Cpf = 6.990531; %kJ/kg, heavy fluid specific heat at pseudo saturation point
kf = 473.6269*1.0e-3; %W/(m*K), heavy fluid thermal conductivity at pseudo saturation
Prg = 2.15091465;%light fluid Prandtl number at pseudo quality 1.0
Cpg = 11.042243;%kJ/kg, light fluid specific heat at pseudo quality 1.0
kg = 147.9898*1.0e-3; %W/(m*K), light fluid thermal conductivity at pseudo quality 1.0

%Ideal gas parameters
R = 8314/18; %J/(mol*K), ideal gas constant
Cp = R/(1-1/1.3)*1.0e-3; %kJ/(kg*K), ideal gas specific heat

%Assembly and fuel variables
d_pin = 0.0102; %m, pin diameter
d_pellet = 8.78e-3; %m, pellet diameter
N_pin = 300; %pin number per assm.
L = 4.27; %m, active length of the core
L_tot = 4.87; %m, total length of the core
d_assm = 0.280; %m, assm. inner side
d_wr = 0.0336; %water rod outer side
N_wr = 36; % water rod number per assm.
N_assm = 145; %assm number of core
Kclad = 21.5e-3; %kW/(m*K), Cladding thermal conductivity
hgap = 5.661; %kW/m^2-K, gap gas conductance
denfuel = 10421*0.95;%kg/m^3, fuel density,95% of the theoretical density
```

```
%Power and flow
massm = 12.71; %kg/s average assem. flow rate at steady state
q_l = 19.2; %kW/m, average linear power per fuel pin
Fpower = 1.3; %radial power factor of hot channel, axially uniform distribution
Fflow = 1.3; %radial flow factor for hot channel

%Inlet conditions
hin = 1229.504148; %kJ/kg, inlet enthalpy
Tin = 280+273.15; %K, inlet temperature

%Inlet orifice coefficient
kin = 20.0;

%Input the initial guess of the dominant root
root_re = -1.0;
root_im = 3.0;

%%%%%%%%%%%%%%%end of the input file
```

B.3 DRSCWR.m listing

```
%Main file
%
%Written by Jiyun Zhao, Feb. 7, 2004

%%%%%%%%% Beginning of the file
clc;
clear all
```

```
global kin denf deng vf vg vfg hf hg hfg P dvisc1 dvisc3 Prf Prg kf kg Cpf Cpg f1 f2 f3 R
Cp G uin L Lnou Lnod Ph Ac De Re1 Re2 Re3 Dh d_pin d_pellet hin qs Tin Kclad hgap
denfuel

DRSCWR_input;

hfg=hg-hf;
denf=1/vf;
deng=1/vg;
vfg=vg-vf;
denfg=denf-deng;

Pw=d_assm*4+d_wr*4*N_wr+pi*d_pin*N_pin; %wetted perimeter
Ph=pi*d_pin*N_pin; %heated perimeter

A_pin=pi/4*d_pin^2; % pin area
Ac=d_assm^2-A_pin*N_pin-d_wr^2*N_wr; %coolant flow area

De=4*Ac/Pw; % equivalent hydraulic diameter
Dh=4*Ac/Ph; % equivalent heated diameter

G=massm/Ac*Fflow; % mass flux at hot channel
uin=G/denf; % inlet velocity
qs=q_l/(pi*d_pin)*Fpower; % surface heat flux

Re1=G*De/dvisc1; % the thermodynamic parameters are set pseudo saturation Temp.
Re3=G*De/dvisc3;
Re2=(Re1+Re3)/2;
f1=(1.82*log10(Re1/8))^-2.0;
f2=(1.82*log10(Re2/8))^-2.0;
f3=(1.82*log10(Re3/8))^-2.0;
```

```
Lnou=(L_tot-L)/2;%upper non-heated part
Lnod=Lnou;

Npsub=(hf-hin)/(hg-hf)*(denf-deng)/deng; % pseudo subcooling number
Nexp=R/(P*Cp)*(qs*Ph/Ac)*L/uin; % expansion number

%Call function nsol.m to solve the characteristic equation

[sol, it_hist, ierr] = nsol([root_re root_im]','DRSCWRf',[1.0e-6 1.0e-6],[100 1 0])

% to determine if it is in three region case
qs_crit=G*Ac*(hf-hin)/(Ph*L);
if (qs<=qs_crit)
   icrit=1;
else
   icrit=0;
end

if (ierr==0)&(icrit==0)
   domin_root=sol(1)+sol(2)*i;
end

 %Calculate the decay ratio

re_domin=real(domin_root);
im_domin=imag(domin_root);
DR=exp(2*pi*re_domin/abs(im_domin));
Freq=abs(im_domin)/(2*pi);

clc;
```

```
%Examine stability characteristic
i_stab=0;
if DR>1.0
   i_stab=1;
end

disp('*************************************')
if i_stab==1
   disp('it is in the unstable region')
else
   disp('it is in the stable region')
end
disp('*************************************')
disp('the dominant root is:')
disp(domin_root)
disp('*************************************')
disp('the decay ratio is:')
disp(DR)
disp('*************************************')
disp('the frequency is:')
disp(Freq)
disp('*************************************')
disp('Expansion number is:')
disp(Nexp)
disp('Pseudo Subcooling number is:')
disp(Npsub)
disp('*************************************')

%%%%%%%%% End of the file
```

B.4 DRSCWRf.m listing

```
%Characteristic equation development
%
%Written by Jiyun Zhao, Feb. 7, 2004

%%%%%%%%% Beginning of the file
function f=DRSCWRf_fuel(v)
a=v(1);
b=v(2);
s=a+b*i;

global kin denf deng vf vg vfg hf hg hfg P dvisc1 dvisc3 Prf Prg kf kg Cpf Cpg f1 f2 f3 R
Cp G uin L Lnou Lnod Ph Ac De Re1 Re2 Re3 Dh d_pin d_pellet hin qs Tin Kclad hgap
denfuel

lamda1=(hf-hin)*G*Ac/(qs*Ph);%length of heavy liquid region
lamda2=(hg-hin)*G*Ac/(qs*Ph);%length of mixture region

xigma1=vfg/hfg*(qs*Ph/Ac);
xigma2=R/(P*Cp)*(qs*Ph/Ac);

%%%%Region 1 pressure oscillation response
n1=400;
dz=lamda1/n1;
Prm=(Prf+Prg)/2;
km=(kf+kg)/2;
Cpm=(Cpf+Cpg)/2;
R1=d_pellet/2;
R2=R1;
R3=d_pin/2;
```

```
Rm=(R1+R3)/2;

Nu1=0.023*Re1^0.8*Prf^0.4;
hwH=Nu1*kf/Dh*1.0e-3;%Kw/m^2C

hcoolH(1)=hin;
TcoolH(1)=Tin;
for j=1:n1+1
   hcoolH(j)=hcoolH(1)+qs*Ph*(j-1)*dz/(G*Ac);
   TcoolH(j)=TcoolH(1)+(hcoolH(j)-hcoolH(1))/Cpf; %degree K
end

for j=1:n1+1
   Ntest=0;
   TfuelH(j)=TcoolH(j)-273.15; %initial guess of fuel temp. degree C

   while Ntest==0
      KfuelH(j)=0.086-1.29e-4*TfuelH(j)+1.0316e-7*TfuelH(j)^2-3.857e-
11*TfuelH(j)^3+5.848e-15*TfuelH(j)^4;
      KfuelH(j)=KfuelH(j)*0.1;%kW/m*K

      Tfuel=(1+(1+Kclad/(R3-R2)/hgap+R1*Kclad/(4*KfuelH(j)*(R3-R2)))*hwH*(R3-
R2)/Kclad)*qs/hwH+TcoolH(j)-273.15;

      if abs(Tfuel-TfuelH(j))>=10
         TfuelH(j)=Tfuel;
      else
         Ntest=1;
      end
   end
```

```
   TfuelH(j)=TfuelH(j)+273.15;%degree K

CpfuelH(j)=296.7*535.285^2*exp(535.285/TfuelH(j))/(TfuelH(j)^2*(exp(535.285/Tfuel
H(j))-1)^2)+2.43e-2*TfuelH(j)+8.745e7*1.577e5/(8.3143*TfuelH(j)^2)*exp(-
1.577e5/(8.3143*TfuelH(j)));
   CpfuelH(j)=CpfuelH(j)*1.0e-3;%kJ/kg-K
end

os_qv=0;

os_hH(1)=0;
for j=1:n1
   Cgm=(R1/R3)^2+(1-(R2/R3)^2)*(6*Rm-(R3-R2))/(12*Rm);
   Fpr=R1^3/((R3-R2)*R3^2)*(Kclad/(4*KfuelH(j))+Kclad/R1/hgap);
   Cqs=1/hwH+2/(s*R3*denfuel*CpfuelH(j))+(Cgm+Fpr)*(R3-R2)/Kclad;
   os_qs(j)=1/Cqs*qs/hwH*0.8/uin+1/Cqs*(R1/R3)^2/(s*denfuel*CpfuelH(j))*os_qv-
1/Cqs/Cpf*os_hH(j);

   os_hH(j+1)=(1-dz*s/uin)*os_hH(j)-qs*Ph*dz/(G*Ac*uin)+os_qs(j)*Ph/Ac*dz/G;
end

os_lamda1=-G*Ac/(qs*Ph)*os_hH(n1+1);

dp1=0;
for j=1:n1
   dp1=dp1+(denf*s+f1*G/De)*dz;
end
dp1=kin*denf*uin+dp1+(f1/De*G^2/(2*denf)+denf*9.81)*os_lamda1;

%%%%Region 2 pressure oscillation response
n2=200;
```

```
dz=(lamda2-lamda1)/n2;
for k=1:n2+1
   um(k)=uin+xigma1*(k-1)*dz;
   denm(k)=G/um(k);
end

os_qvm=os_qv;

Nu2=0.023*Re2^0.8*Prm^0.4;
hwm=Nu2*km/Dh*1.0e-3;%kW/m^2C

hcoolm(1)=hcoolH(n1+1);
Tcoolm(1)=TcoolH(n1+1);
for k=1:n2+1
   hcoolm(k)=hcoolm(1)+qs*Ph*(k-1)*dz/(G*Ac);
   Tcoolm(k)=Tcoolm(1)+(hcoolm(k)-hcoolm(1))/Cpm; %degree K
end

for k=1:n2+1
   Ntest=0;
   Tfuelm(k)=Tcoolm(k)-273.15; %initial guess of fuel temp. degree C

   while Ntest==0
      Kfuelm(k)=0.086-1.29e-4*Tfuelm(k)+1.0316e-7*Tfuelm(k)^2-3.857e-
11*Tfuelm(k)^3+5.848e-15*Tfuelm(k)^4;
      Kfuelm(k)=Kfuelm(k)*0.1;%kW/m*K

      Tfuel=(1+(1+Kclad/(R3-R2)/hgap+R1*Kclad/(4*Kfuelm(k)*(R3-R2)))*hwm*(R3-
R2)/Kclad)*qs/hwm+Tcoolm(k)-273.15;

      if abs(Tfuel-Tfuelm(k))>=10
```

```
        Tfuelm(k)=Tfuel;
      else
        Ntest=1;
      end
    end

    Tfuelm(k)=Tfuelm(k)+273.15;%degree K

Cpfuelm(k)=296.7*535.285^2*exp(535.285/Tfuelm(k))/(Tfuelm(k)^2*(exp(535.285/Tfu
elm(k))-1)^2)+2.43e-2*Tfuelm(k)+8.745e7*1.577e5/(8.3143*Tfuelm(k)^2)*exp(-
1.577e5/(8.3143*Tfuelm(k)));
    Cpfuelm(k)=Cpfuelm(k)*1.0e-3;%kJ/kg-K
end

%Region 2 pressure response calculations
os_hm(1)=os_hH(n1+1);
os_denm(1)=-denf^2*vfg/hfg*os_hm(1);
os_um(1)=1-xigma1*os_lamda1;
for k=1:n2
    Cgm=(R1/R3)^2+(1-(R2/R3)^2)*(6*Rm-(R3-R2))/(12*Rm);
    Fpr=R1^3/((R3-R2)*R3^2)*(Kclad/(4*Kfuelm(k))+Kclad/R1/hgap);
    Cqsm=1/hwm+2/(s*R3*denfuel*Cpfuelm(k))+(Cgm+Fpr)*(R3-R2)/Kclad;

os_qsm(k)=1/Cqsm*qs/hwm*0.8*(os_um(k)/um(k)+os_denm(k)/denm(k))+1/Cqsm*(R1/
R3)^2/(s*denfuel*Cpfuelm(k))*os_qvm-1/Cqsm/Cpm*os_hm(k);

    os_um(k+1)=os_um(k)+dz*vfg/hfg*Ph/Ac*os_qsm(k);
    os_denm(k+1)=denm(k)/um(k+1)*os_um(k)+(um(k)-dz*s)/um(k+1)*os_denm(k)-
denm(k+1)/um(k+1)*os_um(k+1);
    os_hm(k+1)=-hfg/vfg*(1/denm(k+1)^2)*os_denm(k+1);
end
```

```
os_lamda2=-G*Ac/(qs*Ph)*os_hm(n2+1);

dp2=0;
for k=1:n2
   dp2=dp2+2*G*os_um(k+1)+um(k+1)^2*os_denm(k+1)+(s*denm(k)*dz-
2*G+f2*dz*G/De)*os_um(k)+(s*um(k)*dz-
um(k)^2+f2*dz*um(k)^2/(2*De)+9.81*dz)*os_denm(k);
end
dp2=dp2-
(G*xigma1+f2/De*G^2/(2*denf)+denf*9.81)*os_lamda1+(G*xigma1+f2/De*G^2/(2*de
ng)+deng*9.81)*os_lamda2;

%%%%Region 3 pressure oscillation response
n3=100;
dz=(L-lamda2)/n3;
for m=1:n3+1
   uL(m)=uin+xigma1*(lamda2-lamda1)+xigma2*(m-1)*dz;
   denL(m)=G/uL(m);
end

os_qvL=os_qv;

Nu3=0.023*Re3^0.8*Prg^0.4;
hwL=Nu3*kg/Dh*1.0e-3;%kW/m^2-K

hcoolL(1)=hcoolm(n2+1);
TcoolL(1)=Tcoolm(n2+1);
for m=1:n3+1
   hcoolL(m)=hcoolL(1)+qs*Ph*(m-1)*dz/(G*Ac);
   TcoolL(m)=TcoolL(1)+(hcoolL(m)-hcoolL(1))/Cpg; %degree K
```

```
end

for m=1:n3+1
  Ntest=0;

  TfuelL(m)=TcoolL(m)-273.15; %initial guess of fuel temp. degree C

  while Ntest==0
    KfuelL(m)=0.086-1.29e-4*TfuelL(m)+1.0316e-7*TfuelL(m)^2-3.857e-
11*TfuelL(m)^3+5.848e-15*TfuelL(m)^4;
    KfuelL(m)=KfuelL(m)*0.1;%kW/m*K

    Tfuel=(1+(1+Kclad/(R3-R2)/hgap+R1*Kclad/(4*KfuelL(m)*(R3-R2)))*hwL*(R3-
R2)/Kclad)*qs/hwL+TcoolL(m)-273.15;

    if abs(Tfuel-TfuelL(m))>=10
      TfuelL(m)=Tfuel;
    else
      Ntest=1;
    end
  end

  TfuelL(m)=TfuelL(m)+273.15;%degree K

CpfuelL(m)=296.7*535.285^2*exp(535.285/TfuelL(m))/(TfuelL(m)^2*(exp(535.285/Tf
uelL(m))-1)^2)+2.43e-2*TfuelL(m)+8.745e7*1.577e5/(8.3143*TfuelL(m)^2)*exp(-
1.577e5/(8.3143*TfuelL(m)));
  CpfuelL(m)=CpfuelL(m)*1.0e-3;%kJ/kg-K
end

%Region 3 pressure response calculations
```

```
os_hL(1)=os_hm(n2+1);
os_denL(1)=-denL(1)^2*R/(P*Cp)*os_hL(1);
os_uL(1)=os_um(n2+1)+xigma1*os_lamda2-xigma2*os_lamda2;
for m=1:n3
   Cgm=(R1/R3)^2+(1-(R2/R3)^2)*(6*Rm-(R3-R2))/(12*Rm);
   Fpr=R1^3/((R3-R2)*R3^2)*(Kclad/(4*KfuelL(m))+Kclad/R1/hgap);
   CqsL=1/hwL+2/(s*R3*denfuel*CpfuelL(m))+(Cgm+Fpr)*(R3-R2)/Kclad;

os_qsL(m)=1/CqsL*qs/hwL*0.8*(os_uL(m)/uL(m)+os_denL(m)/denL(m))+1/CqsL*(R1
/R3)^2/(s*denfuel*CpfuelL(m))*os_qvL-1/CqsL/Cpg*os_hL(m);

   os_uL(m+1)=os_uL(m)+dz*R/(P*Cp)*Ph/Ac*os_qsL(m);
   os_denL(m+1)=denL(m)/uL(m+1)*os_uL(m)+(uL(m)-dz*s)/uL(m+1)*os_denL(m)-
denL(m+1)/uL(m+1)*os_uL(m+1);
   os_hL(m+1)=-(P*Cp/R)*(1/denL(m+1)^2)*os_denL(m+1);
end

dp3=0;
for m=1:n3
   dp3=dp3+2*G*os_uL(m+1)+uL(m+1)^2*os_denL(m+1)+(s*denL(m)*dz-
2*G+f3*dz*G/De)*os_uL(m)+(s*uL(m)*dz-
uL(m)^2+f3*dz*uL(m)^2/(2*De)+9.81*dz)*os_denL(m);
end

dp3=dp3-(G*xigma2+f3/De*G^2/(2*deng)+deng*9.81)*os_lamda2;

%%%%Non-Heated region pressure drop
dp_nod=f1/De*Lnod*G+s*denf*Lnod;
dp_nou=(f3/De*Lnou*uL(n3+1)^2/2+9.81*Lnou+s*uL(n3+1)*Lnou)*os_denL(n3+1)+(f
3/De*Lnou*G+s*denL(n3+1)*Lnou)*os_uL(n3+1);
```

```
%%%%total pressure response
  dptotal=dp_nod+dp1+dp2+dp3+dp_nou;

f=zeros(2,1);
f(1)=real(dptotal);
f(2)=imag(dptotal);

%%%%%%%%%%%End of the file
```